University of Wollongong

Research Online

University of Wollongong Thesis Collection 1954-2016

University of Wollongong Thesis Collections

2016

Studies of manganese porphyrin-PEDOT and manganese oxide-graphene composites as water oxidation electrocatalysts and photocatalysts

Danijel Boskovic
University of Wollongong

Follow this and additional works at: https://ro.uow.edu.au/theses

University of Wollongong

Copyright Warning

You may print or download ONE copy of this document for the purpose of your own research or study. The University does not authorise you to copy, communicate or otherwise make available electronically to any other person any copyright material contained on this site.

You are reminded of the following: This work is copyright. Apart from any use permitted under the Copyright Act 1968, no part of this work may be reproduced by any process, nor may any other exclusive right be exercised, without the permission of the author. Copyright owners are entitled to take legal action against persons who infringe their copyright. A reproduction of material that is protected by copyright may be a copyright infringement. A court may impose penalties and award damages in relation to offences and infringements relating to copyright material. Higher penalties may apply, and higher damages may be awarded, for offences and infringements involving the conversion of material into digital or electronic form.

Unless otherwise indicated, the views expressed in this thesis are those of the author and do not necessarily represent the views of the University of Wollongong.

Recommended Citation

Boskovic, Danijel, Studies of manganese porphyrin-PEDOT and manganese oxide-graphene composites as water oxidation electrocatalysts and photocatalysts, Doctor of Philosophy thesis, Australian Institute for Innovative Materials, University of Wollongong, 2016. https://ro.uow.edu.au/theses/4755

Research Online is the open access institutional repository for the University of Wollongong. For further information contact the UOW Library: research-pubs@uow.edu.au

Intelligent Polymer Research Institute

Australian Institute for Innovative Materials

Studies of Manganese Porphyrin-PEDOT and Manganese Oxide-Graphene Composites as Water Oxidation Electrocatalysts and Photocatalysts

A thesis submitted in partial fulfilment of the requirements for the award of the degree

Doctor of Philosophy in the Australian Institute of Innovative Materials

from

The University of Wollongong

by

Danijel Boskovic

B Sc. Nanotechnology (Honours)

Supervisors – Dr. Pawel Wagner, Prof. Gerhard Swiegers and A/Prof. Jun Chen

2016

Thesis declaration

I, Danijel Boskovic, declare that this thesis, submitted in partial fulfilment of the requirements for the award of Doctor of Philosophy, in the Australian Institute of Innovative Materials, is wholly my own work unless otherwise referenced or acknowledged. The document has not been submitted for qualification at any other academic institution.

Danijel Boskovic Date 22/03/2016

Acknowledgements

The author would like to acknowledge Dr Lei Tong for his assistance in gas sensing experiments with equipment provided by A/Prof. Attila Mozer at the Intelligent Polymer Research Institute at the University of Wollongong. Elemental analysis was provided by Mrs Sasha Melnitchenko at the Microanalytical Unit of the Australian National University Research School of Chemistry and Ms Sue Butler at the UOW School of Chemistry. The author would like to acknowledge Dr Patricia Hayes at the Intelligent Polymer Research Institute at the University of Wollongong for performing GPC characterisation. Synthesis and testing of solution-based films and deposition of calcium manganese oxide was done in collaboration with Dr Abbas Ranjbar. The electrodeposition and testing of Mn_xO_y films on FTO glass was done in collaboration with Mr Sabeel M. Basheer, visiting Endeavour Fellow PhD candidate from the National Institute of Technology, Trichy, India. LCGO/RLCGO preparation and deposition was done with instructions from Dr Rouhollah Jalili and Prof. David Officer, who developed this method, and with LCGO produced by the Wollongong Node of the Australian Nanofabrication Facility. Work on Mn_xO_y-graphene composites was done in collaboration with Prof. Rob Stranger and Emeritus Prof. Ron Pace from the Australian National University.

Thank you to my colleagues Mr Nicholas Roach, Mr Rhys Mitchell and Mr Brendan Wright, for help and support during these trying times.

Publications

Gerhard F. Swiegers, Douglas R. MacFarlane, David L. Officer, Amy Ballantyne, Danijel Boskovic, Jun Chen, G. Charles Dismukes, Graeme P. Gardner, Rosalie K. Hocking, Paul F. Smith, Leone Spiccia, Pawel Wagner, Gordon G. Wallace, Bjorn Winther-Jensen, and Orawan Winther-Jensen, *Towards Hydrogen Energy: Progress on Catalysts for Water Splitting*, Australian Journal of Chemistry, 2012, 65, 577–582

Jun Chen, Pawel Wagner, Lei Tong, Danijel Boskovic, Weimin Zhang, David Officer, Gordon G. Wallace and Gerhard F. Swiegers, *A light-assisted, polymeric water oxidation catalyst that selectively oxidizes seawater with a low onset potential*, Chemical Science, 2013, 4, 2797

Danijel Boskovic, Gerhard F. Swiegers, *Kinematic Molecular Manufacturing Machines*, submitted for publication.

Danijel Boskovic, Sivakumar Balakrishnan, Jun Chen, Pawel Wagner, and Gerhard F. Swiegers, *Studies of poly(3,4,-ethylenedioxythiophene) (PEDOT) films containing cationic Mn porphyrins. A loading-dependent de-metallation of Mn(III)TPP in PEDOT (Mn(III)TPP=5,10,15,20-tetraphenylporphyrinato manganese(III)),* submitted for publication.

Danijel Boskovic, Sabeel Basheer, Pawel Wagner, Ronald J. Pace, Rob Stranger, and Gerhard F. Swiegers, *Bioinspired Flexible, Amorphous Calcium / Manganese Oxide Graphene Composites as Water Oxidation Catalysts*, prepared and awaiting submission following patenting strategy.

Danijel Boskovic, Ron Pace, Robert Stranger, Gerhard F. Swiegers (Australian National University and the University of Wollongong), *Biomimetic Water Oxidation Catalystw*, Australian provisional patent application – in preparation

Abstract

In this study the biomimetic reproduction of the Oxygen Evolving Centre (OEC) of PSII, consisting of a $CaMn_4O_4$ cluster held in place by the surrounding protein scaffold, was attempted in a simplified manner. In the OEC the water oxidation reaction takes place on one binuclear Mn-O_2-Mn site in a repetitive manner. A mimic of this feature was attempted by using Mn porphyrins in close proximity held in place by a conducting poly(3,4-ethylenedioxythiophene) (PEDOT) matrix. In another approach, an inorganic, crystalline Mn_xO_y deposited on a conducting graphene substrate was used for the same purpose.

Films of Mn porphyrin / PEDOT (PEDOT:PSS in the case of electrochemical polymerisation) were fabricated by embedding the porphyrin in PEDOT during vapour phase polymerisation and electrochemical polymerisation of the conducting polymer. The Mn porphyrin species studied were 5,10,15,20-tetraphenylporphyrinato manganese(III) chloride (MnTPP), 5,10,15,20-tetrakis(4-sulfonatophenyl)porphyrinato manganese(III) chloride sodium salt (MnTPPS), 5,10,15,20-tetrakis(4-methylpyridinium)porphyrinato manganese(III) chloride tetraiodide (MnTMPyP), poly(5-(4-vinylphenyl)10,15,20-tris(4-sulfonatophenyl) porphyrinato manganese(III) chloride sodium salt (MnPVTPPS). The films were tested by linear sweep voltammetry (LSV) and chronoamperometry (CA) under illumination to analyse photocurrent activity in an aqueous electrolyte. The samples were further studied by UV-Vis spectroscopy and elemental analysis to confirm the exact status of the porphyrin - complexed Mn ion in the film corresponding to observed levels of photocurrent activity. The MnTPP/PEDOT composite was singled out for detailed analysis to confirm, by gas chromatography, the evolution of O_2 and H_2 at a constant potential of 0.7 V (*vs*

Ag/AgCl) under illumination. This material was then further studied by elemental analysis and UV-Vis spectroscopy to reveal that the Mn ion was lost, from the porphyrin centre, during the polymerisation step, leaving a free base porphyrin in the film. The gas evolution was therefore linked to decomposition processes rather than the interaction between Mn centres.

Using a different approach, Mn_xO_y - birnessite was electrodeposited on conductive FTO glass as well as graphene - coated substrates. To mimic reaction centre composition, Ca ions were incorporate into manganese oxides. This was achieved by adding Ca ions during an electrodeposition step or embedded into the graphene substrate prior to electrochemical process. These materials underwent a study by linear sweep voltammetry and chronoamperometry to ascertain the most productive combination of the catalytic species and variations of the graphene substrate. While the Ca ion incorporation did not lead to an appreciable increase in water oxidation, the Mn_xO_y/RLCGO composite featured a low onset of water oxidation at 1.1 V (*vs* Ag/AgCl) with electrocatalytic performance surpassing that of Pt in the range 1.1 – 1.3 V (*vs* Ag/AgCl) in an aqueous electrolyte.

Abbreviations

AAS	Atomic absorption spectrophotometer
AIBN	Azobisisobutyronitrile
CA	Chronoamperometry
CV	Cyclic voltammetry
DCM	Dichloromethane
DMF	*N*,*N*-Dimethylformamide
DMSO	Dimethylsulfoxide
EDOT	3,4-Ethylenedioxythiophene
EV	Electrodeposition Vessel
FTO	Fluoride tin oxide
GC	Gas chromatography
GO	Graphene oxide
GPC	Gas permeation chromatography
h	Hour
LCGO	Liquid crystal graphene oxide
LSV	Linear sweep voltammetry
min	Minute
MALDI-TOF	Matrix-assisted laser desorption/ionization – time of flight
MnPVTPPS	Poly(5-(4-vinylphenyl)10,15,20-tris(4-sulfonatophenyl) porphyrin manganese(III) chloride sodium salt
MnTMPyP	5,10,15,20-tetrakis(4-methylpyridinium)porphyrinato manganese(III) chloride tetraiodide
MnTPP	5,10,15,20-tetraphenylporphyrinato manganese(III) chloride

MnTPPS	5,10,15,20-tetrakis(4-sulfonatophenyl)porphyrinato manganese(III) chloride sodium salt
NMR	Nuclear Magnetic Resonance spectroscopy
OEC	Oxygen evolving centre
PEDOT	Poly(3,4-ethylenedioxythiophene)
PEDOT:PSS	Poly(3,4-ethylenedioxythiophene) polystyrene sulfonate
PSII	Photosystem II
RGO	Reduced graphene oxide
RLCGO	Reduced liquid crystal graphene oxide
S	Siemens
Sec	Second
THF	Tetrahydrofuran
UV-Vis	UV-Visible light absorbance spectroscopy
V	Volt
VPP	Vapour phase polymerisation
WOC	Water oxidising complex
ε	Extinction coefficient
ρ	Resistivity
σ	Conductivity
Ω	Ohm

Table of contents

List of figures

List of tables

1 Introduction

1.1 The advance of miniaturisation

Modern-day human society is utterly dependent on efficient machines for the production of goods and energy, transportation, construction and, more recently, processing of information. Our traditional view of machines, however, is based on macro-scale mechanisms utilising kinematics and chemistry to deliver reliable industrial performance in all fields of human endeavour. Thanks to scientific and technological developments in the 20th century there is an increasing trend to turn attention towards inward progress – the miniaturisation of machines.

Miniaturisation as a technological concept arose with the advent of microelectronics in the mid-20th century as one of the first forays into highly structured matter and function on the microscopic scale made by humans. In line with that newfound optimism for technology, Richard Feynman first raised the concept of artificial molecular scale machines in his seminal 1959 talk “There’s Plenty of Room at the Bottom” [1]. The talk revolved around the idea that complex structuring at the nanoscale was a yet unrealised area full of potential, giving rise to the famous challenge of writing the entire Encyclopaedia Britannica on the head of a pin. Feynman posited the idea of utilising near-molecular scale nanotechnology to construct matter at the atomic scale and upwards. The concept was famously explained as a tiny robot the size of a nanoparticle that would have small robot arms to physically attach atoms to one another, building up structures by design. Evoking the imagery of “Maxwell’s Demon” [2], an imaginary microscopic agent able to perform tasks at the atomic level seemingly against the laws of thermodynamics, the concept remains highly speculative and to date not physically achieved. It is nonetheless an inspiring concept and expresses the historic shift in technology, understood as large and impressive in the form of towering ships, bridges and skyscrapers in the past, towards small and efficient, in the form of microchips and robotics.

At the same time biology was entering the molecular scale with Linus Pauling's work on the function of proteins in 1948 [3] and radically advanced with Watson and Crick's discovery of DNA in 1953 [4] as the core mechanism of genetics and therefore life. The continued focus on molecular scale processes in biology has led to the establishment of molecular biology and modern biotechnology. In a similar vein to Feynman's proposal, biological enzymes have been thought of and referred to as machines in the biochemistry community for some time [5]. Expanding on that notion, K. Eric Drexler posited the idea of approaching biological enzymes as machines in 1981 as well as utilising other molecular components and functions like bacterial flagellum, microtubules and intermolecular forces in conjunction for building a nanoscale device [6]. He outlined a strategy of first using proteins to create hybrid systems consisting of a protein with appended molecular components to extend its functionality. Molecular scale analogues to structural components, conductive wires and sensors would need to be utilised to build a macromolecular assembly capable of performing basic tasks on that scale. Building such a device would be painstakingly done at first with macroscopic scale scientific equipment but once such a functioning system exists as a reliable tool, newer more refined models could be made using that tool in progressive iterations to eventually transcend the limitations of the organic system. The challenges of even the first step lie in understanding the critical components that determine the mechanism of action in proteins. Furthermore proteins are folding systems that rely on very specific aqueous conditions and cannot be easily made to function outside of that environment, or branch out into other areas such as forming of crystal lattices.

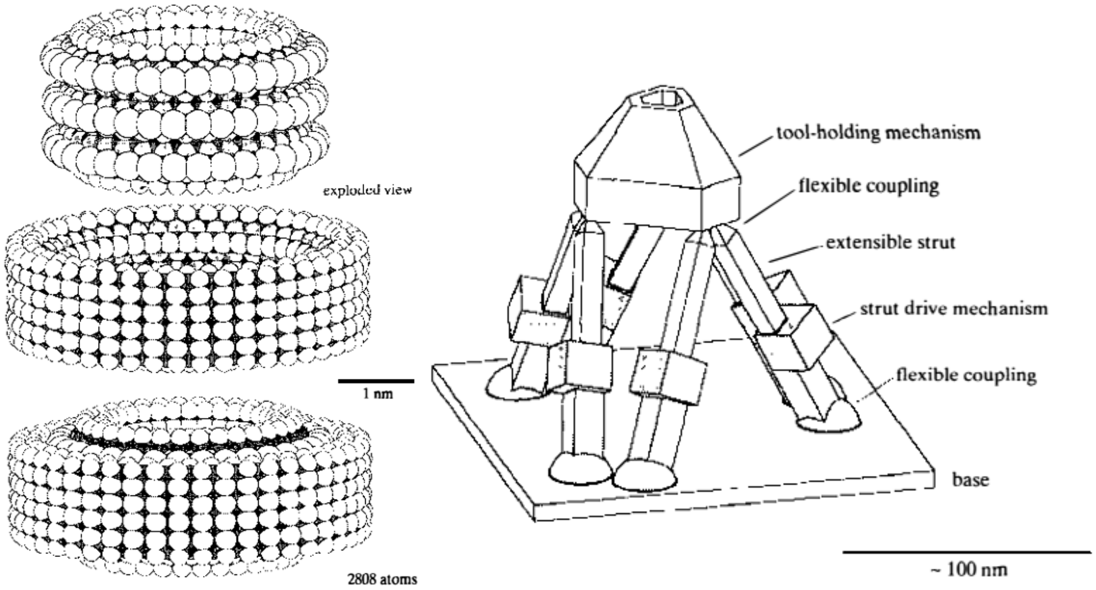

Figure 1.1 A rotary bearing based on modified diamond structure (left) and schematic of a mechanosynthetic device based on a Stewart platform (right). Reproduced with permission from reference [7].

In his following works *Engines of Creation* [8] and *Nanosystems: Molecular Machinery Manufacturing and Computation* in 1992 [9] as well as the review *Molecular Nanomachines - Physical Principles and Implementation Strategies* [7] Drexler has written extensively, albeit entirely theoretically, about the dramatic advantages that would be conferred upon society if we had available to us manufacturing machines that operate in the realm of 1-1000 nm. The previous concept of engineering proteins was expanded upon by proposing an entirely artificial system using ultra-small gears, cogs, and moving parts built from molecular scale crystals of covalently bound carbon structures termed *diamondoids*. Such a device would be capable of transporting reagents to active sites and forming molecules from molecular or atomic substrates in successive steps along an assembly line in a process called *mechanosynthesis* (an example of a nanoscale component and a mechanosynthetic device is shown in Figure 1.1). This technology often referred to as *assembler* or *nanofactory* and *nanobots* in popular media, is based on extensive theoretical modelling of possible structures and function, and hitherto not realised in physical form. It is presented as a design goal to be accomplished by a series of more basic models with which more efficient and smaller models could be fashioned. The existence of such technology in physical form would have profound historic impact on humanity as a whole, quite possibly ending the era of human physical labour altogether as products could be built entirely using a replicator system that performs complex construction from the molecular scale upwards.

Drexler's proposal has however, at best, proven to be exceedingly difficult to realise with current atomic placement techniques, if not impossible. The problem lies in the fact that to date, known enzymatic systems from biology have been proven challenging to reproduce, let alone engineer directly. In other words, full control over enzymes and enzyme-like systems has not yet been accomplished. In this thesis the fundamentals of what would constitute a machine on the molecular level are explored to elucidate the concept of *molecular manufacturing machines*. To date, the only true *molecular manufacturing machines* that exist are the components that comprise living organisms at the cellular level. It is therefore prudent to employ a biomimetic approach, using known biological systems as a precedent, in order to understand the dynamics of machine-like action on the molecular level. The challenge is to arrive at an elegant, reductionist understanding and application of abiological catalysts that are machine-like in their actions.

1.2 The principles of "kinematic manufacturing machines"

As noted in the review of Garcia-Garibay and Vogelsberg [10] a machine is generally defined as a dense, multicomponent assembly of parts that transmits force, motion or energy from one component to another. In a kinematic manufacturing machine, that impulse is used to transform starting materials into new articles or items. The translation of force by movement is defined by the term *kinematic*. A framework can be established, drawing on General System Theory by Ludwig von Bertalanffy [11] and recently extended upon [12]. This framework provides an overview of the features of a machine in an overall sense, which can be applied to the more specific case of kinematic manufacturing machines. The individual components of a kinematic manufacturing machine must typically display certain properties, including the following:

(1) Regular and repetitive action by
(2) a multiplicity of coupled components under the influence of
(3) a transfer of energy, where the individual actions are
(4) restricted to a single degree of freedom that defines the action of the component, and where the
(5) system acts dynamically and rapidly with clear input and output trajectories.

In order to realise its function, the individual components of a machine must typically be precisely designed and machined so as to achieve *structural complementarity* with the other parts with which they interact. Thus, for example, machines commonly use interdigitating cogs. Inter-component structural complementarity of this type is needed to ensure that each part moves only along optimum pathways and trajectories to thereby be *coupled* to the other parts, allowing them all to work collectively as one in a synchronous manner [12, 13]. This also applies to electronic machines such as computers, where the translation of energy is not by movement but by selectively passing current through components. Such collective coupling and optimum trajectories are essential to the efficient transmission of the driving energy impulse with the minimum energy consumption. Without coupling, the required synchronicity of the multi-component assembly is destroyed and the machine cannot achieve its function. Therefore the principles above can be extended on by including the following additional principles which therefore also apply to kinematic manufacturing machines:

(6) The required coupling of the components and their interaction with the input and output are typically achieved by structural complementarity. This has the effect of

(7) restricting the action of the machine components to the optimum pathways and trajectories, to thereby

(8) ensure optimal energy transfer and

(9) ensure synchronicity in the system.

The absence of any one of these features destroys the synchronicity of the assembly and thereby makes the machine action impossible. A final set of features therefore arise from the fact that the above properties are not optional, but required for the sustained functioning of the system. If one of the properties is absent or not optimised, the error compounds non-linearly, leading to the machine not operating properly or not operating at all. This can be likened to having one gear out of place in a clockwork mechanism, resulting in, not one less gear movement overall, but the potential complete breakdown of the mechanism. Such a feature of a machine is known as *synergy*, which refers to the situation where system is capable of producing a result that is more than the sum of its parts [13]. More specifically, this type of synergy is called *functional convergence* in Complex Systems Science [13]. Functional convergence refers to the property of a system where every part functions cooperatively with every other part. That is, their concerted actions and functions converge to create new capabilities that would otherwise not be possible. Therefore, in addition to the previous points, one more crucial property of kinematic manufacturing machines is:

(10) Synergy and specifically a form of synergy called functional convergence.

The above descriptions summarise the set of key principles behind the operation of machines in general. When they are simultaneously present they unequivocally indicate the presence of a machine performing work in a repetitive and sustained fashion. The above rules can be applied to kinematic manufacturing machines, that is, machines that perform work with moving parts in order to manufacture a physical product. In this specific case, the input and output are physical compounds and structures, and the transfer of energy achieved by the motion of components forcing starting materials to interact with one another, forming new products. The actions of biological and abiological catalysts may be assessed in terms of these criteria, as one would analyse the mechanism of action behind a macro-scale manufacturing machine, such as a robotic assembly for automobile construction.

1.3 Enzymes as “molecular manufacturing machines”

Catalysts are species that accelerate chemical reactions without themselves being consumed in the process. Much like macro-scale manufacturing machines, they transform reactants, known as substrates, into new chemical entities, called products. The most efficient catalysts by far are the catalysts of biology known as *enzymes*. The maintenance and creation of life on Earth depends on the ability of enzymes to facilitate chemical transformations in biochemical systems. To this end, enzymes often display truly amazing vigour, specificity, and reliability [13]. The fact that life itself depends on the action of enzymes testifies to their remarkable power.

Our understanding of how enzymes operate has been unfolding over more than 100 years. In 1894, Emil Fischer discovered that the specificity of glycolytic enzymes indicates that they must have a particular shape into which the substrate fits exactly [14]. He described the process of enzyme-substrate interactions as being similar to a key fitting a lock. The substrate only bound and was transformed if its shape was complementary to the docking site presented by the active site of the enzyme. This feature came to be known as *molecular recognition* and the theory as the “*Lock-and-Key*” theory. Modifications were later proposed by Haldane in the 1930’s and Koshland in 1958. In their view, the match between the key and the lock need not be exact, provided that the substrate or the active site could distort to thereby realize an *“induced fit”*[15].

In 1946, Linus Pauling made an important advance. He noted that many enzyme active sites were structurally complementary to the optimum *“transition state”* of the reaction that they catalysed, not the substrate [3]. He suggested that this structural complementarity likely caused the enzyme to form a transition state that was close to ideal, thereby minimizing the energy consumed in the reaction, facilitating its course. This has been supported by subsequent work [16, 17].

One consequence of Pauling's theory was the realization that if enzyme active sites complement their optimum transition state, then they must also control the way in which substrate functional groups approach each other or disengage from each other during reaction. In fact, they must limit this approach or disengagement to trajectories that are close to ideal since the optimum transition state represents the energetically most favourable arrangement for reaction. This realisation spawned a range of theories seeking to capture the concept of "*optimized approach trajectories and collision pathways*" [18-23].

The concept of an "*ideal*" collision between the reactants must necessarily involve repeated, regular motion in the enzyme to mediate such a collision over and over again, with each repeat generating a new product molecule. Starting in the 1970's, biochemists therefore started examining the link between repetitive conformational motion in enzymes and their catalytic properties [24-29]. Evidence has since been collected for the existence of a network of *"coupled protein motions"* that facilitate enzymatic catalysis and that occur on the same timescale as the microscopic rate at which the enzyme generates product molecules [24]. This network appears to comprise of fast, equilibrium thermal motions that contribute to slower conformational changes which control the rate of production [24, 30, 31].

In the early 1990's, Bob Williams, a bio-inorganic chemist at Oxford University put together the concepts of molecular recognition (by structural complementarity), optimised approach trajectories and pathways, and the role of regular, repeated conformational motion along a single degree of freedom in his description of enzymes as "*dynamic mechanical devices*" [32]. In effect, Williams recognised that kinematic mechanical devices also display all of the above elements, albeit at a macro- not at a molecular scale. Thus, just as the interdigitating cogs of a machine harness structural complementarity to interlock their teeth and thereby constrain their trajectories and motions to the optimum, so do the components and active sites of enzymes. That is, protein motions in enzymes guide the substrate through a strictly limited set of optimum movements [32]. They do so in a manner analogous to the way in which the components in mechanical devices are constrained by their structure to interact ideally with each other [32]. These motions are, moreover, driven by regular, repeated conformational flexing on the molecular scale by the enzyme, which is qualitatively identical to the mechanical impulse that drives macro-scale machines.

Swiegers subsequently elaborated upon the proposals of Williams and explained their fundamental origin in his book on "*Mechanical Catalysis*" [12]. D*ynamism in substrate uptake and product expulsion by enzymes* was shown to be another key feature of their action, and that their catalytic properties demonstrate *functional convergence* [12].

1.4 The catalytic basis of kinematic molecular manufacturing machines

Enzymes typically perform at frequencies of up to several million molecules.s^{-1} [33] with often astonishingly high selectivity even in the very mixed feedstock streams of biology. By comparison, man-made catalysts typically achieve nowhere near the above turnover frequencies and have to rely on highly purified feedstock streams because their selectivity is so poor. That is, the catalyst sites do not successfully target specific molecules for uptake and can be easily blocked by other molecules that are not catalysed, whereas an enzyme is capable of interacting with only one type of molecule within a diverse mix of organic compounds that typically exist in its surroundings. One may ask: what fundamental feature of catalysis is generally different in enzymes compared to abiological catalysts? In other words, what is the reason for the high catalytic performance of enzymes compared to abiological, man-made catalysts?

A key insight to answering this question can be realised by comparing the processes in enzymes to that of macro-scale kinematic manufacturing machines, that is, machines that generate a product by the successive interaction of moving parts. In such a manufacturing machine, as noted in a previous section, the great production efficiency is achieved by limiting and synchronising the motion of components to a single, optimum degree of freedom which comprises the manufacturing action. Likewise enzymes are believed to control and direct the movement of substrates, causing them to collide with each other at the optimum point of transition state formation. That is, the transition state arises not as a random statistical probability due to thermal motion but the enzyme moves in such a way as to create ideal collisions between reactants. Like macro-scale kinematic manufacturing machines, enzymes are therefore similarly believed to control and constrain how substrates approach and “collide“ with each other at the optimum point of transition state formation. That is, they are believed to generally create “ideal“ or near ideal collisions between reactants, with their overall rate of catalytic turnover determined by their rate of conformational flexing along the single degree of freedom. By contrast, man-made catalysts would not generally have a capacity for such control; they would have multiple degrees of freedom available to them and be unconstrained in this respect.

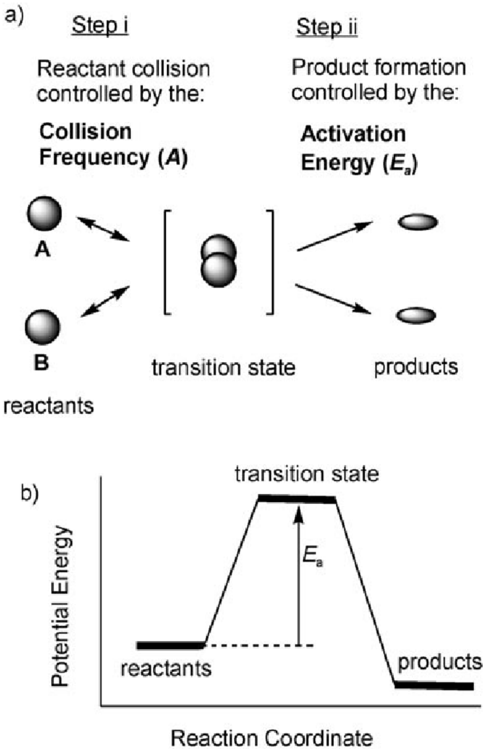

Figure 1.2 Schematic depiction of a non-catalysed chemical reaction as (a) a collision between two molecules, A and B, leading to a chemical reaction where products are formed, and (b) the energy profile throughout this process, showing the minimum energy needed for product formation (termed: the activation energy, E_A). Reproduced with permission from reference [34].

In the classic collision theory model by Max Trautz [35], chemical reaction proceeds by collision between reactants to form products (see Figure 1.2). The overall rate of reaction (k) is given by the Arrhenius equation [Eq. (1)], which consists of two factors: (i) the frequency of collision between the reactant molecules (the pre-exponential term

A, known as the *"Collision Frequency"*), and (ii) the proportion of those collisions that are sufficiently energetic to result in product formation (the exponential term, $-E_A/RT$, where E_A is the *"Activation Energy"* of the reaction) [34]. The rate of all chemical reactions, including by catalysis, is controlled by whichever of these terms is the rate limiting factor.

$$k = A \exp(-E_A/RT)$$

In the case of a kinematic molecular manufacturing machine, the reaction rate must clearly be determined by the collision frequency (A), since this is what the catalyst does – it creates (ideal) collisions. By contrast, a man-made catalyst that does not constrain action along a single degree of freedom is not limited by the collision frequency but rather by the proportion of collisions that are successful – that is, by the exponential term, $-E_A/RT$, and the activation energy (E_A) of the reaction.

This hypothesis is enhanced by observations in enzymology by Michaelis and Menten, who found that the kinetics of enzymes generally depends on a pre-reaction enzyme-substrate complex, termed the "Michaelis Complex" [36]. If enzymes act as kinematic molecular manufacturing machines, the Michaelis complex can be understood as the molecular machine after it has taken up a reactant substrate and while it is going through the process of conformationally flexing along its single degree of freedom leading to product formation. The formation of the Michaelis complex and the switching between it and the free-standing enzyme state can therefore be understood as rate limiting. By comparison, the kinetics of abiological catalysts are not generally limited by such a species, and are instead governed by their activation energy, E_A [12, 34].

1.5 The mechanism of oxygen evolution in photosynthesis: a case study

Natural photosynthesis is the natural process that converts carbon in the atmosphere to organic compounds in plants using sunlight and water. It consists of two major parts, termed Photosystem I and II (PSI, PSII), of which PSII is tasked with oxidising water using sunlight to supply electrons that are transmitted through a complex pathway to PSI where they are eventually utilised to produce metabolic compounds from CO_2 in the atmosphere. In the context of this thesis PSII is of vital importance as its function is to efficiently split water using sunlight. Understanding the process of water splitting and utilising it efficiently is currently a hot topic of interest as it can offer a bountiful source of energy for humans, in the form of captured hydrogen gas [37]. Once this process is fully understood it can be applied, and the resulting hydrogen ions can be easily reduced to form H_2 for use in other applications.

1.5.1 The structure of the oxygen evolving centre in photosystem II

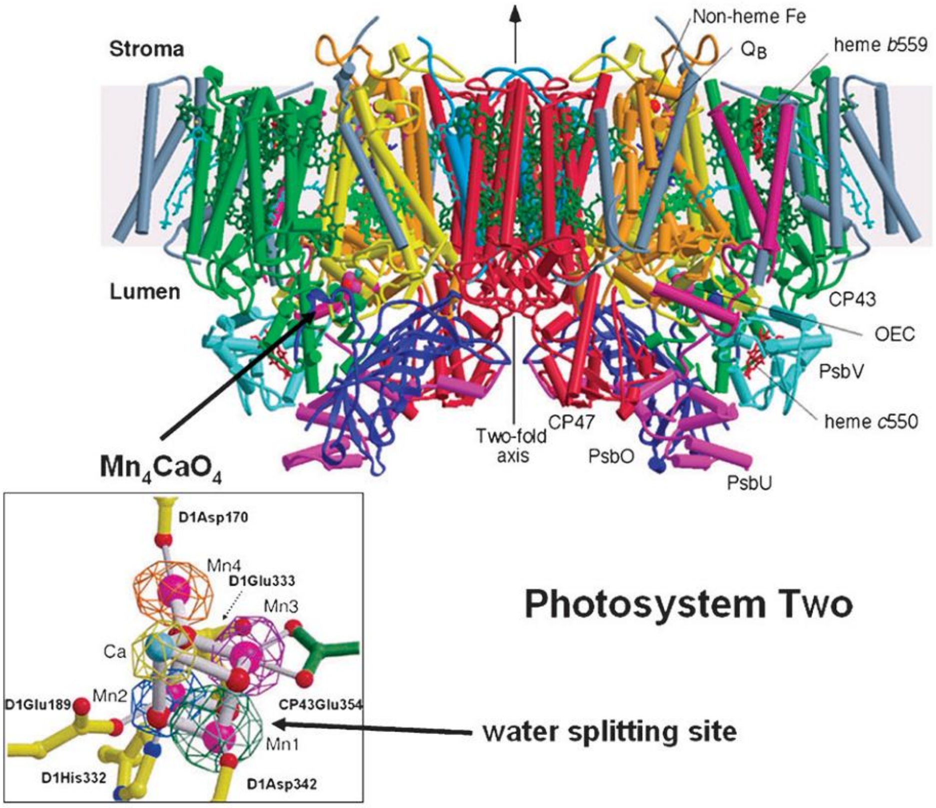

Figure 1.3 Side view of the structure of Photosystem II. Reproduced with permission from reference [37].

Photosystem II (PSII) is a protein complex nested in the thylakoid membrane of plant, algae and cyanobacteria that consists of 19 protein subunits and 57 cofactors that facilitate light absorbance, charge transfer and finally water oxidation (Figure 1.3) [37, 38]. Of special interest is the oxygen evolving centre (OEC), sometimes also called water oxidising complex (WOC), which performs the crucial step of water oxidation. It consists of a cube-shaped molecule made up of four Mn and one Ca atom with surrounding ligands, called a cubane, that was first elucidated by X-Ray crystallography by Ferreira in 2004 [39]. The exact structure of the cubane complex is to date hotly contested, as new crystallographic data becomes available, as well as more detailed analysis on the oxidation state of the individual Mn ions.

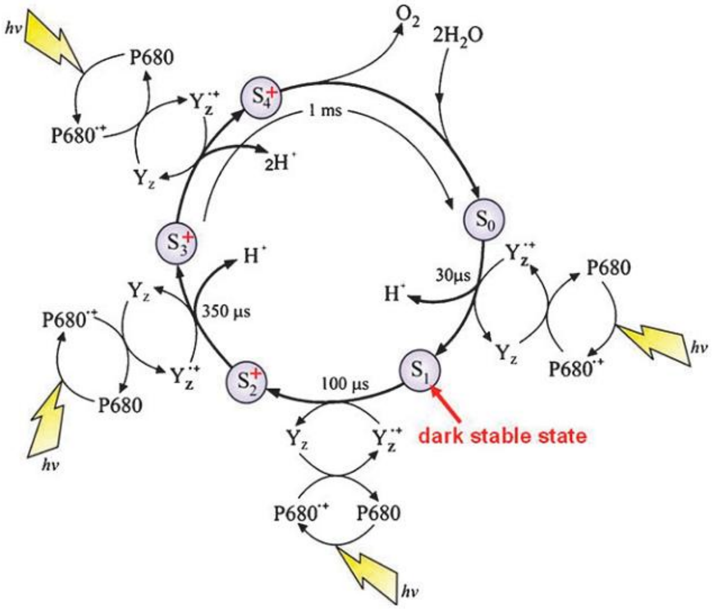

Figure 1.4 S-state cycle of water oxidation by the OEC. Reproduced with permission from reference [37].

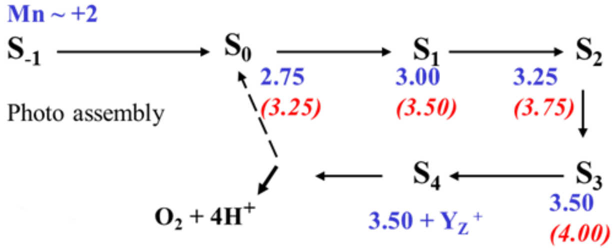

Figure 1.5 S-state cycle of the OEC with mean oxidation states according to Stranger and Pace (blue) and others (red; in brackets), from reference [40-42] [43].

The Mn_4Ca cluster operates through a series of five intermediate states that make up the cyclic mechanism of action of the compound, referred to as the Kok or S-state cycle [44]. The states are advanced by four, light-driven, one-electron oxidations by the P680 reaction centre (see Figure 1.4). Up to state S_3 [45], water molecules can freely exchange with the catalytic site until the final oxidation occurs in a concerted manner at S_4, resulting in subsequent release of O_2. The mean Mn oxidation states proposed by Stranger and Pace [40-42] and others (in brackets) [43] are shown in Figure 1.5. The chemistry performed by the OEC occurs at high turnover (~1000 s^{-1}), is thermodynamically efficient (< 0.3 V overvoltage) and involves Earth abundant elements (Mn, Ca). This makes it a highly attractive candidate for biomimetic studies.

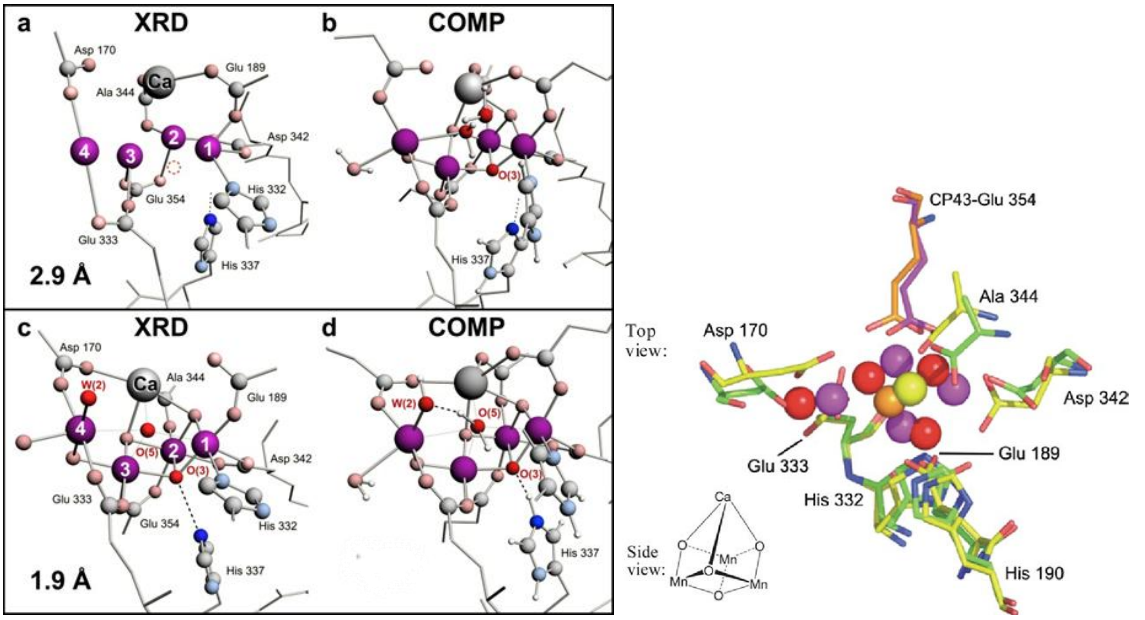

Figure 1.6 The two most recent X-ray crystal structures of the OEC (from references [46, 47]) (left) and dimensionally accurate superimposition of the "London" and "Berlin" OEC structures with a simplified drawing in the inset (right). Reproduced with permission from reference [48].

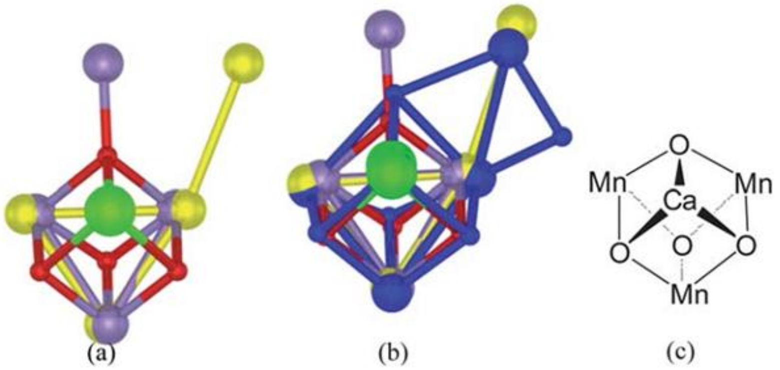

Figure 1.7 Dimensionally accurate superimposition of the (a) “London” (yellow) and “Berlin” (red-purple) OEC structures and the more recent (b) “Osaka” structure (blue) superimposed on the two, and (c) a simplified drawing of the structure, all without surrounding protein. Reproduced with permission from reference [48].

Seven X-ray crystal structures have been reported for the S_1 state, with resolutions from 3.7 Å to 1.9 Å [39, 46, 47, 49-51]. The two most recent [46, 47] reveal all atoms except for hydrogen and are shown in full in Figure 1.6 (a) and (c). A more simplified superimposition of three earlier structures without the surrounding protein [48] is shown in Figure 1.7. Pace and Stranger have performed substantial computational analysis and physical characterisation of the Mn-Mn distances [52, 53] by extended X-ray absorption fine structure (EXAFS) measurements and have determined that the S_1 OEC (as crystallised) can adopt multiple simple tautomeric forms. These forms differ by single-proton internal transfers (see Figure 1.6). These findings point to the Mn-Mn distances being longer than previously reported [43, 50] due to the Mn in the 1.9 Å structure having undergone X-ray induced reduction [54, 55]. The distances were found to be ~2.8-3.0 Å and point to a new model where the oxidation states for individual Mn ions in the S_1 state are III, III, III, II rather than the established III, IV, III, II model [47]. The cumulative findings by Pace and Stranger [52, 53] by means of Time-Dependent DFT

[56] and empirical analysis approaches [40-42] support this paradigm. Furthermore, Pace and Stranger have elucidated the critical role played by the Ca ion in the OEC in transporting water ligands to the nearby ‘cleft’ region between Mn1, 3 and Ca [40, 57].

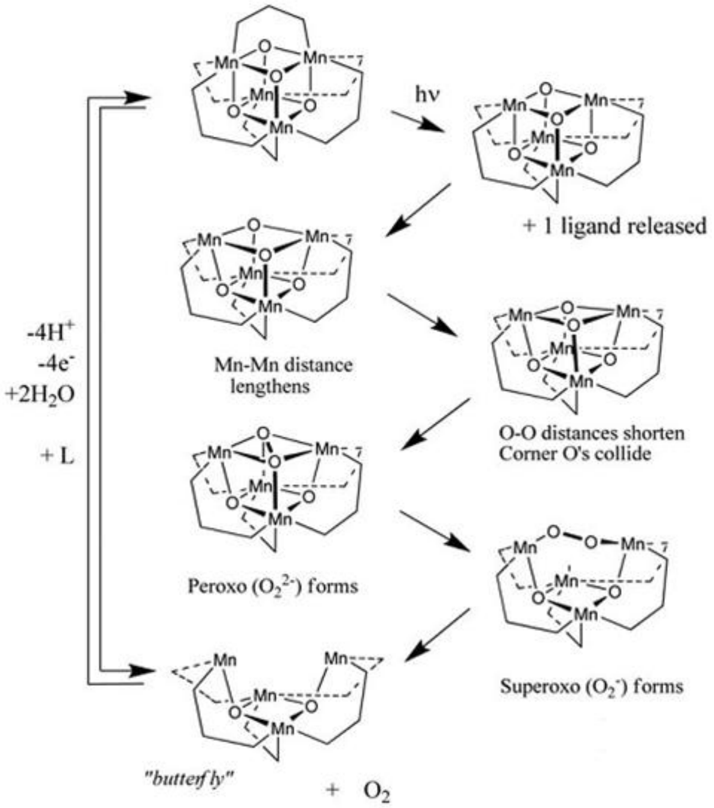

Figure 1.8 Simulation of the model complex $Mn_4O_4L_6$ during catalysis, based on the OEC. Reproduced with permission from reference [48].

Dismukes and Ruettinger performed a simulation of a close cubane mimic to the OEC form, $Mn_4O_4L_6$, where L = (*p*-$MeOC_6H_4$)$2PO_2^-$, showing the physical conformational change in the OEC during the S-State cycle (see Figure 1.8) [58-60]. Information on the precise oxidation state and distance between the Mn ions is crucial when attempting to build biomimetic catalysts that function along those principles. It is therefore vital to replicate as closely as possible the structure of the Mn_4O_4Ca cluster for repeated, sustainable water oxidation, given that complete replication of functioning PSII is, so far, impossible outside of a living cell.

1.6 Abiological bio-inspired catalysts

In this and the following sections several man-made catalysts that can be said to display actions, features, or outcomes that are consistent with a kinematic manufacturing action are reviewed in the context of water oxidation and reduction. The mechanism of action of many catalysts has not been fully clarified. It is therefore often not possible to determine with certainty if a particular catalyst employs a kinematic action or not. In such cases, one can only assess the distinctive features that the catalyst exhibits, or alternatively, the outcome that it achieves, and determine whether these are consistent with such an action.

Porphyrin molecules are of special interest given their versatile photonic and electronic nature, capacity to hold metal ions in precise arrangement and direct presence in biological systems for these reasons. In nature they are used predominantly as light harvesting arrays and charge carriers, and not for direct catalysis. Work has been done however on the capability of porphyrins as catalysts, which is explored in the following sections, focusing on areas directly related to water-splitting.

1.6.1 Cofacial diporphyrin catalysts for oxygen reduction

The central aim of this project is to develop simple, practical, molecular machine-type catalysts based on biological precedents. One of the difficulties in this respect involves finding test groups that are catalytically active only in dimeric and not monomeric form, to utilise the benefit of binuclear reaction sites [61]. Since the “machines” used in nature, such as the OEC, comprise of multiple components, at least two catalytic groups in close proximity are needed. These must further generate a notable catalytic effect only when they interact with each other in an optimal way. Moreover, the interactions must have been studied and characterised in detail previously.

One catalytic group that matches these requirements and is known to be present in numerous enzymatic systems such as PSII, is the group of metalloporphyrins. In co-facial form, metalloporphyrins catalyse numerous reactions. Starting in 1977 a series of catalysts were developed by Collman et al. [62, 63] that involved two metalloporphyrins arranged in an eclipsed, face-to-face assembly of “cofacial” porphyrins. The structure of these catalysts typically includes some form of covalent linkage between the two porphyrins, constraining their motion and position in close proximity to thereby induce catalytic action on substrate molecules between the two porphyrins.

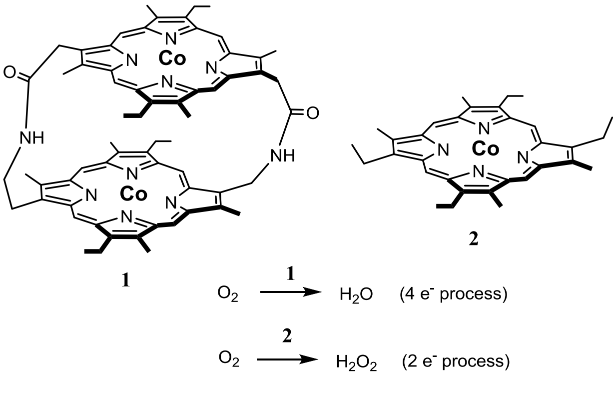

Figure 1.9 Dicobalt diporphyrin oxygen reduction catalyst, from references [62, 63].

Several of these catalysts employ catalytic actions where the facing metalloporphyrins appear to act cooperatively (convergently) to reduce dioxygen, O_2, to two water molecules, H_2O. Such an action would be consistent with the principles of kinematic manufacturing. For example, dicobalt porphyrin **1** (see Figure 1.9), was found to catalyse the 4-electron reduction of O_2 to H_2O at pH <3.5 and at potentials negative of 0.71 V (*vs*. NHE) when adsorbed on a graphite electrode [62, 63]. The corresponding monomer **2** (see Figure 1.9) catalytically generated only the 2-electron product, H_2O_2 under similar conditions. Studies showed that **1** did not catalytically convert H_2O_2 into H_2O, and therefore did not simply perform successive reductions. That is, the catalytic reaction facilitated by **1** was not a sum of two reactions performed by **2**, but rather a different reaction altogether. This indicates a case of synergy, where the result is not a sum of its components, but where the work of separate components converge to create a new product.

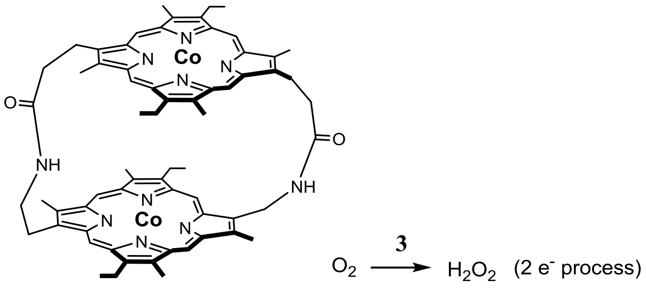

3

Figure 1.10 Dicobalt diporphyrin oxygen reduction catalyst that is free to flex about more than a single degree of freedom, from reference [62, 64].

The species **3** for example (see Figure 1.10) is a variation of the previous catalyst **1**, which differs in having greater conformational freedom due to the presence of an extra carbon in its linkers. Unlike **1**, **3** exclusively generates H_2O_2 in a 2-electron process

[62, 64, 65]. It can be concluded that the covalent links in species **1** likely constrained conformational flexing to oscillation about an eclipsed face-to-face arrangement which was crucial to the catalysis, whereas the more flexible linkage in species **3** allowed for additional lateral movement that was detrimental to the catalytic action. This could be likened to a motor where two gears do not catch each other's movement and therefore do not work in a concerted fashion.

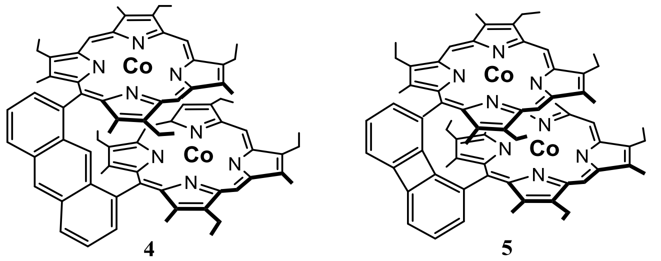

4 **5**

$$O_2 \xrightarrow{\mathbf{4}} H_2O \quad (4\ e^- \text{ process})$$

$$O_2 \xrightarrow{\mathbf{5}} H_2O \quad (4\ e^- \text{ process})$$

Figure 1.11 Dicobalt diporphyrin oxygen reduction catalysts that are constrained to flex about a single degree of freedom, from reference [66-68].

In further studies the linkage between the two cobalt porphyrins was replaced by a rigid aryl linker, as depicted in **4** and **5** (see Figure 1.11) [66-68]. This linker constrained the dicobalt porphyrin assembly even more to a single mode of rapid, repeated longitudinal flexing. The catalyst is therefore commonly referred as a "Pac-Man" catalyst because of this eclipsed face-to-face arrangement. As was the case for species **1**, catalysis by this species was also found to facilitate the 4-electron oxygen reduction process. Clearly, selectivity for the 4-electron reduction of oxygen could be achieved by constraining conformational motion of the two metalloporphyrin components to a single degree of freedom that involves regular, repeated opening and closing of the “bite” of the cofacial metalloporphyins.

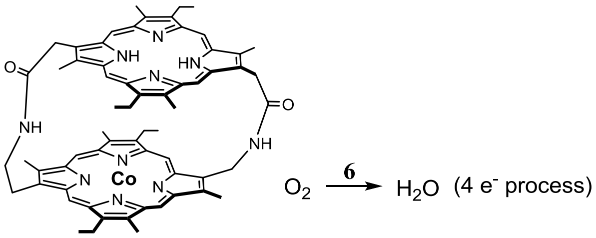

6

Figure 1.12 Monocobalt diporphyrin oxygen reduction catalyst, from reference [69-71].

A later discovery interestingly demonstrated that partial selectivity for oxygen reduction could be achieved with only one redox metal in a diporphyrin assembly [69-71]. Both the monocobalt diporphyrin **6** (see Figure 1.12), which is the partially demetallated variant of **1**, as well as a cobalt-aluminium diporphyrin were found to catalyse the 4-electron reduction of oxygen, albeit in competition with a simultaneous 2-electron process [72]. The second Co ion in **1** was thereby revealed to act as a Lewis acid during catalysis [66, 69-71].

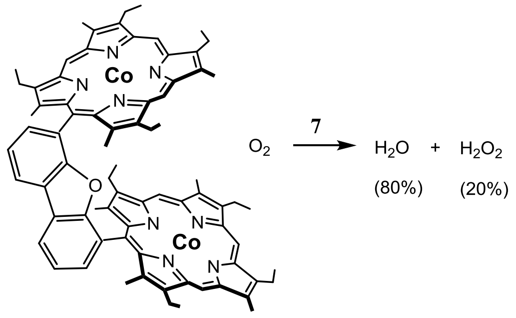

7

Figure 1.13 Dicobalt diporphyrin oxygen reduction catalyst with benzofuran linker, from reference [68].

Another study examined a dicobalt diporphyrin **7** that catalysed the reduction of oxygen, in a catalytic process that also produced H_2O_2. In this case the porphyrins were linked by a dibenzofuran group, which led the two porphyrins to be angled at 56.5° on average (see Figure 1.13); **7** was found to catalyse the conversion of 80% of the O_2 reactants to H_2O [68]. The Co-Co distance was found to be on average 8.624 Å, substantially longer than the average 3.73 Å reported in **4**. The authors also ascribed the catalytic effect to longitudinal flexing.

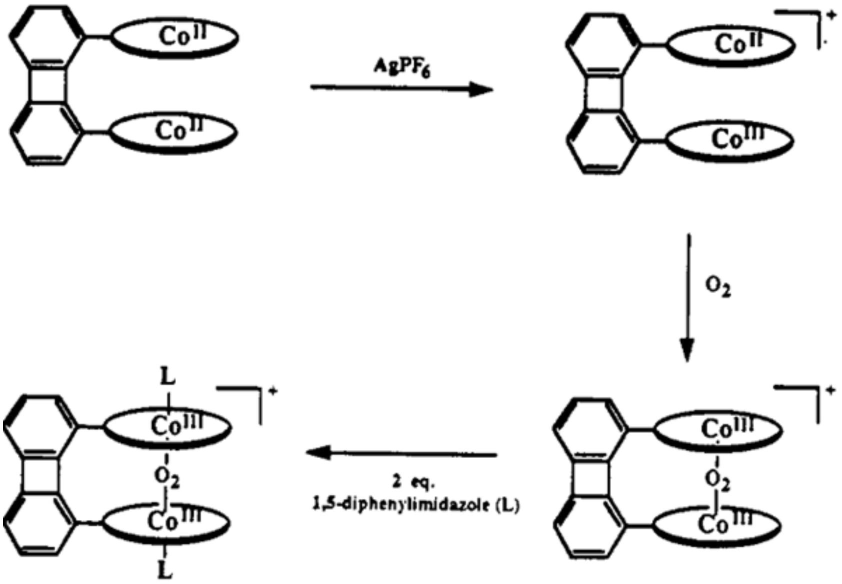

Figure 1.14 Preparation of the μ-superoxo complex of **5** (Reproduced with permission from reference [73]).

Mechanistic studies by Collman et al. showed that O_2 bound to the cofacial dicobalt diporphyrin complex inside the pocket formed between the metal ions, where it is initially bound as a μ-superoxide species that bridges the two Co ions (see Figure 1.14) [73]. The actual catalyst was found to be the $Co^{II}Co^{III}$ form of **1** [66], where the Co^{III} acted as a Lewis acid. The extreme sensitivity of the overall catalysis process to the nature of the conformational flexing brought about by different types of linkers suggests that the O_2 reactant binds very transiently to both of the Co ions. If the catalyst opens and closes in that brief period of time then the O_2 may be, quite literally, pulled apart. That is, the O-O bond may be cleaved by the process of progressively increasing the separation between the two O atoms during the opening of the diporphyrin complex. If the catalyst is unable to pull the O_2 apart in that brief period, or perhaps introduces motion that is not optimal for the cleavage of that bond, then a slower 2-electron process occurs, yielding H_2O_2.

Thus in the 4-electron reduction by **1**, **4** and 5 we arguably see a process governed by the mechanics of conformational flexing, in synchronisation with μ-O_2 binding. In other words the rate of reaction is governed by how the separate processes of regular, repeated conformational flexing and dynamic binding of the reactant to the catalyst overlap [34]. To achieve optimal O-O cleavage these two processes must occur synchronously, which can only happen if the catalyst flexes rapidly and regularly, along a single degree of freedom, about a structure that complements the optimum transition state. When this is achieved, then the two Co porphyrins act in a cooperative, "convergent" manner, as is the case in **1**, **4** and **5**. When it is not achieved, as in **2** or **3**, then the 4-electron reaction does not take place. Instead, 2-electron reduction to H_2O_2 occurs. In the cases of **6** and **7** we can see that there are varying degrees of optimisation possible as well, rather than an outright binary choice between two possible reactions. The synergy in **1**, **4** and **5** yields a new capability, that of O-O cleavage, rather than the sum of the actions of the individual components that would otherwise facilitate the H_2O_2 formation. In a way this can be understood as if one were to alter the length of pistons in an internal combustion engine, in the sense that there is one optimal arrangement that works in synchronisation with the other components. Various arrangements where the desired work done is in suboptimal coexistence with other processes lead to partial combustion or complete breakdown of the engine.

1.6.2 Cofacial diporphyrin catalysts for water oxidation

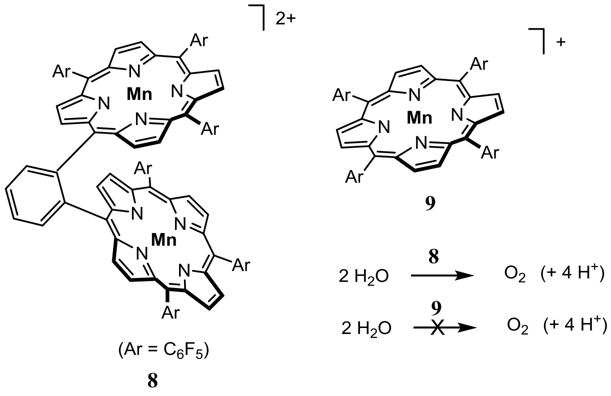

Figure 1.15 Dimanganese diporphyrin water oxidation catalyst from reference [74-76]

In comparison to the field of cofacial diporphyrin catalysts for oxygen reduction there are fewer studies on similar systems for water oxidation. One notable example is the cofacial dimanganese diporphyrin catalyst **8**, which was shown by Naruta and colleagues to catalyse the oxidation of water into O_2 (see Figure 1.15). Species **8** is believed to bind H_2O molecules at each of the two Mn atoms, forming transient $Mn^V=O$ intermediates. Then, upon closing of the bite angle during flexing, the reactive Mn-bound O atoms are brought together into collision, forming O_2, which is immediately expelled. The proposed mechanism for oxygen evolution in this system is therefore the repeated collision of transient $Mn^V=O$ intermediates facilitated by the cofacial stacking and flexing of porphyrins at an appropriate distance [74]. This action is directly analogous to that of a machine as confirmed by the fact that equivalent metaloporphyrin *monomers*, like **9**, are entirely catalytically inactive for the same reaction.

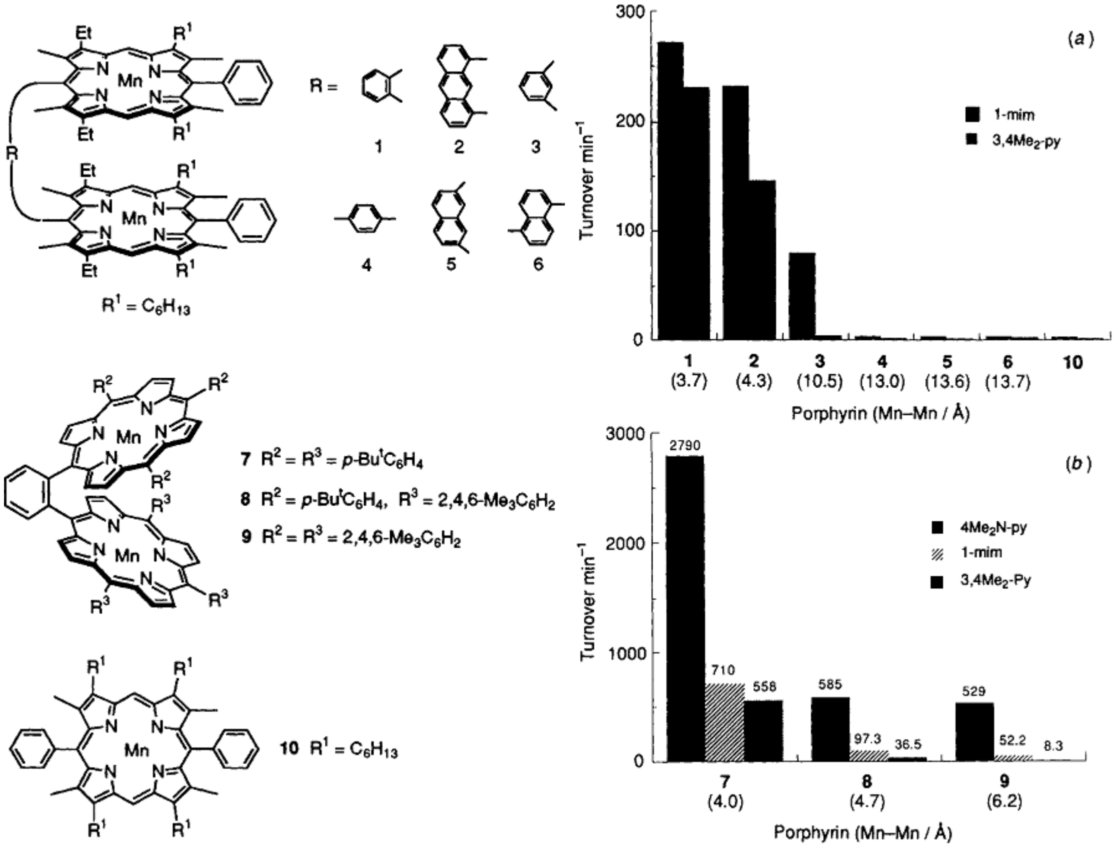

Figure 1.16 Variants of **8** with different linker and porphyrin functionalization, overview of species (left) and turnover numbers for each species with respect to Mn-Mn distance (right). Reproduced with permission from reference [76].

Naruta and colleagues also analysed different linkers as well as meso and β-pyrrolic functionalization on the porphyrin, and compared catalytic rates with special attention to the Mn-Mn distance in the different variants [76]. In this case, O_2 evolution by H_2O_2 disproportionation catalysis was tested in acetonitrile-benzonitrile solvent in the presence of a base. The findings confirmed the critical nature of the Mn-Mn separation with only one catalyst performing at turnover rates of several thousand molecules per minute compared to several hundred at best by the other variants under the same conditions (see Figure 1.16). When the Mn ions were too distant or not in an eclipsed arrangement the reaction would not occur at all.

1.6.3 Intermolecular and matrix assisted organic catalysts

As noted in the previous sections many monomeric metalloporphyrins and also phthalocyanines catalyse the 2-electron reduction of O_2 into H_2O_2 whereas their dimeric, cofacial analogues are capable of 4-electron reduction to H_2O involving O-O bond cleavage. An interesting observation has been made however that some monomeric metalloporphyrins facilitate the former reaction when adsorbed at low concentrations on graphite, but catalyse the latter reaction when adsorbed at higher concentrations [77]. The suggestion was made that some of the molecules adsorbed in a side-on, pairwise fashion whereas some adventitiously arranged in a eclipsed fashion and thereby facilitated catalysis [77].

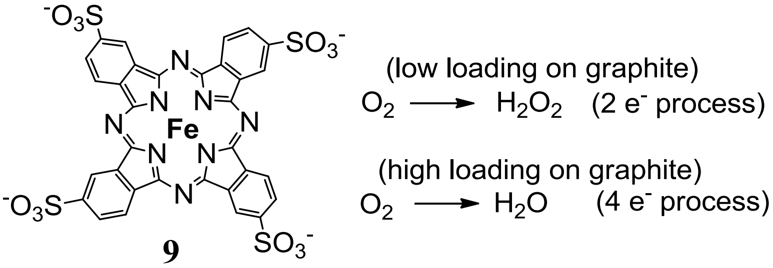

9

Figure 1.17 Phthalocyanine tetrasulfonate Fe(III) complex and its catalytic reactions, from reference [78].

A relevant example is the tetrasulfonated iron phthalocyanine **9** (see Figure 1.17). When adsorbed at low concentrations on graphite it facilitates the electrocatalytic reduction of O_2 by a 2-electron process, giving H_2O_2. However as the concentration is increased, this gives way to the 4-electron reduction to H_2O [77-79]. While establishing the exact mechanism of reaction proved difficult, the observed variation in product as a function of loading is consistent with a cooperative effect.

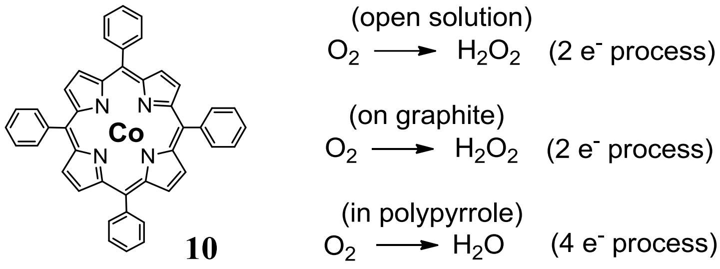
10

Figure 1.18 5,10,15,20-tetraphenylporphyrinato cobalt(II) and its catalytic reactions, from reference [80].

Instead of concentrating monomeric metalloporphyrin at the surface of an electrode, another approach involves concentrating the metalloporphyrin within a conducting matrix, such as a densely-packed conducting polymer. One example is the cobalt complex of the tetraphenylporphyrin **10** [80](see Figure 1.18). This species catalyses exclusively the 2-electron reduction reaction of O_2 into H_2O_2 when dissolved in solution. When adsorbed onto graphite, even at high loadings, it also only facilitates this reaction. However when incorporated into a layer of vapour phase polymerised polypyrrole, which by itself is not a catalyst of O_2 reduction, it was found to facilitate the 4-electron reduction to H_2O [80]. The proportion of the 4-electron product increased with higher loading, reaching close to 100%.

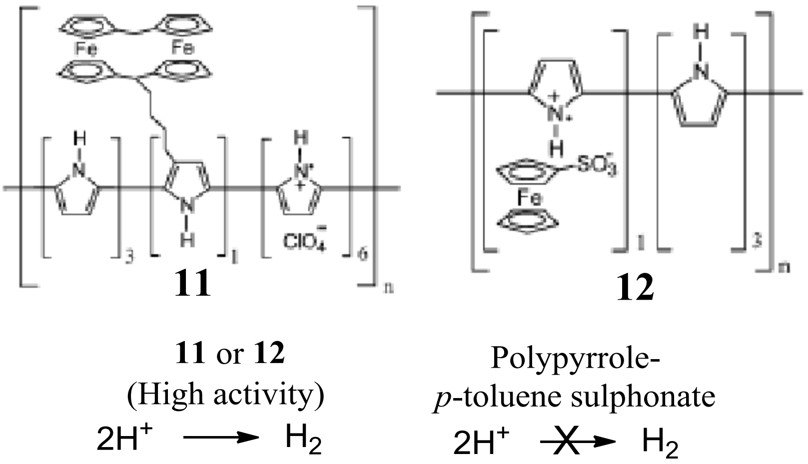

Figure 1.19 Diferrocene and ferrocene sulfonate catalysts in polypyrrole, from reference [81, 82].

A similar example is the catalyst **11** made by Chen and Swiegers [81, 82], which consisted of a powerful hydrogen reduction differocene catalyst [83, 84] tethered to pyrrole and subsequently polymerised as a conductive polymer in a thin layer. The resulting conducting polymer proved to be a powerful hydrogen generating catalyst (see Figure 1.19). An unexpected side product from this experiment was that the control coating **12**, consisting of a monomeric ferrocene sulfonate incorporated into polypyrrole as a counter-ion, also displayed significant hydrogen generating catalysis. In fact it was so powerful that it produced approximately 7 times more hydrogen than an equivalent platinum electrode under similar conditions [81, 82]. The origin of the catalytic activity of **11** was shown to arise from the presence of high loadings of ferrocene sulfonate; a comparable coating containing p-toluene sulfonate as a counter-ion displayed no catalytic effect. It was proposed that a statistically significant proportion of the ferrocene sulfonate adventitiously arranged in close proximity to each other in the poly(pyrrole) so that it was able to act in a similar fashion to the diferrocene variant. While the precise catalytic mechanism remains unclear due to the practical difficulties of studying catalysis in porous conducting polymer the catalytic effect displayed by **12** is certainly remarkable.

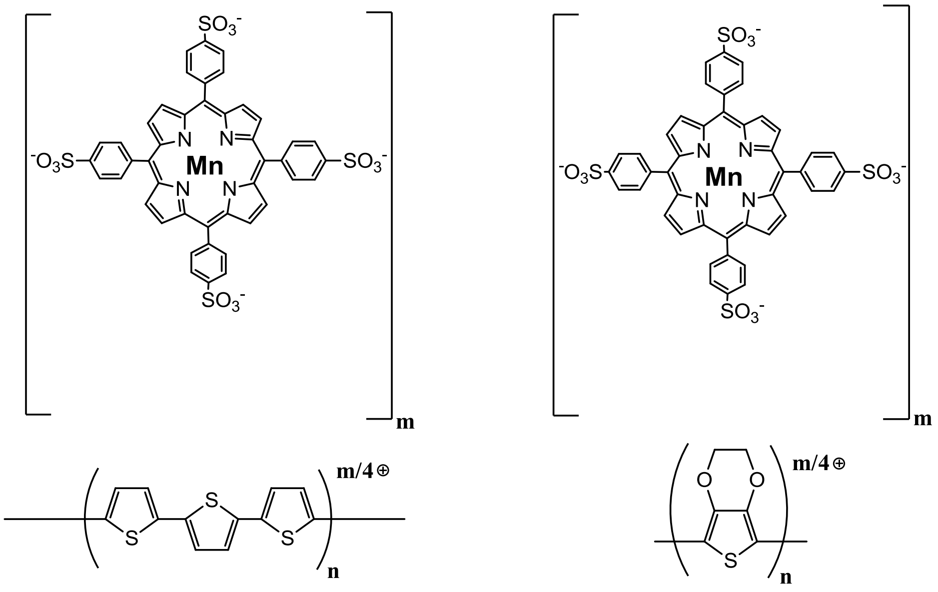

13 **14**

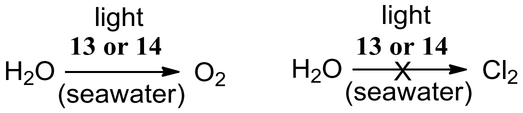

Figure 1.20 Manganese porphyrin embedded in conductive polymer acting as a water oxidation catalyst, from reference [85, 86]

This line of work has recently been extended to include a manganese porphyrin based on the dimanganese porphyrin **8** by Naruta. In this case the monomer was incorporated into poly(terthiophene) (PTTh) **13** [85] or poly(3,4-etheylenedioxythiophene) (PEDOT) **14** [86] within a dense polymeric layer formed by vapour phase polymerisation (see Figure 1.20). The resulting composite material was found to be a powerful light-assisted electrocatalyst for water oxidation.

Electrochemical studies of the resulting electrodes in 0.1 M Na_2SO_4 at pH 7 revealed a significant photocurrent at only 0.25 sun intensity (SoLux daylight MR16 halogen light bulb, 12V, 50W) with a low onset potential. Photocurrent under light illumination was reported as low as 0.68 V in the case of PTTh and 0.32V in the case of PEDOT (both *vs* Ag/AgCl). This is much lower than the theoretically lowest onset potential for water oxidation at pH 7, of 0.6 V (*vs* Ag/AgCl) (0.83 V *vs* SHE). Through gas detection by GC-MS, the photocurrent observed in 0.1 M Na_2SO_4 at pH 7 as well as seawater was correlated to oxygen evolution from water oxidation. Moreover, the selectivity of both **13** and **14** was such that even in seawater they generated only O_2 with no Cl_2 side product detected [85, 86]. While water oxidation ($2H_2O \rightarrow O_2 + 4H^+ + 4e^-$; E^0 1.23 V) is in theory thermodynamically favoured over Cl_2 formation ($2Cl^- \rightarrow Cl_2 + 2e^-$; E^0 1.36 V) in seawater, the lower overpotential of chloride oxidation means that chlorine is inevitably formed in conventional electrolysis of seawater. This is a problem affecting all man-made catalysts unless placed in an ion-exchange resin [87]. The only other known catalyst selective enough to oxidise water in seawater without forming chlorine gas is the biological catalyst system PSII found in marine and hypersaline organisms. This demonstrates the remarkable selectivity of this artificial catalyst system, for which the mechanism of action may well accord with that of a kinematic manufacturing machine.

1.6.4 Cubane catalysts

In a 2011 review Swiegers et al. [48] illustrated the structural similarities between several man-made catalysts based on the OEC template and the OEC itself and found a remarkable overlap in structure and function despite a clear difference in the metal element in the structures.

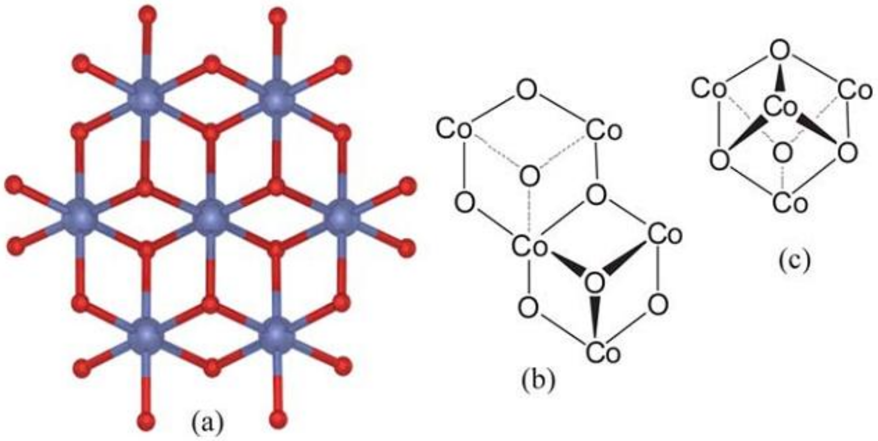

Figure 1.21 Nocera and Kanan’s Co-phosphate water oxidation catalyst, (a) X-ray structural model of the cobaltate cluster, (b) structural arrangement of the surface of the clusters and (c) overall cubane structural motif of the catalyst. Reproduced with permission from reference [48].

One of the more prominent water oxidation catalysts is the Co-phosphate system described by Nocera and Kanan [88-92]. The catalyst was shown to consist of cubical arrays, initially believed to be a heterogenous particulate nanocrystalline catalyst; it was observed that it dissolved in open solution thereby forming a homogeneous catalyst (see Figure 1.21). The surface of the arrays involve an “open-face” checkerboard of puckered Co-O recesses and protrusions, which are formed by crystal grain formation with the base Co_4O_4 cubane as the unit cell. Evidence suggested that it self-assembles and disassembles during turnover [88-92]. The Co-O cubane structure at the surface was believed to disassemble, releasing O_2 during water oxidation.

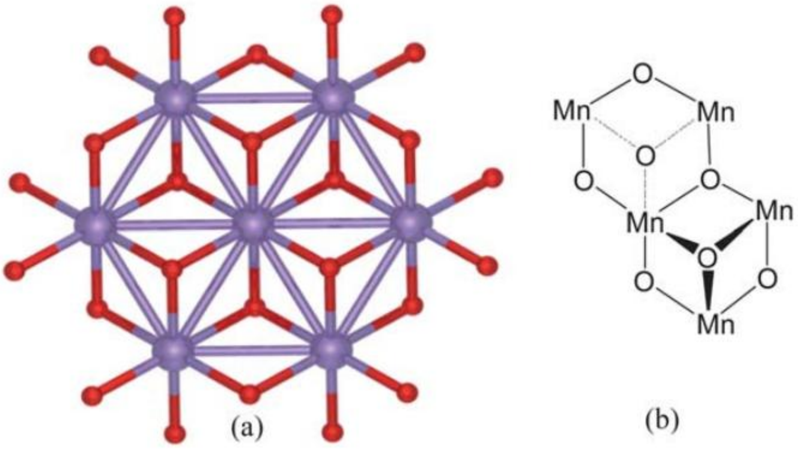

Figure 1.22 Birnessite water oxidation catalyst, (a) single crystal X-ray structure of a Mn-O extended sheet layer in K birnessite (Mn ions purple, O red), (b) structural arrangement of the Mn-O sheet layers in birnessite. Reproduced with permission from reference [48].

A Mn-O birnessite mineral catalyst was reported by Spiccia et al. that formed nanoparticles inside Nafion film under suitable conditions [93]. The birnessite nanoparticles were found capable of catalysing H_2O into O_2. This species consists of a layered structure of stacked, 2D strata of hetero-ions interleaved with 2D extended Mn-O sheets and was hypothesised to be the evolutionary origin of the PSII-WOC [94].

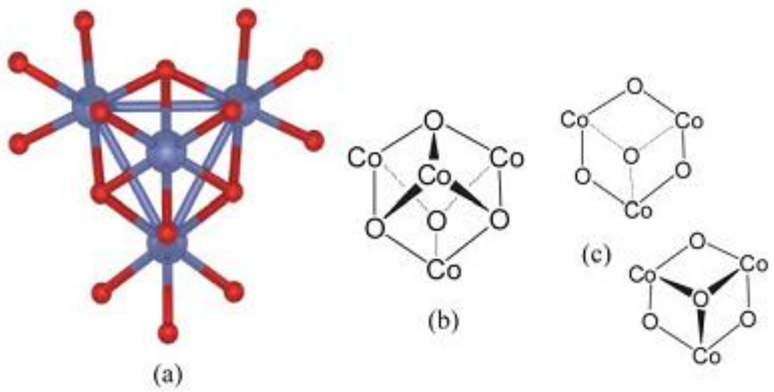

Figure 1.23 Co_3O_4 spinel water oxidation catalyst, (a) single-crystal X-ray structure (Mn blue, O red), (b) the cubane structure of the B-site of the catalyst and (c) structural formations at the surface of the Co_3O_4 spinel that derive from the B-site. Reproduced with permission from reference [48].

Another cobalt catalyst of interest is the Co_3O_4 spinel heterogenous water oxidation catalyst reported by Previtt and further studied by Frei (see Figure 1.23) [95, 96]. It was shown to become highly active for water oxidation in heterogeneous, nanoparticulate (nanorod) form [95]. The structure of the B-site of the spinel comprises of a Co_4O_4 cubane motif which is identical to that of the Co-phosphate catalyst shown previously (Figure 1.23), as well as the PSII-OEC. The surface of this catalyst comprises of a mixture of “open face” A and B sites. Likewise, they feature puckered, half-cube Co-O recesses or protrusions. The activity of the nanoparticulate form is substantially greater than in equivalent microparticulate form [95, 96] and studies indicated that the spinel cycles through Co_4^+ intermediates during water oxidation catalysis [97].

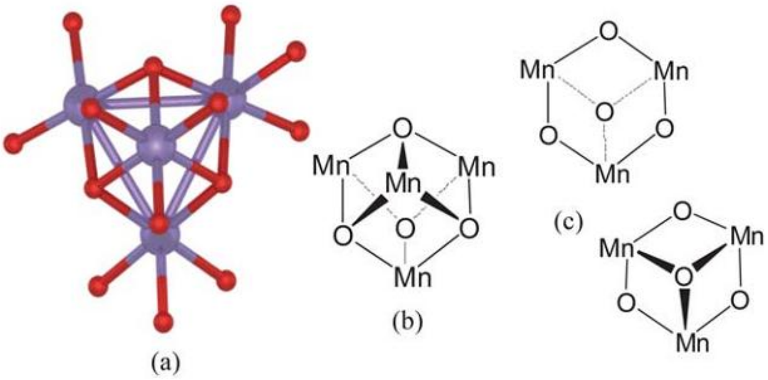

Figure 1.24 (a) X-ray structure of a λ-Mn_2O_4 spinel catalyst (Mn purple, O red), (b) cubane structural motif and (c) structural formations at the surface from the B-site. Reproduced with permission from reference [48].

Recent work by Dismukes et al. showed that the spinel $LiMn_2O_4$, which is inactive for water oxidation, becomes a highly active catalyst when the Li ion is removed from the A-site. The remaining Mn_2O_4 contains a Mn_4O_4 cubane structure in its B-site (see Figure 1.24) [98]. The key structural change resulting from removing the Li ions is the freeing up of the shared μ_3-O atoms in the B-site thus allowing for more motion, which could explain the catalytic effect [48].

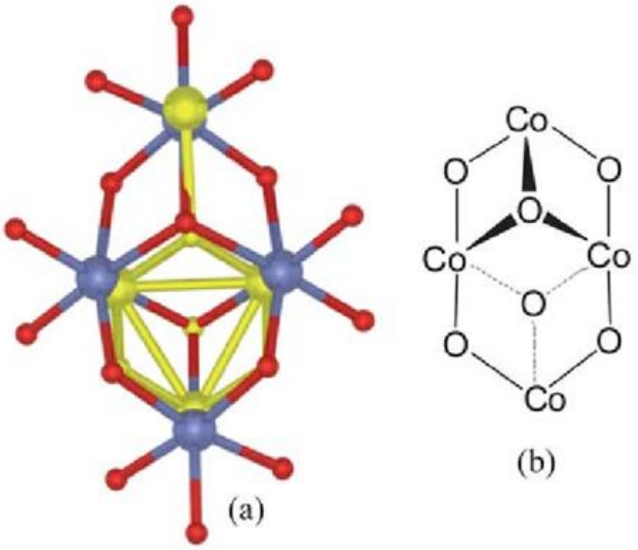

Figure 1.25 (a) Dimensionally accurate superimposition of the reported X-ray structure of a $[Co_4(H_2O)_2(PW_9O_{34})]^{10-}$ polyoxotungstate water oxidation catalyst (red and blue structure) and the "London" X-ray structure of the PSII-WOC (yellow), and (b) the structural arrangement of the $[Co_4(H_2O)_2(PW_9O_{34})]^{10-}$ polyoxotungstate core. Reproduced with permission from reference [48].

The final notable homogeneous water oxidation catalyst is the complex reported by Hill et al. [99], $[Co_4(H_2O)_2(PW_9O_{34})]^{10-}$ (Figure 1.26). This species contains the cubane core and is stabilised by oxidatively resistant bulky poly(oxotungstate) ions. This complex also dynamically self-assembles in water to yield the highest recorded turnover frequency of any abiological catalyst for water oxidation, >5 s^{-1} at pH 8) [99]. While the mechanism of catalysis for this species is unknown, the core structure is effectively that of a cubane. When superimposed with the "London" structure of the OEC (see Figure 1.25) it can be inferred that the catalytically active site includes open-faced arrangements.

Remarkable overlaps exist in these structures in terms of interatomic distances and bond lengths [48], which is especially visible when the X-ray crystallographic structures of the aforementioned catalysts are superimposed on one another, as well as with PSII-WOC structures. This suggests that close mimicking of the PSII-WOC in terms of physical dimensions, if not using the exact same elements, can lead to powerful water oxidation catalysts. The regenerative as well as stabilising aspect of the surrounding protein framework, remains however largely unaddressed, leading to limited turnover numbers as the catalyst can eventually degrade through mismatched action by its components, or blocked by trace impurities in the substrate over time.

1.7 Strategies for creating non-biological *"molecular manufacturing machines"*

Using the above insights two possible routes have been identified in which *molecular manufacturing machines* that are non-biological in their origin, may be created [12, 13]:

1.7.1 Highly structured molecular technique

The first technique consists of constructing highly structured assemblies that closely mimic the enzymatic assemblies found in nature. Likewise, smaller yet precisely engineered components can be built to harness some of the critical parts of enzymatic systems identified as performing a mechanical mode of action [12, 13, 34], such as the aforementioned cofacial porphyrin systems. This approach relies on the proposition that, if enzyme active sites are complementary to their transition states and ideally set up for molecular manufacturing, then covalently-assembled molecular models with similar shapes and constituents should also be. The key problem with this approach however, is that it requires great precision in molecular design and often extreme synthetic complexity to realise a target molecular manufacturing machine.

Recent studies into protein engineering by Dutton and others [100-104] utilised *ab initio* designed simple proteins called foldamers [105-108] in an attempt to study enzyme design. These are a good example of the *highly structured* approach. However, such artificial enzyme species have to be precisely synthesised using biological methods rather than organic chemistry, and are exceedingly difficult to achieve.

1.7.2 Combinatorial intermolecular technique

A potentially easier and more practical approach, involves a *combinatorial* technique [12, 13, 80] like that found in aforementioned porphyrin-polymer systems. In this case monomers containing *un-connected* catalytic groups are concentrated within limited volumes. For simple systems, a small, but statistically significant proportion of them may thereby become trapped in optimal dispositions to facilitate a kinematic mode of catalysis. That small proportion will then be powerful catalysts and perform as *kinematic molecular manufacturing machines*. All of the other catalytic groups that are inopportunely disposed will be inactive. With further experimentation the synthesis and deposition methods may be engineered to maximise the proportion of molecules arranged in a catalytically active fashion. The main advantage of this more indirect technique is that it avoids the often arduous discovery process and complex synthetic procedures needed in the previous technique. As such, it offers a desirable, simpler route to inexpensive and practically useful *molecular manufacturing machines*.

Recent studies [34, 85, 86, 109-111] provide good examples of the combinatorial method as molecules that are structural similar to the critical components found in PSII are identified and mimicked by simpler, man-made variants, such as porphyrins, ferrocenes and cubanes. This method was utilised in this thesis to follow on the established catalytic systems and study them in more detail.

1.8 Research strategy

The aforementioned *combinatorial* technique was used in the research work that forms this thesis. The aim was to develop catalytic systems based on metalloporphyrins and cubanes capable of facilitating the same or similar catalytic reactions as their biological counterparts, whilst avoiding the complexities involved in their synthesis.

1.8.1 Conducting polymers

Conducting polymers were established as a field with the discovery of high intrinsic conductivity in polyacetylene in 1977 [112]. Polyacetylene was found to exhibit an unusually high conduction due to its conjugated backbone when subjected to chemical or electrochemical oxidation [113]. Upon oxidation, a positively charged “hole” is introduced in the backbone, effectively doping the polymer. Further oxidation leads to formation of conduction bands similar to those found in doped semiconductor systems, allowing charge to travel along the polymer chain. This effectively enables electrical conduction along the polymer chain, at conductivities that, under ideal conditions, may approach that of common metallic conductors[114].

A number of studies have been done on the conduction mechanism, as well as other chemical species forming conductive polymers [113, 115, 116]. Of note are the poly-heterocyclic species notably poly(pyrrole) and poly(thiophene), and later poly(3,4-ethylenedioxythiophene) (PEDOT), which increasingly became the focus of conducting polymer work [115, 117, 118]. A recent study also revealed the utility of PEDOT in applications relevant to water splitting [119].

1.8.2 Porphyrins

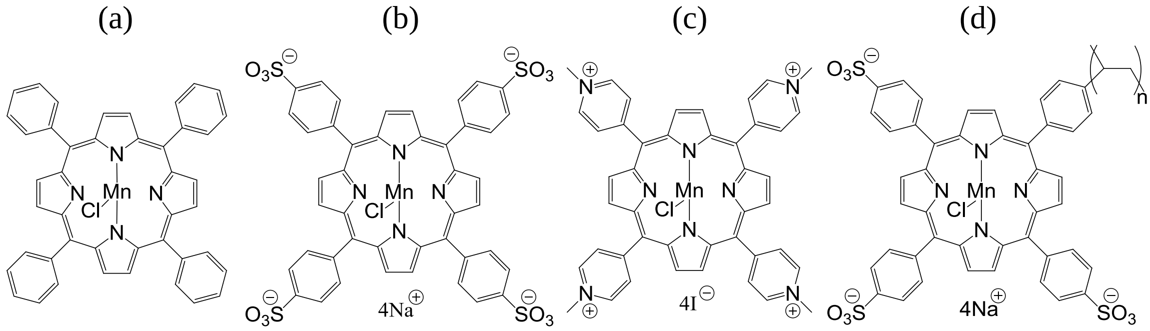

Figure 1.26 Porphyrin species explored in this thesis: (a) 5,10,15,20-tetraphenylporphyrinato manganese(III) chloride (MnTPP), (b) 5,10,15,20-tetrakis(4-sulfonatophenyl)porphyrinato manganese(III) chloride sodium salt (MnTPPS), (c) 5,10,15,20-tetrakis(4-methylpyridinium)porphyrinato manganese(III) chloride tetraiodide (MnTMPyP), (d) poly(5-(4-vinylphenyl)10,15,20-tris(4-sulfonatophenyl) porphyrinato manganese(III) chloride sodium salt (MnPVTPPS).

Previous work [85, 86, 111] was expanded on by incorporating several types of manganese porphyrins into PEDOT (see Figure 1.26). These included the simple (a) 5,10,15,20-tetraphenylporphyrinato manganese(III) chloride (MnTPP) and its functionalised water soluble variants (b) 5,10,15,20-tetrakis(4-

sulfonatophenyl)porphyrinato manganese(III) chloride sodium salt (MnTPPS) and (c) 5,10,15,20-tetrakis(4-methylpyridinium)porphyrinato manganese(III) chloride tetraiodide (MnTMPyP). A polymeric variant, (d) poly(5-(4-vinylphenyl)10,15,20-tri(4-sulfonatophenyl) porphyrinato manganese(III) chloride sodium salt (MnPVTPPS) was also studied. The catalytic performance of each was examined and their specific properties in the deposited films evaluated using UV-Visible light absorbance spectroscopy (UV-Vis). The species (b) and (c) above have the additional feature of dense packing brought about by their charge pairings [120]. This feature was utilised in an attempt to facilitate cofacial aggregation during deposition. The species (d) above consisted of repeating units of porphyrin along a polymer backbone, which can force densely packed arrangements of porphyrins with some fraction achieving co-facial positioning. All of the above contain a Mn(III) ion in the core, raising further similarities to the proposed oxidation states of the Mn in the OEC as described by Pace [47].

The porphyrins embedded in conducting polymer films were extensively studied using UV-visible absorbance spectroscopy due to their highly specific light absorbance spectra, from which structural details could be inferred [121]. Typically a porphyrin produces a strong absorbance peak in the 380-460 nm region called the Soret Band, or B-Band, which is distinctive of its status in the polymer. Its shift can be compared to literature data so as to determine whether the porphyrin contains a metal core and which oxidation state the metal ion is in. A secondary feature is called the Q-Bands, which are typically 2-4 absorbance peaks of smaller intensity. They also change with metal incorporation in the core and are a useful secondary means of analysis with which to confirm the overall state of the porphyrin. Cofacial porphyrins also display excitonic coupling brought on by close face-to-face or side-to-side arrangements, measurable using UV-vis absorbance spectroscopy [122]. Therefore, cofacial packing can also be inferred from the shift of the Soret Band, when applicable.

1.8.3 Graphene oxide and reduced graphene oxide

Since its discovery by Geim in 2004, the aromatic carbon allotrope graphene has become renowned for its promising electronic and physical properties [123-126]. At first the material was made by exfoliating single sheets of sp^2 hybridised carbon arranged in a honeycomb lattice with scotch tape. A new method was established for higher throughput synthesis from an earlier method for the synthesis of graphitic oxide from graphite called the Hummers method [127], with modifications which included, among others, exfoliation by ultrasonic waves [128, 129]. Graphene oxide (GO) has proven to be versatile and preferred by researchers for its enhanced chemical processing features. It is highly water soluble while retaining most of its high conductivity when reduced to graphene. It is often referred to as reduced graphene oxide (RGO) or chemically converted graphene (CCG) [130]. Recent advances by Jalili et al. have led to a new class of graphene oxide called liquid crystalline graphene oxide (LCGO), so named for its remarkable property of acting like a liquid crystal when dispersed in water as big sheets [130-133]. Furthermore graphene oxide contains numerous carboxylic acid and phenolic functional groups on the surface [134, 135] that can be controlled by targeted reduction to strike a compromise between degree of functionalization and conductivity.

1.8.4 Calcium manganese oxide catalysts

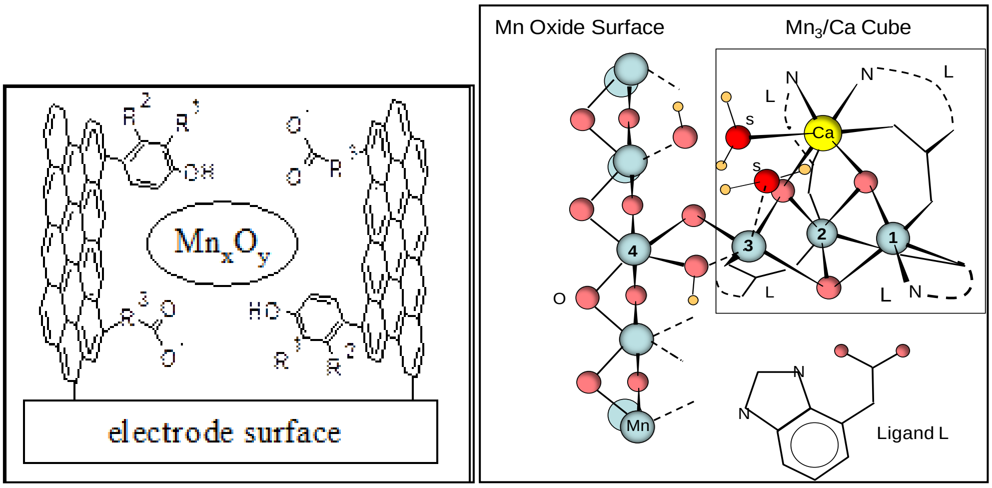

Figure 1.27 Proposed Mn_xO_y-graphene composite structures.

A new OEC-inspired biomimetic Mn_xO_y-graphene composite catalyst material was investigated during the studies for this thesis in collaboration with Assoc. Prof. Ron Pace and Prof. Rob Stranger from the Australian National University (ANU). This catalyst aimed to mimic the matrix-assisted effect of the PSII protein scaffold on the OEC by experimentally depositing known Mn_xO_y [136] as well as $CaMn_xO_y$ [137, 138] catalysts on graphene substrates. These substrates contain carboxylic and phenolic moieties that can serve to mimic the protein scaffold in PSII in direct contact with the OEC, specifically the tyrosine groups that provide H^+/e^- transport pathways to the surrounding system (see Figure 1.27). In the cases where calcium was absent from the Mn catalyst it was added to the graphene oxide by chemical cross-linking [139] in an attempt to bring Ca ions in close proximity to the Mn clusters to mimic its role in the OEC.

1.9 Thesis aims

The aim of this work is to synthesize and carefully examine novel, bio-inspired water oxidation catalysts. This will be attempted through a combinatorial approach to test candidate species embedded in a PEDOT or graphene matrix. The porphyrin-polymer and manganese oxide-graphene composites will be tested in electrochemical experiments to determine the relative magnitude of potential catalytic performance for each species. The most promising samples will be studied in greater detail to reveal more information pertinent to their structure and likely mechanism of action. Within the context of the greater framework of molecular manufacturing machines, only the area of water oxidation will be explored in this study.

1.10 References

1. Feynman, R.P., Engineering and Scienc, 1960. **23**: p. 22-36.
2. Thomson, W., Nature, 1874. **9**: p. 441-444.
3. Pauling, L., Nature, 1948. **161**: p. 707-709.
4. Watson, J.D. and F.H.C. Crick, Nature, 1953. **171**(4356): p. 737-738.
5. Moss, D.W., *Enzymes*1968, London: Oliver & Boyd, Edinburgh.
6. Drexler, K.E., Proceedings of the National Academy of Sciences of the United States of America-Physical Sciences, 1981. **78**(9): p. 5275-5278.
7. Drexler, K.E., Annual Review of Biophysics and Biomolecular Structure, 1994. **23**: p. 377-405.
8. Drexler, K.E., *Engines of Creation: the Coming Era of Nanotechnology*1986, New York: Anchor-Doubleday.
9. Drexler, K.E., 1992, Wiley: New York.

10. Vogelsberg, C.S. and M.A. Garcia-Garibay, Chemical Society Reviews, 2012. **41**(5): p. 1892-1910.

11. Bertalanffy, L.v., *General System Theory - Foundations, Development, Applications*. Revised Edition ed1969, New York: George Braziller.

12. Swiegers, G.F., ed. *Mechanical Catalysis; Methods of Heterogeneous, Homogeneous, and Enzymatic Catalysis*. 2008, John Wiley and Sons: New York.

13. Chen, J., P. Wagner, and G.F. Swiegers, *Bioinspired Catalysis*, in *Bioinspiration and Biomimicry in Chemistry*, G.F. Swiegers, Editor 2012, Wiley: New York.

14. Stryer, L., *Biochemistry*. Third ed1988, New York: W. H. Freeman and Company.

15. Koshland, D.E., Proceedings of the National Academy of Sciences, 1958. **44**(2): p. 98-104.

16. Williams, D.H., E. Stephens, and M. Zhou, Chemical Communications, 2003(16): p. 1973-1976.

17. Herries, D.G., Biochemical Education, 1983. **11**(1): p. 46-46.

18. Bruice, T.C., Annual Review of Biochemistry, 1976. **45**(1): p. 331-374.

19. Bruice, T.C., Accounts of Chemical Research, 2002. **35**(3): p. 139-148.

20. Bruice, T.C. and S.J. Benkovic, Biochemistry, 2000. **39**: p. 6267-74.

21. Dafforn, A. and D.E. Koshland, Proceedings of the National Academy of Sciences, 1971. **68**(10): p. 2463-2467.

22. Storm, D.R. and D.E. Koshland, Proceedings of the National Academy of Sciences, 1970. **66**(2): p. 445-452.

23. Storm, D.R. and D.E. Koshland, Journal of the American Chemical Society, 1972. **94**(16): p. 5805-5814.

24. Tousignant, A. and J.N. Pelletier, Chemistry & Biology, 2004. **11**(8): p. 1037-1042.

25. Hammes-Schiffer, S., Biochemistry, 2002. **41**(45): p. 13335-13343.

26. Hammes-Schiffer, S. and S.J. Benkovic, Annual Review of Biochemistry, 2006. **75**(1): p. 519-541.

27. Benkovic, S.J. and S. Hammes-Schiffer, Science, 2003. **301**(5637): p. 1196-1202.

28. Boehr, D.D., D. McElheny, H.J. Dyson, and P.E. Wright, Science, 2006. **313**(5793): p. 1638-1642.

29. Vendruscolo, M. and C.M. Dobson, Science, 2006. **313**(5793): p. 1586-1587.

30. Eisenmesser, E.Z., D.A. Bosco, M. Akke, and D. Kern, Science, 2002. **295**(5559): p. 1520-1523.

31. Eisenmesser, E.Z., O. Millet, W. Labeikovsky, D.M. Korzhnev, M. Wolf-Watz, D.A. Bosco, J.J. Skalicky, L.E. Kay, and D. Kern, Nature, 2005. **438**(7064): p. 117-121.

32. Williams, R.J.P., Trends in Biochemical Sciences, 1993. **18**(4): p. 115-117.

33. Hilvo, M., L. Baranauskiene, A.M. Salzano, A. Scaloni, D. Matulis, A. Innocenti, A. Scozzafava, S.M. Monti, A. Di Fiore, G. De Simone, M. Lindfors, J. Jänis, J. Valjakka, S. Pastoreková, J. Pastorek, M.S. Kulomaa, H.R. Nordlund, C.T. Supuran, and S. Parkkila, Journal of Biological Chemistry, 2008. **283**(41): p. 27799-27809.

34. Swiegers, G.E., J. Huang, R. Brimblecombe, J. Chen, G.C. Dismukes, U.T. Mueller-Westerhoff, L. Spiccia, and G.G. Wallace, Chemistry A European Journal, 2009. **15**(19): p. 4746-4759.

35. Trautz, M., Zeitschrift für anorganische und allgemeine Chemie, 1916. **96**(1): p. 1-28.

36. Johnson, K.A. and R.S. Goody, Biochemistry, 2011. **50**(39): p. 8264-8269.

37. Barber, J., Chemical Society Reviews, 2009. **38**(1): p. 185-196.

38. Barber, J., Quarterly Reviews of Biophysics, 2003. **36**(1): p. 71-89.

39. Ferreira, K.N., T.M. Iverson, K. Maghlaoui, J. Barber, and S. Iwata, Science, 2004. **303**(5665): p. 1831-1838.

40. Pace, R.J., L. Jin, and R. Stranger, Dalton Transactions, 2012. **41**(36): p. 11145-11160.

41. Pace, R.J., R. Stranger, and S. Petrie, Dalton Transactions, 2012.

42. Chuah, W.Y., R. Stranger, R.J. Pace, E. Krausz, and T.J. Frankcombe, The Journal of Physical Chemistry B, 2014. **118**(13): p. 3553-3558.

43. Haumann, M., C. Müller, P. Liebisch, L. Iuzzolino, J. Dittmer, M. Grabolle, T. Neisius, W. Meyer-Klaucke, and H. Dau, Biochemistry, 2005. **44**(6): p. 1894-1908.

44. Kok, B., B. Forbush, and M. McGloin, Photochemistry and Photobiology, 1970. **11**(6): p. 457-475.

45. Hillier, W. and T. Wydrzynski, Biochimica et Biophysica Acta (BBA) - Bioenergetics, 2001. **1503**(1–2): p. 197-209.

46. Umena, Y., K. Kawakami, J.-R. Shen, and N. Kamiya, Nature, 2011. **473**(7345): p. 55-60.

47. Koua, F.H.M., Y. Umena, K. Kawakami, and J.-R. Shen, Proceedings of the National Academy of Sciences, 2013. **110**(10): p. 3889-3894.

48. Swiegers, G.F., J.K. Clegg, and R. Stranger, Chemical Science, 2011. **2**(11): p. 2254-2262.

49. Kamiya, N. and J.-R. Shen, Proceedings of the National Academy of Sciences, 2003. **100**(1): p. 98-103.

50. Guskov, A., J. Kern, A. Gabdulkhakov, M. Broser, A. Zouni, and W. Saenger, Nat Struct Mol Biol, 2009. **16**(3): p. 334-342.

51. Suga, M., F. Akita, K. Hirata, G. Ueno, H. Murakami, Y. Nakajima, T. Shimizu, K. Yamashita, M. Yamamoto, H. Ago, and J.-R. Shen, Nature, 2015. **517**(7532): p. 99-103.

52. Gatt, P., S. Petrie, R. Stranger, and R.J. Pace, Angewandte Chemie International Edition, 2012. **51**(48): p. 12025-12028.

53. Petrie, S., R.J. Pace, and R. Stranger, Angewandte Chemie International Edition, 2015. **54**(24): p. 7120-7124.

54. Glöckner, C., J. Kern, M. Broser, A. Zouni, V. Yachandra, and J. Yano, Journal of Biological Chemistry, 2013.

55. Luber, S., I. Rivalta, Y. Umena, K. Kawakami, J.-R. Shen, N. Kamiya, G.W. Brudvig, and V.S. Batista, Biochemistry, 2011. **50**(29): p. 6308-6311.

56. Jaszewski, A.R., S. Petrie, R.J. Pace, and R. Stranger, Chemistry – A European Journal, 2011. **17**(20): p. 5699-5713.

57. Pace, R.J., R. Stranger, and S. Petrie, Dalton Transactions, 2012. **41**(24): p. 7179-7189.

58. Ruettinger, W., M. Yagi, K. Wolf, S. Bernasek, and G.C. Dismukes, Journal of the American Chemical Society, 2000. **122**(42): p. 10353-10357.

59. Ruettinger, W.F., C. Campana, and G.C. Dismukes, Journal of the American Chemical Society, 1997. **119**(28): p. 6670-6671.

60. Yagi, M., K.V. Wolf, P.J. Baesjou, S.L. Bernasek, and G.C. Dismukes, Angewandte Chemie International Edition, 2001. **40**(15): p. 2925-2928.

61. Dismukes, G.C., Chemical Reviews, 1996. **96**(7): p. 2909-2926.

62. Collman, J.P., P. Denisevich, Y. Konai, M. Marrocco, C. Koval, and F.C. Anson, Journal of the American Chemical Society, 1980. **102**(19): p. 6027-6036.

63. Collman, J.P., M. Marrocco, P. Denisevich, C. Koval, and F.C. Anson, Journal of Electroanalytical Chemistry and Interfacial Electrochemistry, 1979. **101**(1): p. 117-122.

64. Durand, R.R., C.S. Bencosme, J.P. Collman, and F.C. Anson, Journal of the American Chemical Society, 1983. **105**(9): p. 2710-2718.

65. Le Mest, Y., M. L'Her, J.P. Collman, N.H. Hendricks, and L. McElwee-White, Journal of the American Chemical Society, 1986. **108**(3): p. 533-535.

66. Collman, J.P., P.S. Wagenknecht, and J.E. Hutchison, Angewandte Chemie International Edition in English, 1994. **33**(15-16): p. 1537-1554.

67. Chang, C.K., H.Y. Liu, and I. Abdalmuhdi, Journal of the American Chemical Society, 1984. **106**(9): p. 2725-2726.

68. Chang, C.J., Y. Deng, C. Shi, C.K. Chang, F.C. Anson, and D.G. Nocera, Chemical Communications, 2000(15): p. 1355-1356.

69. Collman, J.P., N.H. Hendricks, K. Kim, and C.S. Bencosme, Journal of the Chemical Society, Chemical Communications, 1987(20): p. 1537-1538.

70. Liu, H.Y., I. Abdalmuhdi, C.K. Chang, and F.C. Anson, The Journal of Physical Chemistry, 1985. **89**(4): p. 665-670.

71. Collman, J.P. and K. Kim, Journal of the American Chemical Society, 1986. **108**(24): p. 7847-7849.

72. Guilard, R., M.A. Lopez, A. Tabard, P. Richard, C. Lecomte, S. Brandes, J.E. Hutchison, and J.P. Collman, Journal of the American Chemical Society, 1992. **114**(25): p. 9877-9889.

73. Collman, J.P., J.E. Hutchison, M.A. Lopez, A. Tabard, R. Guilard, W.K. Seok, J.A. Ibers, and M. L'Her, Journal of the American Chemical Society, 1992. **114**(25): p. 9869-9877.

74. Shimazaki, Y., T. Nagano, H. Takesue, B.-H. Ye, F. Tani, and Y. Naruta, Angewandte Chemie International Edition, 2004. **43**(1): p. 98-100.

75. Naruta, Y., M.-a. Sasayama, and T. Sasaki, Angewandte Chemie International Edition in English, 1994. **33**(18): p. 1839-1841.

76. Naruta, Y. and M.-A. Sasayama, Journal of the Chemical Society, Chemical Communications, 1994(23): p. 2667-2668.

77. Vasudevan, P., Santosh, N. Mann, and S. Tyagi, Transition Metal Chemistry, 2013. **15**(2): p. 81-90.

78. Zecevic, S., B. Simic-Glavaski, E. Yeager, A.B.P. Lever, and P.C. Minor, Journal of Electroanalytical Chemistry and Interfacial Electrochemistry, 1985. **196**(2): p. 339-358.

79. Březina, M., W. Khalil, J. Koryta, and M. Musilová, Journal of Electroanalytical Chemistry and Interfacial Electrochemistry, 1977. **77**(2): p. 237-244.

80. Chen, J., W. Zhang, D. Officer, G.F. Swiegers, and G.G. Wallace, Chemical Communications, 2007(32): p. 3353-3355.

81. Chen, J., J.H. Huang, G.F. Swiegers, C.P. Too, and G.G. Wallace, Chemical Communications, 2004(3): p. 308-309.

82. Chen, J., C.O. Too, G.G. Wallace, and G.F. Swiegers, Electrochimica Acta, 2004. **49**(5): p. 691-702.

83. Bitterwolf, T.E. and A.C. Ling, Journal of Organometallic Chemistry, 1973. **57**(1): p. C15-C18.

84. Mueller-Westerhoff, U.T., T.J. Haas, G.F. Swiegers, and T.K. Leipert, Journal of Organometallic Chemistry, 1994. **472**(1): p. 229-246.

85. Chen, J., P. Wagner, L. Tong, G.G. Wallace, D.L. Officer, and G.F. Swiegers, Angewandte Chemie-International Edition, 2012. **51**(8): p. 1907-1910.

86. Chen, J., P. Wagner, L. Tong, D. Boskovic, W. Zhang, D. Officer, G.G. Wallace, and G.F. Swiegers, Chemical Science, 2013. **4**(7): p. 2797-2803.

87. Brimblecombe, R., J. Chen, P. Wagner, T. Buchhorn, G.C. Dismukes, L. Spiccia, and G.F. Swiegers, Journal of Molecular Catalysis A: Chemical, 2011. **338**(1–2): p. 1-6.

88. Kanan, M.W. and D.G. Nocera, Science, 2008. **321**(5892): p. 1072-1075.

89. Lutterman, D.A., Y. Surendranath, and D.G. Nocera, Journal of the American Chemical Society, 2009. **131**(11): p. 3838-3839.

90. McAlpin, J.G., Y. Surendranath, M. Dincă, T.A. Stich, S.A. Stoian, W.H. Casey, D.G. Nocera, and R.D. Britt, Journal of the American Chemical Society, 2010. **132**(20): p. 6882-6883.

91. Kanan, M.W., J. Yano, Y. Surendranath, M. Dincă, V.K. Yachandra, and D.G. Nocera, Journal of the American Chemical Society, 2010. **132**(39): p. 13692-13701.

92. Jiao, F. and H. Frei, Energy & Environmental Science, 2010. **3**(8): p. 1018-1027.

93. Hocking, R. and L. Spiccia. *Abstract 155*. in *39th International Conference on Coordination Chemistry*. 2010. Adelaide, Australia.

94. Sauer, K. and V.K. Yachandra, Proceedings of the National Academy of Sciences, 2002. **99**(13): p. 8631-8636.

95. Jiao, F. and H. Frei, Angewandte Chemie International Edition, 2009. **48**(10): p. 1841-1844.

96. Liu, X. and C.T. Prewitt, Physics and Chemistry of Minerals, 1990. **17**(2): p. 168-172.

97. Singh, R.N., J.F. Koenig, G. Poillerat, and P. Chartier, Journal of The Electrochemical Society, 1990. **137**(5): p. 1408-1413.

98. Robinson, D.M., Y.B. Go, M. Greenblatt, and G.C. Dismukes, Journal of the American Chemical Society, 2010. **132**(33): p. 11467-11469.

99. Yin, Q., J.M. Tan, C. Besson, Y.V. Geletii, D.G. Musaev, A.E. Kuznetsov, Z. Luo, K.I. Hardcastle, and C.L. Hill, Science, 2010. **328**(5976): p. 342-345.

100. Gellman, S.H., Accounts of Chemical Research, 1998. **31**(4): p. 173-180.

101. Prince, R.B., S.A. Barnes, and J.S. Moore, Journal of the American Chemical Society, 2000. **122**(12): p. 2758-2762.

102. Drexler, K.E., Peptide Science, 2011. **96**(5): p. 537-544.

103. Horne, W.S., Expert Opinion on Drug Discovery, 2011. **6**(12): p. 1247-1262.

104. Martinek, T.A. and F. Fulop, Chemical Society Reviews, 2012. **41**(2): p. 687-702.

105. Koder, R.L. and P.L. Dutton, Dalton Transactions, 2006(25): p. 3045-3051.

106. Koder, R.L., C.C. Moser, and P.L. Dutton, Biochemical Society transactions, 2008. **36**: p. 1106-1111.

107. Nanda, V. and R.L. Koder, Nat Chem, 2010. **2**(1): p. 15-24.

108. Dutton, P.L. and C.C. Moser, Faraday Discussions, 2011. **148**(0): p. 443-448.

109. Brimblecombe, R., A. Koo, G.C. Dismukes, G.F. Swiegers, and L. Spiccia, Journal of the American Chemical Society, 2010. **132**(9): p. 2892-+.

110. Brimblecombe, R., A. Koo, G.C. Dismukes, G.F. Swiegers, and L. Spiccia, ChemSusChem, 2010. **3**(10): p. 1146-1150.

111. Swiegers, G.F., D.R. MacFarlane, D.L. Officer, A. Ballantyne, D. Boskovic, J. Chen, G.C. Dismukes, G.P. Gardner, R.K. Hocking, P.F. Smith, L. Spiccia, P. Wagner, G.G. Wallace, B. Winther-Jensen, and O. Winther-Jensen, Australian Journal of Chemistry, 2012. **65**(6): p. 577-582.

112. Chiang, C.K., C.R. Fincher, Y.W. Park, A.J. Heeger, H. Shirakawa, E.J. Louis, S.C. Gau, and A.G. MacDiarmid, Physical Review Letters, 1977. **39**(17): p. 1098-1101.

113. Bredas, J.L. and G.B. Street, Accounts of Chemical Research, 1985. **18**(10): p. 309-315.

114. Jonas, F. and J.T. Morrison, Synthetic Metals, 1997. **85**(1–3): p. 1397-1398.

115. Street, G.B. and T.C. Clarke, IBM Journal of Research and Development, 1981. **25**(1): p. 51-57.

116. Chiang, C.K., S.C. Gau, J.C.R. Fincher, Y.W. Park, A.G. MacDiarmid, and A.J. Heeger, Applied Physics Letters, 1978. **33**(1): p. 18-20.

117. Andreas Elschner, S.K., Wilfried Lövenich, Udo Merker, Knud Reuter, *PEDOT Principles and Applications of an Intrinsically Conductive Polymer*2011, Boca Raton: CRC Press.

118. Roncali, J., Chemical Reviews, 1992. **92**(4): p. 711-738.

119. Gu, C., B.C. Norris, F.-R.F. Fan, C.W. Bielawski, and A.J. Bard, ACS Catalysis, 2012. **2**(5): p. 746-750.

120. Ruhlmann, L., A. Nakamura, J.G. Vos, and J.-H. Fuhrhop, Inorganic Chemistry, 1998. **37**(23): p. 6052-6059.

121. Harriman, A. and G. Porter, Journal of the Chemical Society, Faraday Transactions 2: Molecular and Chemical Physics, 1979. **75**(0): p. 1532-1542.

122. Satake, A. and Y. Kobuke, Organic & Biomolecular Chemistry, 2007. **5**(11): p. 1679-1691.

123. Novoselov, K.S., A.K. Geim, S.V. Morozov, D. Jiang, Y. Zhang, S.V. Dubonos, I.V. Grigorieva, and A.A. Firsov, Science, 2004. **306**(5696): p. 666-669.

124. Geim, A.K., Science, 2009. **324**(5934): p. 1530-1534.

125. Geim, A.K. and K.S. Novoselov, Nature Materials, 2007. **6**(3): p. 183 - 191.

126. Novoselov, K.S., D. Jiang, F. Schedin, T.J. Booth, V.V. Khotkevich, S.V. Morozov, and A.K. Geim, Proceedings of the National Academy of Sciences of the United States of America, 2005. **102**(30): p. 10451-10453.

127. Hummers, W.S. and R.E. Offeman, Journal of the American Chemical Society, 1958. **80**(6): p. 1339-1339.

128. Shahriary, L. and A.A. Athawale, IJREEE, 2014. **2**: p. 58-63.

129. Kovtyukhova, N.I., P.J. Ollivier, B.R. Martin, T.E. Mallouk, S.A. Chizhik, E.V. Buzaneva, and A.D. Gorchinskiy, Chemistry of Materials, 1999. **11**(3): p. 771-778.

130. Li, D., M.B. Müller, S. Gilje, R.B. Kaner, and G.G. Wallace, Nature Nanotechnology, 2008. **3**(2): p. 101-5.

131. Jalili, R., S.H. Aboutalebi, D. Esrafilzadeh, K. Konstantinov, S.E. Moulton, J.M. Razal, and G.G. Wallace, ACS Nano, 2013. **7**(5): p. 3981-3990.

132. Jalili, R., S.H. Aboutalebi, D. Esrafilzadeh, R.L. Shepherd, J. Chen, S. Aminorroaya-Yamini, K. Konstantinov, A.I. Minett, J.M. Razal, and G.G. Wallace, Advanced Functional Materials, 2013. **23**(43): p. 5345-5354.

133. Naficy, S., R. Jalili, S.H. Aboutalebi, R.A. Gorkin Iii, K. Konstantinov, P.C. Innis, G.M. Spinks, P. Poulin, and G.G. Wallace, Materials Horizons, 2014. **1**(3): p. 326-331.

134. Dimiev, A.M., L.B. Alemany, and J.M. Tour, ACS Nano, 2012. **7**(1): p. 576-588.

135. Konkena, B. and S. Vasudevan, The Journal of Physical Chemistry Letters, 2012. **3**(7): p. 867-872.

136. Zhou, F., A. Izgorodin, R.K. Hocking, V. Armel, L. Spiccia, and D.R. MacFarlane, ChemSusChem, 2013. **6**(4): p. 643-651.

137. Frey, C.E., M. Wiechen, and P. Kurz, Dalton Transactions, 2014. **43**(11): p. 4370-4379.

138. Walsh, D., N.M. Sanchez-Ballester, K. Ariga, A. Tanaka, and M. Weller, Green Chemistry, 2015.

139. Park, S., K.-S. Lee, G. Bozoklu, W. Cai, S.T. Nguyen, and R.S. Ruoff, ACS Nano, 2008. **2**(3): p. 572-578.

2 Experimental

2.1 Introduction

This chapter explains the experimental details of the work in this thesis: materials and reagents used, instrumentation, synthesis methods for the compounds used in experiments, fabrication of samples, characterisation and testing methods. The thesis chapters that follow refer to relevant sections of this chapter when discussing fabrication methods as well as specific experimental details, where applicable.

2.2 Chemicals and reagents used

The following chemicals and reagents were used as received unless stated otherwise.

Reagent name	Grade, Batch #, Preparation	Company
4-Pyridinecarboxyaldehyde		Aldrich
3,4-Ethylenedioxythiophene (EDOT)	distilled	Amsheng Chemical
4-Bromobenzaldehyde	99%, BCBH9835V	Aldrich
Acetone	99.8%	Univar
Ammonia solution	25% (aqueous)	Chem-Supply
Azobisisobutyronitrile (AIBN)	12% in acetone	Sigma
Benzaldehyde	99%, MKBP5021V	Sigma-Aldrich
Calcium acetate monohydrate ($Ca(AcO)_2H_2O$)		Sigma
Calcium chloride ($CaCl_2$)	Anhydrous, 039K0057	Sigma-Aldrich
Calcium hydroxide ($Ca(OH)_2$)		Aldrich
Calcium nitrate tetrahydrate ($Ca(NO_3)_2$)		Aldrich
Chloroform	99.8%, 280091	Chem-Supply
Cyclohexane		Sigma
Dichloromethane (DCM)		Aldrich
Diethyl ether	99.7%, 15 04 0243	RCI Labscan
Diethylhydroxylamine		Sigma Aldrich
Dioxane	99.8%, 03396MMV	Sigma Aldrich
Ethanol	Abs, 268373	Chem-Supply
Graphene oxide (GO)	2.2% wt in water	ANFF Wollongong

n - Hexane	95%, 15 070238	RCI Labscan
Hydrochloric acid (HCl)	32%	Chem-Supply
Hypophosphorous acid	50%	Sigma-Aldrich
Iodomethane (CH_3I)	99%	Biedel-de Haën
Iron(III) p-toluenesulfonate hexahydrate (Fe-pTS)		Aldrich
Liquid crystal graphene oxide (LCGO)	11 mg/mL in water	IPRI
Manganese (II) acetate tetrahydrate ($Mn(AcO)_2 4H_2O$)		Sigma
Manganese chloride ($MnCl_2$)	97%, MKBG4107V	Aldrich
Methanol		Ajax Finechem
Milli-Q water		
N,*N*-Dimethylformamide (DMF)	99.8%, 12 03 0053	RCI Labscan
n-Butyllithium	2.5 M in hexanes, STBD2349V	Aldrich
Poly(sodium 4-styrenesulfonate) (PSS)	18% aqueous soln, AV MW 70,000	Sigma
Potassium carbonate (K_2CO_3)	AR, 1205532	Univar
Potassium hydroxide (KOH)	RG, >/ 90% flakes	Sigma-Aldrich
Potassium permanganate ($KMnO_4$)		Sigma
Powdered silica	40-63 µm, 52	Davisil
Propionic acid	99.5%, 276317	Chem-Supply
Pyridine	RG, PI01232500	Scharlau
Pyrrole	97%, distilled	Merck
Reduced graphene oxide (RGO)	0.05% wt in water	ANFF Wollongong
Sodium borohydride ($NaBH_4$)		Sigma
Sodium dithionite ($Na_2S_2O_4$)		Ajax Finechem
Sodium hydroxide (NaOH)	Pellets	Chem-Supply
Sodium nitrate ($NaNO_3$)		Sigma
Sodium sulfate (Na_2SO_4)	99%, 15327KO	Sigma Aldrich
Sulfuric acid (H_2SO_4)		Ajax
Tetrahydrofuran (THF)	HPLC grade, DK952	Honeywell
Toluene	99.5%, 279723	Chem-Supply
Triethylamine	99.6%, STBD41184	Sigma-Aldrich
Trifluoroacetic acid ($C_2HF_3O_2$)(TFA)		Sigma-Aldrich
Triphenylphosphine	99%, 07521DE	Sigma-Aldrich
Fluoride tin oxide (FTO) glass	<10 Ω/□, >77% transmittance	Zhuhai Kaivo
Epoxy resin		
Pelco conductive silver paint	14352	Ted Pella Inc.
Nail polish		
Copper wire (cladded)	0.5 mm diameter 0.9 mm with cladding	

2.3 Instruments and techniques for fabrication

2.3.1 Spin coating

Figure 2.1 Photograph of the spin coating apparatus.

Spin coating of solutions on glass substrates was performed on a Laurell Model WS-400V-6NPP/LITE spin coating apparatus (Figure 2.1). The general method consisted of placing a piece of cleaned substrate inside the instrument, which held the sample in place by vacuum suction. A small amount of solution (typically 150 µL) containing the desired compound was spread evenly on the surface of the substrate, which was then spun at a high rate (1000 rpm) for a few seconds. The solvent was evaporated by placing the substrate on a hotplate immediately thereafter, leaving a thin film on the substrate.

2.3.2 Sonication

Figure 2.2 Photograph of the bath sonicator (left) and tip sonicator (right).

A Branson B2500R-MTH bath sonicator was used for general chemical workup such as dissolving/dispersing compounds in liquid and cleaning of glass substrates in appropriate solvents. A Sonics Vibracell tip sonicator was employed for more rigorous dispersions of solids in water used for spray coating (see Figure 2.2).

2.3.3 Cleaning of electrodes with UV-Ozone and Plasma treatment

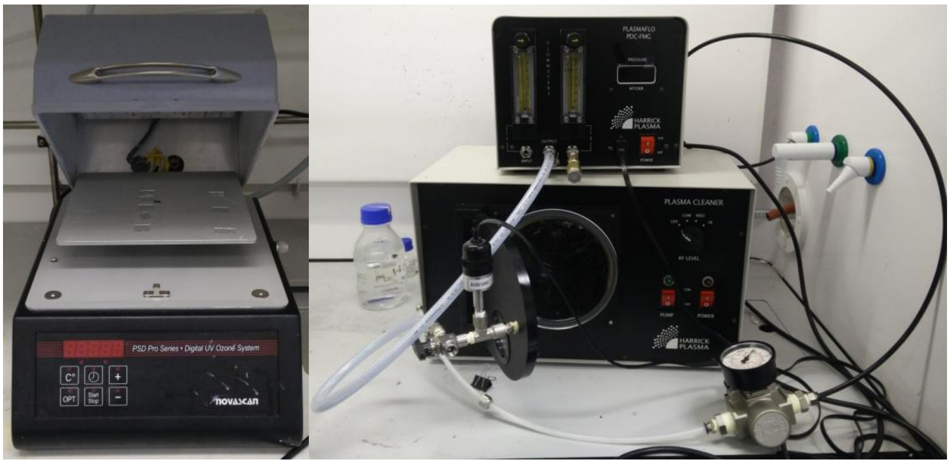

Figure 2.3 Photographs of the UV-Ozone system (left) and plasma cleaning system (right).

Electrode substrates that were prepared for deposition were cleaned in a Novascan PSD Pro Series Digital UV Ozone System or Harrick Plasma PLASMAFLO PDC-FMG (Figure 2.3). This cleaning system was used to degrade potential traces of organic matter left on substrates such as FTO and microscope glass after prior ultrasonic washing in acetone and water. In addition this type of treatment significantly increased the hydrophilicity of the affected substrate [1-3] which was necessary for subsequent coating with materials in aqueous solution or dispersion. A typical procedure consisted of laying the slides onto the platform facing upwards and activating the unit for 10 min of treatment. Afterwards the substrate slides were ready for immediate use in coating and deposition experiments.

2.3.4 Spray coating

Figure 2.4 Photograph of the Sonotek spraying system.

Spray coating of dispersed solids in water (graphene oxide, reduced graphene oxide) was performed using a Sonotek spray coating instrument (Figure 2.4). A sample feeding mechanism pumped the dispersion through an ultrasonication tip which dispersed the sample onto the substrate in a cone shaped spray. The substrate was affixed to a hotplate underneath the spray tip, onto which the tip would spray while moving in a raster type pattern using an XYZ electronic rail system. The liquid flow rate, hotplate temperature, tip sonication speed, tip movement speed and height were adjusted to assure optimal deposition of the sample.

2.3.5 Doctor blade coating

A PK K Control Coater doctor blade instrument was used to coat films of liquid crystalline graphene oxide (LCGO) containing reducing agent. The machine employed a large metal blade that was held in place at a set distance above the base plane upon which the substrate was laid (typically fluoride tin oxide glass or Multapex 75 µm PET sheet). A dispersion of material was spread horizontally in a uniform fashion; when the blade was pulled across the substrate at a controlled, even speed.

2.3.6 Sputter coating

Figure 2.5 Photograph of Edwards FTM6 Auto 306 sputter coater.

An Edwards FTM6 Auto 306 sputter coater (Figure 2.5) was used to prepare Pt coated glass for use as control working electrodes in control experiments. This service was provided under the supervision of Dr Tony Romeo at the University of Wollongong Electron Microscopy Centre.

2.3.7 Laser cutter

Figure 2.6 Photograph of the laser cutter apparatus.

A Universal Laser Systems PLS6MW laser cutter (Figure 2.6) was employed to cut interlocking plates of Perspex that were used to build vessels for experiments. The plates were designed using CorelDraw.

2.3.8 Electrodeposition

Figure 2.7 Photograph of the EDAQ466 unit.

All electrochemical experiments were carried out on an EDAQ466 potentiostat (Figure 2.7), which was employed for electrochemical deposition of catalytic films as well as subsequent electrochemical testing. In the case of deposition, the unit was used in conjunction with a purpose built vessel containing the working electrode, a 1.3 x 1.3 cm Pt mesh counter electrode and a Ag/AgCl miniature reference electrode.

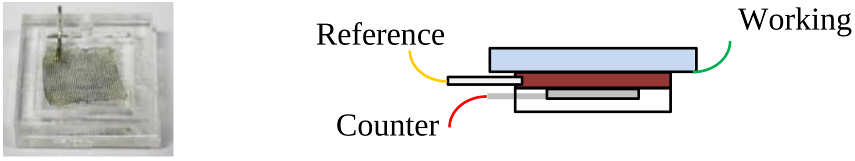

Figure 2.8 Electrodeposition Vessel 1: Photo (left) and schematic (right) of the small volume electrochemical cell used to electrodeposit samples.

Two vessel designs were used for this technique. Electrodeposition Vessel 1 (EV1) was designed for use with very small amounts of reagent (Figure 2.8). A 2 mm thick frame of length and width 2.1 x 2.1 cm, made of laser cut Perspex, was attached to a flat piece of Perspex. The gaps around the edges were sealed by injecting small amounts of chloroform, which dissolved the Perspex to effectively glue the pieces together, with subsequent evaporation of the solvent. A small circular hole, approximately 1.8 mm, wide was cut in the top of the frame to serve as an injection point for reagents as well as a place to insert a miniature Ag/AgCl reference electrode in experiments. A 1 mm circular hole was cut to connect a Pt wire to a Pt mesh counter electrode. The side of the frame facing the substrate was coated with a sealing layer of silicone glue to prevent leakage of liquid when in use.

The full apparatus consisted of a piece of FTO glass of suitable size, cleaned by sonication in acetone and subsequent rinsing and plasma cleaning, with a copper wire (0.5 mm diameter) attached to the surface by silver paint and then epoxy glue. The FTO glass and counter electrode were clamped together and the polymerisation solution injected through the hole in the top (Figure 2.7). The dimensions of this vessel were chosen so as to work with a minimal volume of solution (~0.9 mL), in order to minimise the amount of material needed for each experiment. The miniature Ag/AgCl electrode was inserted so as to close the cell to air and not impede the flow between working and counter. After deposition the cell was taken apart to drain the solution and wash the device; the sample was washed in milli-Q, and dried with pressurised air. The reaction area was limited to the 1.5 x 1.5 cm (2.25 cm^2) inner area of the frame, allowing for ready reproduction of films of fixed (and known) dimensions.

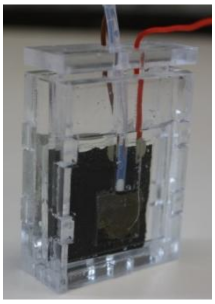

Figure 2.9 Photo of Electrodeposition Vessel 2.

Electrodeposition Vessel 2 (EV2) was made as modified version of the EV1 to allow deposition on more sensitive substrates like graphene films, on Multapex PET and FTO glass, without the tight clamping of the counter electrode causing peeling off of the underlying film. The vessel was a 3.1 x 4 cm box built from interlocking Perspex plates glued together using chloroform (Figure 2.9). Holes were cut in the cover to allow for wires to the electrodes. The working cell comprised the substrate chosen in the experiment, a counter electrode of 1.3 x 1.3 cm Pt mesh affixed to cladded copper wire, and a Ag/AgCl reference electrode. This design required more reagent solution than the previous one (~3 mL) but allowed the deposition substrate to be free standing in solution. After deposition, the vessel was drained of solution and washed with Milli-Q water and dried using pressurised air.

2.4 Characterisation techniques and equipment

2.4.1 Mass spectrometry

Mass spectrometric analysis of porphyrins was performed on a Shimadzu Biotech AXIMA Confidence Linear/Reflectron matrix-assisted laser desorption/ionization – time of flight (MALDI-TOF) mass spectrometer. The molecular mass of each porphyrin was measured and compared to theoretical molecular mass estimates to confirm results. The matrix used for analysis was dithranol.

2.4.2 Nuclear magnetic resonance spectrometry

Nuclear Magnetic Resonance (NMR) A Bruker Ultrashield 400 Plus spectrometer was used to verify porphyrin spectra from samples dissolved in deuterated solvents (DMSO, D_2O, $CDCl_3$) against literature data.

2.4.3 Gas permeation chromatography

A Shimadzu UFLC system equipped with a RID-10A refractive index detector and a Sedere Sedex60LT evaporative light scattering detector was used with a Phenogel column of 10 um particle size and 100 Å porosity, 600 x7.8 mm (phenomenex, part number: 00K-0642-K0) to determine the molecular weight of the polymeric porphyrin. THF was used as the solvent at a flow rate of 1ml/min at room temperature. These characterisations were carried out by Dr Patricia Hayes at the Intelligent Polymer Research Institute at the University of Wollongong.

2.4.4 Elemental analysis

Porphyrin/PEDOT samples were analysed using a Carlo Erba 1106 instrument for CHN combustion analysis and a Varian SpectrAA 220 atomic absorption spectrophotometer (AAS) for the determination of metal ions present. CHN analysis was provided by Mr Sasha Melnitchenko at the Microanalytical Unit of the Australian National University Research School of Chemistry and AAS analysis by Sue Butler at the University of Wollongong School of Chemistry.

2.4.5 Profilometry

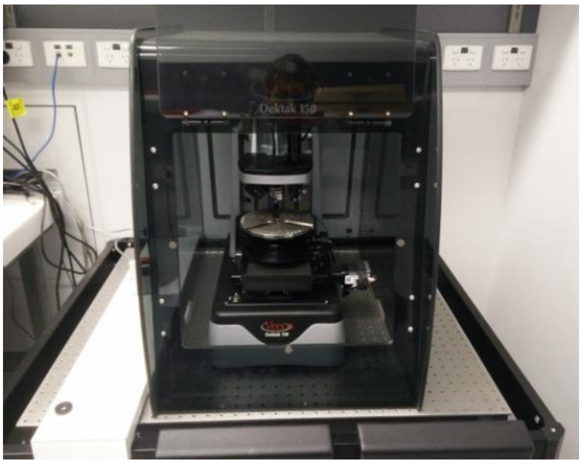

Figure 2.10 Photograph of the Dektak profilometer.

A Veeco Dektak 150 profilometry system (see Figure 2.10) was used to perform thickness measurements of deposited films. This was done by making a scratch in deposited film on a microscope glass slide using a piece of glass. The profilometer gave a height profile by passing a tip over the sample in a straight line across the scratched section. The thickness was determined at several points by calculating the distance between the substrate and the top of the film, and the result averaged to yield an average film thickness result.

2.4.6 Conductivity measurements

Figure 2.11 Photograph of the Jandel 4 point probe unit (top left), the probe tip mechanism (top right) and a closeup of the probe tip (bottom).

A Jandel Model RM3 four point probe was used to measure resistance across deposited films and deduct the conductivity of the sample (Figure 2.11). The forward and reverse resistance was measured on porphyrin/PEDOT films deposited on non-conductive glass and the conductivity calculated using previously obtained thickness of the film from profilometry:

$$\rho = \frac{(\Omega_{FWD} + \Omega_{REV})}{2} \times \frac{t}{10000}$$

$$\sigma = \frac{1}{\rho}$$

Resistivity ρ (in Ω cm) was determined by multiplying the average of forward and reverse resistance Ω_{FWD} / Ω_{REV} (in Ω/□) by the thickness t (in µm converted to cm). The conductivity σ (in S/cm) was obtained by taking the inverse of the resistivity ρ.

2.4.7 UV-visible absorbance spectrometry

Figure 2.12 Photograph of the UV-Vis spectrophotometer.

A Shimadzu UV-1800 Double Slit UV-Vis Spectrophotometer was used for all light absorbance spectroscopy (UV-Vis) in a range of typically 350-700 nm (Figure 2.12). Solutions of porphyrins were characterised in cuvettes having 1 cm path length. Plastic disposable cuvettes were used for water and ethanol and quartz cuvettes for organic solvents. Solid film samples on transparent substrates like FTO glass and microscope slides were affixed to the sample holder with Blu-Tack, facing the oncoming light beam. In all cases the same solvent or piece of clear substrate (where applicable) were used as a reference from which a background spectrum could be taken and automatically subtracted from the result. UV-Vis analysis was important for the characterisation of porphyrins as the wavelengths of absorbance peaks yielded data on the configuration of the molecule under different conditions.

2.4.8 Electrochemical cell

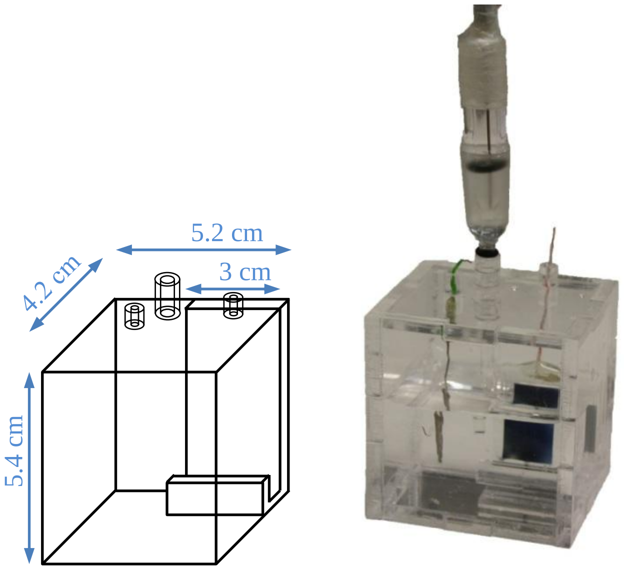

Figure 2.13 Schematic of the laser-cut electrochemical cell (left) and photograph of the cell as used in experiments (right).

An electrochemical cell was designed, consisting of laser cut Perspex panels of 4.5 mm thickness that clipped together to form a cube (Figure 2.13). The panels were attached by injecting a tiny amount of chloroform into the crevices, which melted a small amount of Perspex and acted as glue, sealing the edges with the plastic itself. The cell design employed a fixed sample position and distance between electrodes. It was also relatively easy to alter and redesign by cutting new components or replacing each with a modified version. The main goals of this design were to minimise movement of the electrodes and provide reproducible and stable electrode positions.

The working electrode (sample) was placed inside the vessel by sitting it on the J-shaped component attached to the lid. The wire protruded through the lid allowing the EDAQ terminal cable to be attached with an alligator clip outside the unit. An Ag/AgCl reference electrode was inserted through a hole in the lid close to the working electrode and the Pt mesh counter electrode through another hole approximately 3 cm away from the working electrode surface. The respective terminal cables were attached to the electrode wires with alligator clips, with care taken to reproduce the same electrode positions each time tests were conducted.

2.4.9 Electrochemical testing

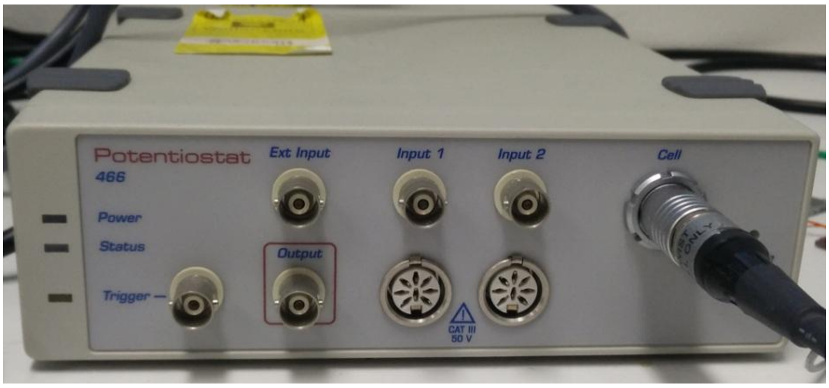

Figure 2.14 Photograph of the EDAQ466 potentiostat.

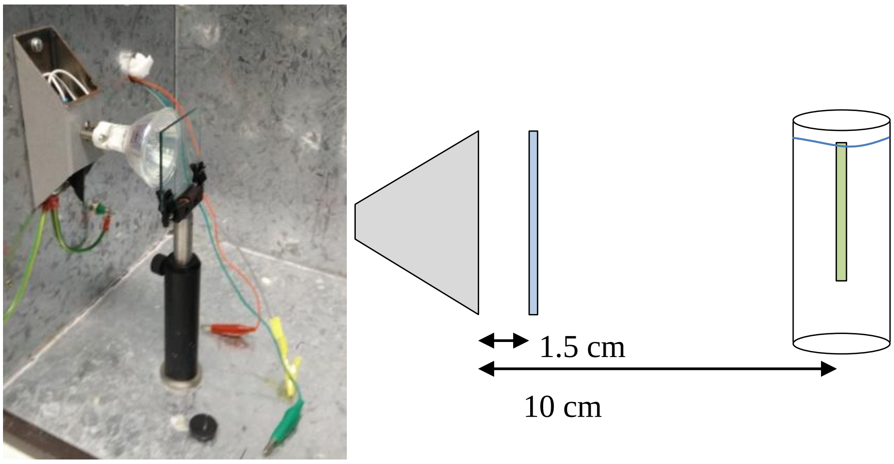

Figure 2.15 Photograph of the light source with IR filter inside a faraday cage cabinet (right) and schematic of the light source setup (right).

Electrochemical testing experiments were carried out on an EDAQ466 potentiostat (Figure 2.14). Samples were inserted into the electrochemical cell as a working electrode. A BASi Ag/AgCl aqueous salt bridge (KOH, 3 M) reference and 1 x 2 cm Pt mesh counter electrode were further incorporated. The prepared films of porphyrin/PEDOT or Mn_xO_y-graphene were used as working electrodes in photoelectrochemical tests to assess the level of catalytic current density at varying voltages (*vs* Ag/AgCl). In the case of Mn_xO_y only dark current was measured. Sodium sulfate (Na_2SO_4) electrolyte solution (0.1 M) was used. The electrolyte was bubbled through with N_2 gas while stirring for 30 min before the experiment. The sample was placed inside the electrochemical cell, which was located inside a closed faraday cage cabinet, 10 cm from an illumination source (a SoLux daylight MR16 halogen light bulb; 12 V, 50 W, 24^{o}; ca. 0.25 sun intensity) with a Thorlabs 315-710 nm visible light bandpass filter present 1.5 cm in front of the light source (Figure 2.15). The bandpass filter removed most of the heat (infra-red wavelengths) generated by the light source. The electrochemical cell consisted of the sample film on FTO glass or PET as the working electrode, platinum mesh (1 x 2 cm) as the counter electrode and Ag/AgCl as the reference electrode. The film sample was aligned to face the light source directly when photocurrent measurements were taken.

Three modes of voltammetry were used on prepared samples for stabilisation and testing. This section will outline the general method and more specific parameters are noted in the experimental section of each individual chapter.

Cyclic Voltammetry (CV) was performed on porphyrin/PEDOT samples in order to electrochemically stabilise the films prior to other testing. Typically, 20 cycles at a scan rate of 10 mV/sec in the range 0-0.7 V (*vs* Ag/AgCl) were performed. This was done to equilibrate the charge transfer over that voltage range, as PEDOT can contain static charges and not fully oxidised regions throughout the film, which would give a skewed result when attempting measurement without conditioning.

MnO_x films on graphene substrates were analysed by linear sweep voltammetric conditioning. Linear sweep voltammetry (LSV) was performed on samples by scanning the current response in the range 0-0.7 V (*vs* Ag/AgCl) for PEDOT and 0-1.6 V (*vs* Ag/AgCl). Typically, 5 scans were taken at a scan rate of 5 or 10 mV/sec until the sample returned identical results over each repeated scan. The last scan was recorded as data and analysed. In photocurrent testing, the light source was then switched on and another 3 scans taken, of which the last was recorded as data. This allowed analysis of the onset potential of the catalytic current when illumination was involved. The resulting data was then divided by the geometric area of the sample to give current density (in $\mu A/cm^2$ and mA/cm^2), allowing ready comparison of separate sample data.

From the data obtained through LSV, suitable voltages were chosen to perform chronoamperometric (CA) testing of each sample. In this mode the sample was poised at a constant potential over time and the current recorded. In the case of PEDOT, the voltages used in CA testing were 0.6 V, 0.65 V and 0.7 V (*vs* Ag/AgCl). Because of possible oxidation of the PEDOT film to its fully oxidised state, samples were typically held at potential for 1 h to allow the current to stabilise. The light source was then switched on and the photocurrent recorded for 10 min, after which the light was switched off. The data was then converted to current density by dividing the current by the geometric area of the sample. The data was normalised by subtracting the baseline current from 1 min before illumination, in order to obtain readily comparable measures of photocurrent density for each sample type. Results are typically shown from 1 min before illumination until 1 min after. In the case of Mn_xO_y samples on graphene substrates, the voltage was set at 1.15 V or 1.6 V (*vs* Ag/AgCl). The data is also shown in full instead of cropping the initial period, as catalysis in dark conditions began with activation of the potentiostat rather than illumination.

2.4.10 Electrochemical testing with gas sensing

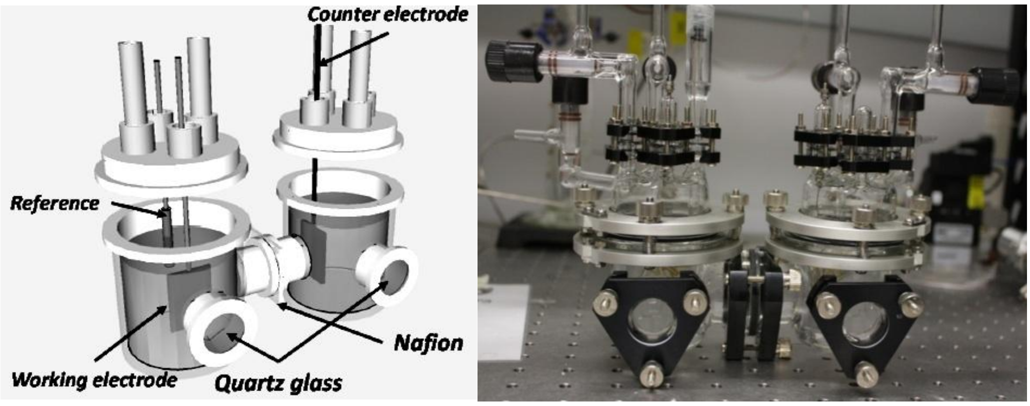

Figure 2.16 Schematic (left) and photograph (right) of the sealed glass electrochemical cell used for photoelectrochemical analysis with gas sensing.

Figure 2.17 Photograph of the complete electrochemistry and gas chromatography apparatus.

Photocurrent testing of high performing porphyrin/PEDOT samples with simultaneous gas detection was done using a specialised apparatus and method developed by Dr Lei Tong with equipment and training provided by A/Prof. Attila Mozer at the Intelligent Polymer Research Institute at the University of Wollongong. The apparatus consisted of a sealed glass electrochemical cell containing the working electrode sample, Ag/AgCl reference electrode and Pt mesh counter electrode (Figure 2.16). The cell was filled with Na_2SO_4 electrolyte (0.1 M) and the electrolyte bubbled with Ar gas overnight to remove all air inside the cell. The Ar gas was continuously bubbled through the electrolyte throughout the photocurrent experiment and used as the carrier gas for a connected gas chromatography unit. The electrodes were connected to a CHI potentiostat unit and gas outlets for the working and counter electrode were connected to a dedicated Shimadzu GC-8A gas chromatograph with copper tubing (Figure 2.17).

The sample was poised at 0.7 V (*vs* Ag/AgCl) in 0.1 M Na_2SO_4 for 1 h, then illuminated with a Newport solar simulator with 1000 W Xenon lamp wth AM 1.5 filter while maintaining an invariant bias. After 4.7 h of testing under illumination, the carrier gas was analysed in a Shimadzu GC-8A gas chromatograph and the results plotted over 30 min of elution time. The carrier gas was tested prior to purging, after purging, and, as mentioned above, after 4.7 h under illumination. Testing prior to purging (carrier gas argon + air) showed the retention time of gas peaks corresponding to argon, oxygen, nitrogen and residual hydrogen. Testing after purging produced gas peaks corresponding to argon only, indicating that any air in the vessel has been fully displaced by argon. Testing after illumination gave a qualitative measure of the gases produced by photoelectrochemical activity of the sample.

2.5 References

1. Vig, J., *UV/Ozone Cleaning of Surfaces*, in *Treatise on Clean Surface Technology*, K.L. Mittal, Editor 1987, Springer US. p. 1-26.

2. Delplanque, A., E. Henry, J. Lautru, H. Leh, M. Buckle, and C. Nogues, Applied Surface Science, 2014. **314**: p. 280-285.
3. Tan, S.H., N.-T. Nguyen, Y.C. Chua, and T.G. Kang, Biomicrofluidics, 2010. **4**(3): p. 032204.

3 Vapour phase polymerised Porphyrin/PEDOT films

3.1 Introduction and Aims

In this chapter the research strategy described in sections 1.8.1 and 1.8.2 was implemented in order to study manganese complex of porphyrins incorporated in conducting polymers as water oxidation photocatalysts, as described previously [1, 2]. Previous work had examined 5,10,15,20-tetrakis(4-sulfonatophenyl)porphyrinato manganese(III) chloride sodium salt (MnTPPS) embedded in poly(terthiophene) (PTTh) [1] and poly(3,4-ethylenedioxythiophene) (PEDOT) [2] matrix as catalysts of the selective, light-assisted oxidation of water. The strategy was based on a replication of the functionality of Naruta's cofacial Mn porphyrin catalyst [3-5] using the indirect matrix-assisted effect of conducting polymer to simulate the effect of direct covalent linkage between two porphyrins.

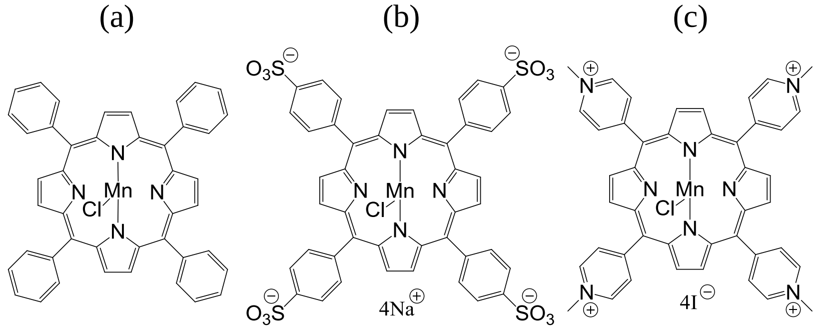

Figure 3.1 Porphyrin species studied in this chapter: (a) 5,10,15,20-tetraphenylporphyrinato manganese(III) chloride (MnTPP), (b) 5,10,15,20-tetrakis(4-sulfonatophenyl)porphyrinato manganese(III) chloride sodium salt (MnTPPS) and (c) 5,10,15,20-tetrakis(4-methylpyridinium)porphyrinato manganese(III) chloride tetraiodide (MnTMPyP).

That work was extended by incorporating several Mn porphyrin species in PEDOT and examining the effect on catalytic performance by this change. The porphyrin species studied in this chapter were: (a) 5,10,15,20-tetraphenylporphyrinato manganese(III) chloride (MnTPP), (b) 5,10,15,20-tetrakis(4-sulfonatophenyl)porphyrinato manganese(III) chloride sodium salt (MnTPPS) and (c) 5,10,15,20-tetrakis(4-methylpyridinium)porphyrinato manganese(III) chloride tetraiodide (MnTMPyP) (Figure 1.26). The Mn porphyrins were incorporated in low to very low loading levels within the PEDOT matrix in order to examine the effects of such loading and illuminate fundamental interactions between the PEDOT and the Mn porphyrins. In the case of the cationic species, low loading levels were also intended to minimise repulsive interactions between the PEDOT and that species.

The catalytic performance of each porphyrin/PEDOT material was evaluated by photoelectrochemical testing and their characteristics in the deposited films analysed using UV-Visible light absorbance spectroscopy (UV-Vis). When combined together, the species (b) and (c) displayed the additional feature of ion-pairing, leading to dense packing [6]. This ion-pairing was utilised in an attempt to bring about cofacial aggregation during deposition. All of the porphyrins contain the Mn(III) ion in the core, which is similar to the proposed oxidation state of the Mn ions in the OEC as described by Pace [7] and therefore of interest.

The porphyrins embedded in PEDOT films were studied using UV-visible absorbance spectroscopy due to their highly characteristic light absorbance spectra, from which structural details could be inferred [8]. Typically, the porphyrin Soret Band, or B-Band, is distinctively shifted in the polymer. Its shift can be compared to literature values so as to determine whether the porphyrin contains a metal ion and in which oxidation state the metal ion is in. Cofacial porphyrins also display excitonic coupling brought about by close face-to-face arrangements, measurable by UV-visible absorbance spectroscopy [9]. Changes in the UV-Vis spectrum of a porphyrin in different chemical environments, such as free solution and embedded in PEDOT, could therefore be used to make an assessment of the underlying physical condition of the molecule.

This chapter aimed to: (a) prepare the above Mn porphyrins, (b) study their incorporation in PEDOT, and (c) examine their photocatalytic properties for water oxidation, including the photocurrent density, and (d) compare the resulting data to each other. To this end, the Mn porphyrin species shown in Figure 1.26 were incorporated into PEDOT by vapour phase polymerisation (VPP). The resulting films were then deposited on conductive FTO glass for electrochemical analysis with illumination by a light source, as well as UV-Vis analysis of the translucent film on the transparent substrate. The better performing samples were then tested further in a photoelectrochemical experiment with detection of the gases produced in order to verify whether catalytic production of O_2 gas from aqueous electrolyte (0.1 M Na_2SO_4) was observed.

3.2 Experimental

3.2.1 Synthesis of 5,10,15,20-tetraphenylporphyrinato manganese(III) chloride (MnTPP)

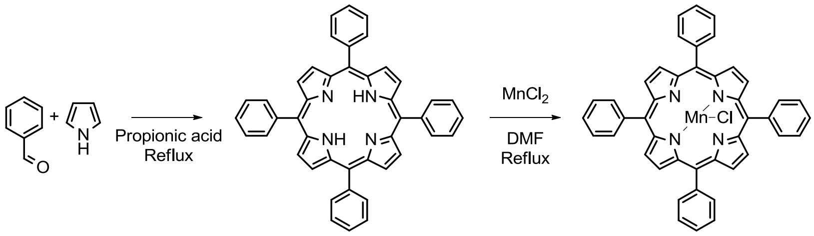

Figure 3.2 Synthesis of 5,10,15,20-tetraphenylporphyrinato manganese(III) chloride (MnTPP).

5,10,15,20-tetraphenylporphyrinato manganese(III) (MnTPP) was synthesised following a literature procedure based on the Adler synthesis method (Figure 3.2) [10-12]. Reagent grade pyrrole (7 mL, 0.1 mol) and benzaldehyde (11.6 ml, 0.1 mol) were added to boiling propionic acid (375 mL,) in a round bottom flask and stirred. The mixture was refluxed for 40 min under air. Afterwards the mixture was cooled down. The solid was filtered through a sintered glass funnel and washed with methanol. The product was dried in a vacuum oven at 60 °C and weighed (3.09 g, 20% yield). It was confirmed as 5,10,15,20-tetraphenylporphyrin (TPP) by MALDI (614.85 MW) and its UV-Vis spectrum was shown to be in agreement with the literature [13].

Manganese insertion was performed by dissolving the TPP (100 mg, 0.16 mmol) with $MnCl_2$ (1 g, 7.94 mmol) in 20 mL dimethylformamide (DMF) and stirring at reflux under air overnight. After cooling, the solvent was removed in vacuo and the product redispersed in water. The product was then extracted with dichloromethane, the solvent evaporated and the product dried in a vacuum oven at 60 °C (120 mg, 100% yield). The

final product was characterised by UV-Vis and its main absorbance peaks and their extinction coefficients were found to agree with published data (
Table 3.1) [14].

UV-Vis absorbance peaks of MnTPP	
Expected (Published) **[nm (ε, 1/1000 M^{-1} cm^{-1})(log ε)]**	**Experimentally Observed** **[nm (ε, 1/1000 M^{-1} cm^{-1})(log ε)]**
478 (119)(5.07)	477.5 (165)(5.22)
529 (6.6)(3.82)	528.5 (8)(3.90)
583 (11.2)(4.05)	582.5 (13.9)(4.14)
618 (13)(4.11)	618 (16)(4.20)

Table 3.1 UV-Vis spectroscopic reference data and experimentally obtained results for MnTPP.

3.2.2 Synthesis of 5,10,15,20-tetrakis(4-sulfonatophenyl)porphyrinato manganese(III) chloride sodium salt (MnTPPS)

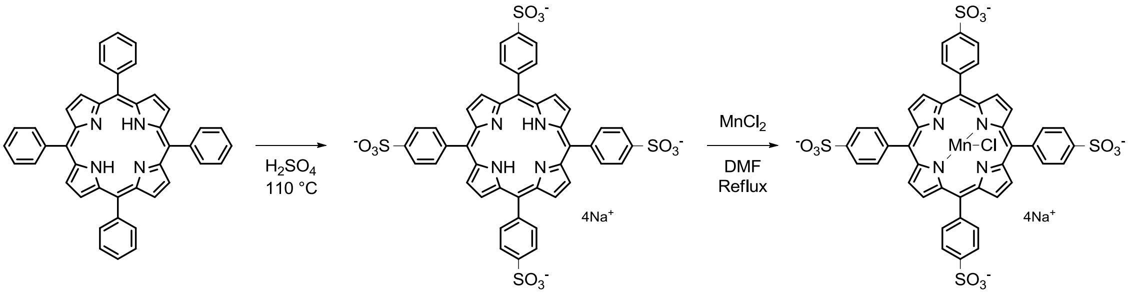

Figure 3.3 Synthesis of 5,10,15,20-tetrakis(4-sulfonatophenyl)porphyrinato manganese(III) chloride sodium salt (MnTPPS).

The synthesis of 5,10,15,20-tetrakis(4-sulfonatophenyl)porphyrinato manganese(III) chloride sodium salt (MnTPPS) was done by sulfonating TPP and then inserting Mn into the core of the new porphyrin species following literature procedure (Figure 3.3) [12, 15].

TPP (2.00 g, 3.25 mmol) was added to sulfuric acid (10 mL), ground into a fine paste with mortar and pestle, and then carefully transferred into a round bottom flask. More sulfuric acid (40 mL) was added and the mixture was stirred and heated in an oil bath (115 °C) for 4 h. Once cooled, the mixture was carefully diluted into a large volume of Milli-Q water (300 mL). Calcium hydroxide was added slowly to the mixture in an ice bath to neutralise the acid, which caused the mixture to change colour from green to red. The solvent was filtered through a sintered glass funnel and the muddy brown/red solid washed numerous times with Milli-Q water and filtered. The solvent was then evaporated off and the solid redissolved in a smaller quantity of Milli-Q water to which sodium hydroxide (1 M) was slowly added until the solution reached a pH of 8-10 (controlled with indicator paper). The solution was filtered again through a sintered glass funnel as well as through paper filters for a number of times. The solvent was then evaporated, the solid redissolved in a small quantity of methanol and precipitated with the addition of acetone. The solid was then vacuum filtered with a sintered glass funnel and dried in a vacuum oven at 60 °C to give the 5,10,15,20-tetrakis(4-sulfonatophenyl)porphyrin (TPPS) (3.27 g, 98% yield). The sample was analysed with UV-Vis and NMR and found to conform with literature data [16].

The next step was metallation, which involved combining TPPS (2.5 g, 2.44 mmol) and $MnCl_2$ (3.2 g, 25.42 mmol) in 100 mL DMF and stirring the mixture at reflux in air for 2 h. Once cooled down the mixture was neutralised with a few drops of triethylamine and the solvent removed under vacuum. The product was redissolved in water and precipitated with acetone. The solid was vacuum filtered through a sintered glass funnel, washed with acetone and dried in a vacuum oven at 60 °C. The resulting product was 5,10,15,20-tetrakis(4-sulfonatophenyl)porphyrinato manganese(III) chloride sodium salt (0.9 g, 33% yield). MnTPPS in water was characterised by UV-Vis spectroscopy and its main absorbance peaks and their extinction coefficients were found to agree with published data (see Table 3.2) [17].

UV-Vis absorbance peaks of MnTPPS	
Expected (Published) [nm (ε, 1/1000 M^{-1} cm^{-1})(log ε)]	**Experimentally Observed [nm (ε, 1/1000 M^{-1} cm^{-1})(log ε)]**
379 (68)(4.83)	378.5 (43)(4.63)
400 (68)(4.83)	399.5 (43)(4.63)
467 (100)(5.00)	466.5 (74.6)(4.87)
564 (10)(4.00)	563 (9.3)(3.97)
598 (7.5)(3.88)	596.5 (6.4)(3.81)
776(0.7)(2.85)	777 (1.2)(3.08)

Table 3.2 UV-Vis spectroscopic reference data and experimentally obtained results for MnTPPS.

3.2.3 Synthesis of 5,10,15,20-tetrakis(4-methylpyridinium)porphyrinato manganese(III) chloride tetraiodide (MnTMPyP)

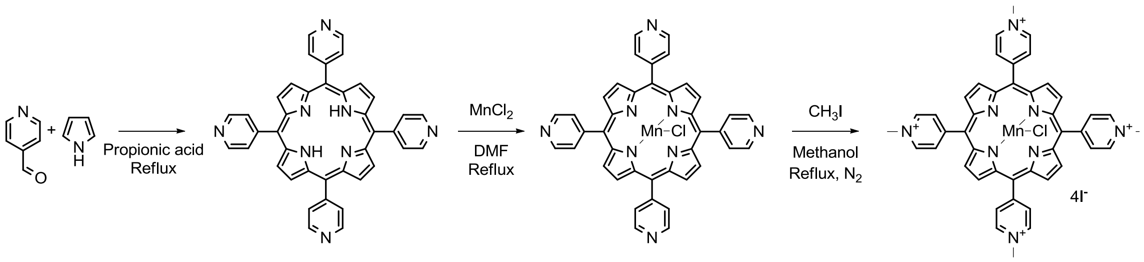

Figure 3.4 Synthesis of 5,10,15,20-tetrakis(4-methylpyridinium)porphyrinato manganese(III) chloride tetraiodide (MnTMPyP).

5,10,15,20-Tetrakis(4-methylpyridinium)porphyrinato manganese(III) chloride tetraiodide (MnTMPyP) was synthesised by preparing the 5,10,15,20-tetra(4-pyridyl)porphyrin (TPyP), metallation followed by subsequent methylation (Figure 3.4).

5,10,15,20-Tetra(4-pyridyl)porphyrin (TPyP) was synthesised following the Adler method [10] by combining 4-pyridinecarboxyaldehyde (14.47 g, 0.14 mol) and pyrrole (0.07 g, 0.14 mol) in refluxing propionic acid (500 mL). The mixture was stirred at reflux under air for 1 h then cooled down and the solvent removed in vacuo. The solid was redissolved in methanol, neutralised with a small quantity of triethylamine which caused the solid to precipitate. The purple solid was then filtered through a sintered glass funnel and washed with methanol, water and acetone and dried in a vacuum oven, resulting in the product TPyP (3.11 g, 3% yield). The finished product was analysed by MALDI, NMR and UV-Vis and the results found to agree with literature [18].

Manganese was inserted into the freebase porphyrin to give 5,10,15,20-tetra(4-pyridyl)porphyrinato manganese(III) chloride (MnTPyP). TPyP (0.5 g, 0.81 mmol) and $MnCl_2$ (2 g, 15.89 mmol) were combined in DMF (50 mL) and stirred at reflux overnight. The solvent was then removed under vacuum and the solid redissolved in water. Triethylamine was added to neutralise the mixture and the product extracted with DCM. The solvent was evaporated off and the product dried in a vacuum oven (60 °C) to give the compound MnTPyP (234 mg, 41% yield). The compound was characterised by MALDI and Uv-Vis and the results found to be in agreement with literature data [18].

The final step was methylating the pyridyl group by combining MnTPyP (56 mg, 0.08 mmol) with excess of iodomethane (2 mL,) in methanol (10 mL) in an ice bath following a modified literature procedure [8]. The mixture was purged with nitrogen gas, heated to reflux and stirred under nitrogen overnight. The solvent was then removed by evaporation (gently blowing nitrogen gas over the mixture) and the product dried in a vacuum oven (60 °C). The product was 5,10,15,20-tetrakis(4-methylpyridinium)porphyrinato manganese(III) chloride tetraiodide (MnTMPyP) (115 mg, 100% yield). MnTMPyP in water was characterised by UV-Vis spectroscopy and its main absorbance peaks and their extinction coefficients were found to agree with published data (see

Table 3.3) [17].

UV-Vis absorbance peaks of MnTMPyP	
Expected (Published) [nm (ε, 1/1000 M^{-1} cm^{-1})(log ε)]	**Experimentally Observed [nm (ε, 1/1000 M^{-1} cm^{-1})(log ε)]**
378 (32)(4.51)	377 (32)(4.51)
399 (32)(4.51)	400 (34)(4.53)
463 (92)(4.96)	462.5 (89)(4.95)
561 (8.4)(3.92)	560 (9.4)(3.97)
681 (0.74)(2.86)	679 (1.4)(3.15)

Table 3.3 UV-Vis spectroscopic reference data and experimentally obtained results for MnTMPyP. Data shown as [nm (ε, 1/1000 M^{-1} cm^{-1})(log ε)]

3.2.4 Fabrication of Porphyrin/PEDOT by vapour phase polymerisation

Vapour phase polymerised (VPP) films of PEDOT with and without porphyrin were prepared following a method adapted from literature [19]. Solutions were prepared containing the oxidant, iron(III) p-toluenesulfonate hexahydrate (Fe-pTS) (85mg,

$1.25\text{x}10^{-4}$ M, 10% by mass), and pyridine at half a molar equivalent of the oxidant (5 μL, $0.625\text{x}10^{-4}$ M), combined in 80% ethanol/water (1 mL). The source method required an alcohol solvent for Fe-pTS whereas most porphyrins used in this study were water soluble (with exception to MnTPP). The ethanol/water mixture was determined as a suitable compromise to ensure both chemical species were fully dissolved. Pyridine was added to the oxidant solution to impede a polymerisation process that did not produce a conductive polymer [19, 20]. The porphyrin species MnTPP, MnTPPS, MnTMPyP and MnTPPS+MnTMPyP were added to the solution at varying concentrations. In the case of the MnTPPS+MnTMPyP mixture, both porphyrins were added in a 1:1 ratio and the concentration used to identify the mixture was the combined concentration of porphyrin species in solution. This was usually done before the addition of Fe-pTS and pyridine to the mixture to ensure that the porphyrin dissolved completely. The porphyrin concentrations in the separate mixtures are shown in Table 3.4. The concentration of porphyrin was varied to test the effect of porphyrin loading on the photocatalytic performance on the films prepared from the porphyrin/oxidant solution by vapour phase polymerisation.

MnTPP	MnTPPS/PEDOT	MnTMPyP	MnTPPS+MnTMPyP
1 mg/mL / 1.42 mM	0.87 mg/mL / 0.78 mM	1 mg/mL / 0.78 mM	1 mg/mL / 0.78 mM
2 mg/mL / 2.84 mM	1.74 mg/mL / 1.57 mM	2 mg/mL / 1.57 mM	2 mg/mL / 1.57 mM
3 mg/mL / 4.27 mM	2.61 mg/mL / 2.35 mM	3 mg/mL / 2.35 mM	3 mg/mL / 2.35 mM

Table 3.4 Porphyrin concentrations in spin coating solutions for vapour phase polymerisation.

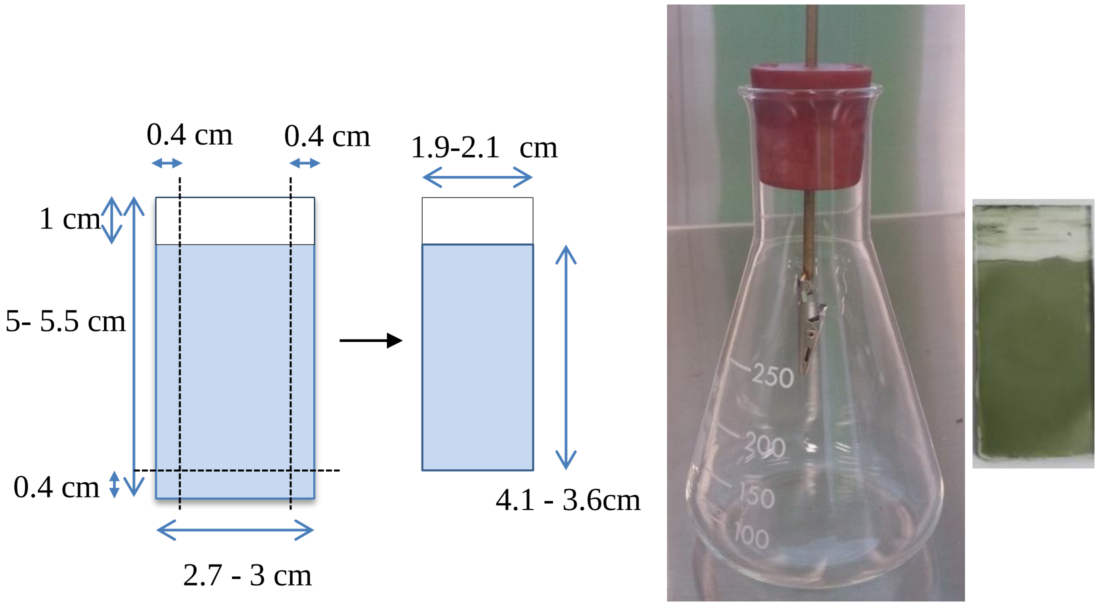

Figure 3.5 Schematic for cutting fluorine doped tin oxide (FTO) glass slides containing PEDOT film (left), photograph of the vessel used for vapour phase polymerisation (right) and of a typical porphyrin/PEDOT film resulting from the process (far right).

Fluorine doped tin oxide (FTO) glass was cut into rectangles with the dimensions 2.7 x 5.5 cm and later 3.0 x 5.0 cm to make full use of the given FTO slab (Figure 3.5). Additionally, a line was drawn 1 cm from the edge on the long side as a marking for later. Microscope glass slides were also cut to 5.5 cm length and cleaned alongside the FTO slides. Slides were cleaned in acetone and then milli-Q water for 20 min each in a sonication bath. Each slide was rinsed with milli-Q water and dried with pressurised air before UV-ozone treatment for 20 min. After that treatment, slides were ready to commence vapour phase polymerisation immediately.

Vacuum distilled EDOT (0.4 ml) was thawed and inserted into a sealed conical flask embedded with an alligator clip to hold a sample above the liquid (Figure 3.5). The Oxidant/porphyrin solutions (Table 3.4) were filtered through 0.2 µm syringe filters before being spin coated onto the slides (1000 rpm, 15 sec, 0.2 mL) followed by immediate drying at 80°C in air on a hotplate for 5 min. To limit the area for polymerisation to precise dimensions, the oxidant film was carefully swabbed off with a cotton tip and ethanol from the 1cm line marking to create a clean zone above the film. The aim was to keep the affected area consistent when the sample was eventually tested in water electrolyte for electrochemical measurements.

The samples were then inserted into the conical flask, which had been heated in an oven to 60°C, then returned to the oven to polymerise in air for 40 min. Samples were thereafter retrieved from the conical flask and left to dry in air at room temperature overnight. The resulting samples were films of PEDOT, MnTPP/PEDOT, MnTPPS/PEDOT, MnTMPyP/PEDOT and MnTPPS+MnTMPyP/PEDOT. Each was washed by submerging in Milli-Q water for 30 s, then letting the liquid run down by holding the slide upright on a paper towel. Tests showed that the use of ethanol as a washing solvent caused the porphyrin to leach out of MnTPP/PEDOT. The sample was dried in air for a few minutes then dried in an oven for 30 min at 60°C in air. After this treatment, films were ready to be tested.

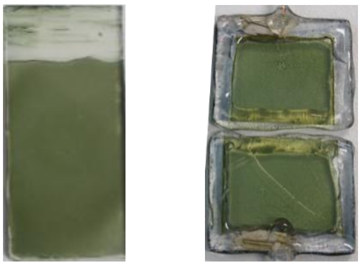

Figure 3.6 Early porphyrin/PEDOT film (left) and later enhanced version (right).

At first, electrochemical tests were conducted on samples by submerging the FTO glass slide in electrolyte up to the edge of the film with the EDAQ electrode attached to the top of the glass slide. In later experiments this was improved by attaching copper wire to the FTO surface with conductive silver paint and epoxy resin (see Figure 3.6). When the silver paste was fully solidified, epoxy glue was used to cover the contact area of the wire as well as any exposed clean FTO glass surface. The FTO glass slides with PEDOT film were also cut in half and each fashioned into a working sample. This allowed ready fabrication of duplicates for each sample. The surface area of film was measured out for every sample and the current data converted to current density to eliminate the influence of size variations on the overall results.

3.2.5 Thickness and conductivity measurement

The thickness and conductivity of each sample was measured using a Dektak profilometer and four point probe as described in sections 2.4.5 and 2.4.6.

3.2.6 Electrochemical testing

The prepared VPP PEDOT and porphyrin/PEDOT samples were subjected to electrochemical testing with the apparatus and methods described in sections 2.4.8 and 2.4.9. In a typical experiment the electrochemical cell was filled with Na_2SO_4 (0.1 M) that had been degassed with N_2 gas and stirred for 1 h. The sample was inserted as the working electrode with a Ag/AgCl reference electrode and platinum mesh counter electrode in their respective places.

Before testing, CV was performed on the film for 20 cycles at 10 mV/sec in order to stabilise the film. LSV sweeps were then performed over the range of 0-0.7 V at a scan rate of 5 mV/sec. Voltages beyond 0.7 V (*vs* Ag/AgCl) were not studied in order to avoid irreversible oxidative damage to the film. In a typical experiment, 5 sweeps were done in the dark and then 3 sweeps with illumination turned on. This ensured that the LSV spectrum remained constant over the course of data recording as it was otherwise affected by charge imbalances brought on by static electricity and low electrolyte mobility. The last of the LSV sweeps with and without illumination were used as data. This method was applied to all of the films in this chapter. In all cases the resulting current (in µA) was converted into current density (in µA/cm^2) by dividing by the geometric area of the film. The geometric area was calculated by measuring the dimensions of the polymer film on the substrate with a ruler. In certain cases, electronic noise brought on by an unknown external interference was removed from the data by subtracting a sine wave function.

Following the LSV measurement, each sample was tested by CA at set potentials of 0.6 V, 0.65 V and 0.7 V (*vs* Ag/AgCl). In a typical experiment the chosen voltage was applied to the film for 1 h without illumination to equilibrate the baseline current. The light was then switched on to measure the resulting photocurrent for 10 min and then turned off. Data shown below was taken from 1 min before illumination to 1 min after illumination. The data (in µA) was normalised by subtracting the baseline before illumination and the results converted to current density (in µA/cm^2) by the same method as above. The same method was also employed in conjunction with a gas sensing mechanism by GC as outlined in section 2.4.10.

3.3 Results and Discussion

3.3.1 VPP porphyrin/PEDOT films

Electrode films were prepared by vapour phase polymerisation (VPP) of 3,4–ethylenedioxythiophene (EDOT) into the conducting polymer PEDOT, commonly on FTO glass and microscope slides. The method described in section 3.2.4 was used to make PEDOT films with and without Mn porphyrin species embedded in the matrix. Contrary to other methods of polymerisation, VPP allows the in situ formation of polymer with an embedded chemical species without the compound having to play a role as counter-ion. The high density of the film allowed for species without high binding affinity to the polymer to stay embedded.

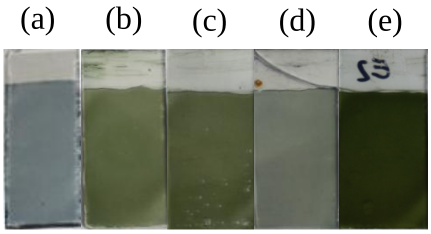

Figure 3.7 Porphyrin/PEDOT films: (a) PEDOT, (b) MnTPPS/PEDOT, (c) MnTMPyP/PEDOT, (d) MnTPPS+MnTMPyP/PEDOT, (e) MnTPP/PEDOT.

Vapour phase polymerisation of PEDOT yielded thin films on glass, which were typically blue for control PEDOT films and green when a doping porphyrin was present (see Figure 3.7). The change in colour was a sign of porphyrin presence and could be studied in more detail through UV-visible light spectroscopy. The absorbance patterns were instrumental in determining the overall state of the porphyrins in the film, with special attention to the state of the metal atom in the core. Five types of films were prepared (see Figure 3.7): PEDOT, MnTPPS/PEDOT, MnTMPyP/PEDOT, MnTPPS+MnTMPyP/PEDOT, MnTPP/PEDOT. Mn Porphyrin was added to the polymerisation solutions at various different concentrations before polymerisation, resulting in films with different levels of porphyrin loading (see Table 3.5).

MnTPPS	**MnTMPyP**	**MnTPPS+ MnTMPyP**	**MnTPP**
0.87 mg/mL / 0.78 mM	1 mg/mL / 0.78 mM	0.78 mM	1 mg/mL / 1.42 mM
1.74 mg/mL / 1.57 mM	2 mg/mL / 1.57 mM	1.57 mM	2 mg/mL / 2.84 mM
2.61 mg/mL / 2.35 mM	3 mg/mL / 2.35 mM	2.35 mM	3 mg/mL / 4.27 mM

Table 3.5 Porphyrin concentrations in solutions for vapour phase polymerisation.

3.3.2 Thickness and Conductivity

The polymer film samples were made on both FTO glass and microscope slide glass in parallel. Microscope slide glass was used for thickness and conductivity testing of the samples as the smooth, non-conducting substrate allowed for easier measurements for both of these tests. The samples yielded the following representative results:

Sample	**Thickness (µm)**	**Conductivity (S cm^{-1})**
PEDOT	0.094	266
MnTPPS/PEDOT	0.076	272
MnTMPyP PEDOT	0.085	242
MnTPPS+MnTMPyP/PEDOT	0.09	195
MnTPP/PEDOT	0.129	109

Table 3.6 Representative thickness and conductivity of the porphyrin/PEDOT films.

The method used for vapour phase polymerisation resulted in fairly thin films of conducting polymer, generally on the order of ~0.1 µm. The conductivity was calculated according to the method described in section 2.4.6. The films generally had a conductivity of 100-300 S cm^{-1}, which was modest compared to values of 800 S cm^{-1} that have been reported in literature [19-25]. The polymerisation itself was performed in air in a sealed vessel at a set temperature (60° C). Minute differences in moisture and air composition have been reported to have significant effects on the polymerisation process, which could not be completely controlled in this case.

3.3.3 Photoelectrochemical testing of PEDOT

Each PEDOT sample was tested in an electrochemical cell as described in section 3.2.6. From this experiment a baseline photocurrent level could be ascertained in order to compare the samples that were modified by the inclusion of porphyrin.

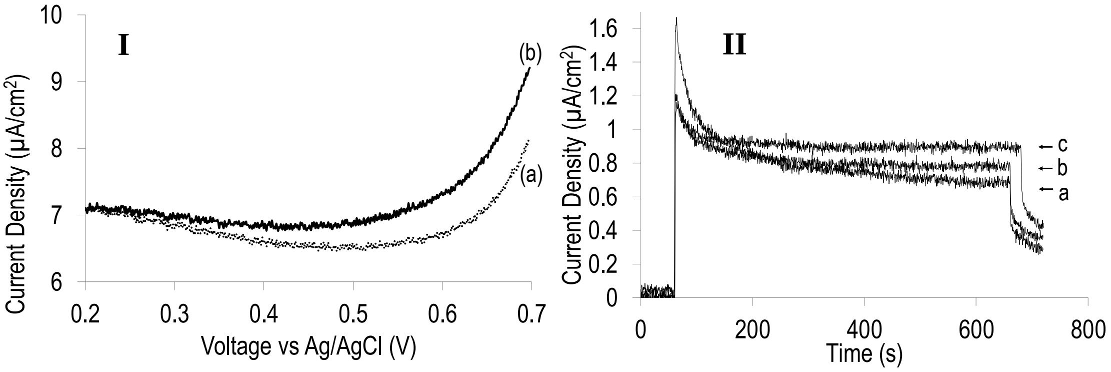

Figure 3.8 (I) LSV of PEDOT, (a) dark, (b) with illumination. (II) CA of PEDOT at (a) 0.6 V, (b) 0.65 V, (c) 0.7 V.

Sample	Current Density (µA/cm^2)		
	0.6 V	**0.65 V**	**0.7 V**
PEDOT	0.68	0.75	0.90

Table 3.7 Photocurrents of PEDOT at different voltages (*vs* Ag/AgCl).

The LSV of the PEDOT film with and without illumination (Figure 3.8) showed an onset potential of 0.55 V. The maximum photocurrent was observed in the region 0.6–0.7 V (*vs* Ag/AgCl).

In the photocurrent test by CA, the control PEDOT produced the following sets of photocurrents: 0.68 µA/cm^2 at 0.6 V, 0.75 µA/cm^2 at 0.65 V, 0.90 µA/cm^2 at 0.7 V (see Table 3.7). The conducting polymer PEDOT has attracted some interest for its potential role in water splitting in the past, albeit more so for water reduction rather than oxidation [20, 26, 27]. While a minor photocatalytic effect was not unexpected, in this case the PEDOT served as a catalyst support rather than a catalyst by itself.

3.3.4 Photoelectrochemical testing of MnTPPS/PEDOT

The electrochemical testing regime described in the previous section was applied to the MnTPPS/PEDOT sample. This allowed for a comparison with unmodified PEDOT, as well as with the literature precedent [2].

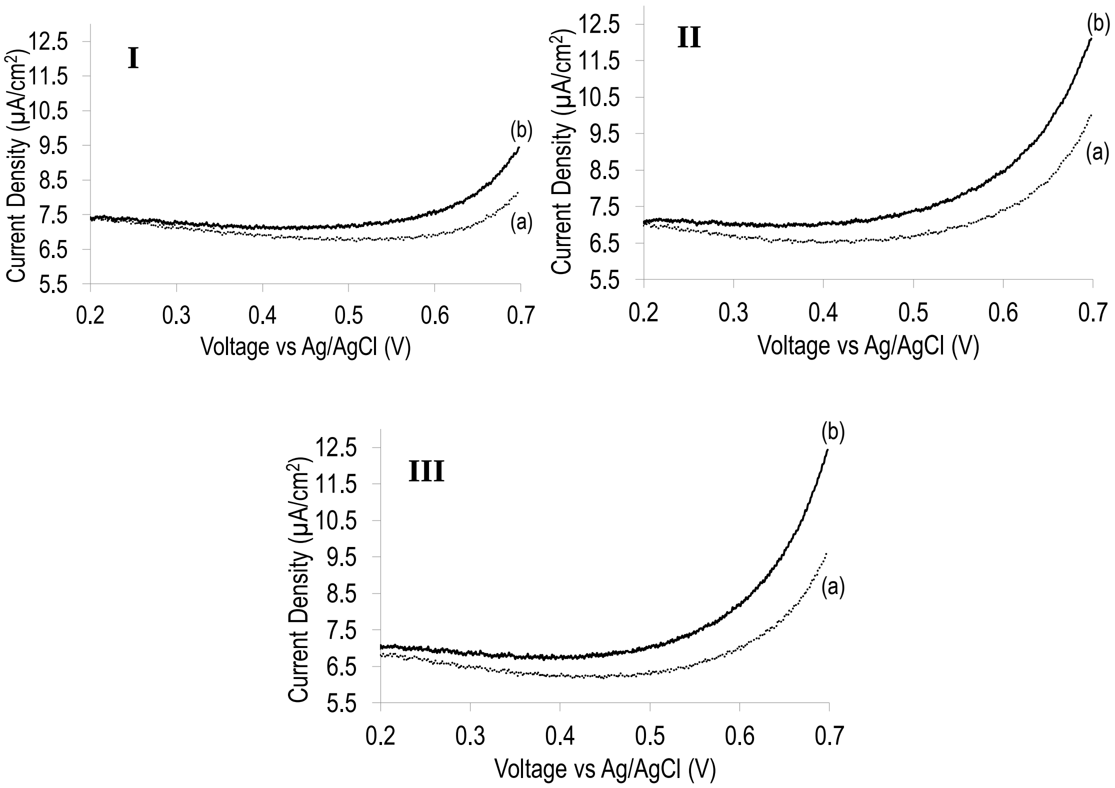

Figure 3.9 LSV of MnTPPS/PEDOT at (**I**) 0.87 mg/mL, (**II**) 1.74 mg/mL, (**III**) 2.61 mg/mL. (a) dark, (b) with illumination.

The LSV spectra of this sample features a similar onset potential as that of control PEDOT, with an increasing photocurrent starting at 0.55 V (Figure 3.9). There was a minor increase in photocurrent with increasing concentration of MnTPPS in LSV but these differences were more pronounced in the potentiostatic measurements.

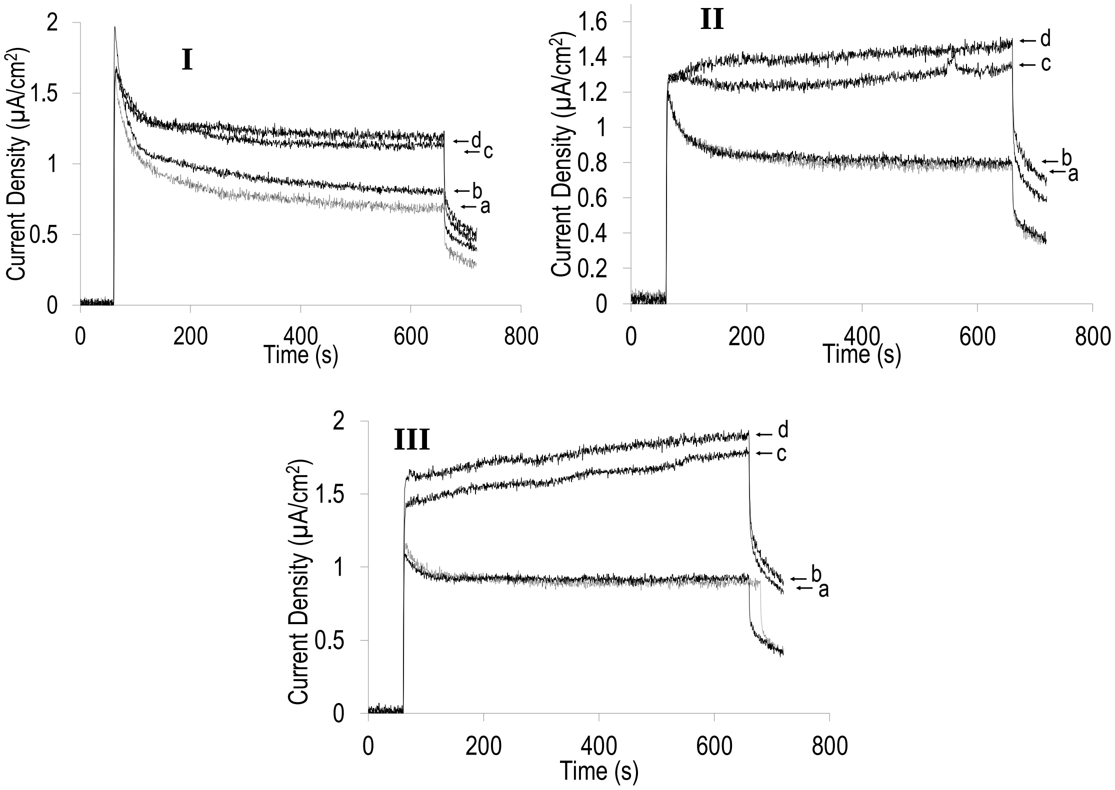

Figure 3.10 CA at (**I**) 0.6 V, (**II**) 0.65 V, (**III**) 0.7 V. (a) PEDOT, (b) MnTPPS/PEDOT at 0.87 mg/mL, (c) 1.74 mg/mL, (d) 2.61 mg/mL.

MnTPPS/PEDOT	**Current Density (µA/cm^2)**		
Porphyrin Loading	**0.6 V**	**0.65 V**	**0.7 V**
0.87 mg/mL / 0.78 mM	0.78	0.83	0.95
1.74 mg/mL / 1.57 mM	1.14	1.32	1.78
2.61 mg/mL / 2.35 mM	1.19	1.46	1.88
PEDOT	0.68	0.75	0.90

Table 3.8 Photocurrent density of MnTPPS/PEDOT at different voltages (*vs* Ag/AgCl)

When poised at the test potentials of 0.6 V, 0.65 V and 0.7 V the samples consistently outperformed PEDOT in photocurrent (see Figure 3.10), indicating enhanced catalytic activity of the porphyrin MnTPPS in the PEDOT matrix. The photocurrent consistently increased with concentration, as well as voltage, reaching a maximum of 1.88 µA/cm^2

at 0.7 V (see Table 3.8). This was comparable to the previously reported result for this kind of material under similar conditions, albeit lower than the reported 2.89 µA/cm^2 [2].

3.3.5 Photoelectrochemical testing of MnTMPyP/PEDOT

The MnTMPyP/PEDOT sample was tested by LSV and CA as per the previous section.

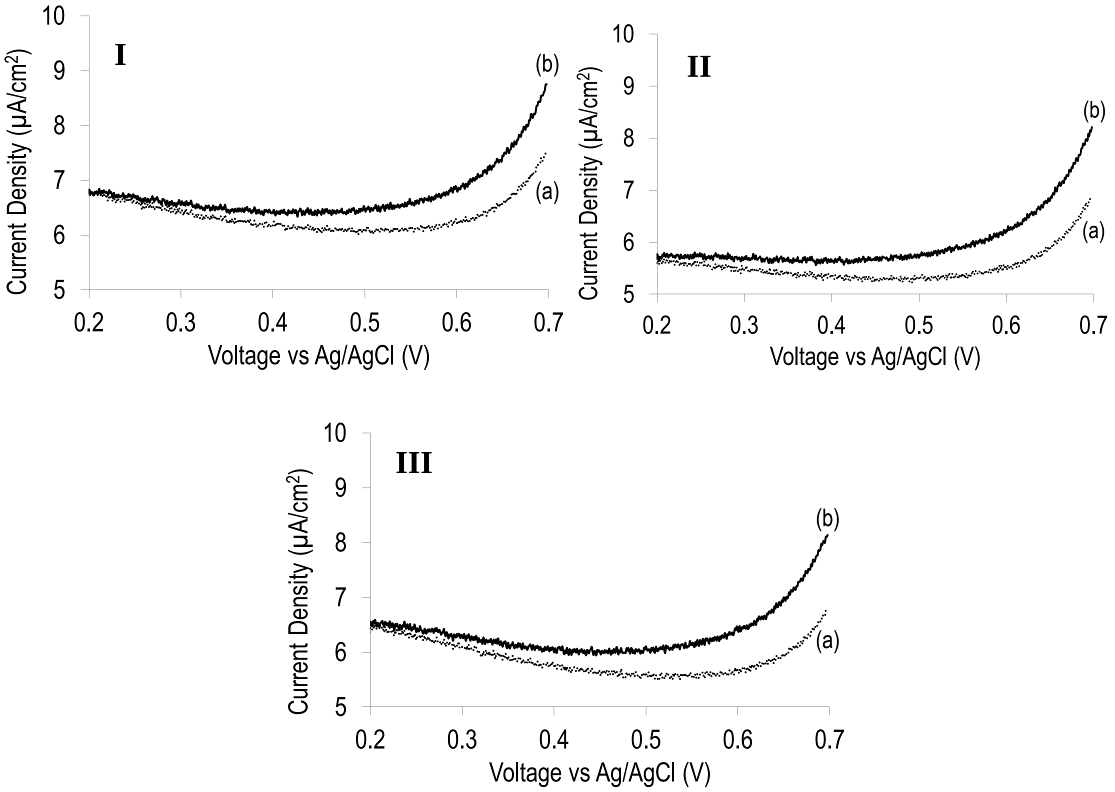

Figure 3.11 LSV of MnTMPyP/PEDOT at (**I**) 1 mg/mL, (**II**) 2 mg/mL, (**III**) 3 mg/mL. (a) dark, (b) with illumination.

The LSV spectrum of this sample showed consistently lower photocurrents compared to MnTPPS/PEDOT, similar in magnitude to that of the sample with PEDOT only (see Figure 3.11). The onset voltage profile was similar to the previous samples.

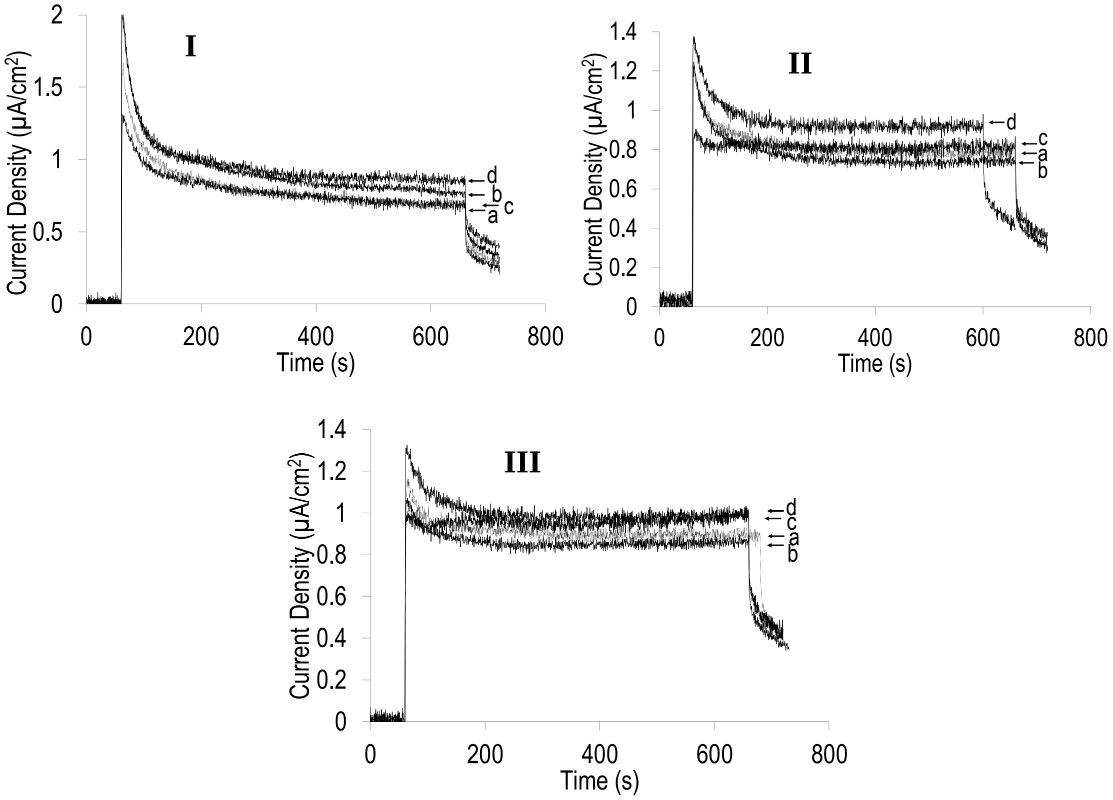

Figure 3.12 CA at (**I**) 0.6 V, (**II**) 0.65 V, (**III**) 0.7 V. (a) PEDOT, MnTMPyP/PEDOT at (b) 1 mg/mL, (c) 2 mg/mL, (d) 3 mg/mL.

MnTMPyP/PEDOT	**Current Density (µA/cm^2)**		
Porphyrin Loading	**0.6 V**	**0.65 V**	**0.7 V**
1 mg/mL / 0.78 mM	0.76	0.75	0.86
2 mg/mL / 1.57 mM	0.67	0.78	0.98
3 mg/mL / 2.35 mM	0.83	0.89	1.01
PEDOT	0.68	0.75	0.90

Table 3.9 Photocurrent density of MnTMPyP/PEDOT at different voltages (*vs* Ag/AgCl).

When poised at the voltages 0.6 V, 0.65 V and 0.7 V, the samples exhibited photocurrents with only minor improvement compared to that of PEDOT (see Figure 3.12). The photocurrent density increased with concentration but the effect was very small compared to MnTPPS/PEDOT (see Table 3.9).

3.3.6 Photoelectrochemical testing of MnTPPS+MnTMPyP/PEDOT

This sample was of particular experimental interest as it was an exploratory trial into ion-paired porphyrins as water oxidation catalysts in PEDOT. It was tested by LSV and CA as the preceding samples.

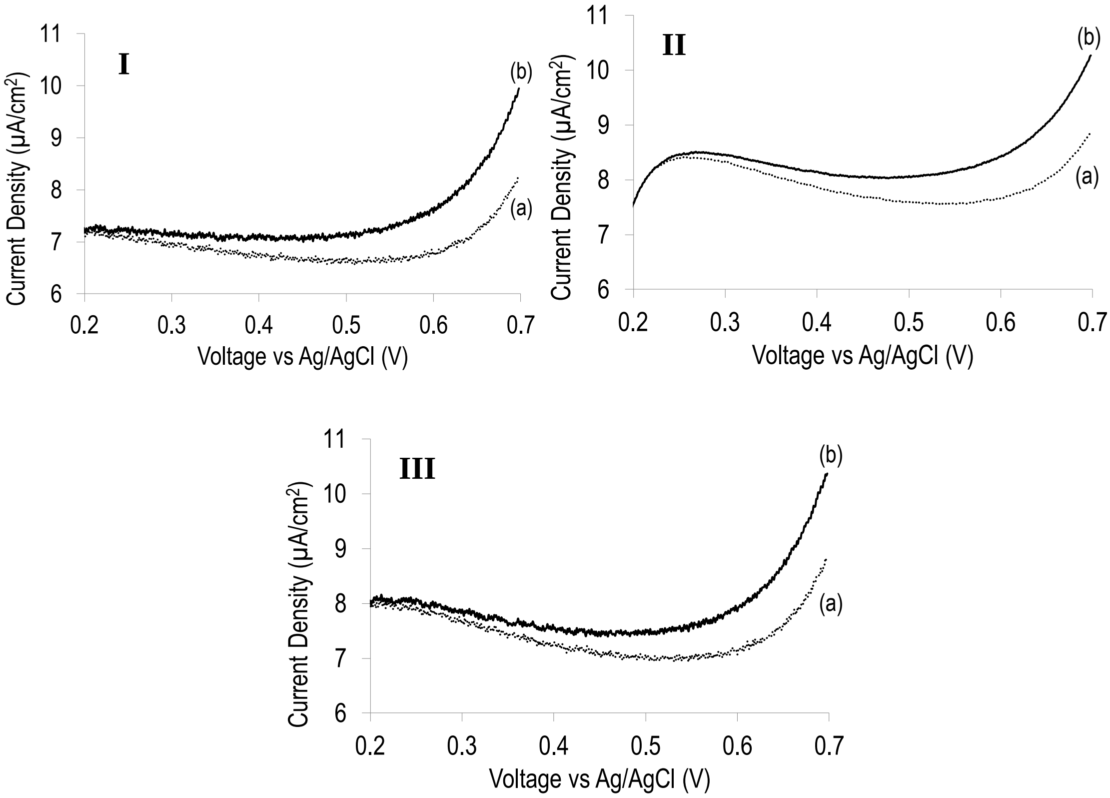

Figure 3.13 LSV of MnTPPS+MnTMPyP/PEDOT at (**I**) 1 mg/mL, (**II**) 2 mg/mL, (**III**) 3 mg/mL. (a) dark, (b) with illumination.

Upon testing using the same electrochemical/photocurrent setup as with previous samples, the combined MnTPPS+MnTMPyP/PEDOT films featured an LSV profile much like that of MnTMPyP/PEDOT (see Figure 3.13).

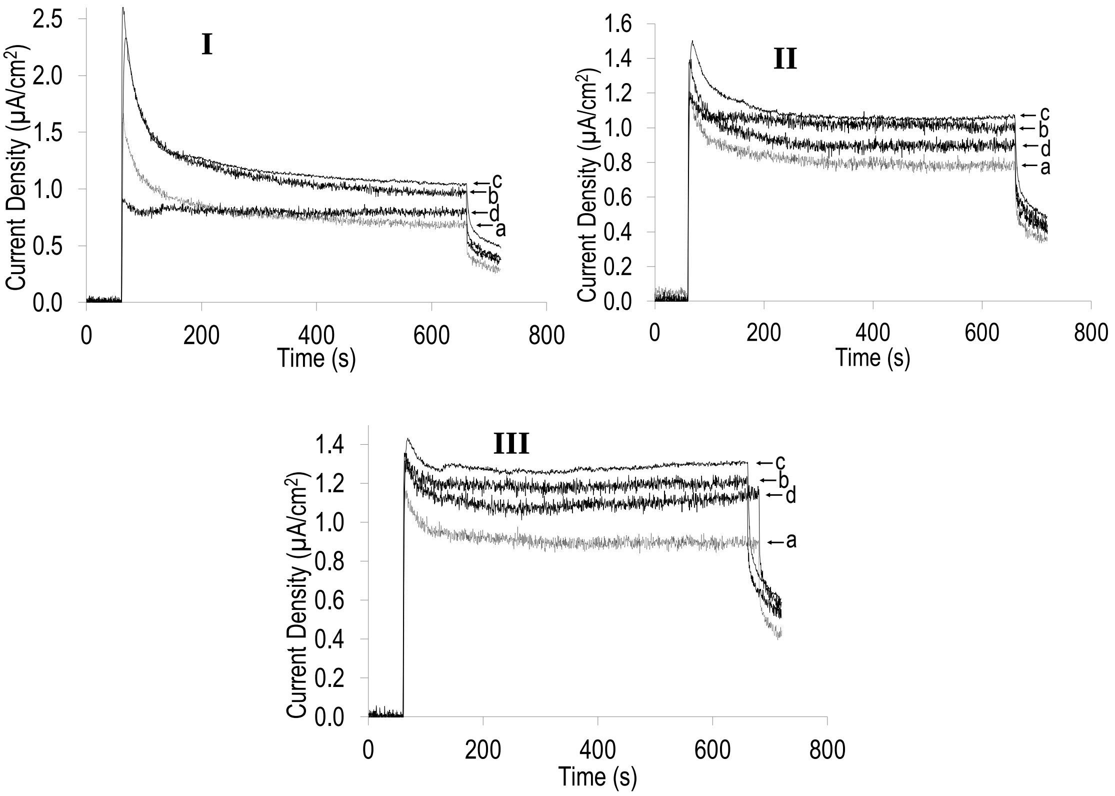

Figure 3.14 CA at (**I**) 0.6 V, (**II**) 0.65 V, (**III**) 0.7 V. (a) PEDOT, MnTPPS+MnTMPyP/PEDOT at (b) 1 mg/mL, (c) 2 mg/mL, (d) 3 mg/mL.

MnTPPS+MnTMPyP/PEDOT	**Current Density (μA/cm^2)**		
Porphyrin Loading	**0.6 V**	**0.65 V**	**0.7 V**
1 mg/mL / 0.78 mM	0.97	1.01	1.22
2 mg/mL / 1.57 mM	1.03	1.07	1.31
3 mg/mL / 2.35 mM	0.80	0.91	1.14
PEDOT	0.68	0.75	0.90

Table 3.10 Photocurrent density of MnTPPS+MnTMPyP/PEDOT at different voltages (*vs* Ag/AgCl).

The photocurrent density obtained from chronoamperometry at set voltages was also small, with very minor gains over that of PEDOT alone (see Figure 3.14 and Table

3.10). The pairing of MnTPPS and MnTMPyP prior to incorporation into PEDOT did not lead to increased photocatalytic performance.

3.3.7 Photoelectrochemical testing of MnTPP/PEDOT films

The MnTPP/PEDOT was tested by LSV and CA as previous samples.

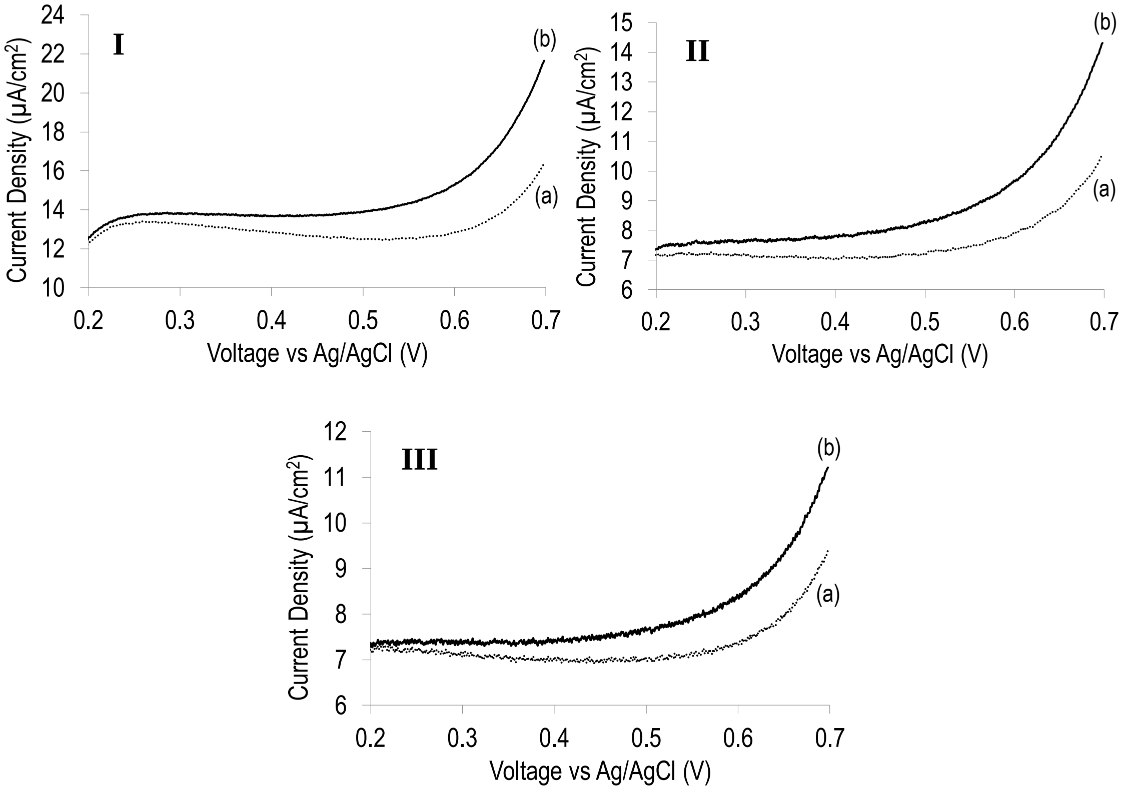

Figure 3.15 LSV of MnTPP/PEDOT at (**I**) 1 mg/mL, (**II**) 2 mg/mL, (**III**) 3 mg/mL. (a) dark, (b) with illumination.

Photoelectrochemical testing of MnTPP/PEDOT films yielded results similar to that of MnTPPS/PEDOT in LSV, but with a higher photocurrent; a more pronounced elevation of light-driven current was found in this type of sample compared to the others (see Figure 3.15).

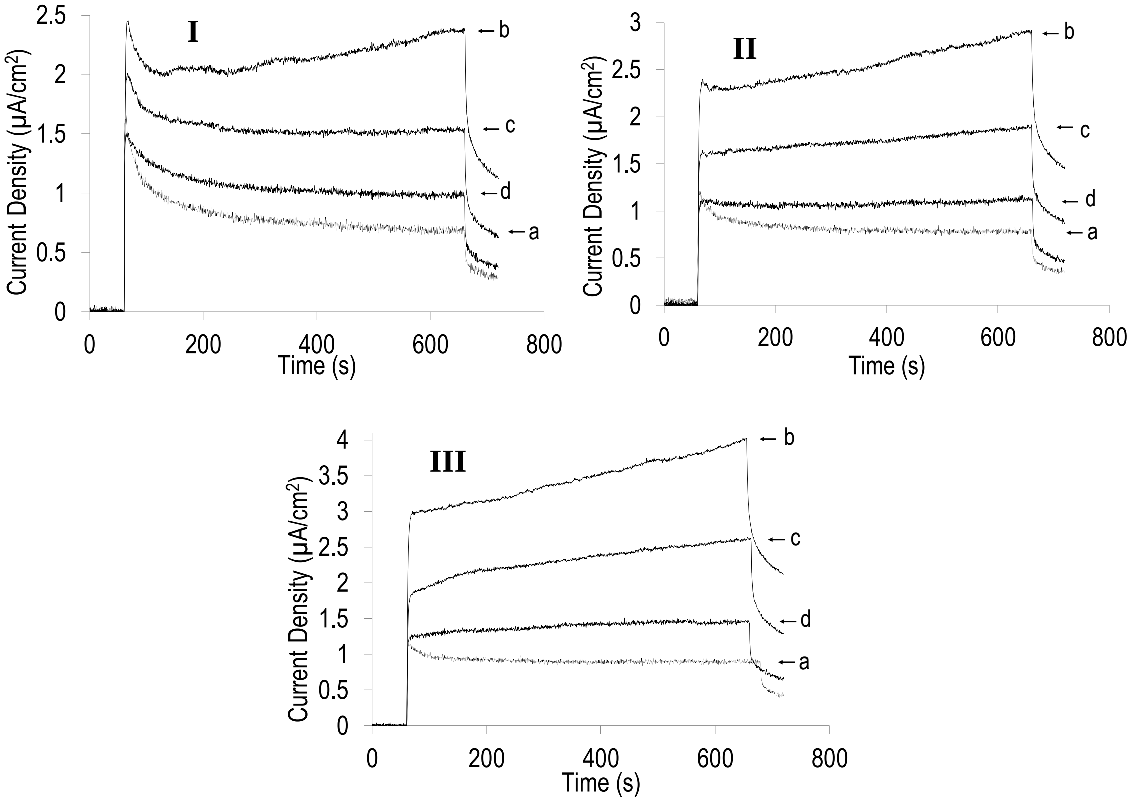

Figure 3.16 CA at (**I**) 0.6 V, (**II**) 0.65 V, (**III**) 0.7 V. (a) PEDOT, MnTPP/PEDOT at (b) 1 mg/mL, (c) 2 mg/mL, (d) 3 mg/mL.

MnTPP/PEDOT	**Current Density (μA/cm^2)**		
Porphyrin Loading	**0.6 V**	**0.65 V**	**0.7 V**
1 mg/mL / 1.42 mM	2.37	2.91	4.01
2 mg/mL / 2.84 mM	1.53	1.89	2.62
3 mg/mL / 4.27 mM	0.99	1.11	1.47
PEDOT	0.68	0.75	0.90

Table 3.11 Photocurrent density of MnTPP/PEDOT at different voltages (*vs* Ag/AgCl)

The CA results showed the highest levels of photocurrent so far in this work, with a maximum photocurrent of 4 μA/cm^2 at 0.7 V (*vs* Ag/AgCl) (see Figure 3.16). What was perhaps most unexpected about the performance of this sample is that it scaled negatively with increasing concentration, as can be seen when the results are tabulated (see Table 3.11): The higher the concentration, the lower the recorded photocurrent. These early findings were deemed significant enough to warrant a more thorough analysis of this porphyrin/polymer combination, which is described in the following chapter.

3.3.8 Photoelectrochemical testing of VPP MnTPP/PEDOT with gas sensing

In light of the results presented in the previous section MnTPP/PEDOT was chosen for a photocurrent test with an attached gas chromatograph to analyse the gas, if any, produced by the sample. Films of MnTPP/PEDOT at 2.133 mM (1.5 mg/mL) porphyrin concentration were made according to the method explained in section 3.2.4 and tested in an electrochemistry cell apparatus specialised for sensitive gas sensing (see section 2.6.10).

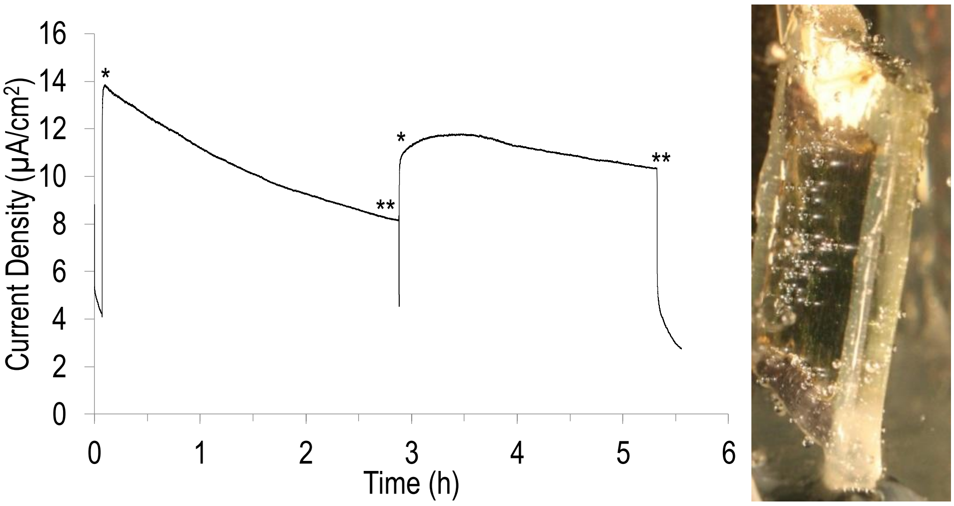

Figure 3.17 CA of MnTPP/PEDOT (1.5 mg/mL) at 0.7 V in 0.1M Na_2SO_4 (left), bubble formation on the electrode surface after prolonged testing (right). (*) light on, (**) light off.

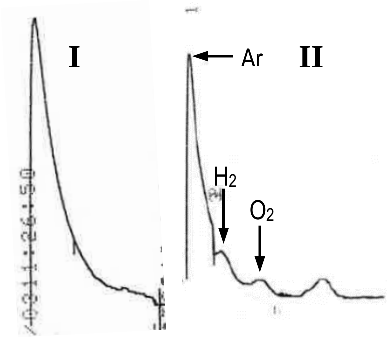

Figure 3.18 GC data taken after overnight purging (I) prior to CA and (II) after 4.7 h of illumination at 0.7 V (*vs* Ag/AgCl) in 0.1 M Na_2SO_4.

The sample was tested by CA by poising the sample at 0.7 V (*vs* Ag/AgCl) in 0.1 M Na_2SO_4 for 1 h, then illuminating with the Xenon lamp while at a steady bias (see Figure 3.17). After 4.7 h the gas was tested in a gas chromatograph and the results plotted over 30 min elution time. Prior to the photocatalytic testing the gas was analysed and found to exhibit only an argon peak, indicating that air in the vessel has been fully removed by the argon carrier gas (see Figure 3.18 (I)). The GC data after 4.7 hours confirmed the presence of oxygen, but, surprisingly, also hydrogen and one other gas that appeared to coincide with the retention time for carbon monoxide, CO (see Figure 3.18 (II)). Nitrogen gas was wholly absent from the gas spectrum after photocatalytic testing of the sample, indicating that the detected gases were not the result of air leaking into the system.

3.3.9 UV-Vis spectroscopy of PEDOT

The films prepared in section 3.2.4 were analysed by UV-Vis spectroscopy, starting with the control PEDOT sample.

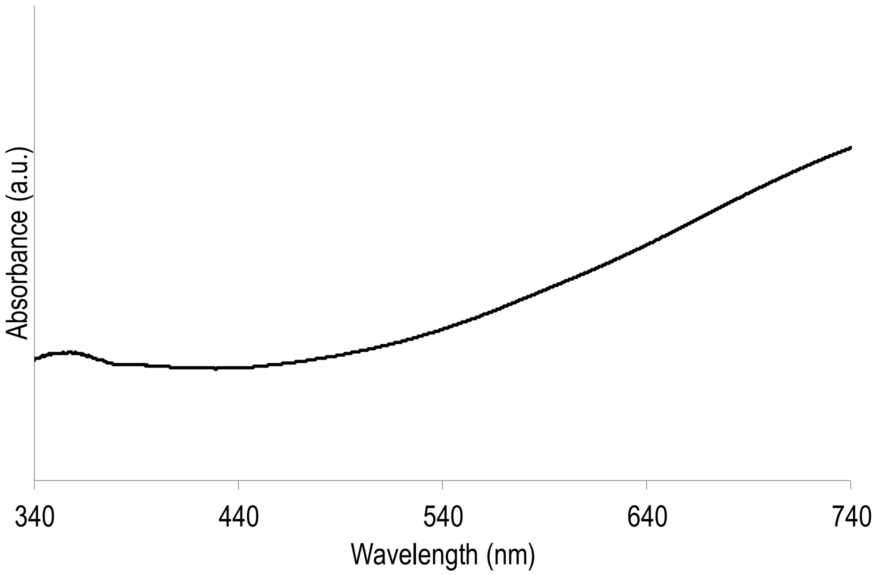

Figure 3.19 UV-Vis spectrum of vapour phase polymerised PEDOT.

The UV-Vis spectrum of PEDOT featured the characteristic conduction band pattern found for PEDOT in the chemical literature (Figure 3.19) [19]. A broad region of increasing absorbance was observed starting from 490 nm and extending well into the infrared.

3.3.10 UV-Vis spectroscopy of porphyrin films

Solutions of the Mn porphyrin species in 80% ethanol/water were prepared and spin coated onto glass slides (see section 3.2.4). The UV-Vis absorbance profile was collected.

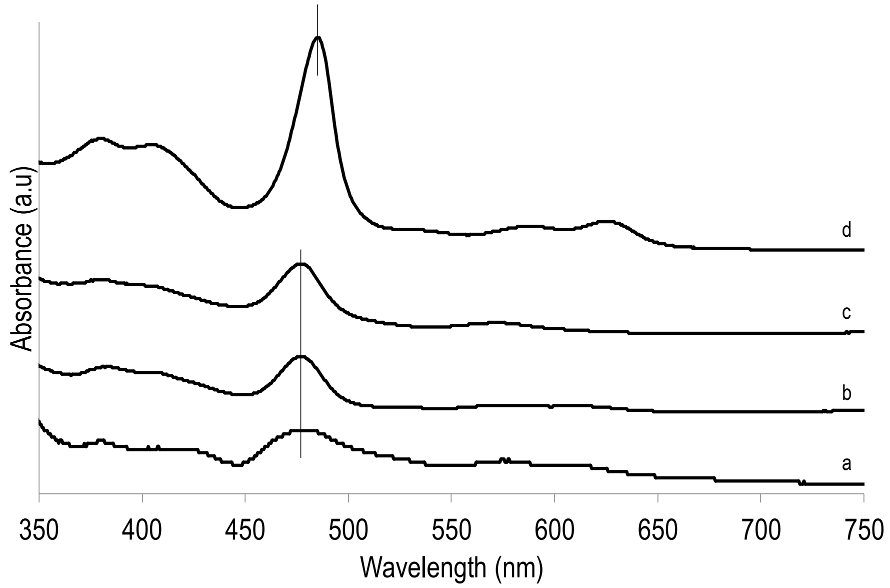

Figure 3.20 Superimposed UV-Vis spectra of porphyrin species deposited on glass in the same fashion as for VPP, but without the oxidant present. (a) MnTPPS+MnTMPyP, (b) MnTPPS, (c) MnTMPyP, (d) MnTPP. The Soret Band peaks were marked with a vertical line.

The Soret Band peaks of MnTPPS, MnTMPyP and MnTPPS+MnTMPyP were observed at 477 nm while that of MnTPP was at 485 nm (Figure 3.20). The peak absorbance for the mixture of the two oppositely charged porphyrins MnTPPS/MnTMPyP remained at the same wavelength but featured a broadened peak with lower intensity at 477 nm. This was consistent with the UV-Vis characteristics reported for this arrangement of porphyrins [6]. The Soret Band of MnTPP was found at 485 nm.

3.3.11 UV-Vis spectroscopy of porphyrin/Fe-pTS films

Solutions of porphyrin species in 80% ethanol/water were then prepared and spin coated onto glass slides following the same method as for VPP porphyrin/PEDOT, including the oxidant and pyridine, and examined by UV-Vis. This experiment demonstrated the UV-Vis absorbance profile of each porphyrin on a glass surface, highlighting possible changes to the porphyrin structure caused by the Fe-pTS oxidant.

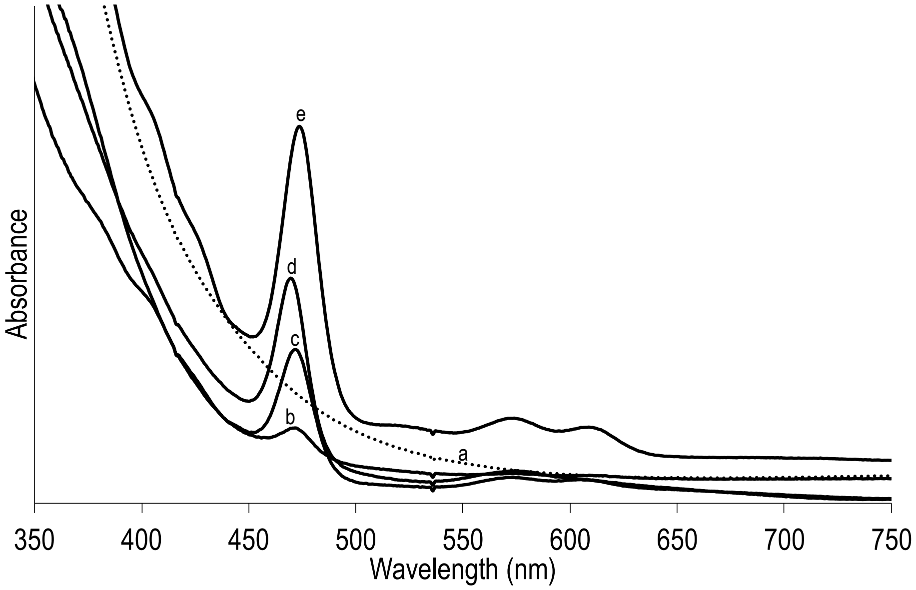

Figure 3.21 Superimposed UV-Vis spectra of porphyrin species deposited on glass in the same fashion as the VPP procedure, including the oxidant but before polymerisation. (a) Fe-pTS+pyridine and (b) MnTPPS+MnTMPyP, (c) MnTPPS, (d) MnTMPyP, (e) MnTPP.

The Soret Bands were observed at 473.5 nm for MnTPP, 469.5 nm for MnTMPyP, 471.5 for MnTPPS and 470.5 nm for MnTPPS/MnTMPyP (Figure 3.21). A broad, intense peak was recorded for Fe-pTS + pyridine starting at 450 nm and extending into the UV region. The depositions consisting of porphyrin and oxidant/base all exhibited this broad peak. A small shift in the Soret Bands wavelength by about 6-10 nm was observed for each porphyrin, compared to the spectra of the films without oxidant (see section 3.3.3 and Figure 3.20. The shift seemed to be consistent throughout the spectra, covering both the Soret and Q Bands, suggesting a shift due to aggregation rather than a change in the structure of the porphyrin. This confirmed that the porphyrins used in this experiment did not react with the oxidant. The polymerisation experiment could therefore proceed with the porphyrins in the oxidant mixture.

3.3.12 UV-Vis spectroscopy of MnTPPS/PEDOT

The MnTPPS/PEDOT films prepared in section 3.2.4 were each tested by UV-Vis spectroscopy in order to observe any significant changes to the spectra compared to that of the porphyrin on glass without PEDOT.

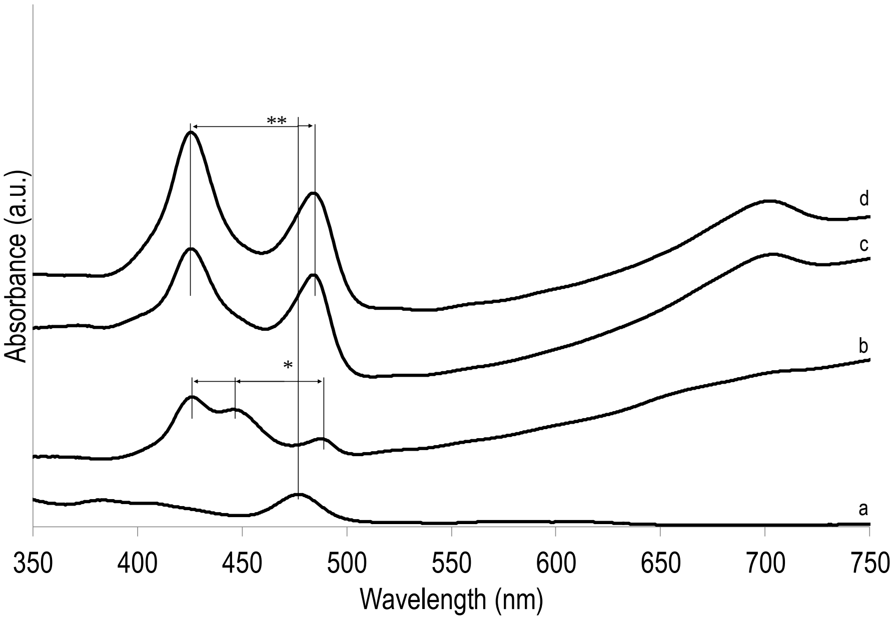

Figure 3.22 UV-Vis spectra of (a) MnTPPS, and (b) MnTPPS/PEDOT films at 0.87 mg/mL, (c) 1.74 mg/mL and (d) 2.61 mg/mL. The Soret Band shifts are indicated with lines and arrows.

The UV-Vis spectra for MnTPPS/PEDOT films exhibited more complexity than that of the porphyrin alone (see Figure 3.22). In the case of 0.87 mg/ml concentration, there were three absorbance peaks visible at 425.5 nm, 446 nm and 487.5 nm (b), shifting from the reference peak for the Mn porphyrin itself at 477 nm (a, *). The peak at 487 nm could be attributed to the porphyrin on the surface that was marginally affected by the PEDOT and shifted to the red region by about 10 nm. The two new peaks indicated a more significant interaction between the porphyrin in the polymer.

3.3.13 UV-Vis spectroscopy of MnTMPyP/PEDOT

The MnTMPyP/PEDOT films prepared in section 3.2.4 were analysed by UV-Vis spectroscopy in the same fashion as the previous films.

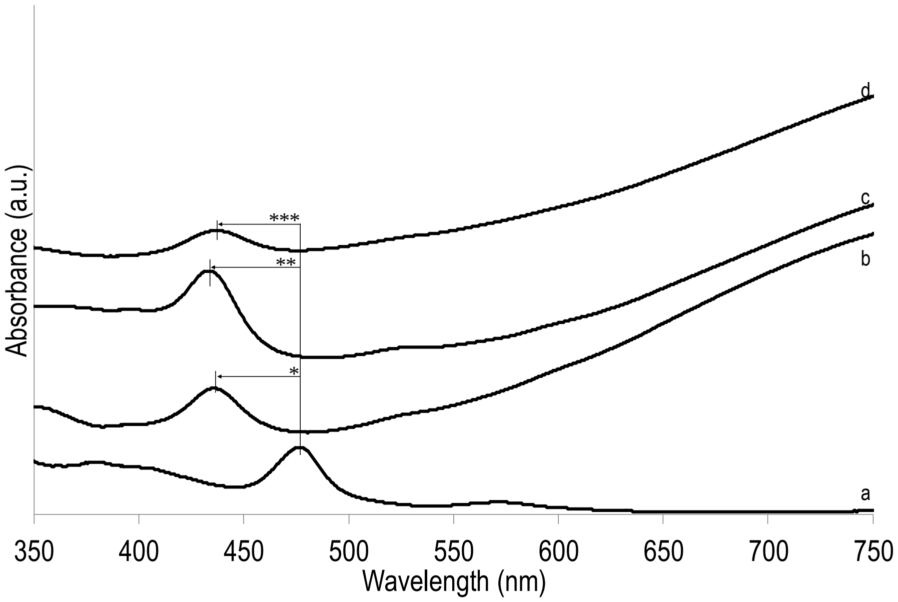

Figure 3.23 UV-Vis spectra of (a) MnTMPyP, (b) MnTMPyP/PEDOT at 1 mg/mL, (c) 2 mg/mL and (d) 3 mg/mL. The Soret Band shifts were indicated with lines and arrows.

The UV-Vis spectra of MnTMPyP/PEDOT films on glass displayed a significant change to the Soret Band compared to that without PEDOT, from 477 nm to 436 nm (see Figure 3.23). At 2 mg/ml the shift was a little more pronounced, with the peak at 433.5 nm. In contrast to MnTPPS, there was a completely uniform change in the light absorbance profile of this species rather than multiple absorbance peaks. This indicates that the porphyrin molecules in the matrix on the whole rearranged to one particular arrangement. However the shift was less than that in MnTPPS/PEDOT, which went to 425.5 nm.

3.3.14 UV-Vis spectroscopy of MnTPPS+MnTMPyP/PEDOT

The MnTPPS+MnTMPyP/PEDOT films prepared in section 3.2.4 were analysed by UV-Vis spectroscopy in the same fashion as the previous films.

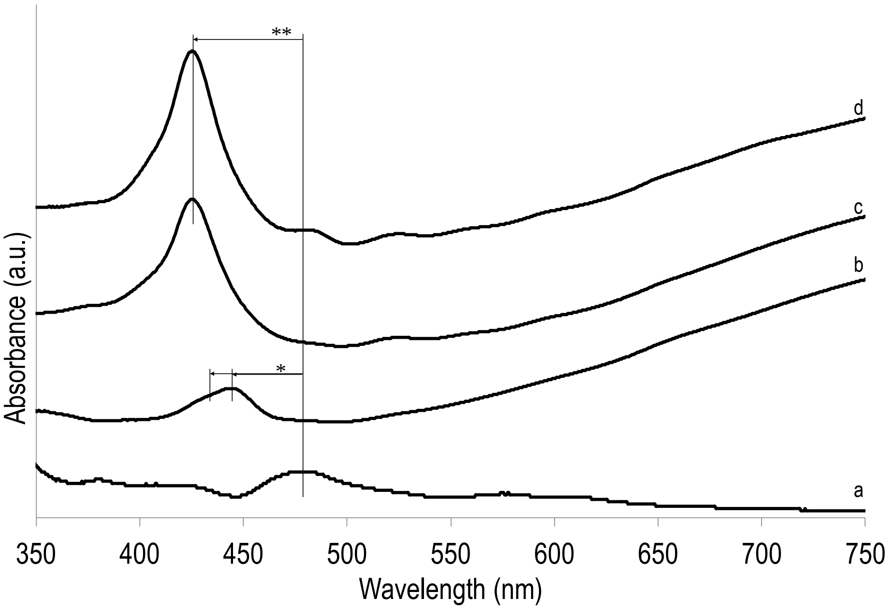

Figure 3.24 UV-Vis spectra of (a) MnTPPS+MnTMPyP, MnTPPS+MnTMPyP/PEDOT at (b) 1 mg/mL, (c) 2 mg/ml and (d) 3 mg/ml. The Soret Band shifts are indicated with lines and arrows.

The UV-Vis spectrum of MnTPPS+MnTMPyP/PEDOT at 1 mg/ml displayed a change in the Soret Band compared to that without PEDOT, moving from from 477 nm to a dominant peak at 444 nm and a shoulder at 433 nm (see Figure 3.24). At 2 and 3 mg/mL the change was more uniform to one peak at 425.5 nm. These spectra very much resembled that of MnTMPyP/PEDOT. What was surprising was the higher absorbance of the Soret Band peaks compared to that of the mixture in solution and cast on the film. It was possible that the polymerisation process of PEDOT had an unexpected effect on the arrangement of the two porphyrins which would otherwise show a lowered absorbance profile compared to that of the porphyrins studied in isolation.

3.3.15 UV-Vis absorbance spectroscopy of MnTPP/PEDOT films

The MnTPP/PEDOT films prepared in section 3.2.4 were analysed by UV-Vis spectroscopy in the same fashion as the previous films. This sample was of interest as it displayed the highest levels of photocurrent density measured in this work.

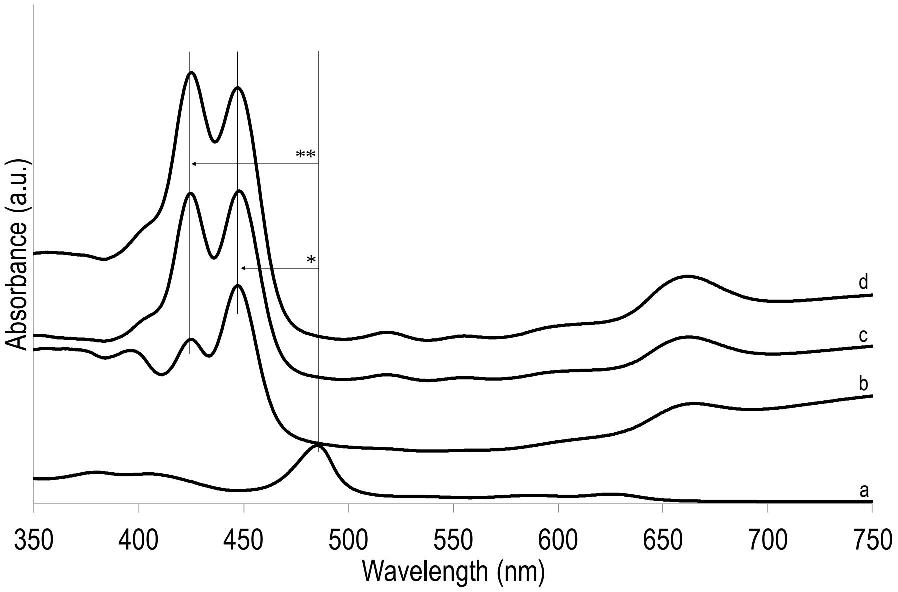

Figure 3.25 UV-Vis spectra of (a) MnTPP, (b) MnTPP/PEDOT at 1 mg/mL, (c) 2 mg/mL and (d) 3 mg/mL. The Soret Band shifts were indicated with lines and arrows.

UV-Vis spectra of MnTPP/PEDOT exhibited interesting behaviour of the porphyrin Soret Band, similar to that of MnTPPS/PEDOT (see Figure 3.25). In all three PEDOT/MnTPP samples, there was a clear change in the peak absorbance wavelength towards two smaller wavelengths, from one peak at 485 nm to two peaks at 425 & 447 nm. This could indicate complex interaction between the porphyrin and the surrounding polymer, leading to face-to-face and/or oblique arrangement [9]. Similarly to MnTPPS the intensity of the peak at 425 nm increased with concentration indicating a preference for one arrangement as concentration increased.

3.3.16 Overview of porphyrin spectroscopic data

The change in Soret Band wavelength of the porphyrins in the PEDOT matrix invited a discussion on the status of the porphyrin, with the main hypothesis being that the metal in the core had changed oxidation state. This would be in line with the active sites of manganese ions with different oxidation states in natural photosynthesis [28-31]. For that purpose, a literature survey was conducted to find the reported Soret Band wavelengths for the oxidation states of the manganese porphyrins used in this study.

Porphyrin	**Mn Oxidation state Wavelength (nm)**			**Ref.**
	II	**III**	**IV**	
MnTPPS (water)	436	469	424	[8, 17]
MnTMPyP (water)	441	463	422	[8, 17]
MnTPP (water emulsion)	432	468	418	[32]
MnTPP (DCM)		478	425	[32]

Table 3.12 Soret Band peaks of Mn porphyrins at different oxidation states.

Sample	Wavelength (nm)		
MnTPPS/PEDOT			
before polymerisation			477
after polymerisation	426		484
MnTMPyP/PEDOT			
before polymerisation			477
after polymerisation		436	
MnTPPS+ MnTMPyP/PEDOT			
before polymerisation			477
after polymerisation	425	444	
MnTPP+PEDOT			
before polymerisation			485
after polymerisation	425	448	

Table 3.13 Overview of Soret Band peaks identified in porphyrin/PEDOT samples.

The results of this survey are summarised in Table 3.12. The experimentally derived results are summarised in Table 3.13. Judging from the UV-Vis data of the porphyrin/PEDOT films there was some similarity between the absorbance wavelengths recorded experimentally to those reported in literature for the oxidation states of Mn porphyrins. At first glance one may raise the hypothesis of a change in oxidation state of the Mn porphyrins in the PEDOT matrix.

A common feature of the higher performing samples (MnTPPS/PEDOT and MnTPP/PEDOT) was the dual peak structure, suggesting the Mn porphyrins in the matrix were simultaneously present in different oxidation states. The close proximity of Mn ions in different oxidation states was identified as a characteristic feature of the OEC found in Nature [33-39]; possible parallels in a synthetic system were therefore of high interest.

3.4 Conclusions

The interaction between the porphyrin species and PEDOT was studied on the basis of UV-Vis absorbance peaks characteristic to each species. By analysing the position of the Soret Band for each porphyrin inside the PEDOT film it was possible to draw a hypothesis on the possible configuration the porphyrins in the film. At this point of the work it remained unclear whether the change in absorbance was due to the change in oxidation state of the Mn core in the porphyrin or due to another yet unknown phenomenon. The UV-Vis data was compared to literature data as much as possible but did not allow for definite confirmation on the exact state of the porphyrin. The common feature of samples that featured high photocurrents was the two peak structure, with one at 425 nm and the other at 445 nm or 484 nm. The absorbance wavelengths were compared to the Soret Band position of Mn(IV), Mn(II) and Mn(III) oxidation states of the corresponding metalloporphyrin in literature. This resulted in some degree of correlation whereby the UV-Vis peaks found in porphyrin/PEDOT samples could be the result of a change in oxidation state of the core Mn ion. The species MnTPP/PEDOT, as it was the highest performing sample type in terms of photocurrent, was chosen to be studied by gas sensing during photoelectrochemistry and featured oxygen gas evolution as recorded by GC. This system was examined in greater detail in the next chapter in order to understand the behaviour of the porphyrin inside the PEDOT matrix.

3.5 References

1. Chen, J., P. Wagner, L. Tong, G.G. Wallace, D.L. Officer, and G.F. Swiegers, Angewandte Chemie-International Edition, 2012. **51**(8): p. 1907-1910.
2. Chen, J., P. Wagner, L. Tong, D. Boskovic, W. Zhang, D. Officer, G.G. Wallace, and G.F. Swiegers, Chemical Science, 2013. **4**(7): p. 2797-2803.
3. Shimazaki, Y., T. Nagano, H. Takesue, B.-H. Ye, F. Tani, and Y. Naruta, Angewandte Chemie International Edition, 2004. **43**(1): p. 98-100.
4. Naruta, Y., M.-a. Sasayama, and T. Sasaki, Angewandte Chemie International Edition in English, 1994. **33**(18): p. 1839-1841.
5. Naruta, Y. and M.-A. Sasayama, Journal of the Chemical Society, Chemical Communications, 1994(23): p. 2667-2668.
6. Ruhlmann, L., A. Nakamura, J.G. Vos, and J.-H. Fuhrhop, Inorganic Chemistry, 1998. **37**(23): p. 6052-6059.
7. Koua, F.H.M., Y. Umena, K. Kawakami, and J.-R. Shen, Proceedings of the National Academy of Sciences, 2013. **110**(10): p. 3889-3894.
8. Harriman, A. and G. Porter, Journal of the Chemical Society, Faraday Transactions 2: Molecular and Chemical Physics, 1979. **75**(0): p. 1532-1542.
9. Satake, A. and Y. Kobuke, Organic & Biomolecular Chemistry, 2007. **5**(11): p. 1679-1691.
10. Adler, A.D., F.R. Longo, J.D. Finarelli, J. Goldmacher, J. Assour, and L. Korsakoff, The Journal of Organic Chemistry, 1967. **32**(2): p. 476-476.
11. Adler, A.D., F.R. Longo, F. Kampas, and J. Kim, Journal of Inorganic and Nuclear Chemistry, 1970. **32**(7): p. 2443-2445.
12. Dong, Z. and P.J. Scammells, The Journal of Organic Chemistry, 2007. **72**(26): p. 9881-9885.

13. Chauvin, B., A. Kasselouri, P. Chaminade, R. Quiameso, I. Nicolis, P. Maillard, and P. Prognon, Analytica Chimica Acta, 2011. **705**(1–2): p. 306-314.
14. Lawson, K., J. Gross, and P.W. Crawford, Helvetica Chimica Acta, 2004. **87**(1): p. 120-132.
15. Barbat, A., V. Gloaguen, V. Sol, and P. Krausz, Bioresource Technology, 2010. **101**(16): p. 6538-6544.
16. Dixon, D.W., A.F. Gill, L. Giribabu, A.N. Vzorov, A.B. Alam, and R.W. Compans, Journal of Inorganic Biochemistry, 2005. **99**(3): p. 813-821.
17. Ramirez-Gutierrez, O., J. Claret, and J.M. Ribo, Journal of Porphyrins and Phthalocyanines, 2005. **09**(06): p. 436-443.
18. Hambright, P., *Chemistry of Water Soluble Porphyrins*, in *The Porphyrin Handbook*, K.M. Kadish, K.M. Smith, and R. Guilard, Editors. 2000, Academic Press: New York. p. 129-210.
19. Winther-Jensen, B. and K. West, Macromolecules, 2004. **37**(12): p. 4538-4543.
20. Gu, C., B.C. Norris, F.-R.F. Fan, C.W. Bielawski, and A.J. Bard, ACS Catalysis, 2012. **2**(5): p. 746-750.
21. Fabretto, M., C. Jariego-Moncunill, J.-P. Autere, A. Michelmore, R.D. Short, and P. Murphy, Polymer, 2011. **52**(8): p. 1725-1730.
22. Fabretto, M., K. Zuber, C. Hall, and P. Murphy, Macromolecular Rapid Communications, 2008. **29**(16): p. 1403-1409.
23. Winther-Jensen, B., J. Chen, K. West, and G. Wallace, Macromolecules, 2004. **37**(16): p. 5930-5935.
24. Andreas Elschner, S.K., Wilfried Lövenich, Udo Merker, Knud Reuter, *PEDOT Principles and Applications of an Intrinsically Conductive Polymer*2011, Boca Raton: CRC Press.

25. Groenendaal, L., F. Jonas, D. Freitag, H. Pielartzik, and J.R. Reynolds, Advanced Materials, 2000. **12**(7): p. 481-494.

26. Winther-Jensen, B. and D.R. MacFarlane, Energy & Environmental Science, 2011. **4**(8): p. 2790-2798.

27. Zhou, C., Z. Liu, Y. Yan, X. Du, Y.-W. Mai, and S. Ringer, Nanoscale Research Letters, 2011. **6**(1): p. 364.

28. Brimblecombe, R., G.C. Dismukes, G.F. Swiegers, and L. Spiccia, Dalton Transactions, 2009(43): p. 9374-9384.

29. Brimblecombe, R., D.R.J. Kolling, A.M. Bond, G.C. Dismukes, G.F. Swiegers, and L. Spiccia, Inorganic Chemistry, 2009. **48**(15): p. 7269-7279.

30. Charles Dismukes, G. and R.T. van Willigen, *Manganese: The Oxygen-Evolving Complex & Models*, in *Encyclopedia of Inorganic Chemistry*2006, John Wiley & Sons, Ltd.

31. Dismukes, G.C., Chemical Reviews, 1996. **96**(7): p. 2909-2926.

32. Carnieri, N., A. Harriman, G. Porter, and K. Kalyanasundaram, Journal of the Chemical Society, Dalton Transactions, 1982(7): p. 1231-1238.

33. Jaszewski, A.R., R. Stranger, and R.J. Pace, The Journal of Physical Chemistry B, 2011. **115**(15): p. 4484-4499.

34. Pace, R.J., L. Jin, and R. Stranger, Dalton Transactions, 2012. **41**(36): p. 11145-11160.

35. Pace, R.J., R. Stranger, and S. Petrie, Dalton Transactions, 2012.

36. Petrie, S., P. Gatt, R. Stranger, and R.J. Pace, Physical Chemistry Chemical Physics, 2012. **14**(13): p. 4651-4657.

37. Brudvig, G.W., Philosophical Transactions of the Royal Society B: Biological Sciences, 2008. **363**(1494): p. 1211-1219.

38. Jaszewski, A.R., R. Stranger, and R.J. Pace, Physical Chemistry Chemical Physics, 2009. **11**(27): p. 5634-5642.

39. Kolling, Derrick R.J., N. Cox, Gennady M. Ananyev, Ron J. Pace, and G.C. Dismukes, Biophysical Journal, 2012. **103**(2): p. 313-322.

4 Analysis of MnTPP/PEDOT

4.1 Introduction and Aims

As noted in the previous chapter, the porphyrin species 5,10,15,20-tetraphenylporphyrinato manganese(III) chloride (MnTPP) was inserted into PEDOT and tested as a photocatalyst of water oxidation [1, 2]. The doping was carried out by vapour phase polymerisation, which is known to produce dense polymer layers that can readily trap bulky species such as neutral or potentially cationic species like MnTPP, within the polymer matrix. The species Mn(III)Cl(TPP) and its cationic counterpart $Mn(III)(TPP)^+$, after dissociation of its Cl^- ligand, may be repelled by PEDOT when the polymer is in its conducting, oxidised state. To minimise this repulsive effect and associated electrochemical changes to the PEDOT, only relatively low levels of MnTPP were incorporated. It was hoped that this would also help illuminate the interactions that occurred between the MnTPP and PEDOT at the most fundamental level.

As noted in the previous chapter, MnTPP/PEDOT proved to be a very unusual and highly distinctive material in that it:

(a) displayed the highest overall performance in terms of photocurrent density of all of the metalloporphyrin/PEDOT composites that were prepared (see Table 4.1),

(b) yielded photocurrents that increased with decreasing loading levels (see Table 3.11), in complete contrast to all of the other metalloporphyrin/PEDOT composites, whose photocurrents increased with <u>increasing</u> doping levels, and

(c) generated, uniquely and unexpectedly, a mixture of oxygen and hydrogen when illuminated with sunlight when poised at 0.7 V (*vs* Ag/AgCl) in 0.1 M Na_2SO_4

(see Figure 3.18 and section 3.3.8). By contrast, MnTPPS/PEDOT generated exclusively oxygen under comparable conditions.

For these reasons, it was decided to subject the MnTPP/PEDOT composite to a more detailed study, which would hopefully elucidate its mechanism of action at least to some extent. New samples of MnTPP/PEDOT were prepared and tested. The tests included more comprehensive UV-Vis spectroscopic analysis of the composite, as well as the species that were leached from the composite when it was washed. The spectroscopic data was compared to that of the same Mn porphyrin under different conditions, such as with different Mn oxidation states. Comparisons were also made with the porphyrin alone, free base and / or protonated state. Such comparisons allowed for an assessment of the likely state of the porphyrin in the PEDOT composites. Elemental analysis of the MnTPP/PEDOT was also carried out.

Sample	Porphyrin Loading	0.6 V	0.65 V	0.7 V
MnTPP/PEDOT	1 mg/mL / 1.42 mM	2.37	2.91	4.01
MnTPPS/PEDOT	2.61 mg/mL / 2.35 mM	1.19	1.46	1.88
MnTPPS+MnTMPyP/PEDOT	2 mg/mL / 1.57 mM	1.03	1.07	1.31
MnTMPyP/PEDOT	3 mg/mL / 2.35 mM	0.83	0.89	1.01

Table 4.1 Summary of the highest CA photocurrent density results (in µA/cm^2) per sample in chapter 3.

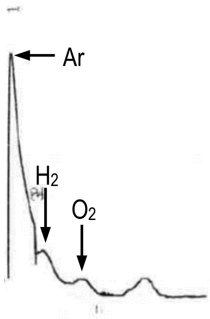

Figure 4.1 GC trace of the gases produced by MnTPP/PEDOT after 4.7 h of illumination at >3 sun, while poised at 0.7 V (*vs* Ag/AgCl) in 0.1 M Na_2SO_4 (from section 3.3.8).

The focus of this chapter is, consequently, on an in-depth analysis of the photoelectronic properties of MnTPP/PEDOT. In addition to elemental analysis, in order to determine the physical composition of the film, porphyrin was also extracted from the MnTPP/PEDOT samples with ethanol and analysed by MALDI spectrography and UV-Vis spectroscopy. The central aim in this chapter was to establish the properties of the porphyrin in the composite and how it changed. MnTPP/PEDOT, at higher loading levels than previously, was also studied in order to determine features that were specific to porphyrin concentration. In iterative tests the most likely state was determined by the overall closest fit between data from the porphyrin inside MnTPP/PEDOT and that of experimentally reproduced species.

4.2 Experimental

4.2.1 Synthesis of 5,10,15,20-tetraphenylporphyrinato manganese(III) chloride (MnTPP)

The porphyrin was synthesised as described in section 3.2.1. The free base species 5,10,15,20-tetraphenylporphyrin (TPP) was also used for analysis in this work.

4.2.1 MnTPP reduction

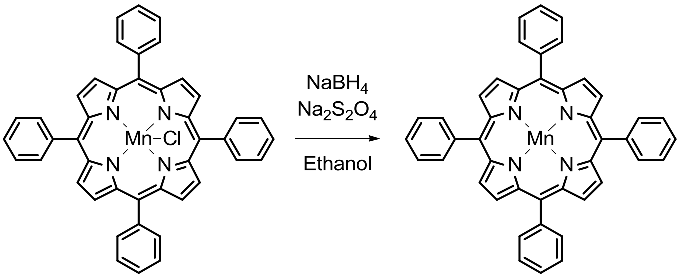

Figure 4.2 Reaction scheme for reduction of Mn(III)TPP to Mn(II)TPP.

Mn(III)TPP was reduced to Mn(II)TPP following a method suggested in literature (see Figure 4.2) [3]. A solution of Mn(III)TPP (0.01 M) in ethanol was transferred to a UV-Vis quartz cuvette . The cuvette was covered with Parafilm to avoid exposure to air, and a Pasteur pipette tip inserted to bubble Argon gas through the solution for 30 min. A small amount of $NaBH_4$ (10 mg) and $Na_2S_2O_4$ (10 mg) were added and the solution continuously bubbled with Ar gas. Care was taken not to expose the solution to air as oxygen readily oxidises the porphyrin back to the Mn(III) state. After 5 min the cuvette was quickly transferred to the UV-Vis spectrometer, whilst maintaining an inert atmosphere inside, and a spectrum taken. The spectrum displayed the characteristic Soret Band, shifted from 466 nm to 432 nm [3]. A small quantity of Milli-Q water (0.5

mL) was then added to the solution. This resulted in a shift of part of the Soret Band to 420 nm, close to that of free TPP at 415 nm, as well as a partial restoration of the characteristic TPP Q-bands at 514, 550, 590 and 645 nm.

4.2.2 Protonation of TPP

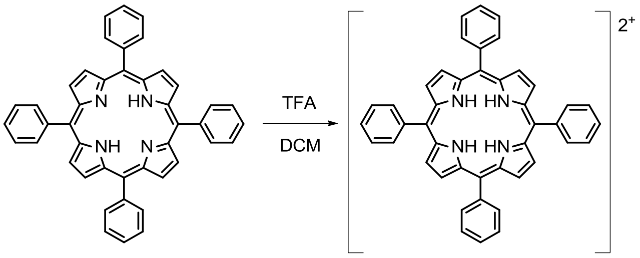

Figure 4.3 Reaction scheme for the protonation of TPP

A small amount of TPP (0.01 M) was dissolved in DCM and a few drops of TFA added to the mixture to protonate the porphyrin (see Figure 4.3). The solution was transferred to a quartz cuvette and the UV-Vis spectrum for the acidified species $(H_4TPP)^{2+}$ was obtained; this featured the Soret Band shifted to 436 nm from the normal 415 nm. There were also two instead of four Q Band peaks at 600 nm and 652 nm [4].

4.2.3 Porphyrin/PEDOT films by VPP deposition

Films of MnTPP/PEDOT and TPP/PEDOT were produced following the method outlined in section 3.2.4. The fabrication process involved cutting the FTO electrode in half after VPP deposition, thereby making two samples from one deposition. As an additional precaution a small amount of epoxy glue was applied to the side and bottom edges of the electrodes to avoid possible distortions in data brought on by edge effects. In each case the geometric surface area of active film was measured with a ruler and the photocurrent converted to current density for accurate comparisons. The MnTPP/PEDOT samples that were prepared are shown in

Table 4.2.

MnTPP/PEDOT	TPP/PEDOT
1.5 mg/mL / 2.13 mM	1.5 mg/mL / 2.44 mM
10 mg/mL / 14.18 mM	
23 mg/mL / 32.71 mM	

Table 4.2 Porphyrin/PEDOT samples prepared for this chapter.

4.2.4 Electrochemical testing

The porphyrin/PEDOT samples were subjected to electrochemical testing with the apparatus and methods described in sections 2.4.8 and 2.4.9. In a typical experiment the electrochemical cell was filled with Na_2SO_4 (0.1 M) that had been bubbled with N_2 gas and stirred for 1 h. The sample was inserted into the test cell as the working electrode with a Ag/AgCl reference electrode and platinum mesh counter electrode in their respective places.

Before the examination, CVs were performed on the film for 20 cycles at 10 mV/s in order to stabilise the film, over the range of 0.0 V - 0.7 V at a scan rate of 5 mV/sec. Voltages beyond 0.7 V (*vs* Ag/AgCl) could lead to irreversible oxidative damage to the film and were therefore avoided. In a typical experiment 5 sweeps were done in the dark and then 3 sweeps with illumination turned on. This ensured that the LSV spectrum remained constant over the course of data recording as it was otherwise affected by charge imbalances brought on by static electricity and low electrolyte mobility. The last of the LSV sweeps with and without illumination were used as data. This method was applied to all of the films examined in this chapter. In all cases the resulting current (in µA) was converted into current density (in µA/cm^2) by dividing by the geometric area of the film. The area was calculated from measuring the dimensions of the polymer film on the substrate with a ruler. Where necessary, electronic noise brought on by an unknown external interference was removed from the data by subtracting a sine wave function.

Following the LSV measurement, each sample was tested by CA at constant potentials of 0.6 V, 0.65 V and 0.7 V (*vs* Ag/AgCl). In a typical experiment the chosen voltage was applied to the film for 1h without illumination in order to equilibrate the baseline current. The light was then switched on to measure the resulting photocurrent for 10 minutes and then turned off. The data shown in the results presented below was taken from 1 min before illumination to 1 min after end of illumination. The data (in µA) was normalised by subtracting the baseline before illumination and the results converted to current density (in µA/cm^2) by the same method as above.

4.3 Results and Discussion

4.3.1 Elemental analysis of MnTPP/PEDOT

To determine the make-up of MnTPP/PEDOT, films were prepared by the method described in section 4.2.3 with a loading level of 1.5 mg/mL (2.13 mM) of MnTPP in the polymerisation reaction mixture. A total of 24 films had to be produced to prepare enough mass of composite (~10 mg) for elemental analysis. The films were scratched off the glass surface with a scalpel and combined in an Eppendorf tube which was then submitted for testing by the Microanalytical Unit at the Australian National University Research School of Chemistry and the University of Wollongong School of Chemistry. The elemental analysis was carried out using an EA 3000 instrument for CNH analysis, a Dionex for S and flame atomic absorption spectroscopy for Mn and Fe (see section 2.4.4).

Element	% expected	% found
C	46.57	44.18
H	2.56	3.20
N	0.54	0.63
S	18.46	18.06
Fe	0	0.41
Mn	0.53	<0.02

Table 4.3 Elemental analysis results of MnTPP/PEDOT; found *vs* expected percentage by weight.

The results of the elemental analysis were quite remarkable and entirely unprecedented in all of the previous work carried out at the University of Wollongong on composites of these types. As shown in Table 4.3, the expected percentages, which were based on the ratio of oxidant to MnTPP in the polymerisation solutions (58.8:1), were not observed. Normally one would expect that all of the oxidant in the polymerisation solution would be used up to polymerise the EDOT monomer, meaning that the mole fraction of the oxidant should correspond to the mole fraction of individual monomer units of PEDOT. The dried coating would then be expected to contain 46.57% C, 2.56% H, 0.54% N, 18.46% S, and 0.53% Mn.

Instead, the coating was found to contain 44.18% C, 3.20% H, 0.63% N, 18.06% S, and 0.00% Mn. Fe was also detected at 0.41%, meaning that trace amounts of the oxidant or

its reduced form were trapped within the film and could not be removed by washing the films with Milli-Q water after polymerisation (see
Table 4.3).

The elemental analysis yielded a startling discovery, namely, that manganese was not present in the MnTPP/PEDOT film submitted for analysis. The manganese ion had somehow been ejected from the porphyrin during fabrication of the film. The porphyrin remained intact after the polymerisation. The loss of the Mn ion from the porphyrin must therefore have occurred during the PEDOT polymerisation process. Given that Mn(III) is very difficult to be removed from the complex, this could only have occurred if the Mn(III) was transformed or cycled through a Mn ion on a different oxidation level. Previous studies on the TPP complexes of Mn(II), Mn(III), Mn(IV) and Mn(V) have shown that only the Mn(II) variant is labile and capable of being removed from the porphyrin core. However, under normal conditions, Mn(II)TPP rapidly and irreversibly forms the kinetically stable Mn(III)TPP when exposed to air oxygen [3, 5, 6].

In order to verify this hypothesis the remaining porphyrin in MnTPP/PEDOT was isolated and analysed separately. The Mn(III)TPP to Mn(II)TPP reaction and subsequent demetallation, was also experimentally reproduced in order to directly study the changes to the system by UV-Vis spectroscopy.

4.3.2 UV-Vis spectroscopy studies of porphyrin leached from MnTPP/PEDOT

In light of the elemental analysis results indicating an absence of Mn in the samples, it was decided to analyse the porphyrin in the MnTPP samples separately from the film itself. MnTPP is highly soluble in ethanol, which was why the MnTPP/PEDOT films were washed with Milli-Q water after fabrication rather than ethanol in order to remove residual EDOT and oxidant.

For this experiment films of MnTPP/PEDOT were prepared by the method described in section 4.2.3 with a loading of 1.5 mg/mL (2.13 mM) of MnTPP in the reaction mixture. A small amount of ethanol was thereafter poured on to the MnTPP/PEDOT film drop-wise and the run-off captured in a sample vial. The ethanol turned a green colour upon contacting the film, indicating ready leaching of the porphyrin from the film. The ethanolic leachate was then analysed by UV-Vis spectroscopy.

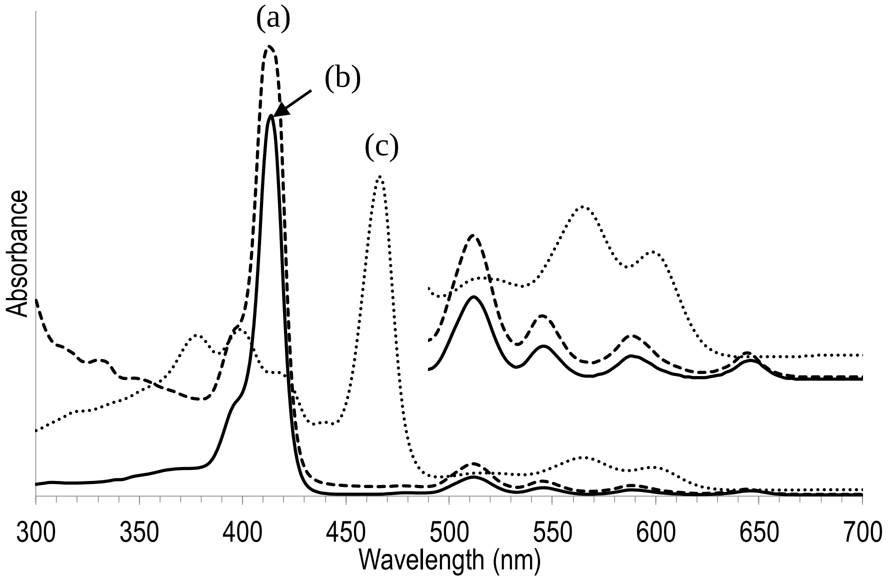

Figure 4.4 UV-Vis spectra of porphyrins in ethanol: (a) porphyrin leached from MnTPP/PEDOT film by washing with ethanol, (b) free base TPP, (c) MnTPP.

As can be seen in Figure 4.4, the Soret band of MnTPP in ethanol fell at 466 nm, while that of the free base TPP fell at 415 nm. The spectrum of the porphyrin rinsed out of MnTPP/PEDOT films using ethanol was identical to that of free TPP, including the Q-bands in the 490-660 nm region. This ethanol rinse was also analysed by MALDI spectrography and showed a major peak at 613 m/z, which corresponded to the free base TPP. These results confirmed the elemental analysis data that had been obtained.

A second sample of MnTPP/PEDOT was prepared in the same way, without the final step of washing the MnTPP/PEDOT in Milli-Q water as is normally part of the fabrication process (see section 3.2.4). This was done in order to examine the state of the porphyrin inside MnTPP/PEDOT without it coming into contact with water at any stage. The porphyrin in that sample was thereafter again leached out with ethanol and analysed using UV-Vis spectroscopy.

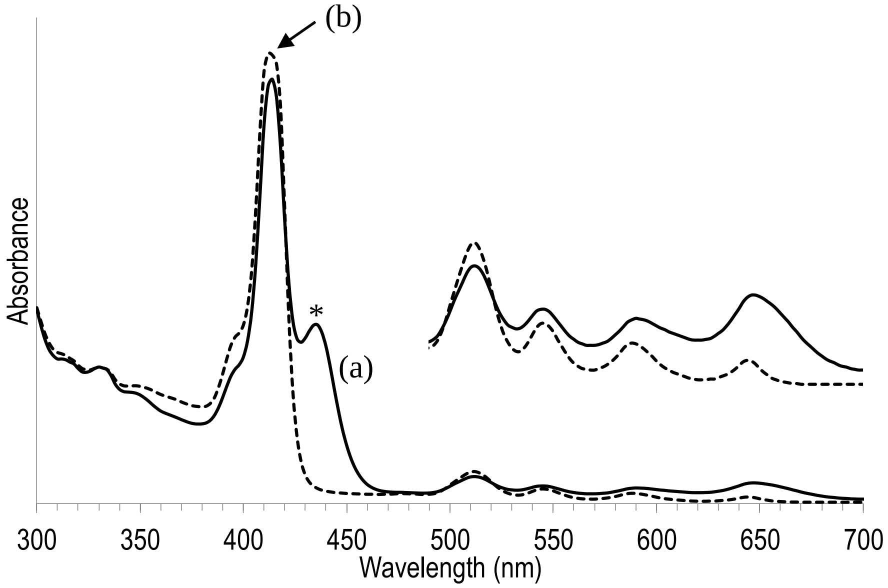

Figure 4.5 UV-Vis spectra of porphyrins in ethanol: (a) porphyrin leached from MnTPP/PEDOT film that had not been exposed to water showing (*) a new peak at 436 nm, (b) free base TPP.

The UV-Vis spectrum of the porphyrin leached out of this sample using ethanol was identical to that of the previous MnTPP/PEDOT sample, except for the presence of an extra peak at 436 nm (Figure 4.5). Neither spectrum indicated that the porphyrin in the film was in the original Mn(III)TPP form; it had clearly already changed within the polymer matrix, even before electrochemical testing.

The absorbance peak at 415 nm for the porphyrin leached out of MnTPP/PEDOT was unequivocally that of the free base porphyrin TPP (see Figure 4.4 and Figure 4.5), indicating that the porphyrin lost its Mn ion during the polymerisation process. To investigate the second peak at 436 nm further experimentation was necessary.

One possible candidate for the peak at 436 nm was the Soret band of Mn(II)TPP [3]. The Q-bands of this particular species may be covered up by the more intense absorbance displayed by the free base TPP. As noted earlier, demetallation of Mn(II)TPP had been reported in literature [3, 5-7]. This suggested that the Mn(III) porphyrin was reduced to the Mn(II) analogue during the formation of the PEDOT conductive polymer, with the metal ion then expelled by interaction with a mildly acidic species. Such a reaction would be highly unusual as reduction of Mn(III) porphyrin normally requires a strong reducing agent and the absence of air oxygen. Given the abundant presence of the strongly oxidising Fe-pTS in the polymerisation mixture, one would expect the presence of an oxidised porphyrin and not a reduced porphyrin.

4.3.3 UV-Vis spectrum of Mn(II)TPP and subsequent demetallation.

Mn(III)TPP in ethanol was reduced to Mn(II)TPP using sodium borohydride under inert atmosphere and subsequently demetallated following the method described in section 4.2.1. The porphyrin species at each step along this pathway were characterised by UV-Vis spectroscopy.

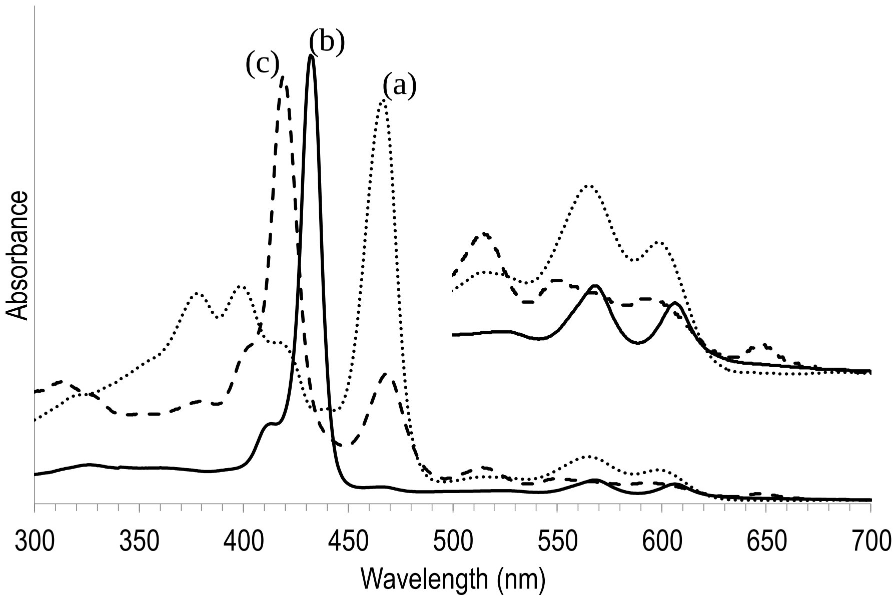

Figure 4.6 UV-Vis spectra of porphyrins in ethanol: (a) Mn(III)TPP, (b) Mn(II)TPP (under inert atmosphere), (c) Mn(II)TPP after the addition of water under inert atmosphere.

As can be seen in Figure 4.6, the Soret band in ethanol of Mn(III)TPP at 466 nm (Figure 4.6(a)) shifted to 432 nm for Mn(II)TPP under inert atmosphere (Figure 4.6 (b)). These data were in agreement with literature data [3]. Exposure of the Mn(II)TPP solution to air resulted in immediate regeneration of Mn(III)TPP. When Milli-Q water was added to the Mn(II)TPP solution (under inert atmosphere), the Soret Band at 432 nm split into two bands at 420 nm (which was close to that of free TPP at 415 nm) and 466 nm (which was characteristic of Mn(III)TPP) (Figure 4.6 (c)). The characteristic Q-bands of free TPP were also observed at 514 nm, 550 nm, 590 nm and 645 nm.

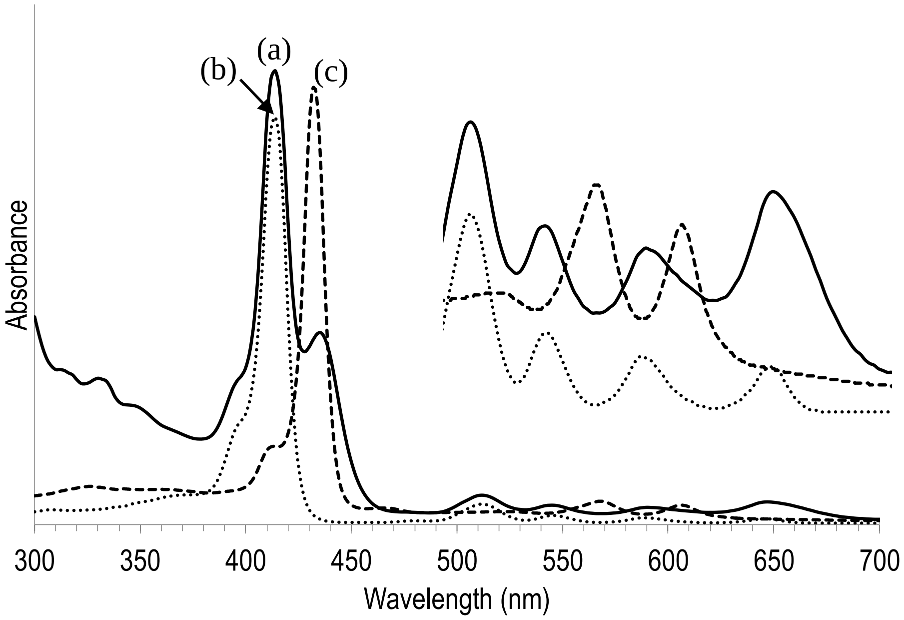

Figure 4.7 UV-Vis spectra of: (a) ethanol wash leached from MnTPP/PEDOT that had not been treated with water during its preparation, (b) free base TPP, (c) Mn(II)TPP.

These spectra were then compared to those of an ethanol wash leached from MnTPP/PEDOT film samples that had not been treated with water at any stage (Figure 4.7). The absorbance bands at 415 nm and 432 nm of the ethanol leachate (Figure 4.7 (a)) could be attributed to the Soret Bands of free base TPP (Figure 4.7 (b)) and Mn(II)TPP (Figure 4.7 (c)). However, the Q Bands of the leached sample did not display any similarity to that of Mn(II)TPP, instead mirroring those of TPP. Mn(II)TPP displayed two distinct absorbance peaks at 567 nm and 606 nm, while the leachate had four absorbance peaks at 514 nm, 550 nm, 590 nm and 645 nm, which corresponded to those of free TPP. This indicated that the second species in the unwashed

MnTPP/PEDOT film may not be Mn(II) TPP. The question then remains, which species absorbed at 432 nm?

4.3.4 UV-Vis spectroscopy of protonated TPP

One more variant of the TPP porphyrin was explored by UV-Vis analysis, namely, that of the protonated free base, H_4TPP^{2+}. In the previous section the additional absorbance peak at 432 nm was compared to Mn(II)TPP and found to not be in full agreement. In a similar experiment, free base TPP was protonated as per the method described in section 4.2.2 and again compared to that of the above ethanol leachate (Figure 4.8).

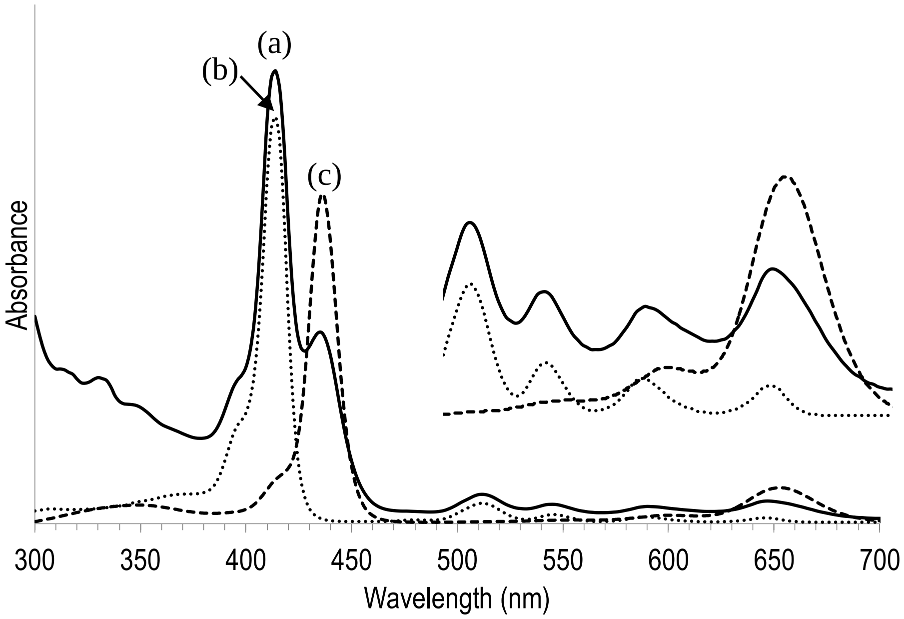

Figure 4.8 UV-Vis spectra in ethanol of: (a) porphyrin leached from MnTPP/PEDOT that had not been treated with water, (b) free base TPP, (c) protonated H_4TPP^{2+}.

The UV-Vis spectrum of protonated H_4TPP^{2+} (Figure 4.8 (c)) displayed a significant overlap with the spectrum of the leachate (Figure 4.8 (a)). Indeed, the Soret Band position of the protonated H_4TPP^{2+} species corresponded well with the absorbance of the leachate at 436 nm. This was in agreement with literature data for UV-Vis analysis of H_4TPP^{2+} [4]. Moreover, the protonated porphyrin featured two instead of four Q Band peaks at 600 nm and 652 nm. This was very close to two of the four TPP Q Band peaks at 588 and 646 nm. The Q Bands in the leachate spectrum additionally exhibited an unusually intense peak at 646 nm; more intense than the corresponding peak in a solution spectrum of free base TPP alone. The leachate spectrum was thereby shown to be a composite spectrum of free TPP mixed with protonated H_4TPP^{2+}, indicating that the porphyrin leached out of the MnTPP/PEDOT was likely a mixture of free TPP and protonated H_4TPP^{2+}.

The common route for demetallation of Mn(III)TPP was identified in literature and consisted of reduction of Mn(III) to Mn(II) and subsequent protonation of the core, leading to loss of the metal ion from the porphyrin [3, 5-7]. The vapour phase polymerisation of PEDOT produces acid groups [8] that could be sufficient to protonate free base TPP, which has a pK_a of 3.9 [9]. However it was unclear how the reduction to Mn(II) could have occurred in an environment containing an excess of oxidising agent.

4.3.5 Effects of higher concentration of porphyrin in MnTPP/PEDOT

To test the unusual relationship between porphyrin concentration and photocurrent, MnTPP/PEDOT samples were prepared with a higher loading of the porphyrin. The method described in section 4.2.3 was used to make films with porphyrin/oxidant mixtures containing 10 mg/mL (14.18 mM) and 23 mg/mL (32.27 mM) of MnTPP. These were assessed by CA as had been done with prior samples. Additionally, the films were analysed by UV-Vis and compared to previous spectra, with the porphyrins contained in them washed out of the film using ethanol.

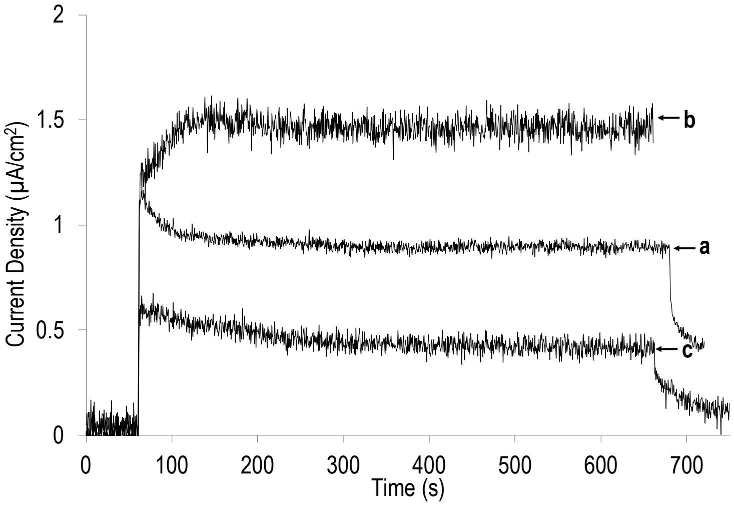

Figure 4.9 CA at 0.7 V (*vs* Ag/AgCl) of (a) PEDOT, MnTPP/PEDOT at (b) 10 mg/mL and (b) and (c) 23 mg/mL.

MnTPP/PEDOT	Current Density (µA/cm^2)
1 mg/mL / 1.42 mM	4.01
2 mg/mL / 2.84 mM	2.62
3 mg/mL / 4.27 mM	1.47
10 mg/mL / 14.18 mM	1.52
23 mg/mL / 32.71 mM	0.40

Table 4.4 Photocurrent density of MnTPP/PEDOT at 0.7 V (*vs* Ag/AgCl) after 10 min of illumination.

Photocurrent density measurements for MnTPP/PEDOT at 10 mg/mL and 23 mg/mL demonstrated significantly lower photocurrents compared to films with lower porphyrin loadings (Figure 4.9). The recorded photocurrent densities after 10 min of illumination were 1.52 µA/cm^2 for 10 mg/mL and 0.40 µA/cm^2 for 23 mg/mL MnTPP/PEDOT. The results of all MnTPP/PEDOT samples are summarised in

Table 4.4.

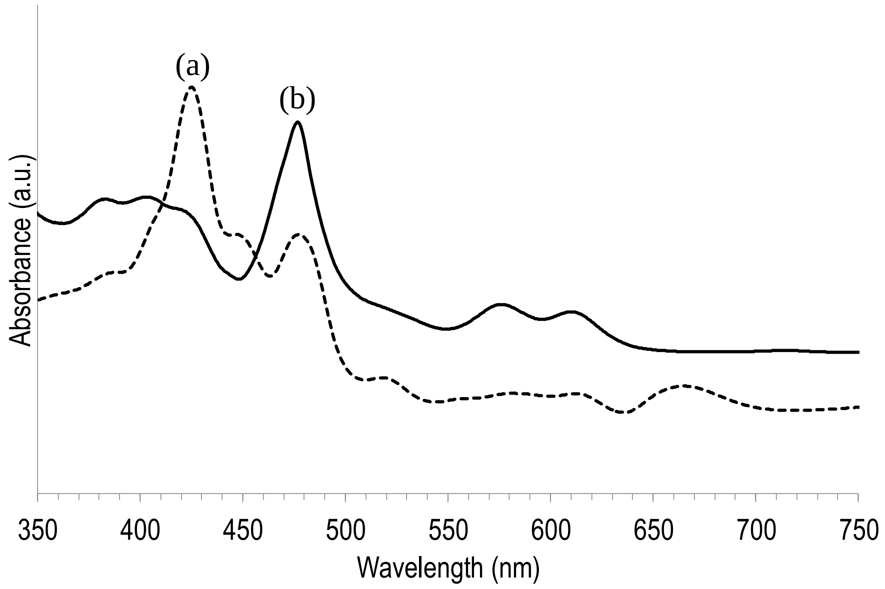

Figure 4.10 UV-Vis spectra of MnTPP/PEDOT with loadings: (a) 10 mg/mL and (b) 23 mg/mL.

The UV-Vis spectra of the two new films with higher concentrations of porphyrin, displayed an interesting phenomenon (Figure 4.10). The 10 mg/mL MnTPP/PEDOT sample exhibited the now familiar absorbance peaks at 425 nm and 447 nm corresponding to free base TPP and H_4TPP^{2+}, as well as a third absorbance peak at 477 nm. The 477 nm peak corresponded to the Soret band of Mn(III)TPP, indicating that at least some of the Mn porphyrin remained in its initial metalloporphyrin state and had not undergone demetallation. The spectrum of the 23 mg/mL MnTPP/PEDOT changed dramatically, closely resembling a typical Mn(III)TPP solution spectrum; the Soret

Band at 477 nm was present as the dominant peak and for the first time the Q Bands at 576 and 610 nm were clearly discernible.

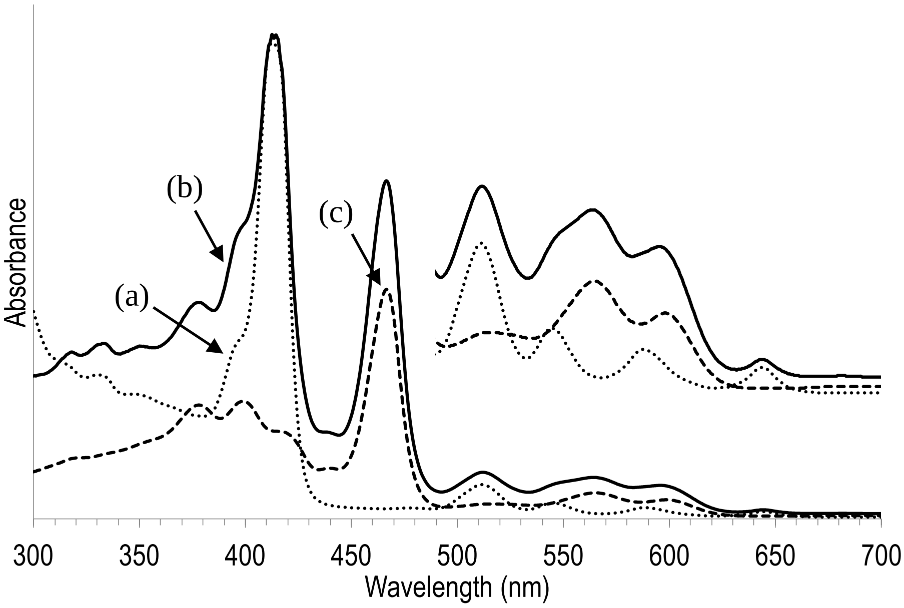

Figure 4.11 UV-Vis spectra of ethanol leachate from MnTPP/PEDOT having loadings of: (a) 1.5 mg/mL, (b) 10 mg/mL and (c) 23 mg/mL.

UV-visible analysis of the ethanol rinse of the 10 mg/mL and 23 mg/mL MnTPP/PEDOT, compared to that of 1.5 mg/mL MnTPP/PEDOT, showed a gradual transition from predominantly H_2TPP in the 1.5 mg/mL film (Figure 4.11 (a)) towards a mixed population of H_2TPP and Mn(III)TPP in the 10 mg/mL film (Figure 4.11 (b)), and then to solely Mn(III)TPP in the 23 mg/mL film (Figure 4.11 (c)). It was thereby clear that the photocurrent activity of the composite MnTPP/PEDOT film was due to the free base form of TPP and, in fact, diminished with higher presence of Mn(III)TPP in the film.

4.3.6 Analysis of the free base porphyrin/PEDOT composite TPP/PEDOT

Given the results of the above analysis, it was prudent to test a film containing free TPP for its photocurrent. Therefore, a TPP/PEDOT film was prepared by vapour phase polymerisation following the same procedure as described in section 4.2.3. This time, TPP (1.5 mg/ml / 2.44 mM TPP) was used in the porphyrin/oxidant mixture. The resulting TPP/PEDOT film was then tested electrochemically under light illumination as described in sections 4.2.4 and 3.2.6, as well as by UV-Vis spectroscopy.

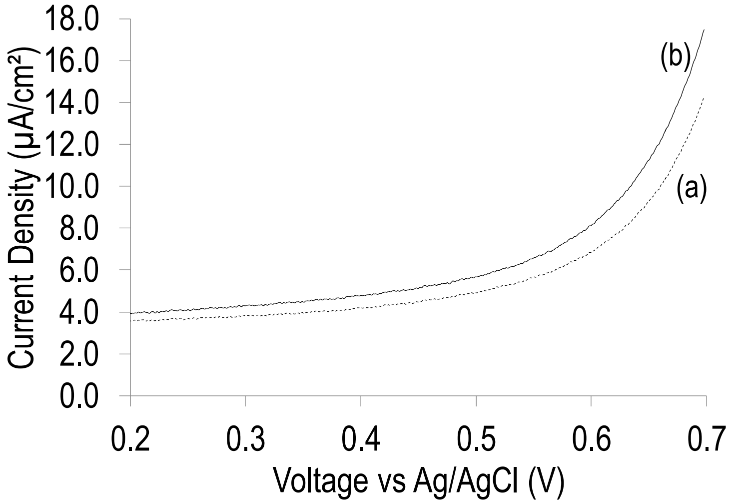

Figure 4.12 LSV of TPP/PEDOT, (a) dark, (b) with illumination.

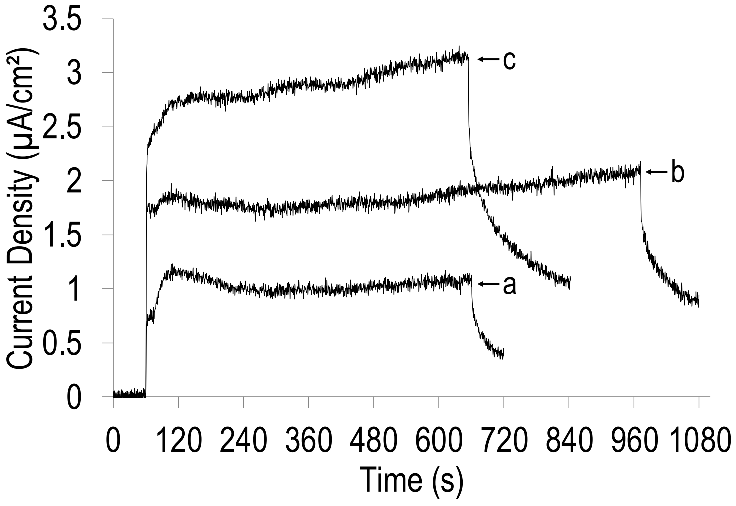

Figure 4.13 CA of TPP/PEDOT at (a) 0.6 V, (b) 0.65 V, (c) 0.7 V (all *vs* Ag/AgCl)

Sample	**Porphyrin Loading**	**Photocurrent Density (μA/cm^2)**		
		0.6 V	**0.65 V**	**0.7 V**
MnTPP/PEDOT	2 mg/mL / 2.84 mM	1.53	1.89	2.62
TPP/PEDOT	1.5 mg/mL / 2.44 mM	1.07	1.9	3.14

Table 4.5 Photocurrent density of MnTPP/PEDOT and TPP/PEDOT at different voltages (*vs* Ag/AgCl).

The TPP/PEDOT sample was tested for photocurrent activity under the same conditions as previously applied to MnTPP/PEDOT and returned very similar results. The LSV of the sample revealed the same onset potential as the MnTPP/PEDOT sample of equivalent concentration examined earlier (Figure 3.9). In CA photocurrent testing after 10 min of illumination, the TPP/PEDOT yielded current densities that were closely comparable (and within experimental error) to those of the equivalent MnTPP/PEDOT (Table 4.5).

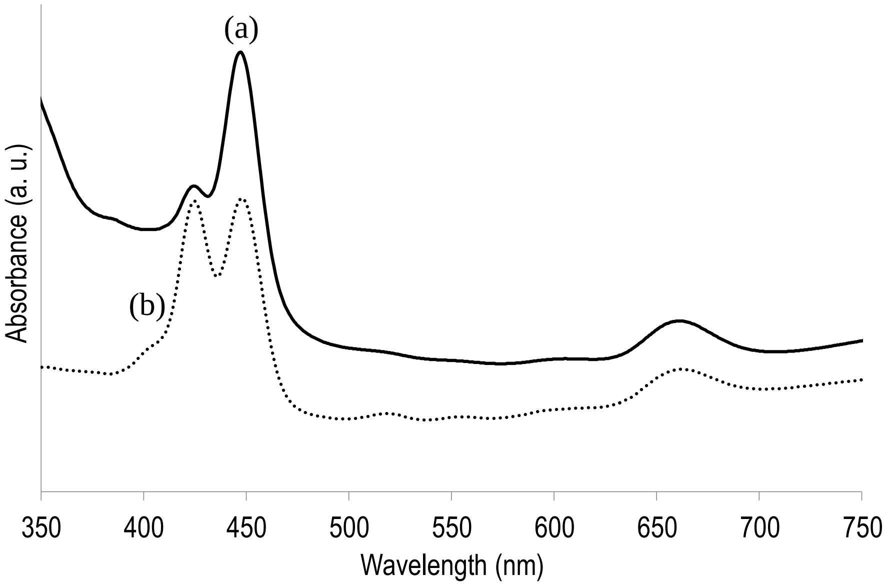

Figure 4.14 UV-Vis spectra of (a) 1.5 mg/mL TPP/PEDOT and (b) 2 mg/mL MnTPP/PEDOT.

A UV-Vis absorbance analysis of the TPP/PEDOT revealed a spectrum similar to that of an earlier prepared 2 mg/mL MnTPP/PEDOT (Figure 4.14). Both featured the characteristic absorbance peaks at 424 and 447 nm, corresponding to the Soret Bands of the free base TPP and H_4TPP^{2+}. They also both showed the characteristic amplified intensity peak at ca. 660 nm that is characteristic of H_4TPP^{2+}. From this comparison of UV-Vis spectra, it could be concluded that, during vapour phase polymerisation of the MnTPP/PEDOT films having low loadings of MnTPP, the Mn ion was ejected from the core of the porphyrin and the film converted to TPP/PEDOT. This did not occur with MnTPP films having higher loading levels of >23 mg/mL MnTPP.

4.4 Conclusions

The underlying assumption in the previous chapter was that the changes in the Soret Band of the porphyrin inside PEDOT were due to close proximity and orientation of individual molecules to one another, as was observed in cofacial porphyrin systems in the past [10-14]. In addition, more significant shifts in wavelength of the Soret Band peaks were thought of in terms of change in the oxidation state of the manganese ion, as was assessed by comparison with literature values (see section 3.3.16). The governing hypothesis was based on a Mn^{III}-Mn^{IV} paradigm, as often found in studies concerning the makeup of natural and artificial photosynthesis systems [15-20].

What was found however was the opposite, namely, that the changes undergone by the metalloporphyrin at low loadings in the conducting polymer matrix were due to reduction of the manganese ion to the Mn(II) state and subsequent ejection from the core. This seemed paradoxical given the highly oxidative conditions in the polymerisation. Indeed, tests were conducted to assess the interaction between the MnTPP and the chemical oxidant species Fe-pTS hexahydrate. These tests showed no discernible chemical reaction between the species, such as oxidation or protonation of the porphyrin (see section 3.3.11).

The findings from this chapter however point clearly to the porphyrin inside the polymer matrix being in its demetallated state when present in low loadings, generating the typical TPP Soret Band peak at 414 nm in solution and 425 nm inside the film. The shift in wavelength when inside the film is likely to arise from aggregation effects. This was confirmed by a comparison of UV-Vis data of the ethanol leachate from MnTPP films with that of free base TPP in a similar solvent (see section 4.3.2). From the UV-Vis data it is apparent that the Soret band peak at 447 nm arises from the acidified TPP in the film meaning that at the point of polymerisation, the MnTPP was converted to H_4TPP^{2+}. Subsequent tests of polymer samples containing free base TPP showed an identical absorbance profile to that of samples containing MnTPP, indicating, without a doubt, that the porphyrin in the film was in its free, demetallated state.

One possible explanation for the change in the oxidation state of the Mn ion exclusively in low loadings, is photoreduction of the starting Mn(III) to Mn(II) by light irradiation. Photoreduction of Mn(III) to Mn(II) when illuminated by light is a well-documented phenomenon in the chemical literature and has been noted to be associated with demetallation as the Mn(II) ion is unstable in solution compared to its more robust Mn(III) counterpart [21]. In the above systems, this was readily evidenced by visible light absorbance analysis of the Soret Band, which shifted from 466 nm (in Mn(III)TPP) to 432 nm (in Mn(II)TPP) as was observed in the above experiments and supported by literature [3]. Considering the similarity between the chosen porphyrin types with regard to Soret Band, it is likely that all samples showing similar change in absorbance peaks due to PEDOT polymerisation underwent loss of Mn ions in that process.

One should note that such a photoreduction did not appear to be observed during preparation of solutions for UV-Vis analysis with Mn(III)TPP and other porphyrins, done in normal laboratory conditions without excessive irradiation. Indeed previous studies of such reductions typically involved a carefully degassed solvent [7, 21, 22], as was also required in our experiments where the porphyrin was reduced in solution by the chemical reducing agent, sodium borohydride (see section 4.3.3). Without an inert atmosphere, the porphyrin would quickly oxidise back to its Mn(III) ion upon even minute exposure to air oxygen. The difficulty of obtaining a Mn(II) spectrum was initially grounds to rule out that kind of reaction, as it was evident that in the same environmental conditions only a strong reducing agent would reduce the Mn(III) to Mn(II)porphyrin.

It is possible that the PEDOT matrix facilitated enhanced photoreduction of the contained porphyrin by ambient light during fabrication after vapour phase polymerisation. This process seemed to go to completion very rapidly without a significant sensitivity to the presence of air oxygen. All of this however took place in the presence of a strong oxidising agent within the polymerisation solution, Fe-pTS, which seemed to have no effect in respect of halting or hindering this photoreduction process. Perhaps most remarkably, the apparent photoreduction process appeared to have dominated only at loadings below ca. 23 mg/mL MnTPP. If the reduction was the facilitated by ambient light it may be possible that the process was hindered either by less transparency of the film due to higher loading, or a saturation effect by the excess of MnTPP.

The simultaneous formation of oxygen and hydrogen when low-loaded MnTPP/PEDOT films were subjected to light illumination at constant potential of 0.7 V (*vs* Ag/AgCl) (Figure 3.18) and the inverse relationship between loading and photocurrent can potentially also be explained. Free base TPP is known to undergo ready photolytic degradation when illuminated with light at its Soret and Q band wavelengths [23]. It appears likely that the free base TPP generated in the PEDOT at low loadings may have undergone the photoelectrolytic degradation, releasing hydrogen and oxygen gases and creating a “photocurrent” that increased as the amount of free base TPP in the coating was increased. Thus, at low loading levels, more of free base TPP was present, yielding higher apparent photocurrents. The origin of the photocurrent in the absence of a catalytic metal species is unclear. One possibility is gradual light-assisted oxidation of the electron rich aromatic structure of the porphyrin when subjected to light and a positive electric bias. The higher photocurrent of samples containing TPP compared to others may be the result of different aggregation behaviour compared to the water soluble porphyrin counterparts. It is possible that the water / alcohol mixture did not fully dissolve the other Mn porphyrin species (MnTPPS, MnTPMPyP) or that they formed different types of aggregates during spin coating compared to a more even and accessible spread of TPP throughout the then forming PEDOT matrix.

4.5 References

1. Chen, J., P. Wagner, L. Tong, G.G. Wallace, D.L. Officer, and G.F. Swiegers, Angewandte Chemie-International Edition, 2012. **51**(8): p. 1907-1910.
2. Chen, J., P. Wagner, L. Tong, D. Boskovic, W. Zhang, D. Officer, G.G. Wallace, and G.F. Swiegers, Chemical Science, 2013. **4**(7): p. 2797-2803.
3. Carnieri, N., A. Harriman, G. Porter, and K. Kalyanasundaram, Journal of the Chemical Society, Dalton Transactions, 1982(7): p. 1231-1238.
4. Chauvin, B., A. Kasselouri, P. Chaminade, R. Quiameso, I. Nicolis, P. Maillard, and P. Prognon, Analytica Chimica Acta, 2011. **705**(1–2): p. 306-314.
5. Morehouse, K.M. and P. Neta, The Journal of Physical Chemistry, 1984. **88**(14): p. 3118-3120.
6. Tsuda, Y., K. Takahashi, T. Yamaguchi, S. Matsui, and T. Komura, Journal of Molecular Catalysis A: Chemical, 1998. **130**(3): p. 285-295.
7. Boucher, L.J., Coordination Chemistry Reviews, 1972. **7**(3): p. 289-329.
8. Winther-Jensen, B. and K. West, Macromolecules, 2004. **37**(12): p. 4538-4543.

9. Hibbert, F. and K.P.P. Hunte, Journal of the Chemical Society, Perkin Transactions 2, 1977(12): p. 1624-1628.

10. Chang, C.J., Z.-H. Loh, Y. Deng, and D.G. Nocera, Inorganic Chemistry, 2003. **42**(25): p. 8262-8269.

11. Chitta, R., L.M. Rogers, A. Wanklyn, P.A. Karr, P.K. Kahol, M.E. Zandler, and F. D'Souza, Inorganic Chemistry, 2004. **43**(22): p. 6969-6978.

12. Durand, R.R., C.S. Bencosme, J.P. Collman, and F.C. Anson, Journal of the American Chemical Society, 1983. **105**(9): p. 2710-2718.

13. Ojadi, E., R. Selzer, and H. Linschitz, Journal of the American Chemical Society, 1985. **107**(25): p. 7783-7784.

14. Satake, A. and Y. Kobuke, Organic & Biomolecular Chemistry, 2007. **5**(11): p. 1679-1691.

15. Brudvig, G.W., Philosophical Transactions of the Royal Society B: Biological Sciences, 2008. **363**(1494): p. 1211-1219.

16. Dismukes, G.C., Chemical Reviews, 1996. **96**(7): p. 2909-2926.

17. Jaszewski, A.R., R. Stranger, and R.J. Pace, Physical Chemistry Chemical Physics, 2009. **11**(27): p. 5634-5642.

18. Kolling, Derrick R.J., N. Cox, Gennady M. Ananyev, Ron J. Pace, and G.C. Dismukes, Biophysical Journal, 2012. **103**(2): p. 313-322.

19. Pace, R.J., R. Stranger, and S. Petrie, Dalton Transactions, 2012.

20. Petrie, S., P. Gatt, R. Stranger, and R.J. Pace, Physical Chemistry Chemical Physics, 2012. **14**(13): p. 4651-4657.

21. Harriman, A. and G. Porter, Journal of the Chemical Society, Faraday Transactions 2: Molecular and Chemical Physics, 1979. **75**(0): p. 1543-1552.

22. Ramirez-Gutierrez, O., J. Claret, and J.M. Ribo, Journal of Porphyrins and Phthalocyanines, 2005. **09**(06): p. 436-443.

23. Horváth, O., Z. Valicsek, G. Harrach, G. Lendvay, and M.A. Fodor, Coordination Chemistry Reviews, 2012. **256**(15–16): p. 1531-1545.

5 Electrochemically polymerised Porphyrin/PEDOT

5.1 Introduction and Aims

While the focus of the previous chapters have been predominantly on monomeric porphyrin species and their interaction with vapour phase polymerised PEDOT, an additional option that was explored involved utilising a simple polymer as a means of covalently linking individual porphyrin molecules to each other and incorporating them into PEDOT. Tethering monomeric species to a polymer may induce close proximities between the individual porphyrin units within a small volume, in the same way that may be achieved by concentrating individual porphyrins within a PEDOT matrix. As in the case in PEDOT, higher overall concentrations of porphyrin attached to the polymer may lead to the presence of localised collections of densely packed porphyrin units within the resulting film.

This concept was inspired by the covalently-linked cofacial porphyrin systems discussed in sections 1.6.1 and 1.6.2 of Chapter 1. However, it differs from the cofacial porphyrins in that the polymer-linked porphyrins explored here are simpler in design with less demanding synthetic procedures than those of the cofacial porphyrins. Rather than relying on carefully crafted covalent linkages between two porphyrin rings to create co-facial architectures, this approach utilised the combinatorial strategy of concentrating porphyrins in catalytically active assemblies inside a conducting polymer matrix.

In this chapter the integration of sulfonated porphyrins into PEDOT was attempted by electrochemical polymerisation of the EDOT monomer as opposed to vapour phase polymerisation. This approach allowed for a more targeted integration of the porphyrin as a counter-ion to the positively charged PEDOT backbone, rather than depending on the matrix-trapping effect of vapour phase polymerisation that is needed when adding porphyrins into PEDOT.

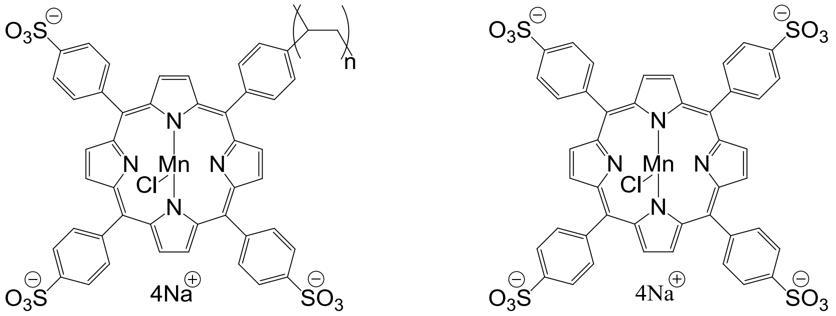

(a) (b)

Figure 5.1 Schematic of (a) poly(5-(4-vinylphenyl)-10,15,20-tris(4-sulfonatophenyl)) porphyrinato manganese(III) chloride sodium salt (MnPVTPPS) and (b) its monomeric counterpart 5,10,15,20-tetrakis(4-sulfonatophenyl)porphyrinato manganese(III) chloride sodium salt (MnTPPS).

The porphyrin species poly(5-(4-vinylphenyl)-10,15,20-tris(4-sulfonatophenyl)) porphyrinato manganese(III) chloride sodium salt (MnPVTPPS) (Figure 5.1) has been reported previously[1]. Because of its close similarity to poly(sodium 4-styrenesulfonate) (PSS), which is a common counter-ion used in the highly conducting PEDOT:PSS [2-6], MnPVTPPS offered a potential counter-ion for electrochemically polymerised PEDOT [4, 7]. Samples of PEDOT with co-incorporated PSS and MnPVTPPS were prepared and studied. That concentration level was set to be comparable to the low loading levels used in the previous two chapters in order to facilitate comparisons with the previous systems studied.

The sodium salt of 5,10,15,20-tetrakis(4-sulfonatophenyl)porphyrinato manganese(III) chloride (MnTPPS) (Figure 5.1) can be considered to be a monomeric counterpart to MnPVTPPS. It was incorporated in electropolymerised PEDOT:PSS along with PSS to ensure proper functioning of the oxidised PEDOT backbone if the porphyrin species is insufficient as a counter-ion. As in the previous chapters, only a relatively low level of MnTPPS (2.25 mg/mL) was incorporated within the polymer in order to study the most fundamental interactions between the metallated porphyrin and PEDOT:PSS.

5.2 Experimental

5.2.1 Synthesis of 5,10,15,20-tetrakis(4-sulfonatophenyl)porphyrinato manganese(III) chloride sodium salt (MnTPPS)

This porphyrin was synthesised as described in section 3.2.2.

5.2.2 Synthesis of poly(5-(4-vinylphenyl)-10,15,20-tris(4-sulfonatophenyl)) porphyrinato manganese(III) chloride sodium salt (MnPVTPPS)

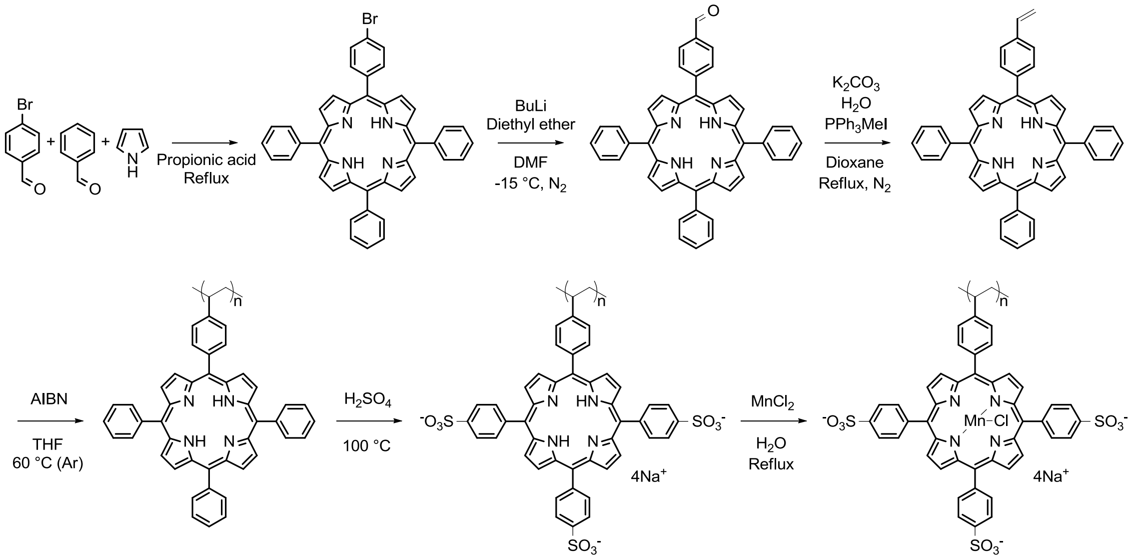

Figure 5.2 Synthesis of poly(5-(4-vinylphenyl)-10,15,20-tris(4-sulfonatophenyl)) porphyrinato manganese(III) chloride sodium salt) (MnPVTPPS).

The synthesis of poly(5-(4-vinylphenyl)10,15,20-tri(4-sulfonatophenyl)porphyrinato manganese(III) chloride sodium salt) (MnPVTPPS) was conducted using a method established in literature (Figure 5.2) [1, 8, 9]. The synthesis required a number of successive steps, starting with the formation of 5-(4-bromophenyl)-10,15,20-triphenylporphyrin, conversion to the formyl derivative by reaction with n-butyllithium and DMF, subsequent vinyl formation by Wittig condensation with triphenylmethylphosphonium iodide, polymerisation of the vinyl group with azobisisobutyronitrile (AIBN), sulfonation, and finally manganese insertion.

5-(4-bromophenyl)-10,15,20-triphenylporphyrin was synthesised following Adler's procedure [10]. 4-bromobenzaldehyde (9.88 g, 52.2 mmol) and benzaldehyde (16.98 g, 160 mmol) were added to propionic acid (800 mL) in a 1:3 ratio at reflux under air atmosphere. Pyrrole (14.22 g, 212 mmol) was then added to the mixture and stirred at reflux for 40 min. Air was bubbled through the mixture for 6 min after removing the vessel from the oil bath and then left to cool overnight. The mixture was filtered through a sintered glass funnel and the solid was then filtered through a silica column twice with DCM. A few drops of triethylamine were added to the mixture to neutralise the solution and the product was recrystallised in DCM with methanol, yielding a purple solid (7.29 g). The compound was analysed by MALDI and found to be a statistical mixture of TPP (612.03 MW), mono bromophenylporphyrin (691.87 MW) and dibromophenylporphyrin (770.21 MW), purification of the mono substituted species was performed in the next step.

The porphyrin mixture (7.29 g) was suspended in diethyl ether (345 mL) in a three-neck flask. The flask was sealed, placed under a nitrogen atmosphere and cooled in a salt ice bath before adding n-butyllithium in cyclohexane (65 mL, 0.66 mol) slowly through a syringe. The mixture was stirred for 2.5 hours, whereafter DMF (20 mL, 0.26 mol) was added and the mixture stirred at room temperature overnight. Hydrochloric acid (5%, 50 mL) was then added to the mixture with stirring. The solvent was evaporated off under vacuum and the product extracted with DCM and Milli-Q water. The mixture was then neutralised with NaOH (1 M, added dropwise). The product was dissolved in DCM and then filtered through a silica column with 60% hexane/DCM as an eluent. Fractions were checked using TLC to isolate the mono formyl porphyrin product from the statistical mixture. TPP would move the fastest and the mono formyl porphyrin the second fastest, which made it possible to correctly isolate the compounds and identify by MALDI. The mono formyl porphyrin structure was confirmed by MALDI as the desired 5-(4-formylphenyl)-10,15,20-tetraphenylporphyrin (MW: 642.76 g/mol calculated, 640.37 g/mol measured). The solvent was evaporated and the product dried in a vacuum oven at 60 °C (0.73 g, 1.14 mmol).

In the next step, the formyl porphyrin (0.73 g, 1.14 mmol) was dissolved in dioxane (70 mL) with K_2CO_3 (12.4 g, 89.72 mmol) and Milli-Q water (1 mL). The mixture was heated to reflux under nitrogen atmosphere. Triphenylmethylphosphonium iodide was separately synthesised by dissolving triphenylphosphine (2.62 g, 9.99 mmol) in toluene (100 mL) at room temperature and slowly adding iodomethane (1.42 g, 10.00 mmol). The formyl porphyrin mixture was stirred for 60 h at room temperature during which time a white precipitate formed. The solid was filtered through a glass sintered funnel and washed with toluene before drying in a vacuum oven at 60 °C (3.40 g, 8.36 mmol, 84% yield). The triphenylmethylphosphonium iodide (1 g, 2.46 mmol) was then added to the porphyrin mixture and stirred at reflux. The mixture was tested periodically by TLC to monitor the reaction and more triphenylmethylphosphonium iodide was added (up to the total 3.4 g, 8.37 mmol) over the course of 12 h. The reaction mixture was then filtered through silica in a sintered glass funnel with DCM and chloroform. The solvent was evaporated under vacuum at 60 °C and the product 5-(4-vinylphenyl)-10,15,20-triphenyl porphyrin (VTPP) obtained (0.49 g, 0.76 mmol, 67% yield). This was confirmed by UV-Vis Analysis, which was in agreement with literature [8].

The vinyl porphyrin VTPP (0.49 g, 0.76 mmol) was then dissolved in a small quantity of THF (0.7 mL) with AIBN (10-20 mg, in 12% acetone solution), which was degassed in an ampoule following the freeze pump thaw method; the mixture was submerged in liquid nitrogen until fully frozen, then a vacuum applied for 20 min. The pump was then disconnected with the flask sealed and the mixture gently thawed in a warm water bath. This procedure was repeated several times (3-5) after which the mixture was stirred at 60 °C under argon atmosphere for 2.5 d. The product was precipitated with acetone and filtered through a sintered glass funnel under vacuum (43 mg, 0.07 mmol, 9% yield). The synthesis had to be repeated several times as TLC tests showed only partial polymerisation in successive steps. The final product poly(5-(4-vinylphenyl)-10,15,20-triphenylporphyrin) (PVTPP) was characterised using gel permeation chromatography (GPC), which reported an average molecular weight of 47 kDa at a fraction of 55%. Smaller polymer chains at 3 kDa and single units at 1 kDa were found at respective fractions of 18% and 27%.

The polymeric porphyrin PVTPP (43 mg, 0.07 mmol) was then sulfonated by dissolving in concentrated H_2SO_4 (2 mL) and stirring at 100 °C for 4 h, after which it was left to cool overnight. The mixture was poured into 25 mL of Milli-Q water and neutralised with a small quantity of NaOH. It was purified using dialysis tubing (12-14 kDa) Milli-Q water over several days with frequent change of water and the product poly(5-(4-vinylphenyl)-10,15,20-tris(4-sulfonatophenyl)porphyrin sodium salt) (PVTPPS) obtained by evaporating the solvent and drying in a vacuum oven at 60 °C (37 mg, 0.04 mmol, 59% yield).

In the final step PVTPPS (37 mg, 0.04 mmol) was dissolved in Milli-Q water (20 mL) and $MnCl_2$ (0.58 g, 4.61 mmol) added. This mixture was stirred at reflux for 25 h after which it was dialysed (12-14000 kDa tubing) and the solvent evaporated under vacuum, giving the desired product poly(5-(4-vinylphenyl)-10,15,20-tris(4-sulfonatophenyl)porphyrinato manganese(III) chloride sodium salt) (MnPVTPPS) (56 mg, 0.05 mmol, 100% yield). UV-Vis analysis of the compound was found to be in agreement with literature findings [1, 8, 9].

5.2.3 Electrochemical polymerisation of porphyrin/PEDOT composite

A method was developed following a literature procedure [4, 7] for electrochemical polymerisation (EP) of PEDOT:PSS in water. A reagent mixture was prepared containing 5 mM EDOT (0.71 mg/ml) and 2.5 mM PSS (by monomer mass 0.46 mg/mL) in water. The EDOT solution was prepared first in 10 mL volume, carefully sonicated and vortex stirred until completely dissolved. Approximately 2 mL were transferred to a second sample vial containing the PSS. The solution was again sonicated and mixed to ensure proper dissolution of the reagents. For the samples containing porphyrin, an amount was weighed out before and the EDOT/PSS mixture added to dissolve into it. The porphyrins MnTPPS (2.5 mg/ml, 2.25 mM) as well as MnPVTPPS (0.86 mg/mL, 0.83 mM) were added to separate EDOT/PSS mixtures. The FTO glass electrode was sonicated in acetone, rinsed with water and allowed to dry before fitting a copper cable with silver paste and epoxy resin to it. Before polymerisation, the electrode was plasma-cleaned for 15 min.

The sample was electropolymerised in EV1 (see section 2.3.8), into which the reagent mixture (~0.9 mL) was injected. A BASi miniature Ag/AgCl reference electrode was inserted. The electrodes were connected to an EDAQ466 potentiostat and cyclic voltammetry (CV) was performed on the sample at -0.4 – +1.2 V (*vs* Ag/AgCl) for 50 cycles at 50mV/s. The sample was submerged in water to wash out impurities, and then left to air dry. Samples were made in duplicate. The finished film was analysed by UV-Vis spectroscopy and electrochemistry.

5.2.4 Electrochemical testing

The electropolymerised PEDOT:PSS and porphyrin/PEDOT:PSS samples were subjected to electrochemical testing using the apparatus and methods described in sections 2.4.8 and 2.4.9. In a typical experiment the electrochemical cell was filled with Na_2SO_4 (0.1 M) that had been bubbled with N_2 gas and stirred for 1 h. The sample was inserted as the working electrode with an Ag/AgCl reference electrode and Pt mesh counter electrode also present.

Before the examination, CV was performed on the film for 20 cycles at 10 mV/sec in order to stabilise the film. LSV sweeps were then performed over the range of 0-0.7 V at a scan rate of 5 mV/sec. Voltages beyond 0.7 V (*vs* Ag/AgCl) were not studied in order to avoid irreversible oxidative damage to the film. In a typical experiment, five sweeps were done in the dark and then three sweeps with light illumination turned on. This ensured that the LSV spectrum remained constant over the course of the data recording as it was otherwise affected by charge imbalances brought on by static electricity. The last of the LSV sweeps with and without illumination were used as data.

This method was applied to all of the films investigated in this chapter. In all cases the resulting current (in µA) was converted into current density (in µA/cm^2). Where necessary, electronic noise brought about by an unknown external interference was removed from the data by subtracting a simple sine wave function.

Following the LSV measurement, each sample was tested by CA at the set potential of 0.65 V (*vs* Ag/AgCl). In a typical experiment the chosen voltage was applied to the film for 1 h without illumination to equilibrate the baseline current. The light was then switched on to measure the resulting photocurrent for 10 min and then turned off. The data shown in the results below were taken from 1 min before illumination to 1 min after the end of illumination. The data (in µA) was normalised by subtracting the baseline before illumination and the results converted to current density (in µA/cm^2).

5.3 Results and Discussion

5.3.1 Electropolymerisation of PEDOT:PSS and porphyrin/PEDOT:PSS

Electropolymerisation of PEDOT:PSS on FTO glass proceeded as described in section 5.2.3 based on literature precedent [7]. In the first run, PEDOT:PSS was synthesised. Thereafter MnTPPS porphyrin or MnPVTPPS (as co-mixtures with PSS) were added at low concentrations, comparable to those employed in the previous two chapters. Only one concentration of MnPVTPPS in PEDOT was studied due to a paucity of the MnPVTPPS.

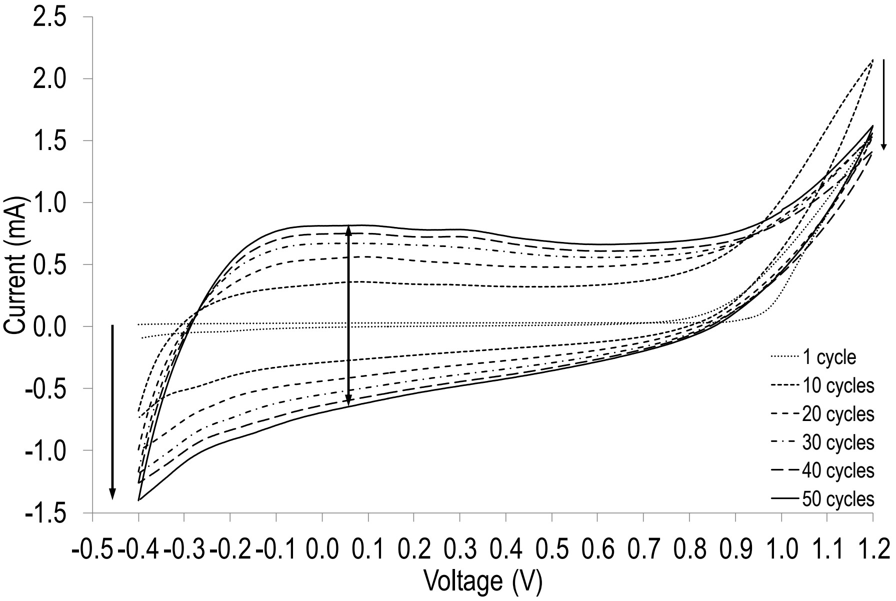

Figure 5.3 Typical CV spectrum of PEDOT:PSS electrodeposition on FTO glass.

The initial trial of PEDOT:PSS, without porphyrin, exhibited the characteristic CV spectrum of gradually increasing capacitive current, which indicated a progressive build-up of conducting polymer on the electrode (Figure 5.3). After this, the method was extended to include the porphyrins MnTPPS or MnPVTPPS (both with PSS), resulting in the samples PEDOT:PSS, MnTPPS/PEDOT:PSS and MnPVTPPS/PEDOT:PSS. The samples were now ready to be tested by electrochemistry.

The films produced by this method exhibited the now familiar deep blue colour of PEDOT:PSS as well as green colour for MnTPPS/PEDOT:PSS and (c) MnPVTPPS/PEDOT:PSS (Figure 5.4).

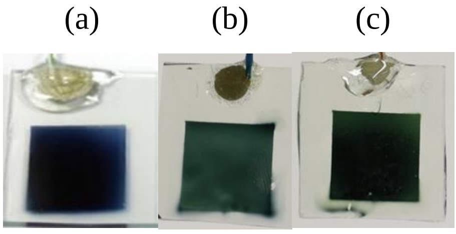

Figure 5.4 (a) PEDOT:PSS, (b) MnTPPS/PEDOT:PSS and (c) MnPVTPPS/PEDOT:PSS.

5.3.2 Photoelectrochemical testing of porphyrin-free, control PEDOT:PSS

The EP PEDOT:PSS film was tested by LSV and CA using the methods described in section 3.2.6 to ascertain the photocurrent produced under illumination.

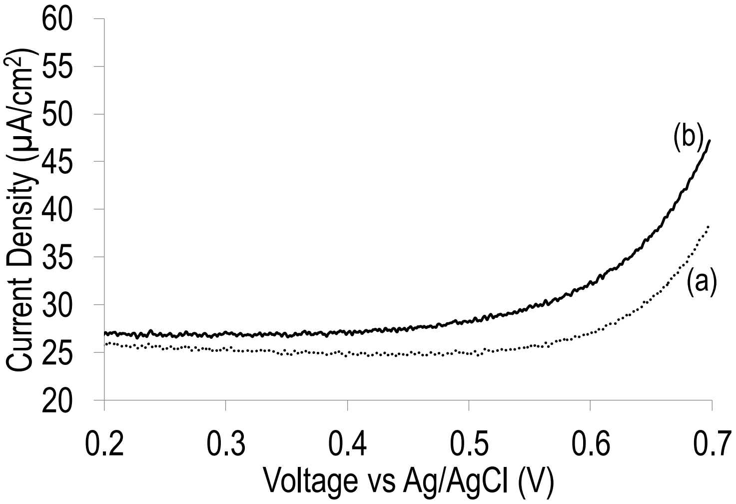

Figure 5.5 LSV spectra of PEDOT:PSS (without MnTPPS), (a) in the dark, (b) with light illumination.

The LSV spectrum of porphyrin-free PEDOT:PSS film featured a slow onset of photocurrent from ca. 0.5 V (*vs* Ag/AgCl) onwards toward more positive applied potentials. This was very similar to that observed for VPP PEDOT in Chapter 3 (see section 3.3.3). However, the overall baseline as well as the photocurrent increase was higher than that of the equivalent VPP sample. While VPP PEDOT typically displayed a photocurrent of ca. 1 µA/cm^2 at 0.65 V in LSV, EP PEDOT:PSS exhibited photocurrent densities up to as high as 8 µA/cm^2. This indicated that the EP PEDOT:PSS was more light active, even without a porphyrin species present.

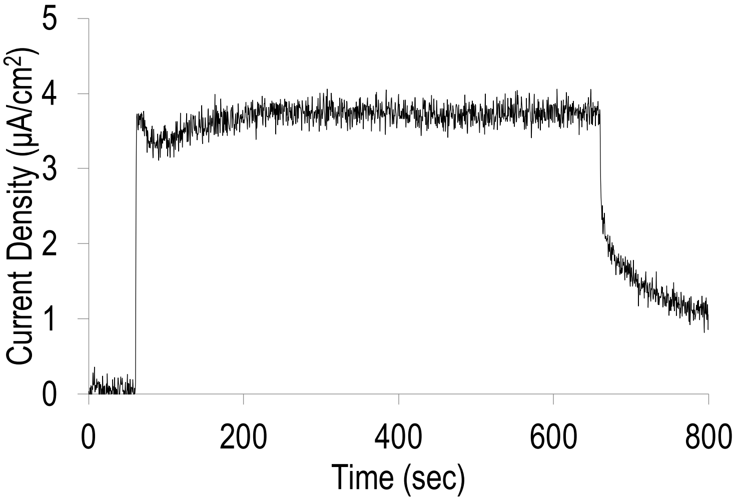

Figure 5.6 CA at 0.65 V (*vs* Ag/AgCl) of PEDOT:PSS.

The CA photocurrent density measurement of PEDOT:PSS reflected the increased photocurrents observed in the LSV experiment, reaching a level of 3.89 µA/cm^2 after 10 min of illumination at 0.65 V. This was far higher than the 0.75 µA/cm^2 measured for VPP PEDOT in Chapter 3 (see section 3.3.3).

5.3.3 Photoelectrochemical testing of control MnTPPS/PEDOT:PSS

The EP MnTPPS/PEDOT:PSS film was tested by LSV and CA following the methods described in section 3.2.6 to measure the photocurrent produced under illumination.

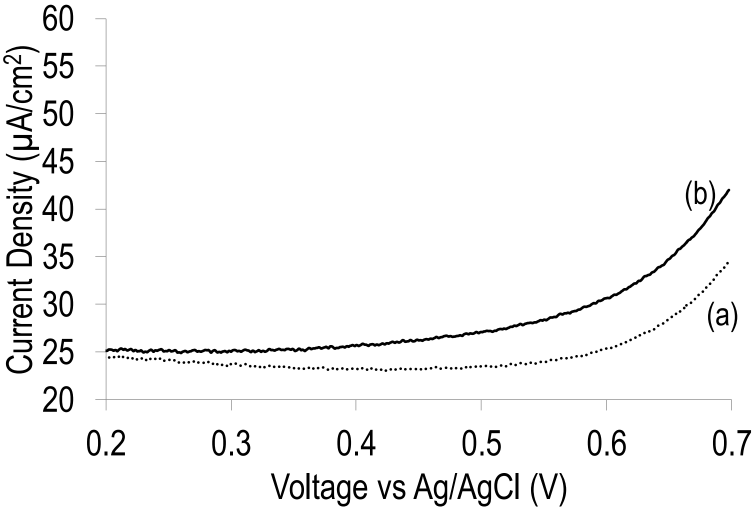

Figure 5.7 LSV spectra of MnTPPS/PEDOT:PSS, (a) in the dark, (b) with light illumination.

The LSV spectrum of MnTPPS/PEDOT:PSS was similar to that of PEDOT:PSS, also featuring an onset potential of photocurrent from ca. 0.5 V (*vs* Ag/AgCl) (Figure 5.7). This was also very similar to that of VPP MnTPPS/PEDOT in Chapter 3 (see section 3.3.4).

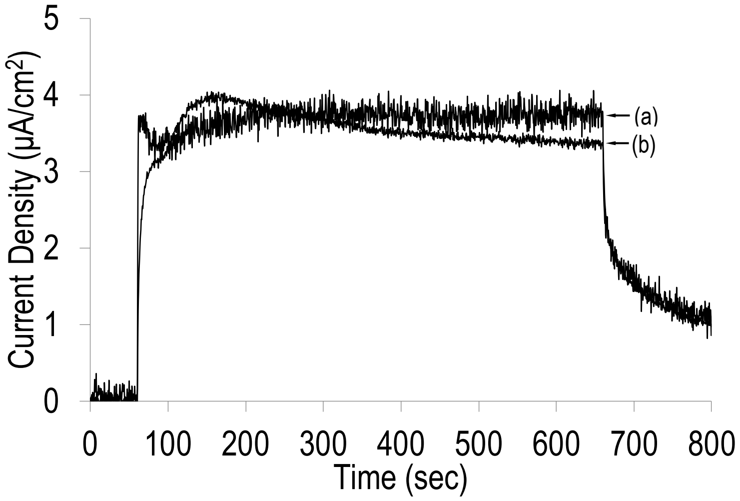

Figure 5.8 CA at 0.65 V (*vs* Ag/AgCl) of (a) PEDOT:PSS and (b) MnTPPS/PEDOT:PSS.

Sample	**Current Density at 0.65 V (µA/cm^2)**
MnTPPS/PEDOT:PSS	3.29
PEDOT:PSS	3.89

Table 5.1 Photocurrent density of MnTPPS/PEDOT:PSS at 0.65 V (*vs* Ag/AgCl).

The CA photocurrent density measurement for MnTPPS/PEDOT:PSS yielded 3.29 µA/cm^2 at 0.65 V (*vs* Ag/AgCl) (Figure 5.8), which was, in fact, marginally lower than that of PEDOT:PSS (see Table 5.1), but higher than that of the highest performing VPP MnTPPS/PEDOT (at 1.46 µA/cm^2 - see section 3.3.4).

5.3.4 Photoelectrochemical testing of MnPVTPPS/PEDOT:PSS

The EP MnPVTPPS/PEDOT:PSS film was tested by LSV and CA following the methods described in section 3.2.6 to ascertain the photocurrent produced under illumination. The LSV spectra of MnPVTPPS/PEDOT:PSS featured, in all cases studied, a photocurrent onset potential of ca. 0.5 V (*vs* Ag/AgCl) (Figure 5.9).

During the CA testing of multiple MnPVTPPS/PEDOT:PSS samples, two distinctly different photocurrent profiles were detected. The samples have been distinguished here as MnPVTPPS/PEDOT:PSS 1 and MnPVTPPS/PEDOT:PSS 2 for clarity. One set of samples (MnPVTPPS/PEDOT:PSS 1) displayed a notably larger photocurrent overall than the other set of samples (MnPVTPPS/PEDOT:PSS 2).

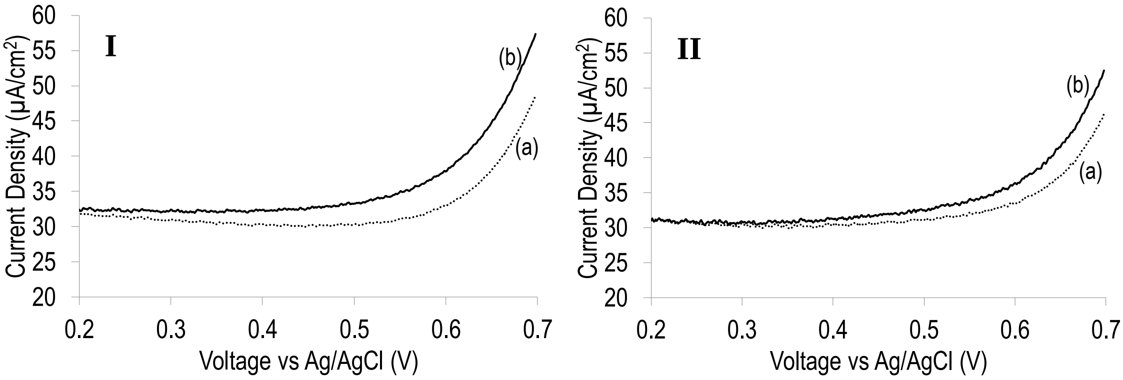

Figure 5.9 LSV spectra of (**I**) MnPVTPPS/PEDOT:PSS 1 and (**II**) MnPVTPPS/PEDOT:PSS 2, (a) in the dark, (b) with light illumination.

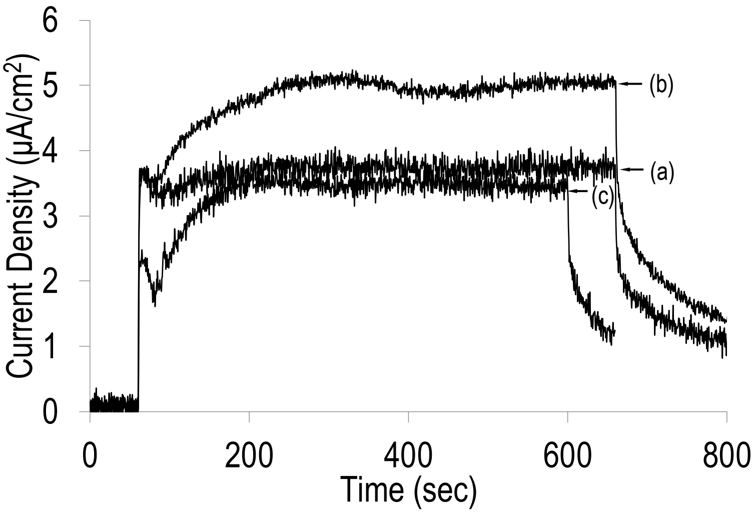

Figure 5.10 CA at 0.65 V (*vs* Ag/AgCl) of (a) PEDOT:PSS, (b) MnPVTPPS/PEDOT:PSS 1 and MnPVTPPS/PEDOT:PSS 2.

Sample	**Current Density at 0.65 V ($\mu A/cm^2$)**
MnPVTPPS/PEDOT:PSS 1	5.00
MnPVTPPS/PEDOT:PSS 2	3.39
PEDOT:PSS	3.89

Table 5.2 Photocurrent density of MnPVTPPS/PEDOT:PSS at 0.65 V (*vs* Ag/AgCl).

When tested by CA at 0.65 V (*vs* Ag/AgCl) with illumination, MnPVTPPS/PEDOT:PSS 1 displayed the highest photocurrent density measured so far in this class of material at 5.00 $\mu A/cm^2$. Interestingly, the duplicate sample MnPVTPPS/PEDOT:PSS 2 made using exactly the same method yielded only 3.39 $\mu A/cm^2$, lower than that of PEDOT:PSS (Figure 5.10, Table 5.2). Despite strenuous attempts to identify physical factors that were different in the preparative procedures for MnPVTPPS/PEDOT:PSS 1 and MnPVTPPS/PEDOT:PSS 2, no clear distinction in this respect could be determined. This phenomenon was not observed when testing the MnTPPS/PEDOT:PSS samples.

5.3.5 UV-Vis analysis of PEDOT:PSS

The EP PEDOT:PSS film was analysed using UV-Vis spectroscopy after fabrication.

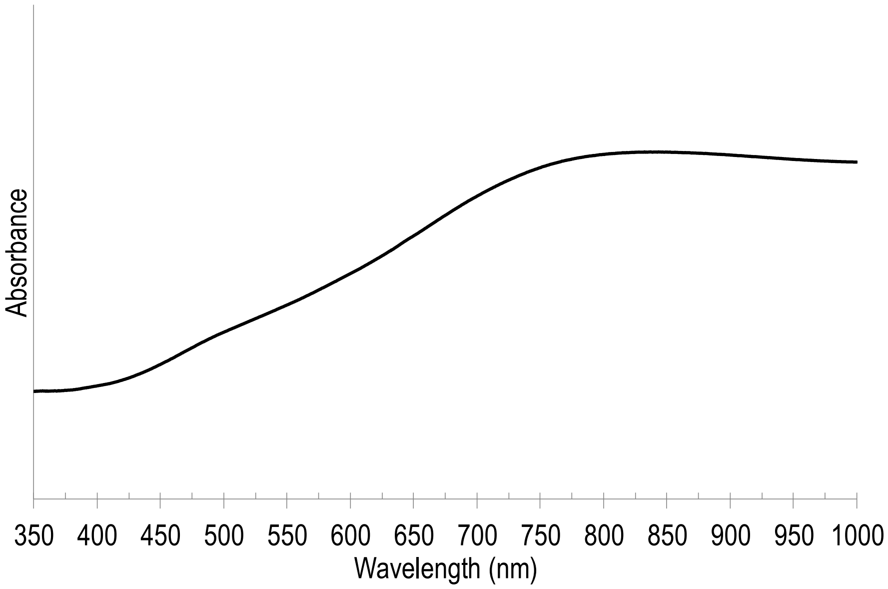

Figure 5.11 UV-Vis spectrum of PEDOT:PSS.

The EP PEDOT:PSS film exhibited the characteristic spectrum of PEDOT in oxidised form (see Figure 5.11); this had also been observed before in VPP PEDOT samples and was in agreement with the literature [7, 11].

5.3.6 UV-Vis analysis of MnTPPS/PEDOT:PSS

The electropolymerised MnTPPS/PEDOT:PSS film was analysed by UV-Vis spectroscopy.

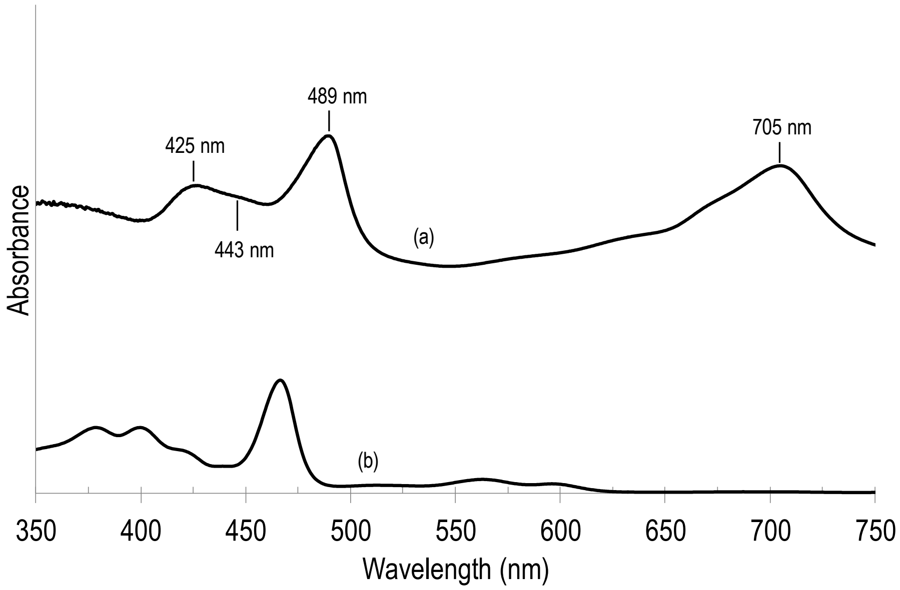

Figure 5.12 UV-Vis spectrum of (a) PEDOT:PSS:MnTPPS and (b) MnTPPS in water.

The UV-Vis spectrum of MnTPPS/PEDOT:PSS featured absorbance peaks at 425 nm, 443 nm and 489 nm (Figure 5.12). These were consistent with the findings from the studies of the low-loading VPP MnTPPS/PEDOT described in Chapter 3, with the exception that the 489 nm absorbance peak fell at ca. 475 nm in that case. The absorbance peaks likely corresponded to the Soret Band of the porphyrin in its initial Mn(III)TPPS form (489 nm) as well as the free H_2TPPS (425 nm) and a very small shoulder (443 nm) likely corresponding to the protonated species H_4TPP^{2+} according to literature [12]. Compared to the spectrum of MnTPPS in water, which featured the Mn(III) Soret Band at 466 nm, the absorbance peak for the MnTPPS/PEDOT:PSS was significantly red shifted to 489 nm, whereas the Soret band of the H_4TPP^{2+} from literature [12] aligned perfectly with the small shoulder at 443 nm. The pronounced peak at 705 nm could only be due to the Q-Band of H_4TPPS^{2+} [12], also significantly red shifted.

Surprisingly some demetallation, with accompanying protonation of the resulting free porphyrin, appears to have also occurred even in this system under electropolymerisation conditions. That is, the demetallation reaction observed at low loading levels in the previous chapter using vapour phase polymerisation, appeared to also occur when electropolymerisation was employed, albeit to a lesser extent. Clearly, the demetallation process was independent of the method of polymerisation.

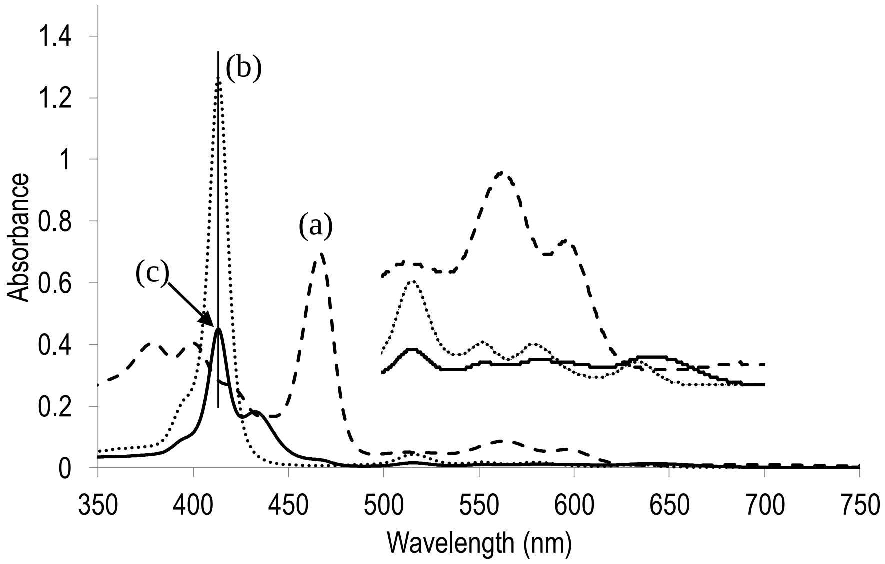

Figure 5.13 UV-Vis spectra in water of: (a) MnTPPS, (b) TPPS, and (c) the water rinse from MnTPPS/PEDOT:PSS after fabrication.

An analysis was conducted on the water rinsed off the MnTPPS/PEDOT:PSS film after electrodeposition (as had been done in Chapter 4). The UV-Vis spectrum of that wash was compared to the spectra of MnTPPS and TPPS in water solution (Figure 5.13). The comparison showed that the porphyrin species washed out of the film after polymerisation was indeed the free TPPS with a Soret Band peak at ca. 410 nm (Figure 5.13 (b) & (c)), rather than MnTPPS (Figure 5.13 (a) & (c)). A small portion of what was likely protonated TPPS was also identified in a band at ca. 440 nm along with an amplified Q-band peak at ca. 650 nm. However it should be noted that these washings represented only the loosely bound species that adhered to the film in excess after polymerisation, and were not characteristic of the entirety of the porphyrins in the sample. The previous UV-Vis spectrum of the MnTPPS/PEDOT:PSS film (Figure 5.12) had demonstrated unequivocally that large proportions of MnTPPS were still present in the film as evidenced by the significant absorbance peak corresponding to Mn(III)TPPS at 489 nm.

5.3.7 UV-Vis analysis of MnPVTPPS/PEDOT:PSS 1 and MnPVTPPS/PEDOT:PSS 2

The samples containing the polymeric porphyrin MnPVTPPS was of great interest as one form of them displayed the highest photocurrent so far recorded in this study for this type of material. As mentioned previously, despite being made by an identical procedure using the same sample of MnPVTPPS, two types of composites were observed – MnPVTPPS/PEDOT:PSS 1 and MnPVTPPS/PEDOT:PSS 2. The former yielded high photocurrents, while the latter yielded photocurrents that were identical to the control PEDOT:PSS. Samples were usually made in duplicate and, after each had been identified as belonging to one of the above groups, analysed separately for consistency. To try to explain the difference in photocurrent performance for MnPVTPPS/PEDOT:PSS 1 and MnPVTPPS/PEDOT:PSS 2, UV-Vis absorbance analysis was carried out in order to establish the state of the porphyrin.

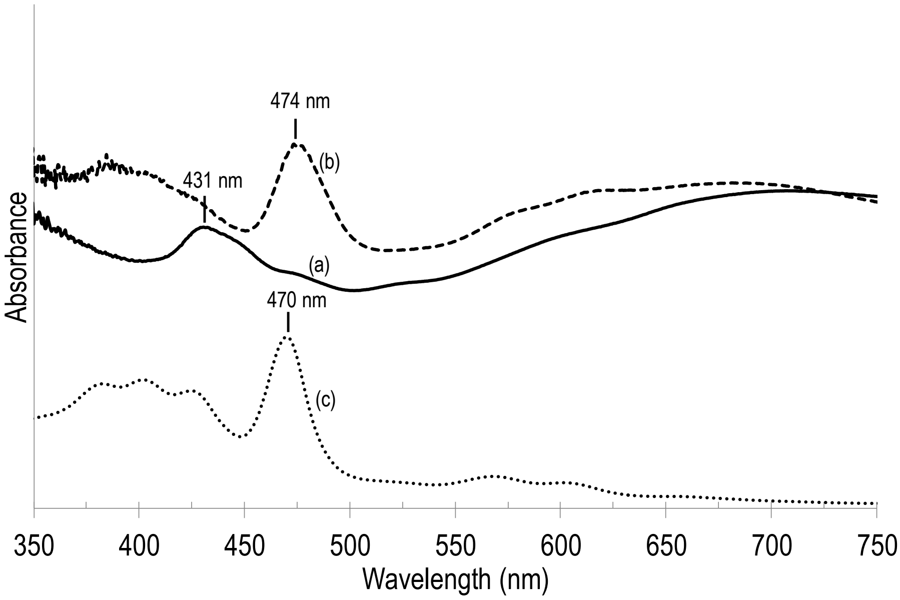

Figure 5.14 Representative UV-Vis spectra of (a) MnPVTPPS/PEDOT:PSS 1, (b) MnPVTPPS/PEDOT:PSS 1 and (c) MnPVTPPS in water.

The UV-Vis spectra of MnPVTPPS/PEDOT:PSS 1 and MnPVTPPS/PEDOT:PSS 2 were compared to that of MnPVTPPS in water solution (Figure 5.14). The high performing material, MnPVTPPS/PEDOT:PSS 1, typically displayed a dominant absorbance peak at 431 nm with a small shoulder at 444 nm and a minor peak at 474 nm. These could be attributed to the free base porphyrin H_2PVTPPS (431 nm), its acidified form (444 nm), and Mn(III)PVTPPS (474 nm) based on the similar Soret Bands observed in the H_2TPPS-H_4TPPS system. As can be seen in Figure 5.14(a), the higher photocurrent of MnPVTPPS/PEDOT:PSS 1 appears to be associated with demetallated porphyrins and a Mn-free coating.

By contrast, the low performing sample, MnPVTPPS/PEDOT:PSS 2, exhibited only one clear absorbance peak in the Soret Band region, at 474 nm. This indicated that the porphyrin in that sample had not been converted to the free porphyrin form. That is, as can be seen in Figure 5.14(b), the lower photocurrent of MnPVTPPS/PEDOT:PSS 2 appears to be associated with a predominance of metallated porphyrins and the presence of Mn in the coating. The fact that the photocurrent of MnPVTPPS/PEDOT:PSS 2 was the same or lower than that of PEDOT:PSS suggests that the observed photocurrent may have been due to the PEDOT:PSS alone, with the porphyrin in MnPVTPPS/PEDOT:PSS 2 being catalytically inactive.

5.4 Conclusions

The photocurrent density measured for MnPVTTPS/PEDOT:PSS was the highest so far recorded for porphyrin/PEDOT systems in this study. At 0.65 V (*vs* Ag/AgCl) the photocurrent density for MnPVTPPS/PEDOT:PSS was 5.00 μA/cm^2 compared to the highest reading of MnTPP/PEDOT at 2.91 μA/cm^2 at the same voltage (in chapter 3). The samples were examined by UV-Vis and found to conform with the results from chapter 4, suggesting that demetallation still occurred in this method of film fabrication.

The phenomenon of demetallation of porphyrins at low concentrations and its connection to unusually high photocurrents was previously noted in the VPP PEDOT films studied in chapter 4. Demetallation was thought, in that case, to be a result of the specific conditions of the vapour phase polymerisation process and the use of low loading levels of porphyrin. However, the above work confirms that it occurs even in electropolymerised composites. Moreover, the phenomenon of smaller photocurrents associated with the presence of the Mn(III) species was also observed in the MnPVTPPS/PEDOT:PSS.

What makes these results remarkable is that the overall concentration of porphyrin present in the polymer coatings was maintained constant during fabrication. That is, whereas demetallation was observed to be dependent on the loading level in MnTPP/PEDOT (with low loading levels leading to demetallation and higher loading levels leading to Mn retention), in the MnPVTPPS/PEDOT:PSS coatings there seems to have been two, concentration-independent pathways, one of which led, almost exclusively, to demetallation and the other to Mn retention almost exclusively. The trigger that led to one pathway over the other remains unclear. What was clear however was that the amount of photocurrent depended on whether the porphyrin in the sample was in its Mn porphyrin or free base form. This further suggests that the origin of the photocurrent in this system was not from the interaction of Mn ions with water but due to a different, yet unconfirmed process.

5.5 References

1. Sumi, K., M. Kimura, and I. Nakamura, Journal of Polymer Science Part A: Polymer Chemistry, 1994. **32**(7): p. 1243-1254.
2. Andreas Elschner, S.K., Wilfried Lövenich, Udo Merker, Knud Reuter, *PEDOT Principles and Applications of an Intrinsically Conductive Polymer*2011, Boca Raton: CRC Press.
3. Groenendaal, L., et al., Advanced Materials, 2000. **12**(7): p. 481-494.
4. Groenendaal, L., et al., Advanced Materials, 2003. **15**(11): p. 855-879.
5. Jonas, F. and J.T. Morrison, Synthetic Metals, 1997. **85**(1–3): p. 1397-1398.
6. Lerch, K., F. Jonas, and M. Linke, J. Chim. Phys., 1998. **95**(6): p. 1506-1509.

7. Asami, R., M. Atobe, and T. Fuchigami, Journal of the American Chemical Society, 2005. **127**(38): p. 13160-13161.

8. Kajiwara, A., et al., Polym J, 1994. **26**(2): p. 215-223.

9. Pomogailo, A.D., V.F. Razumov, and I.S. Voloshanovskii, Journal of Porphyrins and Phthalocyanines, 2000. **4**(1): p. 45-64.

10. Adler, A.D., et al., The Journal of Organic Chemistry, 1967. **32**(2): p. 476-476.

11. Winther-Jensen, B. and K. West, Macromolecules, 2004. **37**(12): p. 4538-4543.

12. Jimenez, H.R., M. Julve, and J. Faus, Journal of the Chemical Society, Dalton Transactions, 1991(8): p. 1945-1949.

6 Manganese oxide / graphene composites

6.1 Introduction and aims

In nature, catalytic water oxidation is facilitated by a Mn cluster inside the Oxygen Evolving Centre (OEC) of Photosystem II (PSII). This Mn cluster consists of a $CaMn_4O_4$-ligand assembly connected to the surrounding protein scaffold, which facilitates light absorbance and charge transfer [1, 2]. In mechanistic studies, the role of the Ca ion in the PSII-OEC was elucidated by Pace and Stranger as a critical component for directing water molecules toward the opening and closing face of the Mn cluster, leading to the highly efficient oxidation of water [3-8]. Mimicking this structure has been the subject of research for some time, resulting in the development of a class of compounds called cubanes [9]. These compounds mimic the cube-like structure of the OEC using crystalline assemblies based on Mn [10, 11], Co [12-18], and W [19]. What had not been explored in such detail was the extent of which the catalytic action could be enhanced by mimicking the role of the surrounding matrix within the PSII.

In this chapter, the incorporation of Ca into synthetic Mn_xO_y clusters was studied in an attempt to mimic the structure of the OEC. The second area of investigation was to mimic the role of the matrix surrounding the OEC, in particular the redox-active tyrosine Y_z [9, 20]. Both of these aims were addressed using the same combinatorial approach as described the previous chapters, that is, by creating a composite material where statistically favoured local assembly.

To this end, the organic conducting material graphene was selected as an electrode substrate, applied in a similar combinatorial fashion to PEDOT in previous chapters.

Graphene and graphene oxide have previously been explored as a carrier substrate for inorganic water splitting catalysts and related species [21], such as TiO_2 [22-28] and CdS [29, 30]. Therefore, graphene was selected because of its stability at electrochemical potentials relevant to water oxidation under dark (non-illuminated) conditions [31, 32]. In the current work, a novel, liquid crystalline form of graphene oxide (LCGO) was chosen as it offered a more consistent and larger sheet size (of ~5 µm), as well as a capacity to form reduced graphene oxide (RLCGO) [33-36]. The carboxylic functional groups on the surface of LCGO may further serve as a mimic of the same functional groups present on the co-factors of the OEC in order to facilitate efficient electron exchange between the catalyst and the substrate.

In this chapter a bio-inspired route to replicating the PSII-OEC was explored through experimental synthesis of known Mn_xO_y catalytic species and combination with liquid crystalline graphene / graphene oxide. An electrodeposition technique for synthesis of the manganese oxide, birnessite [37], was chosen as it allowed for in situ formation of the catalytic species on the graphene substrate. This method was found to be more likely to facilitate interaction between the residual surface functional groups on graphene during the formation of the Mn_xO_y. A series of iterative experiments were conducted to examine the effect of Ca cations addition into the birnessite system. These involved either: (i) attempted direct incorporation during synthesis of the Mn_xO_y species and (ii) by addition to the substrate in a more indirect, combinatorial route, such as modifying the substrate with Ca ions beforehand. The central aim was to recreate the conditions of the OEC in a composite, to thereby maximise overall catalytic performance. To this end, a preliminary screening study was conducted in which different combinations of substrates and catalytic species were tested for their practical potential. The higher performing variations were noted for future studies and the less performing types disregarded. The methods were guided by the work and findings of Prof. Rob Stranger and Prof. Ron Pace of the Australian National University (described in detail in Chapter 1), with whom this chapter was done in close collaboration.

6.2 Experimental

6.2.1 Preparation of substrates

6.2.1.1 FTO and Pt-coated FTO glass electrodes

FTO glass was cut into ~2 x 3 cm rectangles, cleaned by sonication in acetone for 20 min, rinsed with milli-Q water and then dried with pressurised air. A cladded copper wire was stripped at both ends and the oxide layer scratched off with a scalpel. The bare wire was attached to the FTO with conductive silver paint and epoxy glue. The resulting substrates were used for electrodeposition of Mn_xO_y films, as well as control samples for electrochemical analysis. Prior to deposition, the glass was cleaned with plasma treatment for 10 min and used immediately.

Platinum was sputter coated to a thickness of 100 nm on FTO glass that was cleaned in the same way, and a cable was subsequently attached. The resulting Pt-coated substrate was used as a benchmark for water splitting catalysis (for which Pt is considered an industry-standard), against which experimental samples were compared.

6.2.1.2 Spray-coating of graphene films

Graphene oxide (GO) was synthesised following the modified Hummer’s method [38]. GO was dispersed in Milli-Q water (2.2% wt) and used as is. Reduced graphene oxide (RGO) in Milli-Q water dispersion (0.05% wt) was obtained by chemically reducing graphene oxide with hydrazine and ammonia solution [35]. Both GO and RGO materials were synthesised and supplied by Dr Syed Ashraf from the Wollongong Node of the Australian National Fabrication Facility, and used as is.

A GO dispersion (0.86 g; 2.2 wt% in water) was diluted in Milli-Q water (50 mL) by gentle sonication and vortex stirring. The mixture was then sprayed onto 5 x 10 cm FTO glass (cleaned by sonication in acetone for 20 min then plasma treated for 10 min) with a Sonotek spray coater. The glass was placed on a hotplate heated to 140 °C and the dispersion sprayed on at a flow rate of 0.25 mL/min for 100 or 50 cycles in a raster pattern. Afterwards the glass was kept at 140 °C for 1 h to fully dry and anneal the film to the substrate. The thickness of the two spray-coated films was measured with a Dektak profilometer and found to be 138 nm for the sample sprayed for 100 cycles and 69 nm for the sample sprayed for 50 cycles

6.2.1.3 Reduced liquid crystal graphene oxide (RLCGO)

Liquid crystalline graphene oxide (LCGO) dispersion in water (11 mg/mL) was prepared following an established literature method [33-36]. LCGO (10 mL, 11 mg/mL) was transferred to a small sample bottle and hypophosphorous acid (1 mL, 50% wt) added as the reducing agent. The reagents were mixed using a vortex mixer with subsequent stirring using a magnetic stirrer for 30 min. The mixture was then subjected to bath sonication to remove bubbles of trapped air in the viscous liquid. It was critical to achieve a homogenous mixture without trapped air bubbles for the subsequent casting step.

The mixture was then coated on a Multapex 75 µm PET sheet of 12 x 30 cm in size with a PK K Control Coater doctor blade instrument at a gauge height of 0.6 mm. The film was left in an oven at 80 °C overnight in air to reduce the graphene oxide to graphene. . The resulting reduced liquid crystalline graphene oxide film on PET (RLCGO-PET) was then submerged in Milli-Q water to wash out all excess reagents and dried in air. Pieces of roughly 2.5 x 2 cm were cut from this film and a cladded copper wire attached with silver paint and epoxy glue.

6.2.1.4 Post-reduction treatment of reduced liquid crystal graphene oxide film with Ca (RLCGO+Ca-PET)

In one experiment, strips of RLCGO-PET were treated with a $CaCl_2$ solution (1 M) in an attempt to bind calcium ions to the surface of the film after reduction and casting. The resulting film is termed here: RLCGO+Ca-PET.

RLCGO strips were soaked in $CaCl_2$ solution (1 M) overnight and dipped in water to remove the excess solution. The strips were then dried in air overnight and fabricated into electrodes by attaching copper wire with conductive silver paint and epoxy resin.

6.2.1.5 Ca-containing reduced liquid crystal graphene oxide film (CaRLCGO-FTO / CaRLCGO-PET)

In an alternative procedure, the LCGO was modified by the addition of $CaCl_2$, to modify the material with Ca^{2+} ions, as established in a literature procedure [39]. The LCGO was then reduced and cast in the same fashion as described previously.

LCGO (10 mL, 11 mg/mL) was transferred to a sample bottle to which 0.2 mL of $CaCl_2$ (1 M) was added. This noticeably increased the viscosity of the dispersion. Milli-Q water (5 mL) was added to dilute the mixture to a less viscous state. The mixture was then gently stirred and hypophosphorous acid (0.5 mL) added. Once the reducing agent was added, the mixtures were gently mixed for a period of time (30 min). Challenges presented themselves by mixing the sample too vigorously which introduced bubbles in the liquid. This was to be avoided as these bubbles were difficult to eliminate due to the viscosity of the liquid, and would result in irregularities in the deposited films. The sample was sonicated in brief intervals to bring bubbles to the surface.

The mixture was then coated on a Multapex 75 µm PET sheet of 12 x 30 cm size with a PK K Control Coater doctor blade instrument at a gauge height of 0.6 mm. The film was left in an oven at 80 °C overnight in air to reduce the graphene oxide. The resulting film was denoted Ca-modified reduced liquid crystal graphene oxide on PET (CaRLCGO-PET). It was submerged in Milli-Q water to wash out all excess reagents and dried in air. Pieces of 2.5 x 2.0 cm were cut from this film and a cladded copper wire attached with silver paste and epoxy glue. The edges of the film were sealed with clear nail polish to avoid detachment when exposed to water.

The coating was also done on FTO glass. FTO glass of dimensions ca. 4.5x7.5 cm was sonicated in acetone and then in water (20 min each), dried and treated with plasma for 10 min before coating. Films were coated onto the glass using the same blade coater at a 0.1 mm height gauge setting. The wet film was left to dry initially over 8 h before being heated to 80 °C in an oven in air overnight. After that it was submerged in water for 5 min to wash out the excess $CaCl_2$ and reducing agent. The film was found to adhere to the FTO glass substrate when in contact with water. It was then cut into pieces of 1.5 x 1.3 cm and a copper wire attached to the edge with silver paste and epoxy resin. Nail polish was used to seal the edges to prevent water penetrating underneath the film in later experiments. The resulting films were denoted Ca-modified reduced liquid crystal graphene oxide on FTO (CaRLCGO-FTO).

6.2.2 Electrodeposition of Mn_xO_y films

6.2.2.1 Basic electrodeposition procedure

Electrodeposition of Mn_xO_y films on substrates was carried out using a literature procedure [37]. Aqueous $NaNO_3$ solution (20 mL, 1 M) was prepared, to which $Mn(AcO)_2$ was added (10 mM). The solution was observed to darken and precipitate out of solution over the course of 1 day, due to MnO_2 formation. It was therefore freshly prepared for every experiment and used within 2 h.

The material was deposited onto the working electrode by applying a galvanostatic current density of 200 µA/cm^2 for a set deposition time using the electrodeposition vessels specified previously (see section 2.3.8). After deposition, the substrate containing the Mn_xO_y film was dipped in Milli-Q water to rinse off remaining reagents and gently dried with N_2 gas. The sample was then heat-treated at 90 °C for 30 mins in air on a hotplate and stored in a desiccator afterwards.

6.2.2.2 Electrodeposition on FTO glass substrates

The procedure was modified in an attempt to include Ca into the Mn_xO_y film. Aqueous $NaNO_3$ solution (20 mL, 1 M) was prepared, from which two separate solutions with 10 mM $Mn(AcO)_2$ and $Ca(AcO)_2$ were made. From this, an series of coating solutions were prepared, each containing a mixture of the two reagents ranging from 100% $Mn(AcO)_2$: 0% $Ca(AcO)_2H_2O$ to 0% $Mn(AcO)_2$: 100% $Ca(AcO)_2$ in steps of 10%.

Each mixture was used as the electrolyte during electrodeposition on ~2 x 3 cm rectangular pieces of FTO glass prepared as electrodes as described in section 6.2.1.1. The substrate was affixed to EV1 (see section 2.3.8) and the coating solution injected to fill the cavity. This electrodeposition vessel was found to facilitate uniformly sized films on the electrodes, thereby ensuring every sample had the same geometric surface area (2.25 cm^2). A galvanostatic current density of 200 $\mu A/cm^2$ was applied for 10 min for each coating solution. After deposition the sample was dipped in Milli-Q water to rinse out reagents and gently dried with N_2 gas. The sample was then heat treated at 90 °C for 30 mins in air on a hotplate and stored in a desiccator.

Control experiments were done with the exclusion of $Ca(AcO)_2$ and extended to deposition over a range of time periods (1 min, 2.5 min, 5 min, 10 min and 15 min) on FTO glass. An overview of Mn_xO_y film samples created with this method is shown in Table 6.1 below.

Sample Type	Substrate	Deposition Parameters	Sample Name
Experimental coating	FTO glass	$Mn(AcO)_2$ / $Ca(AcO)_2$ 0:100% - 100:0% in 10% increments 10 min deposition time	$CaMn_xO_y$-FTO Mn/Ca ratio specified in text
Control coating	FTO glass	$Mn(AcO)_2$ 1 min, 2.5 min, 5 min, 10 min, 15 min deposition time	Mn_xO_y-FTO X min

Table 6.1 Mn_xO_y films electro-coated on FTO glass

6.2.2.3 Electrodeposition on graphene substrates

The electrodeposition experiment was extended to the graphene substrates prepared using the parameters described in section 6.2.2.1 (for sprayed GO and RGO, RLCGO-PET, RLCGO+Ca-PET, CaRLCGO-PET and CaRLCGO-FTO).

Spray-coated graphene substrates were electrocoated in EV1 and the other graphene substrates were electrocoated in EV2 (see section 2.3.8). The design of EV2 allowed for the working electrode sample to be free standing in solution. This eliminated the possibility that the graphene film would be damaged by contact with other components. The electrocoating thereafter followed the standard method outlined in 6.2.2.1. The samples created with this method are listed in

Table 6.2 below.

Substrate	**Deposition time**	**Sample Name**
GO-FTO 138 nm	10 min	Mn_xO_y-GO-FTO 138 nm
GO-FTO 69 nm	10 min	Mn_xO_y-GO-FTO 69 nm
RLCGO-PET	2.5, 5, 10 min	Mn_xO_y-RLCGO-PET X min
RLCGO+Ca-PET	2.5, 10 min	Mn_xO_y-RLCGO+Ca-PET X min
CaRLCGO-PET	2.5, 5, 10 min	Mn_xO_y-CaRLCGO-PET X min
CaRLCGO-FTO	2.5, 5, 10 min	Mn_xO_y-CaRLCGO-FTO X min

Table 6.2 Mn_xO_y films electrodeposited on graphene substrates

6.2.3 Electrochemical testing of the samples

All samples in this chapter were inserted into the box cell electrochemical apparatus described in section 2.4.8. The cell was filled with aqueous Na_2SO_4 electrolyte (0.1 M), which was stirred and bubbled with Ar gas for 1 h prior to testing. The full cell consisted of the sample as the working electrode, a Pt mesh counter electrode and an Ag/AgCl reference electrode. Unless stated otherwise, the voltage referred to in subsequent sections is against the Ag/AgCl reference electrode.

The samples were tested using the method described in 2.4.9, but without illumination. Specifically, each sample was subjected to three LSV scans at 5 mV/sec over the voltage range of 0.0 – 1.6 V (*vs* Ag/AgCl), without illumination. The scan shown in the data presented below was the last scan of the three for each sample. Where shown, the LSV data was normalised for each sample and converted to current density by dividing by the area of each sample, which was estimated by measuring the dimensions of the sample with a ruler (typically 2 – 3 cm^2). The samples exhibiting high current density were then tested using a CA procedure, as described in section 2.4.9.

6.3 Results and discussion

6.3.1 Mn_xO_y films on different substrates

The Mn_xO_y material studied in this chapter was electrodeposited following the method described in section 6.2.2 on the previously prepared substrates, as explained in section 6.2.1. This yielded a variety of graphene substrates with Mn_xO_y electrodeposited upon them for varying time periods (
Table 6.1,
Table 6.2).

In the first set of experiments, incrementally varying mixtures of $Mn(AcO)_2$ / $Ca(AcO)_2$ were used as aqueous coating solutions to deposit films on FTO glass for 10 min, in order to determine whether Ca could be included in electrodeposited Mn_xO_y-FTO. In a following control experiment, Mn_xO_y was deposited on FTO glass for 1 min, 2.5 min, 5 min, 10 min and 15 min. This formed the initial testing of the Mn_xO_y deposition method on a regular conducting substrate (
Table 6.1).

In the following experiments, the Mn_xO_y was deposited using $Mn(AcO)_2$ on the graphene substrates explained in section 6.2.1. This included spray-coated GO on FTO glass at 138 and 69 nm thickness (GO-FTO 138 and GO-FTO 69), reduced liquid crystalline graphene oxide on PET (RLCGO-PET), reduced liquid crystalline graphene oxide on PET soaked in $CaCl_2$ (RLCGO+Ca-PET), Ca-modified reduced liquid crystalline graphene oxide on PET (CaRLCGO-PET) and FTO (CaRLCGO-FTO) (see Table 6.2).

6.3.2 Electrochemical testing of control substrates

The control electrodes in section 6.2.1 were tested electrochemically to establish the baseline water splitting catalytic performance for each. These included: (i) the FTO glass substrates, (ii) spray-coated GO on FTO glass at 138 nm and 69 nm thickness (GO-FTO 138 nm and GO-FTO 69 nm), (iii) reduced liquid crystalline graphene oxide on PET (RLCGO-PET), (iv) reduced liquid crystalline graphene oxide on PET soaked in $CaCl_2$ (RLCGO+Ca-PET), (v) Ca-modified reduced liquid crystalline graphene oxide on PET (CaRLCGO-PET) and (vi) FTO (CaRLCGO-FTO). The Pt-FTO film was also tested as a catalytic benchmark to compare to experimental samples.

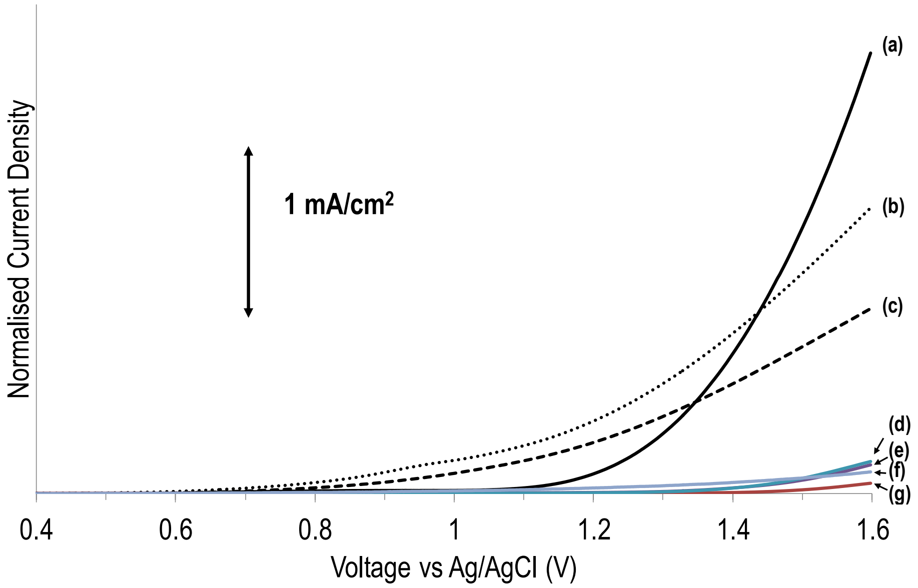

Figure 6.1 Normalised LSV spectra of control substrates: (a) Pt-FTO, (b) RLCGO-PET, (c) CaRLCGO-PET, (d) GO-FTO 69 nm, (e) GO-FTO 138 nm, (f) CaRLCGO-FTO, (g) uncoated FTO.

The Pt-FTO control electrode produced the highest overall current response with very clear formation of gas bubbles on the electrode when subjected to voltages above 1.2 V; a clear onset of current was observed from 1.1 V (Figure 6.1). A current density of 2.52 mA/cm^2 at 1.6 V (*vs* Ag/AgCl) was observed for the Pt-FTO sample, and subsequently the data of this electrode served as a benchmark against which to compare experimental catalysts.

The control substrates, that is, the substrates that were eventually used to deposit catalyst material on, overall showed a very negligible electrochemical response (<0.1 mA/cm^2) at voltages that were relevant for water oxidation above 1.1 V (*vs* Ag/AgCl) (Figure 6.1). The substrates RLCGO-PET and CaRLCGO-PET however featured significant electrochemical current which gradually increased from 0.8 V onwards. This was likely due to formation of electroactive oxygen species on the surface, which has been reported previously in literature [31, 32].

In the following oxidative electrochemical tests, the LSV current density data of the relevant substrate was included in each diagram for ready comparison between the experimental sample and the substrate. This allowed for determination as to whether the Mn_xO_y deposited on the substrate had influenced oxidative current.

6.3.3 Electrochemical testing of Mn_xO_y-FTO

An array of samples of electrodeposited Mn_xO_y-FTO were prepared from coating solutions with varying ratios of $Mn(AcO)_2$ to $Ca(AcO)_2$ (see section 6.2.2.2). In this experiment the possibility of inclusion by electrocoating, of Ca into a deposited Mn_xO_y film was examined, and whether this affected the water oxidation performance of the catalytic material.

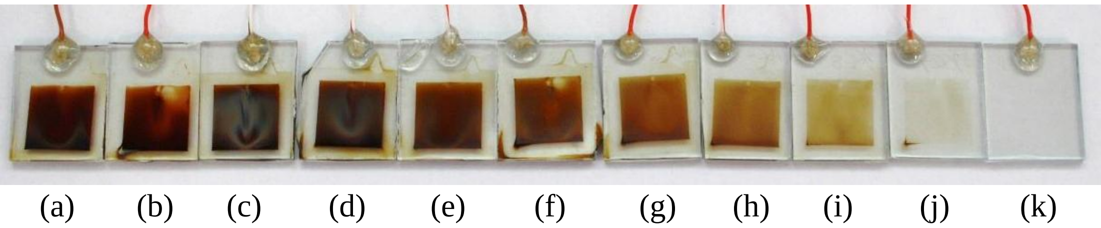

Figure 6.2 Electrodeposited films in order of decreasing Mn/Ca ratio on FTO: (a) 1/0 mL Mn/Ca, (b) 0.9/0.1 mL Mn/Ca, (c) 0.8/0.2 mL Mn/Ca, (d) 0.7/0.3 Mn/Ca, (e) 0.6/0.4 mL Mn/Ca, (f) 0.5/0.5 mL Mn/Ca, (g) 0.4/0.6 mL Mn/Ca, (h) 0.3/0.7 mL Mn/Ca, (i) 0.2/0.8 mL Mn/Ca, (j) 0.1/0.9 mL Mn/Ca, (k) 0/1 mL Mn/Ca.

The electrodeposition resulted in brown-orange films on the FTO glass surface. As the concentration of $Mn(AcO)_2$ decreased and $Ca(AcO)_2$ increased, the films gradually diminished in colour towards almost clear FTO glass at the 100% $Ca(AcO)_2$ setting (see Figure 6.2).

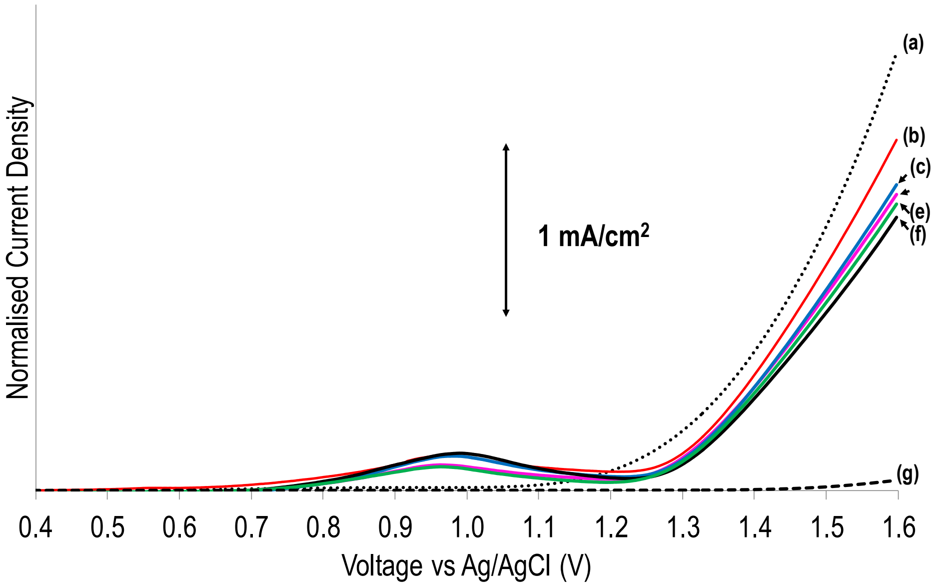

Figure 6.3 Normalised, dark, LSV spectra of electrodeposited films with varying Mn/Ca ratio on FTO: (a) Pt-FTO, (b) 1/0 mL Mn/Ca, (c) 0.8/0.2 mL Mn/Ca, (d) 0.9/0.1 Mn/Ca, (e) 0.6/0.4 mL Mn/Ca, (f) 0.7/0.3 mL Mn/Ca, (g) uncoated FTO.

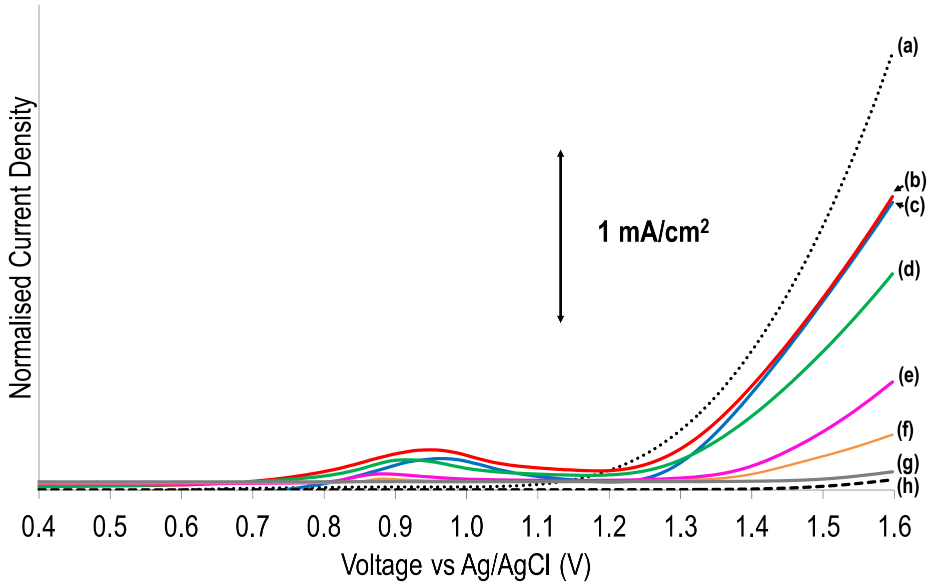

Figure 6.4 Normalised, dark, LSV spectra of Mn_xO_y-FTO with varying Mn/Ca ratio on FTO: (a) Pt-FTO, (b) 0.4/0.6 mL Mn/Ca, (c) 0.5/0.5 mL Mn/Ca, (d) 0.3/0.7 mL Mn/Ca, (e) 0.2/0.8 mL Mn/Ca, (f) 0.1/0.9 mL Mn/Ca, (g) 0/1 mL Mn/Ca, (h) uncoated FTO.

The samples were then each tested by LSV (in the dark, without light illumination), allowing for direct comparison of their electrocatalytic performance (Figure 6.3 and Figure 6.4). All Mn-containing samples displayed similar overall electrochemical behaviour, differing only in their current density. The sample made from the solution containing $Mn(AcO)_2$ only displayed the highest current density overall in the water oxidation region, with an onset potential at 1.25 V, rivalling that of the Pt benchmark. The maximum current density measured was 2.02 mA/cm^2 at 1.6 V. The other samples showed incrementally decreasing current densities with increasing concentration of $Ca(AcO)_2$ used in the reaction mixture, ultimately falling to as low as that of the FTO substrate by itself. The current peak observed in the region 0.8 – 1.1 V is likely due to partial oxidation of water and adsorbance of oxygen species on the substrate. This demonstrated that the addition of $Ca(AcO)_2$ did not lead to beneficial effects on the water oxidation performance of this catalyst. Therefore, inclusion of Ca by this method was not studied further in later experiments.

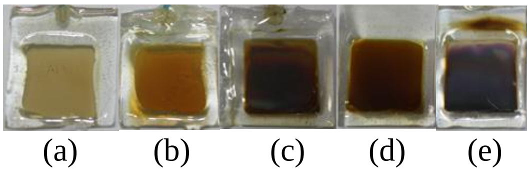

Figure 6.5 Photographs of Mn_xO_y-FTO electrodeposited for (a) 1 min, (b) 2.5 min, (c) 5 min, (d) 10 min, (e) 15 min.

The experiment was then extended to test the effect of varying deposition time on the resulting water oxidation performance. Samples of Mn_xO_y on FTO were prepared with deposition times of 1 min, 2.5 min, 5 min, 10 min and 15 min (see Figure 6.5). An increasing intensity in colour was observed with increasing deposition time, likely due to increasing thickness of the film.

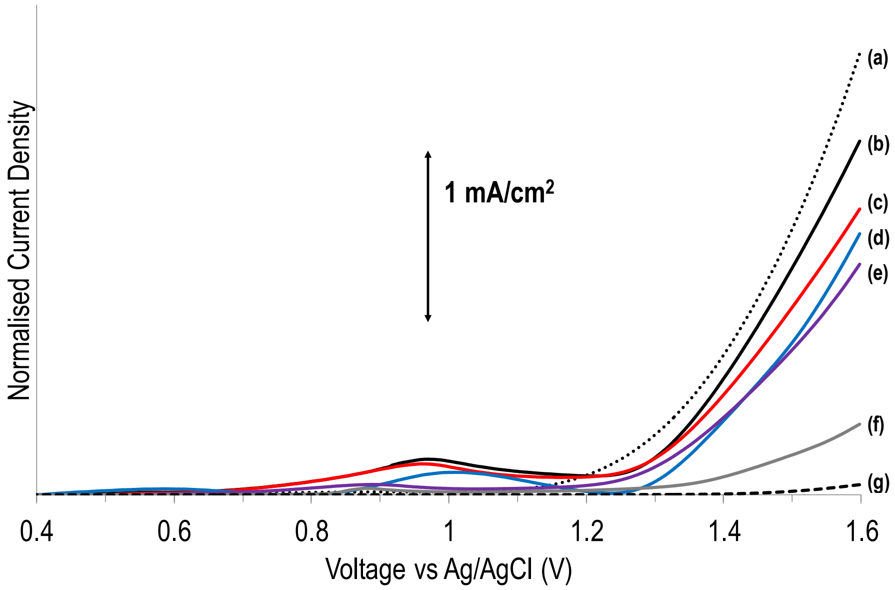

Figure 6.6 Normalised, dark, LSV of Mn_xO_y-FTO at varying deposition time: (a) Pt-FTO, (b) Mn_xO_y-FTO 10 min, (c) Mn_xO_y-FTO 5 min, (d) Mn_xO_y-FTO 15 min, (e) Mn_xO_y-FTO 2.5 min, (f) Mn_xO_y-FTO 1 min, (g) FTO.

The samples were tested by LSV (without illumination) and shown to display current densities that depended on the deposition time (Figure 6.6). The sample deposited for 10 min showed the highest current density, with the others featuring diminishing water oxidation current. Interestingly, both longer and shorter deposition times delivered a lower result, indicating 10 min as a stable optimum in deposition time for this substrate.

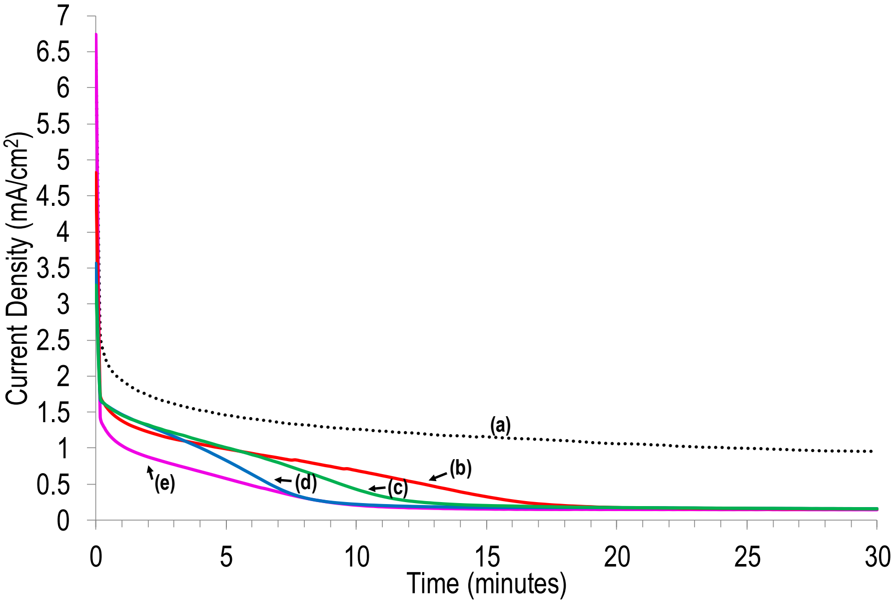

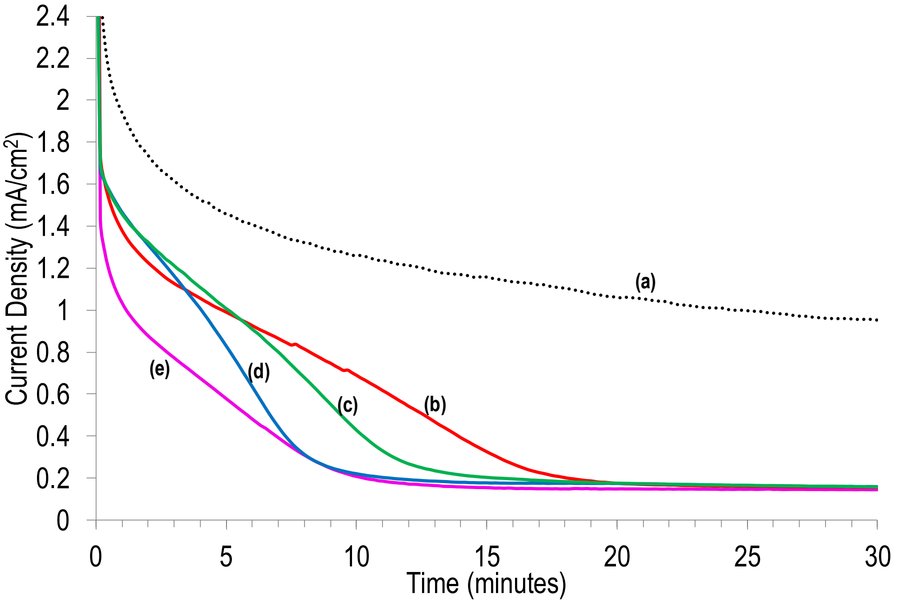

Figure 6.7 CA of Mn_xO_y-FTO and Pt at 1.6 V (*vs* Ag/AgCl) full view (top) and zoomed in (bottom): (a) Pt-FTO, (b) Mn_xO_y-FTO 5 min, (c) Mn_xO_y-FTO 15 min, (d) Mn_xO_y-FTO 10 min, (e) Mn_xO_y-FTO 2.5 min.

These samples were then tested by CA at a set potential of 1.6 V over 30 min (Figure 6.7). This elucidated the long-term catalytic performance of the films. Pt-FTO was also tested and the spectrum kept for benchmarking. From the data it is clear that the current densities of the Mn_xO_y-FTO samples decayed much faster than that of Pt-FTO, indicating a lower activity and probable degradation of the film during water oxidation. Pt-FTO achieved a current density of 0.95 mA/cm^2 after 30 min while most Mn_xO_y samples dropped to ca. 0.1 mA/cm^2 around the 12 min mark. The 5 min deposition sample lasted the longest at 15 min before losing its activity. Whilst capable of delivering high current densities with some gas bubble formation, the long term performance of this catalyst was still limited, at least in its current form.

6.3.4 Electrochemical testing of Mn_xO_y-GO-FTO

Mn_xO_y was deposited on spray-coated GO-FTO (see section 6.2.2.3) to test the effect of GO substrate on the water oxidation performance of the catalyst. The resulting films exhibited the familiar orange-brown colour of Mn_xO_y on top of the light brown GO-FTO substrates (Figure 6.8).

(a) (b) (c) (d)

Figure 6.8 Photograph of GO-FTO at thickness of (a) 138 nm and (b) 69 nm. Mn_xO_y on GO-FTO of substrate thickness (a) 138 nm and (b) 69 nm.

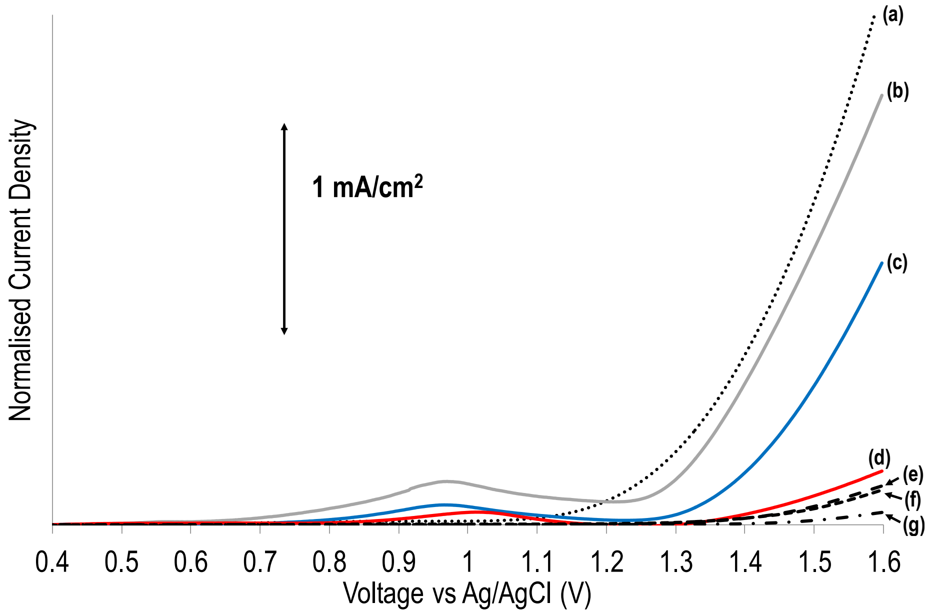

Figure 6.9 Normalised, dark, LSV of Mn_xO_y-GO-FTO samples in comparison with reference data: (a) Pt-FTO, (b) Mn_xO_y-FTO 10 min, (c) Mn_xO_y-GO(69 nm)-FTO, (d) Mn_xO_y-GO(138 nm)-FTO, (e) GO(69 nm)-FTO, (f) GO(138 nm)-FTO. All of this data is not corrected for internal resistance of the substrate.

The samples were then tested by LSV without light illumination, which showed that the addition of GO to the electrodeposited Mn_xO_y system overall did not increase the water splitting performance relative to Pt-FTO and best performing Mn_xO_y–FTO (although this was raw data that did not take account of the higher internal electrical resistance of the GO relative to FTO and Pt) (Figure 6.9).

6.3.5 Electrochemical testing of Mn_xO_y-RLCGO-PET

Mn_xO_y was electrodeposited on RLCGO-PET as per the method explained in section 6.2.2.3. RLCGO-PET was previously synthesised and cast by blade-coating on the PET by Dr Rouhollah Jalili, using the method explained in section 6.2.1.3. The Mn_xO_y films were deposited for 2.5 min, 5 min and 10 min.

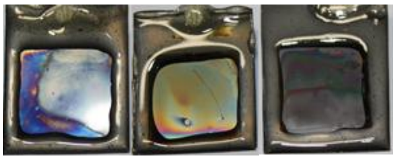
(a) (b) (c)

Figure 6.10 Photograph of Mn_xO_y-RLCGO-PET, where the Mn_xO_y layer had been electrodeposited for (a) 2.5 min, (b) 5 min, (c) 10 min.

The electrodeposition of Mn_xO_y on the graphene-PET substrate RLCGO-PET was successful as could be evidenced by visible colouration of the surface. (Figure 6.10). The different patterns likely come about through subtle variations on the surface and thickness of deposition across the sample.

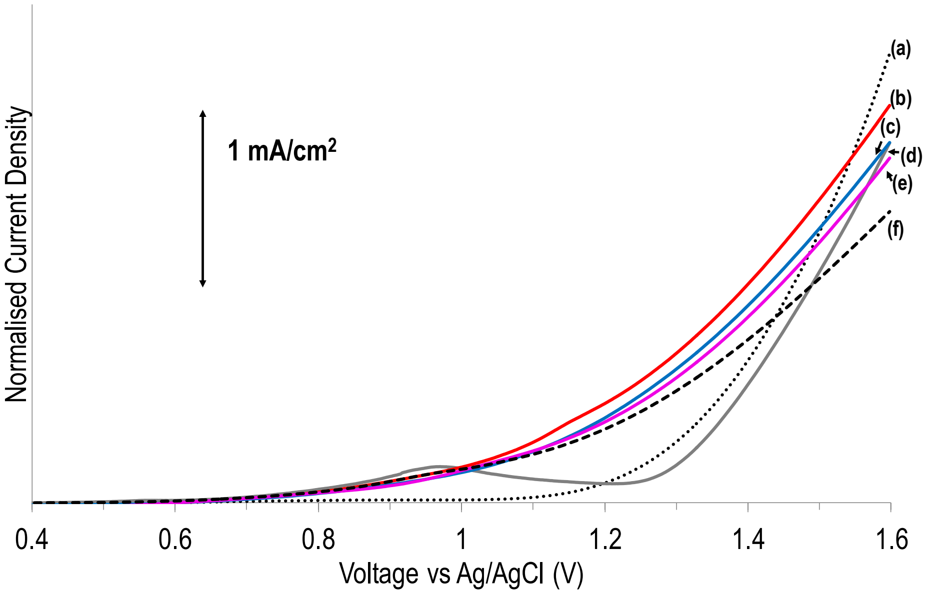

Figure 6.11 Normalised, dark, LSV of Mn_xO_y-RLCGO-PET compared to reference spectra: (a) Pt-FTO, (b) Mn_xO_y-RLCGO-PET 5 min, (c) Mn_xO_y-RLCGO-PET 2.5 min, (d) Mn_xO_y-FTO 10 min, (e) Mn_xO_y-RLCGO-PET 10 min, (f) RLCGO-PET.

The samples were tested by LSV without light illumination (Figure 6.11). The Mn_xO_y-RLCGO-PET with 5 min deposition time exhibited the highest current density so far recorded for the experimental samples, yielding 2.23 mA/cm^2 at 1.6 V. The highest was Mn_xO_y-FTO at 2.02 mA/cm^2. An interesting point to note was the higher current density in the region of 1.2 – 1.6 V for the Mn_xO_y-RLCGO-PET compared to Mn_xO_y-FTO and even Pt-FTO.

The prior LSVs did not take account of the higher internal electrical resistance of the RLCGO substrate relative to the more highly conducting FTO or Pt substrates in the control samples. In samples with such a substrate, a significant ohmic potential drop occurs in the plane of the electrode when operating, since the current is collected at the edge. The effect of this ohmic drop can be corrected for as follows:

If Sheet Resistance is R_s (Ω /□), then total linear resistance R_L, of sheet area L (length) x W (width) (along L direction) is:

$$R_L = R_s \times L/W \ (\Omega)$$

In the tested samples, L = W (~ 1.4 cm) and R_L equals R_s = 30 Ω . The average resistance of the active area along the L direction is therefore half of this, namely, R_L /2 = 20 Ω. The sheet resistance-corrected electrochemical voltage, ***V*** (corrected), corresponding to an operating current density of ***I*** (mA/cm^2) is therefore:

$$V\,(\text{corrected}) = V\,(\text{measured}) - \boldsymbol{I} \cdot L \cdot W \cdot 15 \cdot 10^{-3} \ (\text{Volts})$$

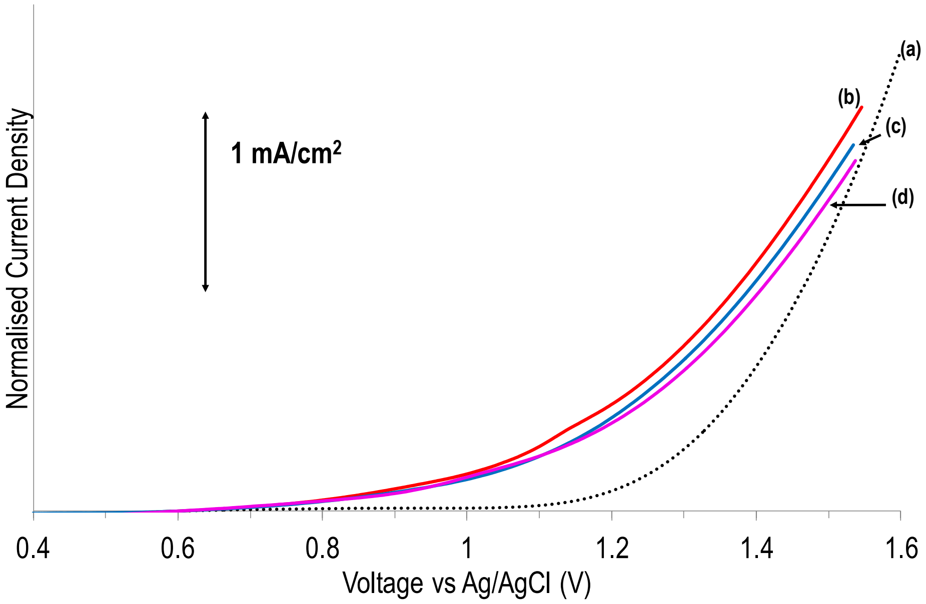

Figure 6.12 Normalised, IR-corrected LSV of Mn_xO_y-RLCGO-PET: (a) Pt-FTO, (b) Mn_xO_y-RLCGO-PET 5 min, (c) Mn_xO_y-RLCGO-PET 2.5 min, (d) Mn_xO_y-RLCGO-PET 10 min

This was applied to the Mn_xO_y-RLCGO-PET LSV data (Figure 6.12). Perhaps the most remarkable results of this thesis was observed when using this approach to take into account the much higher internal resistance of the RLCGO substrate relative to FTO or Pt. Under those circumstances, the Mn_xO_y-RLCGO-PET at 5 min deposition time exhibited a higher current density than the Pt-FTO control over the entire region 0.8 – 1.6 V (*vs* Ag/AgCl). In this respect, the above data testifies to a notable catalytic power in water oxidation catalysis by the combination of a Mn_xO_y (birnessite) layer on a reduced, liquid crystalline graphene oxide layer.

The films were further tested by CA to examine their performance over longer periods of time. CA experiments of this type cannot be adjusted to take into account the internal resistance because the constantly changing current density means that the internal resistance also changes constantly.

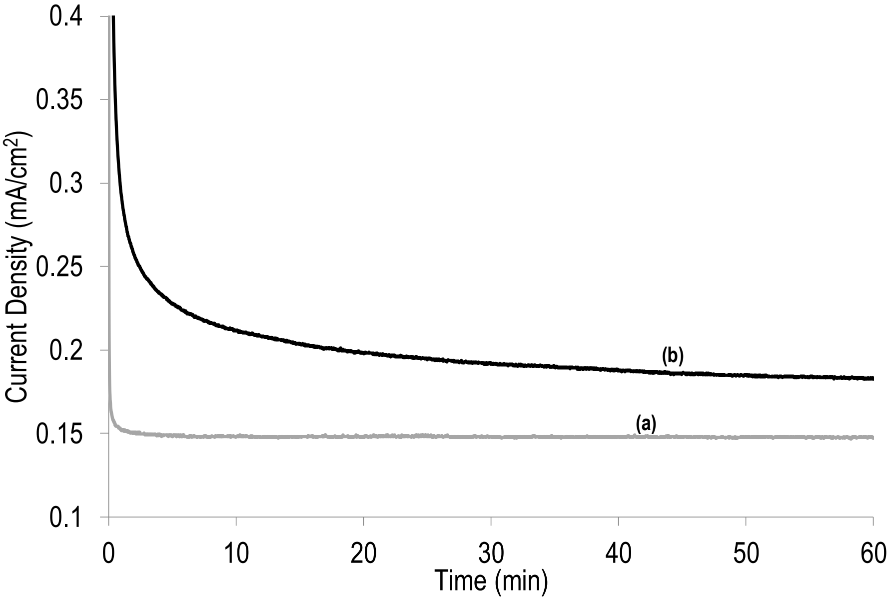

Figure 6.13 CA, without iR-correction, of (a) Pt-FTO, (b) Mn_xO_y-RLCGO-PET 5 min at 1.1 V (*vs* Ag/AgCl).

The first CA experiment involved maintaining a fresh Mn_xO_y-RLCGO-PET 5 min sample at a voltage of 1.1 V (*vs* Ag/AgCl) (Figure 6.13). Even without correction for the internal resistance of the RLCGO substrate, the current density displayed by Mn_xO_y-RLCGO-PET consistently stayed above that of Pt for the full 60 min measurement time. The Mn_xO_y-RLCGO-PET therefore provides a sustained, powerful catalytic effect in water oxidation. This effect clearly exceeded the activity of Pt at low applied voltages.

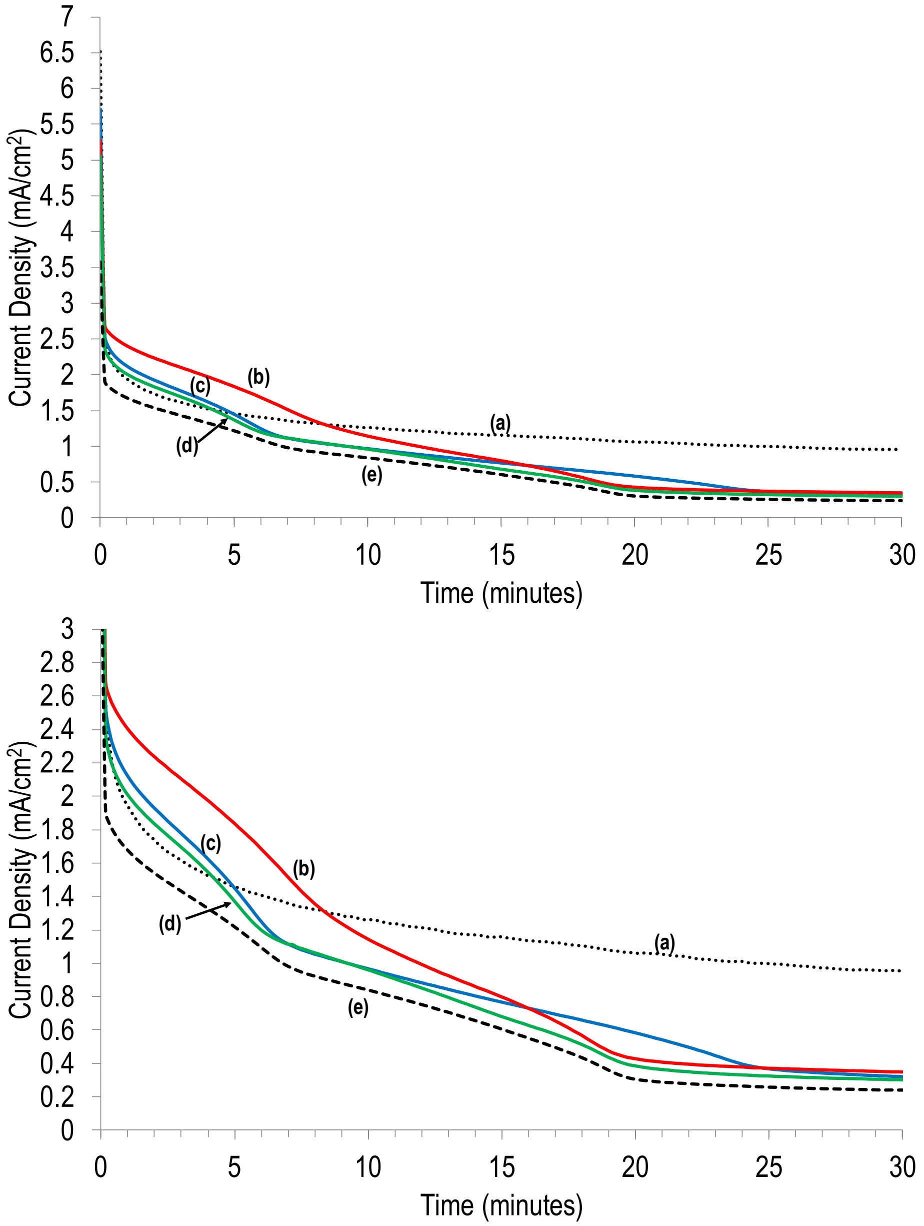

Figure 6.14 CA of Mn_xO_y-RLCGO-PET and reference samples at 1.6 V (*vs* Ag/AgCl), full view (top) and zoomed in (bottom): (a) Pt-FTO, (b) Mn_xO_y-RLCGO-PET 5 min, (c) Mn_xO_y-RLCGO-PET 2.5 min, (d) Mn_xO_y-RLCGO-PET 10 min, (e) RLCGO-PET.

The films were also tested by CA at 1.6 V to examine their performance at higher applied voltages over longer periods of time (Figure 6.14). The testing had again to be done without correction for the internal resistance of the RLCGO substrate. Pt-FTO achieved around 1 mA/cm^2 after 30 min under these conditions. All Mn_xO_y-RLCGO samples however displayed a gradual decrease over time, towards a current density of ca. 0.2 - 0.4 mA/cm^2 after 30 min. Furthermore two distinctive declines were observed in the 0 – 7 min and 10 – 20 min regions. It is unclear what caused these decreases.

6.3.6 Electrochemical testing of Mn_xO_y-RLCGO+Ca-PET

Mn_xO_y was electrodeposited on RLCGO-PET modified by soaking in $CaCl_2$ solution (1 M) prior to deposition (see section 6.2.1.5), resulting in Mn_xO_y-RLCGO+Ca-PET, as per the method outlined in section 6.2.2.3. The sample was electrodeposited with Mn_xO_y for 2.5 min or 10 min. The modification to the substrate was done in an attempt to incorporate Ca into the RLCGO with the Mn_xO_y film deposited on top.

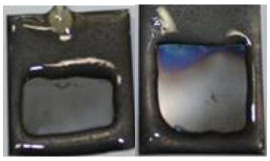

(a) (b)

Figure 6.15 Photograph of Mn_xO_y-RLCGO+Ca-PET electrodeposited for (a) 2.5 min, (b) 10 min

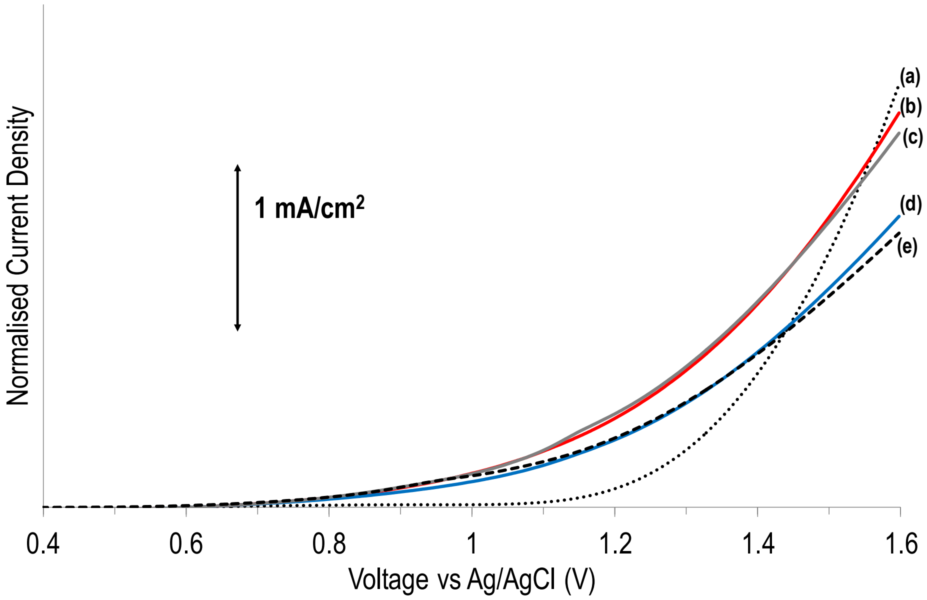

Figure 6.16 Normalised, dark, LSV without iR-correction of Mn_xO_y-RLCGO+Ca-PET compared to reference spectra: (a) Pt-FTO, (b) Mn_xO_y-RLCGO+Ca-PET 2.5 min, (c) Mn_xO_y-RLCGO-PET 5 min, (d) Mn_xO_y-RLCGO+Ca-PET 10 min, (e) RLCGO-PET.

The resulting samples produced less visible films than on RLCGO–PET though still noticeably coloured (Figure 6.15). The samples were then tested by LSV without taking into account the internal resistance of the RLCGO+Ca substrate (Figure 6.15). The Mn_xO_y-RLCGO+Ca-PET having 2.5 min deposition time, exhibited a current density comparable to that of the previous high performing sample Mn_xO_y-RLCGO-PET without Ca. The current density maximum was nonetheless slightly above that with 2.35 mA/cm^2 at 1.6 V.

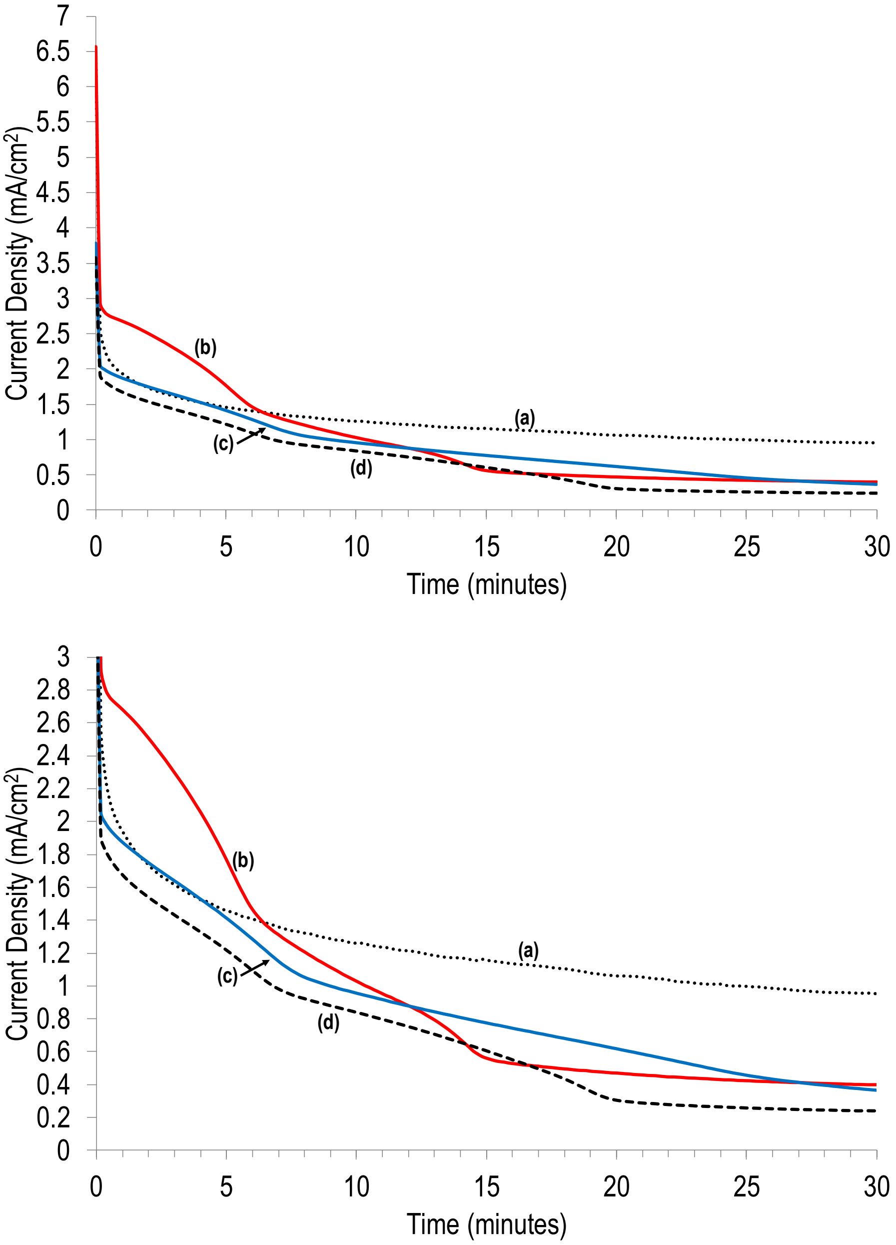

Figure 6.17 CA of Mn_xO_y-RLCGO+Ca-PET films at 1.6 V (*vs* Ag/AgCl), full view (top) and zoomed in (bottom): (a) Pt-FTO, (b) Mn_xO_y-RLCGO+Ca-PET 2.5 min, (c) Mn_xO_y-RLCGO+Ca-PET 10 min, (d) RLCGO-PET.

The films were then tested by CA at 1.6 V, without correction for internal resistance, to examine their performance over longer periods of time (Figure 6.17). All samples showed a gradual decrease over time towards a current density of ca, 0.2 – 0.4 mA/cm^2. The two distinct declines in the regions 0 – 7 min and 10 – 20 min that were seen previously, were also observed in these experiments. It was unclear at this point what caused this stepwise decrease. It was possible that there was a stepwise degradation of the MnO_x-RLCGO system due to overoxidation.

6.3.7 Electrochemical testing of Mn_xO_y-CaRLCGO-FTO

In this experiment, Mn_xO_y was deposited onto RLCGO that had been previously modified by the addition of $CaCl_2$ during the chemical reduction step and casting onto FTO glass (see sections 6.2.1.5 and 6.2.2.3).

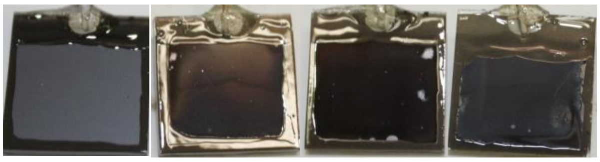

Figure 6.18 Photograph of Mn_xO_y-CaRLCGO-FTO, from left to right: CaRLCGO-FTO substrate, 2.5 min, 5 min and 10 min deposition of Mn_xO_y.

The electrodeposition of Mn_xO_y was carried out on the CaRLCGO substrate for 2.5 min, 5 min and 10 min, resulting in a more obvious, deposited orange layer on the CaRLCGO surface (Figure 6.18).

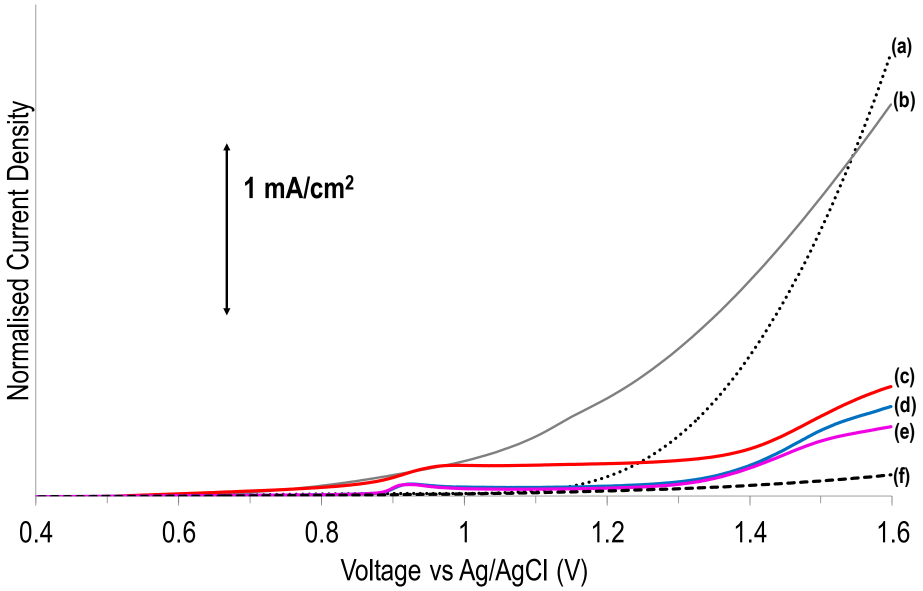

Figure 6.19 Normalised,dark, LSV of Mn_xO_y-CaRLCGO-FTO compared to reference spectra: (a) Pt-FTO, (b) Mn_xO_y-RLCGO-PET 5 min, (c) Mn_xO_y-CaRLCGO-FTO 10 min, (d) Mn_xO_y-CaRLCGO-FTO 5 min, (e) Mn_xO_y-CaRLCGO-FTO 2.5 min, (f) CaRLCGO-FTO.

The Mn_xO_y-CaRLCGO-FTO films were then tested by LSV without correction for the internal resistance of the CaRLCGO substrate (Figure 6.19) and returned lower current densities than the earlier-studied Mn_xO_y-RLCGO-PET film (Figure 6.19(b)). The Mn_xO_y-CaRLCGO-FTO films additionally exhibited clear signs of crumpling and detachment of the Mn_xO_y film from the CaRLCGO substrate, which explains their irregular LSV spectra at voltages positive of ca. 1 V (Figure 6.19(c)-(e)).

6.3.8 Electrochemical testing of Mn_xO_y-CaRLCGO-PET

Following from the CaRLCGO casting on FTO glass, the same material was prepared and cast on Multapex PET as in the initial RLCGO-PET experiment (see 6.2.1.5). A layer of Mn_xO_y was then electrodeposited on these electrodes for 2.5 min, 5 min and 10 min.

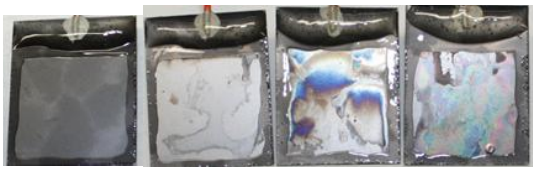
(a) (b) (c) (d)

Figure 6.20 Photograph of (a) CaRLCGO-PET substrate, and Mn_xO_y-CaRLCGO-PET electrodeposited for (b) 2.5 min, (c) 5 min, (d) 10 min.

The electrodeposition experiment resulted in colourful films atop the substrate (Figure 6.20). Interestingly, the CaRLCGO-PET featured large dark speckles on the substrate surface that were not observed before on either RLCGO-PET or CaRLCGO-FTO. This could indicate a degree of inhomogeneity in the film, which could make results difficult to reproduce.

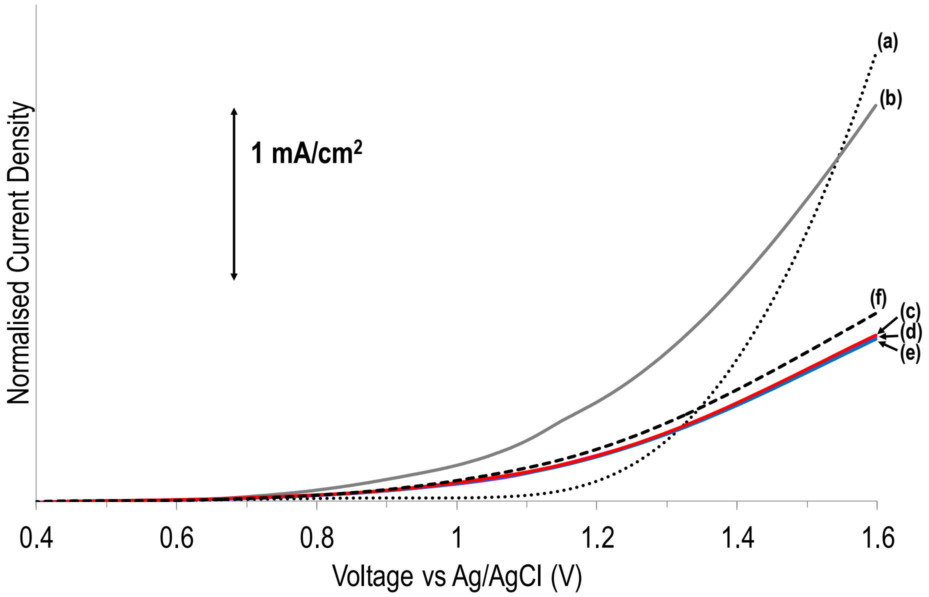

Figure 6.21 Normalised, dark, LSV of Mn_xO_y-CaRLCGO-PET compared to reference spectra: (a) Pt-FTO, (b) Mn_xO_y-RLCGO-PET 5 min, (c) Mn_xO_y-CaRLCGO-PET 2.5 min, (d) Mn_xO_y-CaRLCGO-PET 10 min, (e) Mn_xO_y-CaRLCGO-PET 5 min, (f) CaRLCGO-PET.

The Mn_xO_y-CaRLCGO-PET films were tested by LSV without correction for internal resistance (Figure 6.21), and exhibited lower raw current densities than the Mn_xO_y-RLCGO-PET (Figure 6.21(b)). Indeed the substrate without Mn_xO_y seemed to deliver current densities higher than that of the electrodeposited samples.

6.4 Conclusions

In this chapter the addition of Ca to the Mn_xO_y birnessite system was attempted by means of either during the electrodeposition step or by modifying the substrate material to contain Ca ions. When $Ca(AcO)_2$ was added to the $Mn(AcO)_2$ reagent mixture used for electrodeposition the resulting samples featured a clearly diminished catalytic current, therefore this method of addition was discontinued. Because of time constraints the more promising of these composites were studied in greater detail while those underperforming were ruled out after initial testing. As the samples were made following a literature procedure [37] the resulting material was assumed to contain birnessite given the similar water oxidation behaviour, however the precise crystallographic properties of the material were not studied due to time constraints.

The Mn_xO_y-RLCGO-PET samples delivered the highest current densities in this chapter, rivalling the performance of the control Pt sample and demonstrating an improvement over Mn_xO_y on FTO. Additionally, after 60 minutes of electrolysis at a constant potential of 1.1 V (*vs* Ag/AgCl) the material featured a higher catalytic current than that of Pt, with 0.184 mA/cm^2 *vs* 0.148 mA/cm^2 for Pt. Though not optimised, this presents a benefit for water oxidation at near-neutral pH.

The subsequent attempts at improving that performance through the addition of Ca in the substrate did not deliver an increase in current density. The Ca modified RLCGO, whether deposited on FTO or PET, did not lead to an increase in electrochemical activity of the Mn_xO_y-graphene composite material. The role of Ca in the OEC could not be replicated by this process as it was likely not incorporated into the Mn_xO_y crystal structure. The notable difference between the $CaMn_4O_4$ cluster in nature and this artificial structure is that the biological catalyst consists of a single metal oxide molecule rather than a continuous crystal lattice with localised active sites. This limits the viability of the combinatorial approach used in this study as opposed to a more precise assembly method.

6.5 References

1. Barber, J., Quarterly Reviews of Biophysics, 2003. **36**(1): p. 71-89.
2. Barber, J., Chemical Society Reviews, 2009. **38**(1): p. 185-196.
3. Chuah, W.Y., R. Stranger, R.J. Pace, E. Krausz, and T.J. Frankcombe, The Journal of Physical Chemistry B, 2014. **118**(13): p. 3553-3558.
4. Pace, R.J., L. Jin, and R. Stranger, Dalton Transactions, 2012. **41**(36): p. 11145-11160.
5. Pace, R.J., R. Stranger, and S. Petrie, Dalton Transactions, 2012. **41**(24): p. 7179-7189.
6. Gatt, P., S. Petrie, R. Stranger, and R.J. Pace, Angewandte Chemie International Edition, 2012. **51**(48): p. 12025-12028.
7. Petrie, S., R.J. Pace, and R. Stranger, Angewandte Chemie International Edition, 2015. **54**(24): p. 7120-7124.
8. Terrett, R., S. Petrie, R.J. Pace, and R. Stranger, Chemical Communications, 2014. **50**(24): p. 3187-3190.
9. Swiegers, G.F., J.K. Clegg, and R. Stranger, Chemical Science, 2011. **2**(11): p. 2254-2262.
10. Robinson, D.M., Y.B. Go, M. Greenblatt, and G.C. Dismukes, Journal of the American Chemical Society, 2010. **132**(33): p. 11467-11469.

11. Hocking, R. and L. Spiccia. *Abstract 155*. in *39th International Conference on Coordination Chemistry*. 2010. Adelaide, Australia.

12. Kanan, M.W. and D.G. Nocera, Science, 2008. **321**(5892): p. 1072-1075.

13. Lutterman, D.A., Y. Surendranath, and D.G. Nocera, Journal of the American Chemical Society, 2009. **131**(11): p. 3838-3839.

14. McAlpin, J.G., Y. Surendranath, M. Dincă, T.A. Stich, S.A. Stoian, W.H. Casey, D.G. Nocera, and R.D. Britt, Journal of the American Chemical Society, 2010. **132**(20): p. 6882-6883.

15. Kanan, M.W., J. Yano, Y. Surendranath, M. Dincă, V.K. Yachandra, and D.G. Nocera, Journal of the American Chemical Society, 2010. **132**(39): p. 13692-13701.

16. Jiao, F. and H. Frei, Energy & Environmental Science, 2010. **3**(8): p. 1018-1027.

17. Jiao, F. and H. Frei, Angewandte Chemie International Edition, 2009. **48**(10): p. 1841-1844.

18. Liu, X. and C.T. Prewitt, Physics and Chemistry of Minerals, 1990. **17**(2): p. 168-172.

19. Yin, Q., J.M. Tan, C. Besson, Y.V. Geletii, D.G. Musaev, A.E. Kuznetsov, Z. Luo, K.I. Hardcastle, and C.L. Hill, Science, 2010. **328**(5976): p. 342-345.

20. Dismukes, G.C., R. Brimblecombe, G.A.N. Felton, R.S. Pryadun, J.E. Sheats, L. Spiccia, and G.F. Swiegers, Accounts of Chemical Research, 2009. **42**(12): p. 1935-1943.

21. Yeh, T.-F., J. Cihlář, C.-Y. Chang, C. Cheng, and H. Teng, Materials Today, 2013. **16**(3): p. 78-84.

22. Kim, H.-i., G.-h. Moon, D. Monllor-Satoca, Y. Park, and W. Choi, The Journal of Physical Chemistry C, 2012. **116**(1): p. 1535-1543.

23. Lv, X.-J., W.-F. Fu, H.-X. Chang, H. Zhang, J.-S. Cheng, G.-J. Zhang, Y. Song, C.-Y. Hu, and J.-H. Li, Journal of Materials Chemistry, 2012. **22**(4): p. 1539-1546.

24. Xiang, Q., J. Yu, and M. Jaroniec, Nanoscale, 2011. **3**(9): p. 3670-3678.

25. Xiang, Q., J. Yu, and M. Jaroniec, Journal of the American Chemical Society, 2012. **134**(15): p. 6575-6578.

26. Zhang, X., Y. Sun, X. Cui, and Z. Jiang, International Journal of Hydrogen Energy, 2012. **37**(1): p. 811-815.

27. Zhang, X.-Y., H.-P. Li, X.-L. Cui, and Y. Lin, Journal of Materials Chemistry, 2010. **20**(14): p. 2801-2806.

28. Zou, F., Y. Yu, N. Cao, L. Wu, and J. Zhi, Scripta Materialia, 2011. **64**(7): p. 621-624.

29. Cao, A., Z. Liu, S. Chu, M. Wu, Z. Ye, Z. Cai, Y. Chang, S. Wang, Q. Gong, and Y. Liu, Advanced Materials, 2010. **22**(1): p. 103-106.

30. Zeng, P., Q. Zhang, T. Peng, and X. Zhang, Physical Chemistry Chemical Physics, 2011. **13**(48): p. 21496-21502.

31. Moo, J.G.S., A. Ambrosi, A. Bonanni, and M. Pumera, Chemistry – An Asian Journal, 2012. **7**(4): p. 759-770.

32. Pumera, M., Electrochemistry Communications, 2013. **36**: p. 14-18.

33. Jalili, R., S.H. Aboutalebi, D. Esrafilzadeh, K. Konstantinov, S.E. Moulton, J.M. Razal, and G.G. Wallace, ACS Nano, 2013. **7**(5): p. 3981-3990.

34. Jalili, R., S.H. Aboutalebi, D. Esrafilzadeh, R.L. Shepherd, J. Chen, S. Aminorroaya-Yamini, K. Konstantinov, A.I. Minett, J.M. Razal, and G.G. Wallace, Advanced Functional Materials, 2013. **23**(43): p. 5345-5354.

35. Li, D., M.B. Müller, S. Gilje, R.B. Kaner, and G.G. Wallace, Nature Nanotechnology, 2008. **3**(2): p. 101-5.

36. Naficy, S., R. Jalili, S.H. Aboutalebi, R.A. Gorkin Iii, K. Konstantinov, P.C. Innis, G.M. Spinks, P. Poulin, and G.G. Wallace, Materials Horizons, 2014. **1**(3): p. 326-331.

37. Zhou, F., A. Izgorodin, R.K. Hocking, V. Armel, L. Spiccia, and D.R. MacFarlane, ChemSusChem, 2013. **6**(4): p. 643-651.

38. Kovtyukhova, N.I., P.J. Ollivier, B.R. Martin, T.E. Mallouk, S.A. Chizhik, E.V. Buzaneva, and A.D. Gorchinskiy, Chemistry of Materials, 1999. **11**(3): p. 771-778.

39. Park, S., K.-S. Lee, G. Bozoklu, W. Cai, S.T. Nguyen, and R.S. Ruoff, ACS Nano, 2008. **2**(3): p. 572-578.

7 Summary and conclusions

7.1 Porphyrin/PEDOT

The matrix-assisted effect of PEDOT on photocatalytic species of Mn porphyrins was explored in greater detail in a systematic study. MnTPPS was identified as a efficient photocatalyst when embedded in VPP PEDOT [1] and used in this study as a starting point. This was expanded on by testing the species MnTMPyP, ion-paired MnTMPyP+MnTPPS and MnTPP at varying concentrations in VPP PEDOT in order to study critical parameters to the photoelectrochemical activity of the material in water. In a following experiment the inclusion of MnTPPS as well as MnPVTPPS in PEDOT:PSS by electrochemical polymerisation was successfully demonstrated. The composite materials were tested in a voltage range of 0-0.7 V (*vs* Ag/AgCl) where the photocurrent was correlated to water oxidation in the absence of any other species that could be oxidised at that potential. The materials were then examined by UV-Vis spectroscopy to investigate the nature of the metalloporphyrins in the composite film samples.

Of the VPP PEDOT based composites, MnTPP/PEDOT has shown to feature the highest photocurrent density, 4.01 μA/cm^2 for a porphyrin concentration of 1 mg/mL at 0.7 V (*vs* Ag/AgCl) and was singled out for further study. The material was tested in a combined photoelectrochemical and gas chromatography apparatus confirming the evolution of oxygen gas. The material was then studied in greater detail by elemental analysis. UV-Vis analysis of the porphyrin that leached out of the material was also carried out. It was found that the porphyrin had become free base during vapour phase polymerisation and no longer contained the Mn ion in the core. The resulting material was then shown to be identical to the free base TPP/PEDOT. At higher concentrations of MnTPP this phenomenon did not occur and the presence of Mn(III)TPP was confirmed by UV-Vis analysis.

The demetallation process undergoes through reductive step from Mn^{3+} to Mn^{2+} what was demonstrated experimentally and is in agreement with the published studies [2, 3]. However, how the reduction process occurs in highly oxidative environment is not obvious. The exact mechanism of this reaction remains unclear and will require further studies which are not the scope of this thesis. It was therefore shown that the combination of Mn porphyrins with PEDOT at lower concentration did not leave the metalloporphyrin intact. The mentioned above composite resulted in the simultaneous production of H_2 and O_2 in photoelectrochemical experiments, which was confirmed by gas chromatography (GC). However, the source of the gases is, likely, the photoelectrochemical decomposition of the TPP inside the PEDOT matrix.

The electrochemically polymerised species MnPVTPPS/PEDOT:PSS also featured a high photocurrent of 5.00 $\mu A/cm^2$ at the lower voltage of 0.65 V (*vs* Ag/AgCl). Further analysis of the material revealed a similar phenomenon to that found in the MnTPP/PEDOT system, that the Mn ion was lost from the porphyrin during the fabrication of the composite material.

7.2 Mn_xO_y-graphene

In subsequent studies a cubane-like birnessite Mn_xO_y catalyst made by electrodeposition [4] was investigated. In this case the effect of reduced liquid crystalline graphene on the Mn oxide and the effect of Ca ions in close proximity were examined. The Mn_xO_y species were electrodeposited on the substrates, namely, (i) FTO glass, (ii) graphene oxide (GO) sprayed on FTO glass, (iii) reduced liquid crystalline graphene oxide (RLCGO) blade-coated onto PET. Furthermore, reduced liquid crystalline graphene was modified with Ca ions prior to the reduction step, resulting in CaRLCGO on PET and FTO glass.

It has been proven that Ca addition to the Mn oxides was not beneficial to the electrochemical activity of the catalyst in an aqueous electrolyte. The Mn_xO_y-RLCGO-PET composite featured high current densities in the region 1.1 – 1.6 V (*vs* Ag/AgCl), were performing better than those of a comparative Pt film. Those results indicate the high performance of this type of material in a near-neutral aqueous electrolyte, in contrast to the high pH environments typically used in water oxidation catalysis. The low overpotential necessary for the efficient catalytic water oxidation by this system is an important advantage as the composite is made of Earth abundant, inexpensive reagents and would function under relatively benign operating conditions that do not require a high pH. This makes the material a prime contender for future studies in order to deeper investigate the critical factors for optimal performance. A more thorough investigation and optimisation of this composite system is currently scheduled pending patent approval.

7.3 Conclusions and future work

The investigation of porphyrin/PEDOT and Mn_xO_y-graphene composite materials in this work has yielded the following conclusions:

Low concentrations of Mn porphyrin added to PEDOT during polymerisation, regardless of the method, leads to demetallation of the complex. This is an unusual finding as the ion is labile only in the Mn(II) oxidation state of the Mn porphyrins tested [2, 3] whereas in Mn(III) and Mn(IV) remains stable. This would imply that reduction of the porphyrin has occurred in the fabrication of the composite which seems counter-intuitive considering the oxidative chemical environment in the process of fabrication. This might be the result of light-driven reaction and a possible other catalytic effect with a small turnover number. In order to retain the Mn in the porphyrin core a higher concentration of Mn porphyrin in PEDOT is needed. Further research would be necessary to fully explain this phenomenon.

Reduced liquid crystalline graphene oxide offers a novel substrate material for water oxidation catalysis. In this study it was shown that RLCGO enhances the catalytic activity of Mn_xO_y. It is likely that further optimisation could lead to a very efficient catalytic species that operates reliably in water conditions that are more similar to natural water systems than what is currently employed for water electrolysis. This new, innovative material will be approached by more detailed study of the formation of the catalytic species on the substrate. Furthermore it is likely that the graphene substrate can be chemically altered to facilitate a better integration of and interaction with catalyst. The follow-up of this important finding will be done in collaboration with Dr Ron Pace at the Australian National University.

7.4 References

1. Chen, J., P. Wagner, L. Tong, D. Boskovic, W. Zhang, D. Officer, G.G. Wallace, and G.F. Swiegers, Chemical Science, 2013. **4**(7): p. 2797-2803.
2. Morehouse, K.M. and P. Neta, The Journal of Physical Chemistry, 1984. **88**(14): p. 3118-3120.
3. Tsuda, Y., K. Takahashi, T. Yamaguchi, S. Matsui, and T. Komura, Journal of Molecular Catalysis A: Chemical, 1998. **130**(3): p. 285-295.
4. Zhou, F., A. Izgorodin, R.K. Hocking, V. Armel, L. Spiccia, and D.R. MacFarlane, ChemSusChem, 2013. **6**(4): p. 643-651.